

# SQuAre: Scalable Qubit Arrays for Quantum Computation and Optimisation

Boyko Nikolov

---

## Abstract

The work described in this thesis summarises some of the key milestones achieved in the development of the UK's first quantum computer based on arrays of neutral atoms, delivered in partnership with M Squared Lasers Ltd. These milestones include the commissioning of the 1064 nm optical dipole trapping system for holographic array generation, assembly and testing of a low phase noise microwave source used for global single qubit rotations and the calibration of the Rydberg laser system locked to a narrow linewidth ultralow expansion reference cavity.

Using  $^{133}\text{Cs}$  atoms, we demonstrate high-fidelity control over large scale arrays with over 225 trap sites ( $> 100$  qubits) by performing randomised benchmarking (RB). The recorded average single qubit gate fidelity of  $0.99993(2)$ , achieved using a global microwave driving field with composite pulses, is the highest recorded fidelity on any platform of this size and comfortably meets the thresholds of many error correction codes. To further advance the field towards realising error correction, we also present the first practical application of a non-destructive readout (NDRO) procedure based on a cycling transition in alkali atoms. By increasing the trap depth and reducing the array size to 49, the largest array size achieved with this technique to date, we are able to demonstrate suppression of state preparation and measurement errors during RB by a factor of 1.7 without affecting the average gate fidelity.

Finally, we present some early analogue simulation results of the quantum one-dimensional Ising spin model on arrays of up to 9 atoms. Using this simple, classically tractable problem, we characterise the performance of our platform as an analogue optimisation device and identify key areas of improvement as the experiment evolves into a state where more challenging two-dimensional geometries can be simulated with a view of demonstrating quantum advantage in optimisation problems with practical relevance.

# SQuAre: Scalable Qubit Arrays for Quantum Computation and Optimisation

Boyko Nikolov

---

A thesis submitted in partial fulfilment  
of the requirements for the degree of  
Doctor of Philosophy



Department of Physics  
University of Strathclyde

January 27, 2024

# Contents

	Page
<b>Contents</b>	<b>i</b>
<b>List of Figures</b>	<b>iv</b>
<b>Declaration</b>	<b>vi</b>
<b>1 Introduction</b>	<b>1</b>
1.1 Why Do We Need Quantum Computers? . . . . .	1
1.2 Competing Architectures . . . . .	4
1.3 State of the Art for Rydberg Atom Arrays . . . . .	6
1.4 Analogue Quantum Computing & Optimisation . . . . .	9
1.5 The SQuAre Project . . . . .	9
1.6 Future Research Directions . . . . .	11
1.7 Scope of This Work . . . . .	13
1.8 Publications Arising From This Work . . . . .	14
1.9 Contributions of Others . . . . .	14
<b>2 Theoretical Background</b>	<b>16</b>
2.1 Alkali Atom Wavefunctions . . . . .	17
2.1.1 The Quantum Defect & Central Field Approximations	17
2.1.2 Alkali Wavefunctions in Different Bases . . . . .	20
2.2 Interaction with Static Fields . . . . .	21
2.2.1 Static Magnetic Fields (Zeeman Shift) . . . . .	21
2.2.2 Static Electric Fields (DC Stark Effect) . . . . .	23
2.3 Interaction with Oscillating Fields . . . . .	24
2.3.1 Dipole Matrix Elements . . . . .	24
2.3.2 Magnetic Dipole Matrix Elements . . . . .	27
2.3.3 Optical Two-level System . . . . .	28
2.3.4 Hyperfine Qubit Two Level System . . . . .	32
2.3.5 Propagator for Two-Level System in RWA . . . . .	35
2.3.6 Bloch Sphere Representation . . . . .	36
2.3.7 AC Stark Shift . . . . .	38
2.3.8 Two-Photon Transitions . . . . .	40
2.4 Rydberg Dipole-Dipole Interactions . . . . .	44

<b>3</b>	<b>Experimental Set Up</b>	<b>51</b>
3.1	Vacuum Chamber . . . . .	52
3.2	Magneto Optical Traps (MOTs) & Sub-Doppler Cooling . . .	59
3.2.1	Cooling Laser System . . . . .	59
3.2.2	2D MOT . . . . .	62
3.2.3	3D MOT . . . . .	65
3.2.4	Polarisation Gradient Cooling . . . . .	68
3.3	Holographic Atom Arrays . . . . .	72
3.3.1	Confining Atoms with Light . . . . .	72
3.3.2	Red-Detuned Traps . . . . .	76
3.3.3	Moving Tweezer Trap . . . . .	85
3.4	Fluorescence Imaging of Single Atoms . . . . .	87
3.5	State Preparation & Detection . . . . .	91
3.5.1	Optical Pumping . . . . .	91
3.5.2	State Detection . . . . .	97
3.5.3	Laser Shutters . . . . .	100
3.6	Microwave System . . . . .	101
3.7	Rydberg System . . . . .	110
3.7.1	Lasers . . . . .	110
3.7.2	Narrow-Linewidth Laser Locking . . . . .	115
3.7.3	Rydberg State Detection . . . . .	118
3.7.4	Rydberg System Calibration . . . . .	119
3.7.5	Rydberg Laser Noise Eating . . . . .	125
3.8	Experimental Control System . . . . .	128
<b>4</b>	<b>Microwave Single Qubit Gates</b>	<b>131</b>
4.1	Characterising Qubit Coherence with MWs . . . . .	132
4.2	BB1 Composite Pulses . . . . .	147
4.3	BB1 Pulse Calibration . . . . .	151
4.4	Clifford Group Randomised Benchmarking . . . . .	153
4.5	Randomised Benchmarking Results . . . . .	158
4.6	Conclusion . . . . .	165
<b>5</b>	<b>Non-Destructive Readout (NDRO)</b>	<b>167</b>
5.1	Principle of Operation of NDRO . . . . .	168
5.2	Transfer Sequence for NDRO . . . . .	171
5.2.1	MW Transfer Sequence Simulation . . . . .	171
5.2.2	MW Transfer Sequence Experiment . . . . .	177
5.2.3	NDRO Optical Pumping Simulation . . . . .	180
5.3	Experimental Realisation . . . . .	182
5.4	NDRO for SPAM Error Suppression . . . . .	197
5.5	Conclusion . . . . .	200
<b>6</b>	<b>Analogue Quantum Computation</b>	<b>202</b>
6.1	Quantum Ising Model for 1D Spin Chains . . . . .	202

---

6.2	System Calibration . . . . .	206
6.2.1	Rabi Frequency $\sqrt{N}$ Enhancement . . . . .	207
6.2.2	Dipole-Dipole Interaction Energy Calibration . . . . .	209
6.3	Rydberg Quantum Simulation Results . . . . .	213
6.3.1	Initial Guess for Ramp Parameters . . . . .	215
6.3.2	Experimental Realisation . . . . .	217
6.3.3	Experimental Imperfections . . . . .	220
6.4	Conclusion . . . . .	227
<b>7</b>	<b>Conclusions and Outlook</b>	<b>229</b>
7.1	Conclusion . . . . .	229
	<b>Appendices</b>	<b>233</b>
<b>A</b>	<b>Single Qubit Clifford Gates</b>	<b>234</b>
	<b>Bibliography</b>	<b>236</b>

# List of Figures

Figure	Page
2.1 Core potential plot for caesium $n = 6$ states . . . . .	19
2.2 Two-level system optical Bloch equation time-evolution . . . . .	31
2.3 Illustration of power broadening effect on a transition due to the spontaneous emission incorporated into the OBE model. . . . .	32
2.4 Bloch sphere representation of two-level system . . . . .	38
2.5 Two-photon excitation level diagram . . . . .	40
2.6 Rydberg atom dipole-dipole interactions . . . . .	44
2.7 Rydberg pair potential simulation . . . . .	47
2.8 Rydberg blockade . . . . .	50
3.1 SQuAre experiment vacuum chamber . . . . .	52
3.2 Pressure verification measurement using temporary 3D MOT . . . . .	56
3.3 In-vacuum aspheric lens assembly . . . . .	57
3.4 Caesium D2-line laser frequencies required for cooling and optical pumping . . . . .	59
3.5 Schematic diagram of the 852 nm cooling and repump laser systems . . . . .	60
3.6 852 nm laser modulation transfer lock . . . . .	62
3.7 2D MOT assembly . . . . .	64
3.8 3D MOT beam configuration . . . . .	65
3.9 Photo of the main chamber for the experiment . . . . .	67
3.10 3D MOT loadcurve . . . . .	69
3.11 Polarisation gradient cooling of 3D MOT . . . . .	71
3.12 1064 nm trapping laser schematic . . . . .	76
3.13 Procedure for loading single atoms in 1064 nm traps . . . . .	79
3.14 1064 nm trap temperature and lifetime measurements . . . . .	81
3.15 1064 nm trap frequency measurement. . . . .	83
3.16 1064 nm trap intensity feedback on D1 line . . . . .	85
3.17 SQuAre single atom imaging system schematic . . . . .	88
3.18 Single atom counting using sCMOS camera . . . . .	90
3.19 D1 optical pumping into clock state . . . . .	94
3.20 D2 optical pumping into stretched state . . . . .	97
3.21 Schematic diagram of push out beam in the lab coordinate frame . . . . .	98
3.22 Home-built laser shutter activation response . . . . .	100
3.23 Master oscillator phase noise to fidelity conversion . . . . .	102

3.24	Schematic diagram of 9.2 GHz microwave electronics . . . . .	104
3.25	Microwave spectroscopy of caesium hyperfine ground states . . .	107
3.26	Clock state Rabi frequency calibration . . . . .	109
3.27	Rydberg excitation scheme . . . . .	111
3.28	SQuAre Rydberg laser schematic diagram . . . . .	113
3.29	Rydberg ULE cavity lock measurements . . . . .	117
3.30	Rydberg excitation timing diagram . . . . .	120
3.31	Rydberg resonance calibration methods . . . . .	121
3.32	Rydberg $80S_{1/2}$ Rabi oscillation . . . . .	124
3.33	Rydberg beam waist calibration . . . . .	126
3.34	Rydberg laser intensity stabilisation . . . . .	128
3.35	Typical experimental timing diagram . . . . .	129
4.1	MW Ramsey fringe on 225 site array . . . . .	134
4.2	Ambient temperature drift effect on qubit coherence . . . . .	138
4.3	Microwave spin echo measurements . . . . .	142
4.4	BB1 pulse implementation . . . . .	148
4.5	Variation in microwave resonance across 225 site array . . . .	153
4.6	Single qubit gate randomised benchmarking results on 225 site array . . . . .	159
4.7	Random gate string distributions . . . . .	162
4.8	Randomised benchmarking parameter sensitivity simulation . .	164
5.1	Principle of operation of NDRO . . . . .	169
5.2	16-level hyperfine manifold for microwave transitions . . . . .	173
5.3	Microwave transfer sequence simulations for NDRO . . . . .	175
5.4	Ramsey MW transfer sequence to prevent leakage . . . . .	177
5.5	MW transfer sequence experimental realisation. . . . .	179
5.6	State transfer using NDRO light simulation results . . . . .	183
5.7	Example camera images from NDRO process . . . . .	184
5.8	NDRO optical pumping transfer sequence experimental test . .	185
5.9	NDRO experimental optimisation . . . . .	187
5.10	NDRO leakage error parameter sensitivity . . . . .	194
5.11	Randomised benchmarking with NDRO . . . . .	197
6.1	Mapping of quantum Ising model to Rydberg Hamiltonian . . .	204
6.2	$\sqrt{N}$ enhancement of Rabi frequency . . . . .	208
6.3	Calibration of dipole-dipole interaction strength . . . . .	211
6.4	1D Rydberg atom chain simulation . . . . .	215
6.5	1D atom chain experimental results . . . . .	219
6.6	Focussed vs. collimated beam AOM performance . . . . .	221
6.7	1D atom chain experimental results with upgraded AOM . . .	222
6.8	Population dynamics explaining truncated detuning ramps . .	224
6.9	Maximum likelihood state reconstruction . . . . .	228

## Declaration

I confirm that no part of the material offered has previously been submitted by myself for a degree in this or any other University. Where material has been generated through joint work, the work of others has been indicated.

Boyko Nikolov  
Glasgow, January 27, 2024

The copyright of this thesis rests with the author. No quotation from it should be published without their prior written consent and information derived from it should be acknowledged.

## Acknowledgements

I would like to thank my supervisor, Dr Jonathan Pritchard, for bringing neutral atom quantum computing to the UK. I am also grateful that he gave me the opportunity to work on his project despite my unusual background and for the time he spent training me on the fundamentals of experimental physics work. I did my best to repay his trust and even though I must have made at least one thousand mistakes during my PhD, I can confidently say that it wasn't for lack of trying.

My experience was enriched by everyone on the SQuAre team and I would like to thank you all for contributing to my growth as a physicist: Dr Nicholas Spong, Dr Jonathan Bass, Dr Andre de Oliveira, Dr Daniel Walker and my fellow PhD students soon-to-be-Drs Elliot Diamond-Hitchcock and Paul Ireland. I've enjoyed your company and I look forward to seeing what you all do next. The entire EQOP Group and the wider Physics department have been a pleasure to work with. Special mention goes to the guys in the mechanical and electronics workshops: Bob, Euan, John, Ged, Jerry, and their teams, as well as John Gillan who carries the whole John Andreson Building on his shoulders. We appreciate all the work you do.

I would also like to thank the academics at Strathclyde who supported me on my path from an engineering undergraduate student to starting a PhD in physics. Firstly I am grateful to Dr Helena Gleskova, for her mentorship and encouragement. I would also like to thank Dr Daniel Oi for supporting my summer project funding application and being generous with his time to help me learn about quantum optics. My thanks also go to Dr Lucia Caspani for supervising my final year project in physics, as well as Prof. Stefan Kuhr and Prof. Erling Riis for tolerating a confused engineering student in their fourth year physics classes. I am also grateful to Dr Paul Murray for supporting the VIP programme at Strathclyde, and for all the Wednesday afternoons he spent teaching us about classification algorithms and image processing. Special thanks to Dr Michael Lengden for the entertaining lectures on electromagnetism and for tipping me off about the SQuAre project. I may have ended up in Bristol if he hadn't.

Finally, I would like to thank my parents. I could never pay you back for everything that you've done for me, so I can only hope to pay it forward.

# Chapter 1

## Introduction

### 1.1 Why Do We Need Quantum Computers?

At the time of writing this document, there is significant activity around the world surrounding the theme of quantum computing. The United Kingdom government has allocated a £33 million annual budget to this research theme for the period 2019-2024 [1], Germany has allocated €3 billion for the period up to 2026 and the United States has planned to spend \$844 million in 2023 alone [2]. Given these figures and the increasing media coverage related to quantum technologies, is it still necessary to ask the question why society needs quantum computers more than 40 years since the idea was first proposed in a famous publication by Richard Feynman [3]? Undoubtedly, quantum mechanics has been a successful theory in physics that has given birth to many of the technological advances that characterise modern society and advanced our scientific understanding, but the field is difficult to penetrate without a grounding in the mathematics which describe it.

One of the fundamental challenges in understanding systems described by quantum mechanics is that as the number of particles in a system grows, its information content grows exponentially [4]. In many of these cases the physical models cannot be solved analytically and in scenarios with more than

$\sim 100$  interacting quantum particles, it becomes challenging to even numerically simulate the behaviour of such systems on reasonable timescales using classical supercomputers. This problem is what Feynman's original idea was intended to address by suggesting that the dynamics of an unknown quantum system can be simulated by mapping it onto another quantum system over which we have a high-degree of physical control. The physics community has made tremendous progress in the years since this proposal and we are now able to realise this idea on a variety of different hardware platforms operating in what is referred to as the analogue quantum computing modality [5] that has already produced results which could not have been obtained otherwise [6]. So one answer to the question of why we need quantum computers is that they help us improve our scientific understanding of quantum many body systems. In terms of benefits to society, this understanding could manifest in the discovery of improved materials such as room temperature superconductors, for example, which could boost the efficiency of nuclear fusion reactors [7], enable the roll-out of magnetically levitated trains [8] or hybrid electrical aircraft for reduced emissions [9]. Conveniently, this analogue simulation approach has more general applications than it might first seem. The mathematics that describe a many body quantum system can also be used to describe a range of other problems of general interest to industry and society such as the traveling salesperson problem in logistics and the modelling of turbulent flow with relevance to aerospace engineering [10].

The analogue approach is more amenable to the current era of noisy intermediate scale quantum (NISQ) devices [11] because it exploits the specific hardware platform capabilities by only trying to solve problems which can be mapped to the native Hamiltonian of the system and use the knowledge of this Hamiltonian to account for errors [12]. But quantum computers could also be designed to operate in a digital modality similarly to the binary, gate-based logic used in classical computers, but the binary bits are now replaced by quantum objects, referred to as qubits, and the ideal gate op-

erations take the form of unitary operators on the qubit subspace [4]. This approach holds perhaps even greater promise because it has even wider applicability to a range of different problems, but it is also more challenging to realise experimentally because of the reduced tolerance to noise and computational errors compared to the analogue modality [13]. This increased sensitivity is due to the fact that, unlike in classical computing, the discretisation of the information carriers (qubits) only happens at the point of final measurement, but maintaining coherence and utilising the continuous complex Hilbert space which describes the qubit state are necessary even in gate-based quantum computing<sup>1</sup>. In this sense, it is a misnomer to speak of digital quantum computing. Since quantum logic gates are analogue operations, they will always have a finite error rate, and because one needs to perform many thousands of gate-based operations to simulate any problem of practical interest, the error probability scales exponentially with both system size and circuit depth (number of consecutive gates executed on a single qubit). Faced with the reality that all physical devices are subject to some finite degree of noise, the idea of fault-tolerant quantum computation has emerged as a solution [14], but it comes with a cost. It requires an overhead in terms of the number of qubits required to encode a single logical qubit and with requirements for long-range interactions between qubits which are more difficult to implement [15].

Many of the flagship algorithms associated with quantum computing are based on the digital computation modality such as Shor's prime number factoring algorithm [16], which could disrupt current encryption schemes, and Grover's search algorithm [17], which could provide a quadratic speed up for a range of computational problems that use an unstructured search. However, the NISQ era devices we have available today are many orders of magni-

---

<sup>1</sup> In classical digital computing, the information carriers are logical bits which are represented physically by continuous analogue voltages which have been discretised into two logic levels. The classical computation is performed on these discretised objects, thus reducing the noise sensitivity of classical digital computers compared to classical analogue computers.

tude smaller in size [18, 19] than what would be required to execute these flagship algorithms on any meaningful scale. The qubit requirements can range from  $10^8$  [20] to  $10^4$  qubits [21] depending on the assumptions made in the calculation about the error per gate and the specific error-correction code. Nonetheless, the potential encryption code breaking capabilities of future quantum devices have already drawn the attention of governments and banking institutions to give rise to the field of post-quantum cryptography [22, 23] as a way of preparing for the eventuality of large-scale, fault-tolerant quantum computers becoming available. Additionally, applications in quantum chemistry and materials science tend to focus on the gate-based quantum computing modality because of its greater generality and the ability to map a larger variety of physical systems onto the same physical hardware [24]. Such applications can benefit pharmaceutical drug discovery [25] and lead to improved understanding of biological process such as nitrogen fixation [26] which could revolutionise food production by eliminating the need for chemical fertilizers. However, quantum chemistry applications are currently some of the most challenging ones in terms of system requirements. This is partially due to the computational overhead incurred when mapping fermionic statistics to the current generation of NISQ devices which are not natively fermionic [27].

## 1.2 Competing Architectures

A range of different implementations of quantum computers have emerged over the years, based on different physical systems which can meet the DiVincenzo criteria for a useful quantum computer [28]. Only a few of the major achievements in some of the leading modalities will be briefly mentioned to provide a point of reference for the discussion of the current state of the art for neutral atom quantum computing in the next section.

Superconducting qubits have been adopted as the platform of choice for many of the large-scale corporate efforts to develop useful quantum computers with headline results from Google [29] and IBM [30], who have already made some of their devices accessible online. The relative strength of the superconducting platform are their fast qubit readout times of the order 10 ns as well as gate fidelities exceeding 99.99% for single qubit gates and 99 % for two qubit gates [31]. Large system sizes have been achieved with the current record for the platform reaching up to 433 qubits [32]. Superconducting devices incur a large calibration overhead due to fabrication challenges in achieving qubit uniformity [31]. The superconducting approach has also been successful in the analogue computation domain with dedicated quantum annealing devices [33] which can efficiently solve certain optimisation problems, but do not meet the requirements for universal quantum computing.

Trapped ions are one of the oldest and most promising platforms for the development of quantum computers with the highest two qubit gate fidelities demonstrated to date ( $> 99.9\%$ ) between two ions [34, 35], but the gate fidelity is reduced when larger number of ions are confined in the same trap [36]. They also have very low single qubit gate errors below the  $10^{-5}$  level and very long qubit coherence times [36]. Scalability is the largest challenge facing trapped ion quantum computers, but proposals have been put forward on how it can be addressed using ion shuffling and microfabricated surface traps [37] in combination with integrated waveguides [38, 39] or magnetic field gradients [40, 41] for single site addressing. There are also significant engineering challenges which need to be overcome in terms of how the control systems required to implement ion shuttling and gates scale with the number of qubits [42].

A promising emerging platform for quantum computing, closely related to the work discussed in this thesis, is based on tweezer arrays of polar molecules made up of two or more alkali atoms [43]. This approach benefits from the

experimental advances in the cooling and trapping of single neutral atoms, whilst affording a richer energy landscape for the qubits including rotational and vibrational molecular states and an alternative to Rydberg excitation for creating interactions in the form of intrinsic dipole molecular interactions [44]. This approach could provide an advantage over the single atom approach in terms of two qubit gate fidelities due to reduced sensitivity to noise [45].

Photonic quantum computation has also emerged as a competitive platform which benefits from the robustness to noise of the non-interacting photons it uses as information carriers, but it also requires unique approaches to achieve interactions between photonic qubits such as probabilistic, measurement-based linear optical quantum computing [46] or deterministic gates using matter to mediate photon-photon interactions [47–49]. Finally, there are qubits based on the spin of charge carrier particles in semiconductors such as quantum dot devices [50] and nitrogen vacancies in diamond [51] which are showing great promise for hosting large numbers of qubits in a small device package.

### 1.3 State of the Art for Rydberg Atom Arrays

The quantum computing architecture which is the subject of this work is based on neutral atoms confined in arrays of optical dipole traps, with interactions mediated by excitation to high-lying Rydberg states with principal quantum numbers  $\geq 50$  [30, 52, 53]. As the name implies, the information carriers are neutral atoms, typically alkalis, alkaline earth metals [54] or lanthanides [55], which are trapped in arrays of far-off-resonant, tightly-focussed optical dipole traps [56]. Hundreds up to thousands of such trapping potentials can be generated in two dimensions using currently available laser powers and a range of different approaches including passive optical elements [57, 58], acousto-optic deflectors (AODs) driven with a multi-tone signal [59]

and holographic arrays [60]. The latter two approaches have the advantage that they are also reconfigurable. Three-dimensional geometries have also been demonstrated using holographic methods [61] and micro lens arrays [62]. The atoms are usually loaded into the optical trapping potentials from a magneto-optical trap which can result in multiple atoms in a single trap. To reach the single atom regime, light-assisted collisions [63] are engineered between the atoms which typically results in  $\sim 50\%$  occupancy of the traps with a stochastic distribution of atoms across the array. Alternative schemes using blue-detuned light can reach trap occupancies as high as 90 % [64, 65], but even then it is still necessary to perform additional manipulations to ensure deterministic availability of a qubit register. This additional manipulation takes the form of a dynamic re-arrangement of the available atoms in every experimental realisation to deterministically fill a dense subset of trap sites using a moving tweezer beam. This has been realised either by changing the frequency components in a multi-tone-driven AOD to translate certain atoms and switch off vacant trap sites [59], or by driving a crossed XY AOD with a single tone of variable frequency for each axis to realise a moving beam that can pick up and move atoms from site to site in an underlying array generated by other methods [66]. The probability of achieving a defect-free register of qubits is contingent on the trap lifetime and the size of the target array, but is typically  $\sim 40\%$  for arrays of hundreds of qubits in a room-temperature set up [67].

The qubit states are encoded in hyperfine ground states for alkali elements, while multi-valance electron atoms typically use a metastable excited state with a narrow linewidth and a ground state. Single qubit rotations are performed using either microwaves [68] or Raman laser excitation [69] with fidelities exceeding 0.9999 [70]. The original theoretical proposals for two qubit interaction gates were made by Jaksch *et al.* [71] and Lukin *et al.* [72] and are based on accessing the large dipole moments of Rydberg states to engineer long-range interactions in what is known as the Rydberg blockade

regime. This mechanism is described in Section 2.4, and it has been the basis of most successful Rydberg quantum computing experiments to date, but it should be noted that there have also been numerous theoretical proposals and experimental demonstrations of alternative Rydberg interaction regimes [73]. The first experimental demonstration of a Rydberg blockade CNOT gate was performed on a pair of  $^{87}\text{Rb}$  atoms by Isenhower *et al.* [74] with a gate fidelity of 0.73. Since then advances in the gate design [75, 76] and improved Rydberg state coherence through the use of filter cavities [77] have led to significant improvements with the current state of the art for alkali atoms recently reaching a controlled Z two-qubit gate fidelity of 99.5 % applied globally to arrays of up to 60 atoms in parallel [78]. In terms of scale this compares favourably with the similar scale demonstrations on other platforms such as superconducting qubits by Google [79] and ion traps by the publicly-listed spin-out company IonQ [80]. Importantly, even though Rydberg CZ gates in [78] were applied between adjacent atoms separated by a few  $\mu\text{m}$ , the demonstration in reference [81] provided convincing evidence that all-to-all connectivity can be achieved in this type of system by transporting atoms from site to site on  $\mu\text{s}$  timescales without significant loss of entanglement fidelity. These two recent developments make it possible for Rydberg atom based systems to consider implementing topological error correcting codes [82] which can tolerate error rates of up to 1% [83]. Combined with the recent experimental demonstration of small-scale quantum algorithms on a neutral atom device in reference [84], these developments strengthen the position of neutral atom quantum computers as a viable platform for digital quantum computing.

## 1.4 Analogue Quantum Computing & Optimisation

Building on a legacy of successful analogue simulations using ultracold atoms trapped in optical lattices [85], tweezer arrays of Rydberg atoms have also performed some large-scale simulations of many-body quantum systems. By utilising the native Rydberg blockade regime Hamiltonian, large scale analogue simulations of the phase transitions in a 2D Ising model spin problem mapped to arrays with  $>200$  qubits have been realised [86, 87], as well as observations of topological order in a spin liquid on a 219-atom programmable Rydberg atom quantum simulator [88]. Using the exact same hardware and system Hamiltonian, a demonstration of analogue quantum optimisation of the maximum independent set (MIS) problem was performed with some evidence emerging from this work that for specific problem types the quantum hardware can outperform classical simulated annealing [89]. A subsequent publication has called this specific result into question by highlighting that more advanced classical algorithms could complete the computation faster [90], but the same publication also provided examples of instances where they expect to observe a quantum advantage. The work on MIS optimisation has also motivated commercial exploitation of these types of system with the intention of tackling a range of graphical optimisation problems in logistics and finance [91]. Some of the spin-out companies that have emerged based on this technology have already performed optimisation on real world problems such as EV charging [92] and drug discovery [93].

## 1.5 The SQuAre Project

Many of these state-of-the-art developments have taken place in the United States and France. The aim of the Scalable Qubit Arrays (SQuAre) project,

which will be described in this work, is to deliver the first quantum computer based on Rydberg atoms in the United Kingdom. The project is carried out in collaboration with M Squared Lasers Ltd., who provided a full range of low-noise, high-power titanium sapphire lasers for dipole trap generation, Rydberg excitation and Raman single qubit rotations. The availability of high power lasers in their product range at key wavelengths such as the 20 W 1064 nm custom Equinox system for our red-detuned dipole traps and the 1 W 459 nm SolsTiS + ECD-F laser system for Rydberg excitation, for example, is what informed the decision to operate with  $^{133}\text{Cs}$  atoms instead of the more commonly used  $^{87}\text{Rb}$  atoms. In addition, because of its larger mass, caesium can be cooled down to lower temperatures compared to rubidium which is favourable for both loading atoms into shallower traps and for improved qubit coherence, which is a function of atom temperature. As the project name implies, the objective of this work is to achieve scalable operation with large numbers of high-fidelity qubits and the long-term goal of tackling industry-relevant problems in both the digital and analogue modalities of quantum computation. One of the drawbacks of operating with caesium is its large nuclear spin of  $7/2$  which gives rise to a larger number of  $m_F$  hyperfine sub-levels compared to rubidium which makes achieving high fidelity optical pumping for state initialisation more challenging.

The first iteration of this system is the subject of this thesis which describes the commissioning of the key sub-systems and details how their performance was characterised in terms of qubit coherence and single qubit gate fidelity as presented in Chapters 3 and 4 respectively. The characterisation of two qubit gate operations on our experimental platform will be the subject of future theses from our group. However, the two qubit gate fidelity of a commercial prototype closely based on our experiment has already been described in a white paper by our industry partners from M Squared Lasers Ltd. [94]. A preliminary demonstration of our system's ability to tackle analogue optimisation problems has been achieved on the 1D antiferromagnetic Ising model

as described in Chapter 6.

In addition to delivering a working large-scale hardware platform, the experiment will implement a number of novel features. The first one to be realised is the use of non-destructive readout (NDRO) for error suppression on arrays of up to 49 qubits, which is the subject of Chapter 5. Future theses from our group will also cover our work on blue-detuned bottle beam traps for the trapping of both ground and Rydberg states. These traps will allow us to make full use of the long Rydberg state lifetimes which are not accessible when operating with conventional red-detuned dipole traps which are repulsive for Rydberg states and have to be switched off during the excitation process [95].

## 1.6 Future Research Directions

With the recent high fidelity two qubit gate demonstration in a Rydberg array experiment [78], a common thread in future research will be the drive towards reaching a fault-tolerant operation regime on this type of hardware platform. While this recent CZ gate demonstration has exceeded the minimum 1% error threshold for implementing the surface code [96], the encoding overhead could be significantly reduced by further reductions in the two qubit gate error rates. These reductions can be achieved through hardware upgrades such as improved Rydberg laser excitation powers which will enable operation with a larger intermediate state detuning to suppress off-resonant scattering and better background noise suppression which may allow operation at higher principal quantum numbers for increased Rydberg state lifetime and shorter gate durations. Operating at cryogenic temperatures can result in significantly longer atom lifetimes [97] necessary for sorting of large arrays with 1000s of qubits and also provide suppression of background blackbody radiation (BBR) for improved effective Rydberg state lifetimes. By operat-

ing with different atomic species with complex energy level structure such as strontium [98] and ytterbium [99] new features such as erasure conversion of certain types of errors could be utilised to reduce the encoding overhead of error correction codes [100].

Another area which requires attention, if fault-tolerant operation is to be realised, is state detection. Conventional detection using a push-out beam as described in Section 3.5.2 results in atom loss<sup>2</sup>, which is incompatible with the repeated measurements on the same qubit required for syndrome extraction<sup>3</sup>. The non-destructive readout (NDRO) technique which has been implemented in this work for error suppression through post-selection, could in principle also be used as a mid-circuit measurement as demonstrated in reference [102], but the issues of cross-talk between adjacent data and ancilla qubits and the state detection speed would need to be addressed if the approach is to become practically useful. Conventional fluorescence imaging which takes several milliseconds in state of the art experiments is too slow compared to the hyperfine-encoded qubit coherence times and requires the application of dynamical decoupling pulses as shown in reference [102]. Alternative detection schemes with much faster qubit readout times  $\sim \mu\text{s}$  such as using collectively-enhanced fluorescence from ensembles of Rydberg atoms [103] or placing the atoms inside an in-vacuum optical cavity [104] have been demonstrated on small scales, but not yet extended to hundreds or even tens of atoms. Optical cavities have also been identified as a means of delivering distributed quantum computing with the added benefit of increased error tolerance along the interface qubits [105]. In terms of addressing the issues of cross-talk, operating with a dual-species array as implemented in reference [106] is a promising way of achieving this with the added benefit of enabling interesting new quantum computing modalities such as execut-

---

<sup>2</sup>This is what is meant by destructive read out in this work.

<sup>3</sup>Syndrome extraction is the measurement of the ancilla qubits in an error-corrected device. The outcome of this measurement is indicative of the type of error that has occurred and it is used to inform the subsequent error-correction steps [101].

ing circuits with local qubit operations using only global Rydberg beams [107]. In addition to all of these developments, new ways of exploiting atom re-arrangement in these types of platforms have been proposed. Examples include using atom sorting to achieve a lower error correction encoding overhead using quantum low-density parity-checking codes [108] and accessing new simulation modes that uses tweezers to implement tunnelling gates for fermionic quantum simulation [109]. One of the outstanding challenges specific to the neutral atom based quantum computers is the need to develop platform-specific compilation tools which can cope with the dynamically-reconfigurable nature of Rydberg atom arrays which needs to be exploited for optimal performance [110]. An additional area of active investigation is cross-talk free single site addressing for large-scale atom arrays with proposals emerging on how to achieve this by either using segmented spatial-light modulator (SLM) displays in combination with an acousto-optic deflector (AOD) to switch between holograms on a  $\mu\text{s}$  timescale [111] or by shining an SLM-generated array of beams onto a digital micromirror device (DMD) used to toggle the light on and off for specific target sites [112].

## 1.7 Scope of This Work

The author's involvement with the project began at the construction stage, starting with an empty lab in July 2020. The first two years of the project were dedicated to setting up the necessary sub-systems required to realise a fully-functioning neutral atom quantum computer. These steps included vacuum assembly, setting up 2D and 3D magneto-optical traps (MOTs), building a single atom imaging system and generating holographic arrays of red detuned dipole traps for single atom trapping using a spatial light modulator (SLM). Furthermore, a low phase noise microwave system for single qubit rotations and a two-photon Rydberg laser excitation system used to generate entanglement between different atoms were assembled and charac-

terised during this period. In parallel, work was carried out to implement single atom sorting using a moveable tweezer trap to achieve deterministic loading in a subset of the underlying holographic array. The individual contributions to these achievements are outlined in Section 1.9. By integrating some of these sub-systems the author was able to achieve the largest scale demonstration of state read out without atom loss in an alkali atom experiment using a stretched state cycling transition, as well as the highest single qubit gate fidelity for any system with more than 100 qubits measured using Clifford group randomised benchmarking. Finally, an early demonstration of our system's analogue quantum simulations capabilities was performed as a group effort with contributions from the entire team of theoreticians and experimentalists. We used a simple, classically-tractable 1D Ising spin chain model as our problem of choice to demonstrate that our platform can correctly identify the lowest energy state after adiabatically evolving systems of up to 11 atoms in a row. This will serve as the starting point for future work on quantum simulation problems in two dimensions which is in line with the current state of the art in the field.

## 1.8 Publications Arising From This Work

B. Nikolov, *et al.*, "Randomized Benchmarking Using Nondestructive Readout in a Two-Dimensional Atom Array", *Phys. Rev. Lett.* **131**, 030602 (2023)

## 1.9 Contributions of Others

The majority of the design work for the experimental hardware and the ARTIQ computer control system was carried out by the principal investigator, Dr. Jonathan Pritchard, with contributions from one of the post doctoral

researchers working on the project, Dr. Nicholas Spong (April 2020 - June 2022). The author's contributions to the project (July 2020 - November 2023) include the assembly of the 2D and 3D magneto optical trap laser systems, as well as the implementation and characterisation of polarisation gradient cooling. The 1064 nm laser system including the spatial light modulator set up used for tweezer array generation was built by Dr. Spong and maintained by the author after Dr. Spong's departure from the project. The microwave system used to drive single qubit gates was assembled and characterised by the author. The Rydberg laser system was built by the second postdoctoral researcher on the project, Dr. Jonathan Bass (January 2021 - December 2023). The moving tweezer system for single atom sorting was built by Dr. Spong and maintained and improved by the second PhD student on the project, Elliot Diamond-Hitchcock (August 2020 - July 2024). The respective contributions of the postdoctoral researchers Dr. Daniel Walker and Dr. Andre de Oliveira, who joined the team in September 2022, were developing an improved atom sorting algorithm used in Chapter 6 and setting up the arbitrary waveform generator (AWG) that was used to drive shaped light pulses for adiabatic ramps in our analogue simulation results. The computer code used to implement and analyse randomised benchmarking with composite BB1 pulses was written by the author. All data shown in this thesis was taken and analysed by the author with the exception of the data in Chapter 6 which was a collective effort of the entire team including our theory collaborator, Dr. Gerard Pelegri.

## Chapter 2

# Theoretical Background

The aim of this chapter is to introduce the fundamental theoretical background required to understand the workings of a quantum computer based on arrays of neutral alkali atoms excited to Rydberg states. The chapter is structured in increasing levels of complexity, starting with a simple discussion of alkali atom wavefunctions and how they can be calculated. What follows in Section 2.2 is a discussion of atomic interactions with static electric and magnetic fields which are relevant to electric field nulling for Rydberg states and how we define our qubits using Zeeman-resolved hyperfine levels. Since the work contained in this thesis covers both electric dipole optical transitions and magnetic dipole microwave transitions in caesium, the relevant theory for both is grouped under the heading of oscillating field interactions in Section 2.3. The final section of this chapter is dedicated to the dipole-dipole interactions between atoms in highly-excited Rydberg states which is the fundamental physical mechanism for entangling qubits in this approach to quantum computing.

## 2.1 Alkali Atom Wavefunctions

The SQuAre project uses neutral atoms of  $^{133}\text{Cs}$ , a stable bosonic isotope with  $Z = 55$  and nuclear spin,  $I = 7/2$ . Alkali elements are a common choice in quantum computing experiments because of their simple electronic structure with a single valence electron and the availability of high-power, low-noise lasers and microwave sources that have been developed over decades of experimental work in atomic clocks [113] and laser cooling [114]. Their Rydberg transitions and energy levels are well-studied and understood, with existing simulation packages such as ARC<sup>4</sup> [115] and *pairinteraction* [116] providing quick access to high-accuracy data and numerical simulation tools. The calculation of eigenstates and eigenenergies of all multi-electron atoms, including alkalis, must be done numerically and is typically performed using the quantum defect and central field approximations. This is because the Schrödinger equation for multi-electron atoms cannot be solved analytically due to the term containing the electron-electron electrostatic repulsion [117]. And because this term is too large to be treated as a perturbation, the most commonly used method to find a solution for the valence electron wavefunctions and energies of alkali atoms is the central field approximation.

### 2.1.1 The Quantum Defect & Central Field Approximations

Firstly, the quantum defect approach allows us to compute the energy levels of alkalis using a simple correction factor applied to the Rydberg energy formula developed for hydrogen [117]. The quantum defect is denoted as  $\delta_{l,j}(n)$  and it is applied to the Rydberg energy formula as

---

<sup>4</sup> Alkali.ne Rydberg Calculator

$$E_n = -\frac{Ry}{\left(n - \delta_{l,j}(n)\right)^2}, \quad (2.1)$$

where  $Ry$  is the mass-corrected Rydberg constant given by

$$Ry = R_\infty \frac{M}{(M + m_e)}. \quad (2.2)$$

$R_\infty$  is the Rydberg constant with a value of  $109737.31568076(96) \text{ cm}^{-1}$  [118],  $M$  is the mass of the nucleus, and  $m_e$  is the mass of an electron. The physical justification for this approach is that due to the spherical symmetry of electronic wavefunctions, we can consider an effective central core potential comprised of the combined electric field of the nucleus and all electrons in the filled shells of the atom. These inner electrons can be thought to "screen" the positive charge of the nucleus and reduce its magnitude when seen by more energetic electrons whose radial wavefunction is peaked in regions further away from the core. This approximation is least crude in the case of alkali atoms because of their single electron in the outermost shell, and it is a very good approximation for alkali atom wavefunctions with angular momentum quantum number  $l \geq 3$  because of the centrifugal barrier [119]. This barrier acts as an effective repulsive force that reduces the radial wavefunction overlap with the core potential for these states with large  $l$  as illustrated in in Fig. 2.1 created using the ARC software package [120]. This overlap is referred to as core penetration.

The value for the quantum defect of a given state can be calculated using a series expansion

$$\delta_{l,j}(n) = \delta_{0,l,j} + \frac{\delta_{2,l,j}}{(n - \delta_{0,l,j})^2} + \dots \quad (2.3)$$

The values  $\delta_{i,l,j}$  are obtained from fits to experimental measurements of

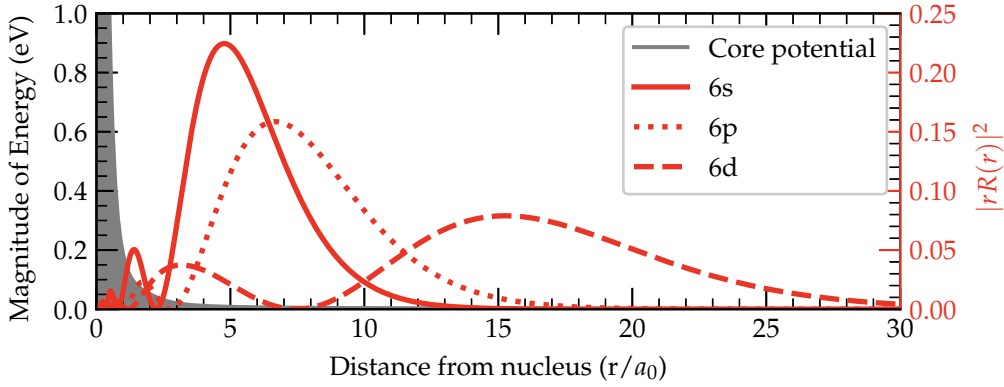


Figure 2.1: Plot of the magnitude of the core potential and the electronic probability density functions for Cs  $n=6$  states with different  $l$  principal quantum numbers. This plot illustrates the reduced core penetration for wavefunctions with larger orbital angular momentum due to the centrifugal barrier.

atomic transition wavelengths. For caesium, the values of these expansion coefficients for the  $nS_{1/2}$ ,  $nP_{1/2}$ ,  $nP_{3/2}$  and  $nD_{5/2}$  states are available in [121], while values for the  $nD_{3/2}$ ,  $nF_{5/2}$ , and  $nF_{7/2}$  are available in [122].

The second tool for dealing with the fact that the alkali atom Hamiltonian is not analytically solvable is the central field approximation. It allows us to find a good approximation of the eigenstates and eigenenergies of the valence electron by defining an effective central field potential and solving the Schrödinger equation numerically. The general idea of the approach consists of re-stating the Hamiltonian of the atomic system in such a way that the large, non-perturbative electron-electron interaction term is split into two parts. The larger part is absorbed into an effective central field potential,  $Z_{\text{eff}}$ , that replaces the nuclear charge and whose value can be found in atomic or chemistry reference texts such as [123]. The remainder of the electron-electron interaction term is small enough to be treated perturbatively and thereby obtain the single electron wavefunctions and energies. This approach is described in [117] and [124] and a numerical implementation is implemented in [115].

### 2.1.2 Alkali Wavefunctions in Different Bases

The pertinent eigenbases for describing the energy structure of caesium atoms are the hyperfine structure basis for ground states, where the good quantum numbers are  $n, l, j, I, F, m_F$ , and the fine structure basis for highly-excited Rydberg states, where the good quantum numbers are  $n, l, j, m_j$ . The angular momentum eigenstates of the valance electron in one basis can be expressed in terms of linear combinations of the eigenstates in another basis using the Clebsch-Gordan coefficients,  $C_{j, m_j, I, m_I}^{F, m_F} = \langle j, m_j, I, m_I | F, m_F \rangle$  [125] which can be calculated using

$$C_{j, m_j, I, m_I}^{F, m_F} = (-1)^{j-I+m_F+F} \sqrt{2F+1} \begin{pmatrix} j & I & F \\ m_j & m_I & -m_F \end{pmatrix}. \quad (2.4)$$

The final term in equation (2.4) is a Wigner 3-j symbol [126] and its value for a specific set of quantum numbers can be obtained from a textbook such as [127], or calculated using a computer software package such as ARC [120].

The reason why Rydberg states are usually described in the fine structure basis is the scaling of the hyperfine splitting as a function of the quantum-defect-corrected principal quantum number  $n$ . The hyperfine energy splitting is given by

$$\Delta E_{\text{HFS}} = \frac{A_{\text{HFS}}}{2[n - \delta_{l_j}(n)]^3} K + \frac{B_{\text{HFS}}}{[n - \delta_{l_j}(n)]^3} \frac{\frac{3}{2}K(K+1) - 2I(I+1)j(j+1)}{2I(2I-1)2j(2j-1)}, \quad (2.5)$$

where

$$K = F(F+1) - I(I+1) - j(j+1), \quad (2.6)$$

$A_{\text{HFS}}$  is the magnetic dipole constant and  $B_{\text{HFS}}$  is the electric quadrupole

constant whose values are obtained from experimental measurements and are available from atomic physics reference data such as [128]. For states with  $j = 1/2$ , only the  $A_{\text{HFS}}$  term is non-vanishing<sup>5</sup>. If we consider the scaling relation with  $n$  from equation (2.5) and the fact that the larger term,  $A_{\text{HFS}}$ , is of the order of GHz [130], we can estimate that for states with principal quantum numbers  $>30$ , the hyperfine splitting would be of the order of 100s of kHz, narrower than the typical power-broadened Rydberg state linewidths of the order of a few MHz. For example, the exact measured values of  $A_{\text{HFS}}$  for the caesium  $28S_{1/2}$  level was 1.2(2) MHz and for  $49S_{1/2}$  it was 0.147(4) MHz based on reference [131].

## 2.2 Interaction with Static Fields

### 2.2.1 Static Magnetic Fields (Zeeman Shift)

In the absence of an externally applied magnetic field, the different  $m$  levels of a given quantum state are degenerate in energy and therefore not resolvable in a spectroscopic measurement. This degeneracy is lifted when a static (DC) magnetic field is applied to the system. This effect is referred to as the Zeeman shift and it is highly relevant to this work because we define our computational basis using two resolved hyperfine  $m_F$  states of caesium with a weak bias magnetic field applied. Furthermore, the Zeeman Shift can introduce long-term drifts and noise into our system. If the DC magnetic field amplitude is not stable, it can cause variations in the second-order differential Zeeman shift between our computational states  $6S_{1/2}|F = 4, m_F = 0\rangle = |1\rangle$  and  $6S_{1/2}|F = 3, m_F = 0\rangle = |0\rangle$  resulting in a loss of gate fidelity.

<sup>5</sup> One could also consider a third order magnetic-octupole moment which has been measured for the caesium  $6P_{3/2}$  half state, but it only modifies the energy levels by  $\approx 0.5$  kHz [129]. Such small corrections are unresolvable even with our Rydberg laser linewidths of  $\approx 100$  kHz when measured over 100 ms which are the narrowest linewidth lasers available in our experiment.

In the case of  $^{133}\text{Cs}$  ground state atoms, the hyperfine structure splitting is  $\sim 9.2$  GHz and the Zeeman shifts produced in our experiments are three orders of magnitude smaller. Therefore, the correct approach is to work in the hyperfine basis because the coupling between the electronic and nuclear angular momenta is stronger than their individual couplings to the applied magnetic field. In this case the good quantum number is  $F$  and the interaction with the bias field is added as a perturbation in the hyperfine-structure basis using the Hamiltonian.

$$\hat{H}_B = \mu_B g_F F_z B_z, \quad (2.7)$$

where  $\mu_B$  is the Bohr magneton, the dimensionless term  $g_F$  is the hyperfine structure g-factor<sup>6</sup>, and for simplicity, the magnetic field,  $B_z$ , is assumed to be acting along the  $z$ -axis following standard convention in quantum mechanics. For the interaction regime relevant to this work, this Zeeman shift is linear in the field amplitude and the energy associated with it can be evaluated to lowest order using the simple formula shown in equation (2.8). This is referred to as the anomalous Zeeman effect.

$$\Delta E_{|F, m_F\rangle} = \mu_B g_F m_F B_z. \quad (2.8)$$

Finally, it should be noted that for intermediate strength magnetic fields the perturbative treatment is no longer valid and an exact diagonalization method must be used to numerically solve the combined hyperfine and Zeeman Hamiltonian as implemented in [115]. An analytical solution, referred to as the Breit-Rabi formula [132], exists only for the case when  $j = 1/2$ . In this work only magnetic fields strictly in the linear Zeeman shift regime have been used, but the Breit-Rabi formula is still relevant because it can be used

<sup>6</sup> The electron g-factors serve as scaling factors which incorporate various corrections required to achieve agreement with experiment and are tabulated in [128] for caesium based on high-precision measurements.

to calculate the second order shift on the clock state transition between the  $|F = 4, m_F = 0\rangle$  and  $|F = 3, m_F = 0\rangle$  states of caesium which have zero first-order shift. The formula is

$$\Delta\omega_{\text{clock}} = \frac{(g_J - g_I)^2 \mu_B^2}{2\hbar\Delta E_{\text{HFS}}} B^2. \quad (2.9)$$

For the caesium clock states this evaluates to

$$\Delta\omega_{\text{clock}}/B^2 = 2\pi \times 427.45 \text{ Hz/G}^2. \quad (2.10)$$

## 2.2.2 Static Electric Fields (DC Stark Effect)

Table 2.1: Static polarizability values for key ground [133] and Rydberg [128] states used in the experiment.

State	$\alpha_0$ (Hz cm <sup>2</sup> V <sup>-2</sup> )	$\alpha_2$ (Hz cm <sup>2</sup> V <sup>-2</sup> )
$6S_{1/2}$	0.1001	0
$6P_{1/2}$	0.3416	0
$6P_{3/2}$	0.4087	-0.06529
$65S_{1/2}$	$307.16 \times 10^6$	0
$70S_{1/2}$	$460.18 \times 10^6$	0
$75S_{1/2}$	$729.14 \times 10^6$	0

The response of an atomic system to an externally-applied static electric field was discovered by Johannes Stark [134] and named after him. The Hamiltonian describing this interaction in the fine structure basis is

$$\hat{H}_E = -\frac{1}{2}\alpha_0 E_z^2 - \frac{1}{2}\alpha_2 E_z^2 \frac{3J_z^2 - j(j+1)}{j(2j-1)}, \quad (2.11)$$

where  $\alpha_0$  and  $\alpha_2$  are the scalar and tensor polarizabilities respectively and the electric field has been assumed to have a polarisation along the quantisation axis. The tensor polarizability term is only non-vanishing for states with  $j > 1/2$ . Also, unlike the Zeeman shift, levels with the same magnitude

for the relevant  $m$  quantum number remain degenerate upon the application of a static electric field<sup>7</sup>. The  $\alpha_0$  term scales as  $n^7$  therefore the magnitude of the DC Stark shift for a given externally-applied electric field is many orders of magnitude lower for ground state atoms compared to highly-excited Rydberg atoms as illustrated in Table 2.1 [135]. This increased sensitivity to external electric fields makes Rydberg atoms useful for electric field sensing [136, 137], but it also requires careful electric field nulling in the context of quantum computing to avoid rapid decoherence due to electric field noise during Rydberg excitation. Similarly to the Zeeman effect, the DC Stark effect for Rydberg atoms is treated in the fine structure basis because it dominates over the weak hyperfine interaction of Rydberg electrons with the nucleus. For the experiments considered in this work, only fields of the order of 10 V/m (0.1 V/cm) were applied for the purpose of nulling any stray electric fields present in the lab that could interfere with our Rydberg experiments. Ground state Stark shifts at such field magnitudes are negligible.

## 2.3 Interaction with Oscillating Fields

### 2.3.1 Dipole Matrix Elements

Dipole matrix elements characterise the transitions strength between dipole-coupled states when driven by an external oscillating field. The driving field could be an electric or magnetic field, depending on the transition. Both cases are relevant to the work described in this thesis, so a brief of summary of how they are calculated will be given in this section.

<sup>7</sup> For example, for  $6S_{1/2}$   $F=4$ ,  $m_F = 2$  and  $m_F = -2$  are degenerate in energy.

## Electric Dipole Matrix Elements

We define the electric dipole operator for the valence electron of an alkali atom as

$$\hat{d} = e\hat{r} \cdot \boldsymbol{\epsilon}. \quad (2.12)$$

where  $e$  is the charge of the electron,  $\hat{r}$  is the operator for the radial distance of the electron from the nucleus, and  $\boldsymbol{\epsilon}$  is the unit vector describing the polarisation of the electric field. The symmetry properties of the atomic wavefunctions manifested in the spherical harmonics that describe their angular momentum make the spherical basis the natural choice for tackling the problem. The unit vectors of this basis,  $\boldsymbol{\epsilon}_q$ , are defined in terms of the Cartesian unit vectors,  $\boldsymbol{x}$ ,  $\boldsymbol{y}$ , and  $\boldsymbol{z}$ , as

$$\boldsymbol{\epsilon}_0 = \boldsymbol{z}, \quad (2.13a)$$

$$\boldsymbol{\epsilon}_{-1} = \frac{1}{\sqrt{2}}(\boldsymbol{x} - i\boldsymbol{y}), \quad (2.13b)$$

$$\boldsymbol{\epsilon}_{+1} = -\frac{1}{\sqrt{2}}(\boldsymbol{x} + i\boldsymbol{y}). \quad (2.13c)$$

It should be noted that the orthonormality relations are different compared to using Cartesian unit vectors<sup>8</sup> which gives rise to the convention that  $q = \{-1, 0, +1\}$  corresponds to  $\{\sigma^+, \pi, \sigma^-\}$  atomic transitions. Because of a mathematical property of electric dipole operators (they are rank-one irreducible tensors), one can apply the Wigner-Eckart theorem [126] to decompose the dipole matrix element in the uncoupled basis into a reduced matrix element,  $\langle l||d||l' \rangle$ , which depends only on  $l$  and  $n$ , and a Wigner-3j symbol which carries the angular dependence [127] in the following way

<sup>8</sup> Specifically,  $\boldsymbol{\epsilon}_{+1} \cdot \boldsymbol{\epsilon}_{-1} = \boldsymbol{\epsilon}_{-1} \cdot \boldsymbol{\epsilon}_{+1} = -1$ . See Appendix B.3 in reference [138] for details.

$$\langle n, l, m_l | d_q | n' l' m_l' \rangle = (-1)^{l-m_l} \begin{pmatrix} l & 1 & l' \\ -m_l & q & m_l' \end{pmatrix} \langle l || d || l' \rangle. \quad (2.14)$$

The Wigner-3j symbol contains the selection rules for a given dipole transition and evaluates to zero when they are violated. The reduced matrix element in equation (2.14) can in turn be expressed in terms of the overlap integral between the radial wavefunction of the valence electron and the dipole moment as

$$\langle l || d || l' \rangle = (-1)^l \sqrt{(2l+1)(2l'+1)} \begin{pmatrix} l & 1 & l' \\ 0 & 0 & 0' \end{pmatrix} \langle n, l | er | n', l' \rangle. \quad (2.15)$$

The approach is also applicable when considering the coupling between states in the fine structure and hyperfine structure bases [127].

### Fine Structure Basis

$$\langle n, l, j, m_j | d_q | n', l', j', m_j' \rangle = (-1)^{j-m_j} \begin{pmatrix} j & 1 & j' \\ -m_j & q & m_j' \end{pmatrix} \langle j || d || j' \rangle, \quad (2.16)$$

where

$$\langle j || d || j' \rangle = (-1)^{l+s+j'+1} \delta_{s,s'} \sqrt{(2j+1)(2j'+1)} \begin{Bmatrix} j & 1 & j' \\ l' & s & l \end{Bmatrix} \langle l || d || l' \rangle. \quad (2.17)$$

Terms of the type  $\begin{Bmatrix} F & 1 & F \\ j' & I & j \end{Bmatrix}$  are Wigner 6j symbols. Similarly to Wigner 3j symbols, the values for Wigner 6j symbols are tabulated in atomic physics textbooks [127] or they can be calculated numerically using the ARC Python library [115].

### Hyperfine Structure Basis

$$\langle n, l, j, I, F, m_F | d_q | n', l', j', I', F', m'_F \rangle = (-1)^{F-m_F} \begin{pmatrix} F & 1 & F' \\ -m_F & q & m'_F \end{pmatrix} \langle F || d || F' \rangle, \quad (2.18)$$

where

$$\langle f || d || f' \rangle = (-1)^{F+I+F'+1} \delta_{I,I'} \sqrt{(2F+1)(2F'+1)} \begin{Bmatrix} F & 1 & F' \\ j' & I & j \end{Bmatrix} \langle j || d || j' \rangle. \quad (2.19)$$

### 2.3.2 Magnetic Dipole Matrix Elements

The same mathematical formalism applies to evaluating the magnetic dipole matrix elements required to calculate microwave-driven ground state hyperfine level transitions. However in this case, we are interested in evaluating the coupling of the magnetic dipole moment,  $\hat{\mu}$ , to an oscillating magnetic field with polarisation unit vector,  $\epsilon$ , given by

$$\hat{\mu} = \frac{\mu_B}{\hbar} g_F \hat{\mathbf{F}} \cdot \epsilon, \quad (2.20)$$

where  $\hat{\mathbf{F}}$  is the total angular momentum vector of the nucleus and the valance electron in the hyperfine structure basis. For practical calculations to the accuracy required in this work, the coupling to the nuclear spin angular momentum vector,  $\hat{\mathbf{I}}$ , can be neglected because it amounts to a small correction  $\sim 10^{-4}$ . This means we can use

$$\hat{\mu} = \frac{\mu_B}{\hbar} (g_J \hat{\mathbf{J}} + g_I \hat{\mathbf{I}}) \cdot \epsilon. \quad (2.21)$$

For a transition between two hyperfine states  $|F, m_F\rangle \rightarrow |F', m'_F\rangle$  driven

by a field with a spherical polarisation component  $\epsilon_q$  we can evaluate the strength of a microwave transition,  $\hat{\mu}_q$ , by using the Wigner-Eckart theorem to separate out the  $m_F$  dependence in the magnetic dipole matrix element

$$\langle F, m_F | \hat{\mu}_q | F', m'_F \rangle = g_J \frac{\mu_B}{\hbar} (-1)^{F-m_F} \begin{pmatrix} F & 1 & F' \\ -m_F & q & j \end{pmatrix} \langle F || J || F' \rangle. \quad (2.22)$$

We can then evaluate the reduced matrix element,  $\langle F || J || F' \rangle$  in the fine structure basis as [127]

$$\langle F || J || F' \rangle = (-1)^{F'+j+I+1} \delta_{II'} \sqrt{(2F+1)(2F'+1)} \begin{Bmatrix} F & 1 & F' \\ j' & I & j \end{Bmatrix} \langle j || J || j' \rangle. \quad (2.23)$$

Following the derivation in [127], we can use symmetry properties to evaluate the reduced matrix element in the fine structure basis as follows

$$\langle j || J || j' \rangle = \hbar \delta_{jj'} \sqrt{j(j+1)(2j+1)}. \quad (2.24)$$

The final result is given by

$$\mu_q = g_J \frac{\mu_B}{\hbar} (-1)^{f'+j+I+1+F-m_F} \sqrt{(2F+1)(2F'+1)j(j+1)(2j+1)} \begin{Bmatrix} F & 1 & F' \\ j' & I & j \end{Bmatrix} \begin{pmatrix} F & 1 & F' \\ -m_F & q & m'_F \end{pmatrix}. \quad (2.25)$$

### 2.3.3 Optical Two-level System

A good starting point for describing the light-matter interactions used in this work is the most basic and fundamental system which approximates the

complex energy level structure of a real alkali atom as two energy levels: a ground state,  $|g\rangle$ , and a single excited state,  $|e\rangle$ , separated in energy by  $\hbar\omega_{eg}$ . This simple model can be a reasonable approximation in situations where selection rules prohibit excitation to all but a single state which has a single decay path back into the ground state, such as a stretched state transition. The rotating wave approximation (RWA) has been applied to remove the time dependence of the driving field from the Hamiltonian and the assumption has been made that the driving field's wavelength  $\lambda \gg a_0$ , the approximate spatial extent of the atomic wavefunction (dipole approximation) [139]. As we do not operate in the single photon regime in our set up, the light field will be treated classically and the quantum effects resulting from spontaneous decay will be modelled phenomenologically using the optical Bloch equations (OBEs) [117]. The Hamiltonian of the system then takes the form [139]

$$\hat{H}_{\text{int}} = \frac{\hbar}{2} \begin{pmatrix} \Delta & \Omega^* \\ \Omega & -\Delta \end{pmatrix}, \quad (2.26)$$

where we have defined a detuning from resonance,  $\Delta = \omega_{\text{laser}} - \omega_{eg}$ , and a generalised angular Rabi frequency,  $\Omega_{\text{eff}} = \sqrt{\Omega^2 + \Delta^2}$ .  $\Omega$  is the resonant angular Rabi frequency resulting from a coupling with a driving electric field,  $E = E_0 \cos(\omega_{\text{laser}}t - \phi_0)$ , given by

$$\Omega = \frac{E_0 \langle e | \hat{d} | g \rangle}{\hbar} \quad (2.27)$$

in a frame co-rotating with the driving field frequency and assuming that the phase offset  $\phi_0 = 0$  for simplicity. The definition of  $\Omega$  including a non-zero phase is discussed in Section 2.3.5.

Because the electromagnetic radiation field is treated classically, this model fails to capture the finite lifetime / linewidth of the excited state which result from the quantum effect of spontaneous emission [117]. This effect

results naturally from a quantum treatment of the light field as described in [140, 141]. However, we will proceed to describe these inherently quantum effects in a phenomenological model based on the optical Bloch equations (OBEs) because we are not concerned with single-photon-level changes in the field intensity. The equations are derived in the density matrix formalism with a density matrix,  $\rho_{ij} = |i\rangle\langle j|$ , which can account for loss of qubit coherence. Using the Lindblad Master Equation [142], one can calculate the time evolution of a density operator using

$$\dot{\rho} = \frac{i}{\hbar}[\rho, \hat{H}_{\text{int}}] + \mathcal{L}(\rho), \quad (2.28)$$

where  $\mathcal{L}(\rho)$  is a Lindblad operator defined as [143]:

$$\mathcal{L}(\rho) = \sum_i c_i \rho c_i^\dagger - \frac{1}{2}(c_i^\dagger c_i \rho + \rho c_i^\dagger c_i). \quad (2.29)$$

In the specific case of only accounting for decay due to spontaneous emission, the single collapse operator is  $c = \sqrt{\Gamma}|g\rangle\langle e|$ . Using this definition, the final form of the OBEs becomes [144]

$$\dot{\rho}_{gg} = \frac{i\Omega}{2}(\tilde{\rho}_{ge} - \tilde{\rho}_{eg}) + \Gamma\rho_{ee}, \quad (2.30a)$$

$$\dot{\tilde{\rho}}_{ge} = -(i\Delta + \Gamma/2)\tilde{\rho}_{ge} - \frac{i\Omega}{2}(\rho_{ee} - \rho_{gg}), \quad (2.30b)$$

$$\dot{\tilde{\rho}}_{eg} = (i\Delta - \Gamma/2)\tilde{\rho}_{eg} + \frac{i\Omega}{2}(\rho_{ee} - \rho_{gg}), \quad (2.30c)$$

$$\dot{\rho}_{ee} = -\frac{i\Omega}{2}(\tilde{\rho}_{ge} - \tilde{\rho}_{eg}) - \Gamma\rho_{ee}, \quad (2.30d)$$

where the terms  $\tilde{\rho}_{ge} = e^{-i\omega t}\rho_{ge}$  and  $\tilde{\rho}_{eg} = e^{i\omega t}\rho_{eg}$  are the slow-rotating terms introduced in making the RWA. The effect of the added spontaneous emission can be seen in Fig. 2.2 which shows an ARC simulation of the system dynam-

ics of the stretched state transition on the D2 line of caesium for  $\Delta = 0$  and  $\Omega/2\pi = 28$  MHz based on our typical operating laser powers. The system dynamics under the OBE reach a decohered steady state due to the effects of spontaneous emission.

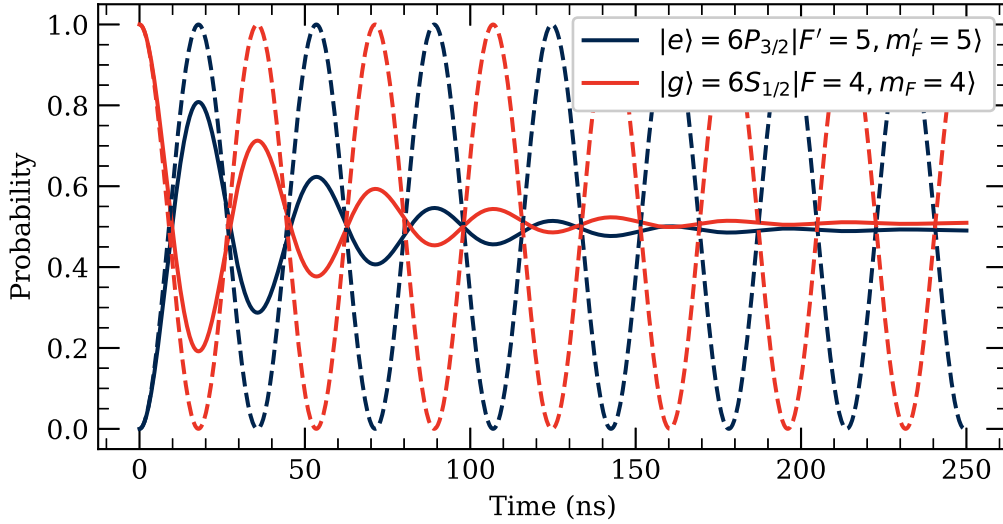


Figure 2.2: ARC simulation of the resonant dynamics of the stretched state transition on the D2 line of caesium with a Rabi frequency of 28 MHz. Solid lines represent the time evolution of the system under the OBE and the dashed line represent the simple two-level model time evolution without accounting for the excited state decay rate due to spontaneous emission.

The OBE formalism is commonly used in atomic physics experiments to describe incoherent light scattering during processes such as loading a magneto-optical trap (MOT) [145] or fluorescence imaging of atoms [146]. To obtain the relevant equations for the steady-state solutions ( $\rho_{ij}^{SS}$ ), we set  $\dot{\rho}=0$  and obtain the expressions

$$\rho_{ee}^{SS} = \frac{1}{2} \frac{s}{(1 + s + (2\Delta/\Gamma)^2)}, \quad (2.31a)$$

$$\tilde{\rho}_{eg}^{SS} = \frac{s}{\Omega} \frac{(\Delta - i\Gamma/2)}{(1 + s + (2\Delta/\Gamma)^2)}, \quad (2.31b)$$

where we have defined a saturation intensity,  $I_{\text{sat}}$ , as [117]

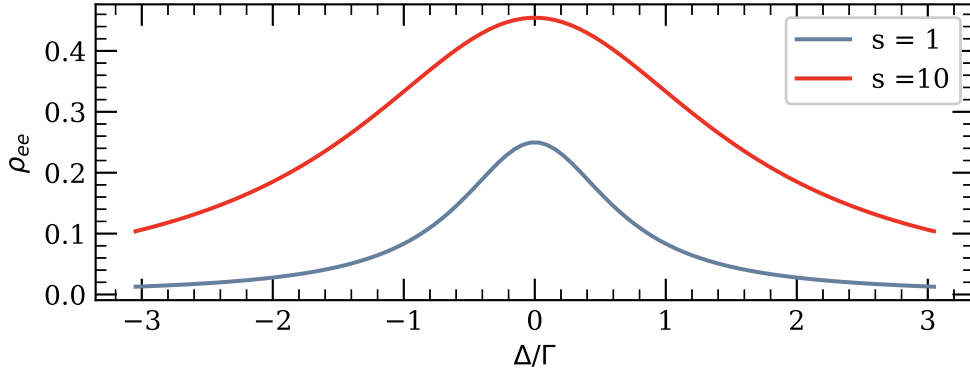


Figure 2.3: Illustration of power broadening effect on a transition due to the spontaneous emission incorporated into the OBE model.

$$I_{\text{sat}} = \frac{2\pi^2\hbar\Gamma c}{3\lambda^3}, \quad (2.32)$$

and a saturation parameter  $s = I/I_{\text{sat}}$ . One can also re-define the angular Rabi frequency,  $\Omega$ , using the saturation intensity and the excited state linewidth as

$$\Omega = \Gamma \sqrt{\frac{I}{2I_{\text{sat}}}}. \quad (2.33)$$

By inspecting equations (2.31), we can identify that saturation effects emerge as a result of spontaneous emission by considering the asymptotic behaviour of  $\rho_{ee}$  as the light intensity tends to infinity: it reaches a maximum of 0.5. By definition saturation intensity occurs when  $s = 1$  and  $\rho_{ee} = 1/4$ . There is also a power broadening effect that results from the OBE treatment which is illustrated in Fig. 2.3 so that the effective transition linewidth becomes,  $\Gamma' = \Gamma\sqrt{1+s}$ .

### 2.3.4 Hyperfine Qubit Two Level System

In the case of hyperfine ground state qubits, the two-level interaction Hamiltonian now describes a coupling of the valance electron's magnetic dipole

moment to a GHz-frequency magnetic field. The form of the Hamiltonian is the same, but the Rabi frequency in the RWA is now given by

$$\Omega = \frac{\mu_q B_q}{\hbar}, \quad (2.34)$$

where  $B_q$  is the amplitude of the driving magnetic field with polarisation component,  $q$ , and a frequency  $\omega_{eg}$ , and  $\mu_q$  is the magnetic dipole matrix element from equation (2.25).

To now account for the effects of decoherence in this simple two-level model, we will use a modified version of the optical Bloch equations (OBEs). The main difference is that the timescale for spontaneous decay of a hyperfine ground state is many orders of magnitude longer than in the case of an optical transition<sup>9</sup>. Therefore, spontaneous emission is no longer the dominant dephasing mechanism. Following the established convention, we will use the nuclear magnetic resonance (NMR) imaging terminology which describes a longitudinal and transverse dephasing time,  $T_1$  and  $T_2$  respectively. The resulting equations are [147]

$$\dot{\rho}_{gg} = \frac{i\Omega}{2}(\tilde{\rho}_{ge} - \tilde{\rho}_{eg}) + \frac{\rho_{ee}}{T_1}, \quad (2.35a)$$

$$\dot{\tilde{\rho}}_{ge} = -(i\Delta + \frac{1}{T_2})\tilde{\rho}_{ge} - \frac{i\Omega}{2}(\rho_{ee} - \rho_{gg}), \quad (2.35b)$$

$$\dot{\tilde{\rho}}_{eg} = (i\Delta - \frac{1}{T_2})\tilde{\rho}_{eg} + \frac{i\Omega}{2}(\rho_{ee} - \rho_{gg}), \quad (2.35c)$$

$$\dot{\rho}_{ee} = -\frac{i\Omega}{2}(\tilde{\rho}_{ge} - \tilde{\rho}_{eg}) - \frac{\rho_{ee}}{T_1}. \quad (2.35d)$$

The longitudinal relaxation time,  $T_1$ , is a measure of the timescale required for an atom in the excited hyperfine state to decay down to the ground state with the release of energy. Therefore, it appears in the diagonal elements

<sup>9</sup> The spontaneous emission rate scales as  $\propto \omega^3$ .

of the state density matrix because it affects the state populations. It is similar to the spontaneous decay, but the physical mechanisms that lead to it are different. In spontaneous decay the mechanism is the coupling of the atomic oscillator to the vacuum modes of the quantised electromagnetic field. In the case of the longitudinal relaxation of a single atom in a dipole trap, the mechanism is usually off-resonant scattering from the optical dipole trap laser field that can cause transitions between the hyperfine ground and excited state with a typical  $T_1$  value for caesium atoms trapped in 1 mK-deep 1064 nm dipole trap  $\sim 9$  s [147]. The longest experiments conducted in this work are  $< 500$  ms and we operate with much shallower trap depths during microwave gate operations, so the effect of spin relaxation due to off-resonant light scattering is negligible.

The transverse relaxation time,  $T_2$ , is the dominant dephasing mechanism which manifests as a result of the statistical averaging across multiple realisation of the experiment that must be carried out to extract information from a quantum system. In each realisation of the experiment the atom inside the dipole trap could occupy a different distribution of motional modes which affects the time-averaged trapping potential it samples. Combined with variations in the environment from shot to shot, this leads to variation in the experimentally resolvable resonance frequency of each atom in every shot of the experiment. This affects the off-diagonal elements of the density matrix, referred to as coherences, because when we average the results of multiple measurements as required for a quantum computation, what we see is a reduction in the contrast of the Rabi oscillation. As discussed in Chapter 4.1, some of these effects can be undone through the use of experimental techniques if the dephasing mechanism is reversible. This is why the transverse relaxation time can be represented as a sum of two terms as shown in equation (2.36).

$$\frac{1}{T_2} = \frac{1}{T_2'} + \frac{1}{T_2^*}, \quad (2.36)$$

where  $T_2'$  is the irreversible and  $T_2^*$  is the reversible dephasing time constant.

### 2.3.5 Propagator for Two-Level System in RWA

An alternative approach for calculating the dynamics of a two-level system is to use the propagator formalism which will be convenient for modelling composite microwave pulses and randomised benchmarking sequences in Section 4.4. A propagator is a unitary time evolution operator,  $\hat{U}(t, t_0)$ , with the definition [148]

$$|\psi(t)\rangle = \hat{U}(t, t_0)|\psi(t_0)\rangle, \quad (2.37)$$

where  $t > t_0$ . Based on this definition we can see that a propagator evolves a state in time. By substituting the right hand side of equation (2.37) into the time-dependent Schrödinger equation, it can be shown that

$$\frac{\partial \hat{U}(t, t_0)}{\partial t} = -\frac{i}{\hbar} \hat{H} \hat{U}(t, t_0). \quad (2.38)$$

Solving this equation is non-trivial in the case of a time-dependent Hamiltonian, but for the purposes of this thesis it is sufficient to only consider the simplest case of a time-independent Hamiltonian for which we can write

$$\hat{U}(t, t_0) = e^{-i(t-t_0)\hat{H}/\hbar}. \quad (2.39)$$

We will use the two-level Hamiltonian from eq. (2.26), where the driving field is now a magnetic field defined as  $B = B_q \cos(\omega_{eg}t - \phi_0)$  and the levels  $|g\rangle$  and  $|e\rangle$  represent hyperfine ground state  $m_F$  levels with a magnetic dipole coupling  $\mu_q$ . The key difference from previous sections is that the phase of

the driving field will need to be considered because it determines the axis of rotation of the qubit state vector, i.e. whether we are applying an  $R_x$  or an  $R_y$  pulse. In previous sections the phase was assumed to be zero for simplicity, but when modelling single qubit gates we cannot make this assumption. If we apply the RWA transformation to the modified Hamiltonian, then the time-dependence of the driving field will still be removed from the Rabi frequency term,  $\Omega$ , but now the non-zero phase results in

$$\Omega = |\Omega_0|e^{i\phi_0}. \quad (2.40)$$

By substituting this value of  $\Omega$  into the two-level Hamiltonian from eq. (2.26) and using this modified Hamiltonian in eq. (2.39), the propagator,  $U(t)$ , can be derived<sup>10</sup> as

$$U(t) = \begin{pmatrix} \cos(\frac{1}{2}\Omega_{\text{eff}}t) + i\frac{\Delta}{\Omega_{\text{eff}}}\sin(\frac{1}{2}\Omega_{\text{eff}}t) & -i\frac{\Omega}{\Omega_{\text{eff}}}e^{i\phi_0}\sin(\frac{1}{2}\Omega_{\text{eff}}t) \\ -i\frac{\Omega}{\Omega_{\text{eff}}}e^{-i\phi_0}\sin(\frac{1}{2}\Omega_{\text{eff}}t) & \cos(\frac{1}{2}\Omega_{\text{eff}}t) - i\frac{\Delta}{\Omega_{\text{eff}}}\sin(\frac{1}{2}\Omega_{\text{eff}}t) \end{pmatrix}. \quad (2.41)$$

This form of the propagator was used to model the randomised benchmarking gate sequences in Section 4.5 with the pulse area  $\theta = \Omega_{\text{eff}}t$  and the driving field phase  $\phi_0$  setting the gate axis of rotation  $\varphi$  such that  $\phi_0 = 0$  implements an  $R_x$  rotation and  $\phi_0 = \pi/2$  an  $R_y$  rotation.

### 2.3.6 Bloch Sphere Representation

The Bloch Sphere representation is a convenient visual representation of the dynamics of a two-level quantum system (a qubit). Its invention is attributed to Felix Bloch [149], but it first appeared in the academic literature in its present day form in reference [150]. It amounts to mapping two complex-

<sup>10</sup> See reference [138] or [125] for a derivation.

valued coefficients that describe a qubit to two real-valued parameters as shown in equation (2.42)

$$|\psi\rangle = c_g|0\rangle + c_e|1\rangle \rightarrow |\psi\rangle = \cos\frac{\theta}{2}|0\rangle + e^{i\phi}\sin\frac{\theta}{2}|1\rangle, \quad (2.42)$$

where we have used the properties of a quantum state that  $\sum_i |c_i|^2 = 1$  (conservation of probability) and the fact that only the relative phase between the two states is necessary to describe the system. The conservation of probability assumes that there is no dissipation to states outside of the computational basis. Using this mapping, we can define a three-dimensional real vector,  $\mathbf{n}$ , as

$$\mathbf{n} = \begin{pmatrix} n_x \\ n_y \\ n_z \end{pmatrix} = \begin{pmatrix} r \sin\theta \cos\phi \\ r \sin\theta \sin\phi \\ r \cos\theta \end{pmatrix}, \quad (2.43)$$

where  $\theta \in [0, \pi]$ ,  $\phi \in [0, 2\pi]$ , and  $r$  is the length of the vector  $\mathbf{n}$ . The parameter  $r$  always takes the value of 1 if we are representing a pure state  $|\psi\rangle$ . This means that a pure state maps onto the surface of a Bloch sphere. Using values of  $r < 1$  allows us to also visualise mixed state density matrix operators onto the Bloch sphere. In this case the length of the arrow represents the purity of the mixed state defined as

$$\text{Tr}(\rho^2) = \frac{1 + \mathbf{n} \cdot \mathbf{n}}{2} = \frac{1 + \|\mathbf{n}\|^2}{2} = \frac{1 + r^2}{2}, \quad (2.44)$$

where a pure state has  $\text{Tr}(\rho^2) = 1$  and a maximally mixed state has  $\text{Tr}(\rho^2) = 1/d$  with  $d = 2$  for a two-level system. Figure 2.4 shows an example Bloch sphere representation of the first 3/4 cycle from the time evolution presented in Fig. 2.2 without including the decoherence effects resulting from spontaneous emission (a) and with these effects included (b). The reduced size of the final Bloch vector shown in (b) represents the loss of coherence.

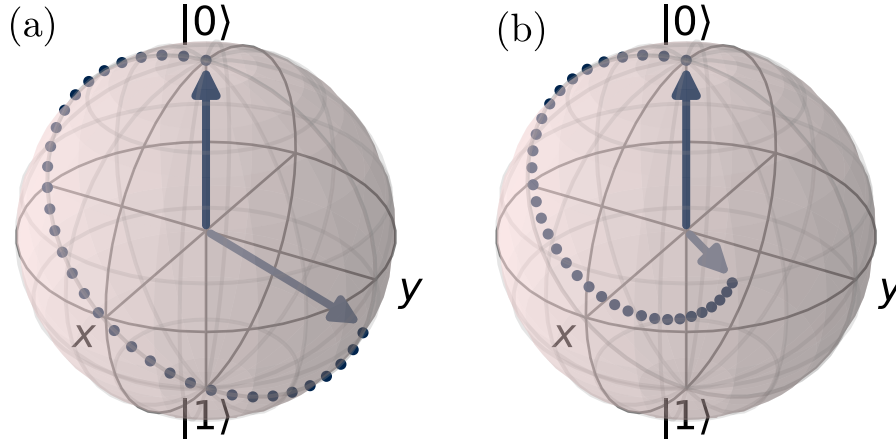


Figure 2.4: Example Bloch sphere representation of a two-level system time evolution created using the QuTip library for Python [151]. (a) Pure state time evolution. (b) Mixed state evolution obtained with OBE. Notice how the length of the Bloch vector shrinks as the system decoheres due to the finite linewidth effects incorporated into the OBE.

### 2.3.7 AC Stark Shift

The AC Stark shift, also referred to as the dynamic Stark shift, describes the energy shifts that result from the application of an oscillating electromagnetic field to a quantum system. The effect can be described either using a semi-classical approach or a fully-quantised treatment with the differences highlighted in reference [152]. In the limit of a high laser intensity (i.e. large occupation of a single quantised radiation field mode), the two methods converge to the same result. For the purposes of this work, the calculated Stark shifts relate to trapping of single atoms in optical dipole traps (ODTs) and two-photon Rydberg excitation where the field intensities applied to the atoms are high and the semi-classical treatment is valid.

An approximate formula for the magnitude of the AC Stark shift can be derived by diagonalizing the basic two-level Hamiltonian from equation (2.26) and considering its energy eigenvalues,  $\lambda_{\pm} = \pm \frac{\hbar}{2} \sqrt{\Omega^2 + \Delta^2}$ , in the limit of a large detuning as defined above. This result is referred to as the resonant AC Stark shift and it takes the form

$$\Delta E_{\text{AC}} = \hbar \frac{\Omega^2}{4\Delta}. \quad (2.45)$$

However, if we consider the 1064 nm ODT used in our experiment with relation to the 852 nm D2-line in Cs, for example, then we see that the RWA is no longer a good approximation because the angular frequency sum and difference terms ( $\omega_{\text{laser}} \pm \omega_{eg}$ ) that appear in the process of making the RWA now only differ by a factor of five in magnitude. Furthermore, in a real atomic system there are dipole couplings to multiple states so even when modelling a two-level system, one needs to consider these couplings, referred to as off-resonant shifts, in the overall AC Stark shift calculation to obtain better agreement with experiment. This is done by considering all ground state dipole moment couplings to the polarisation component  $q$  of the Stark-shifting field and applying time-dependent perturbation theory to find the total energy shift,  $\Delta E$ , resulting from the contributions due to each dipole-coupled state [119]. When expanded into spherical tensors using the Wigner-Eckart theorem [127], the expressions for the AC Stark shift take the form

$$\Delta E = -\frac{1}{4} \sum_{n',j',I',F',m'_F} \frac{1}{\hbar\Delta'_{nm}} |E_q|^2 \begin{pmatrix} F & 1 & F' \\ -m_F & -q & m'_F \end{pmatrix} |\langle n, j, I, F || d || n', j', I', F' \rangle|^2, \quad (2.46)$$

where we have defined  $\Delta'_{nm}$  as follows:

$$\frac{1}{\hbar\Delta'_{nm}} = \frac{1}{\hbar(\omega_{nm} - \omega_{\text{laser}})} + \frac{1}{\hbar(\omega_{nm} + \omega_{\text{laser}})} \quad (2.47)$$

The standard procedure outlined in Section 2.3.1 can then be applied to reduce equation (2.46) into a function of Wigner 3j and 6j symbols following the approach in [153]. It should be noted that the expression in eq. (2.46)

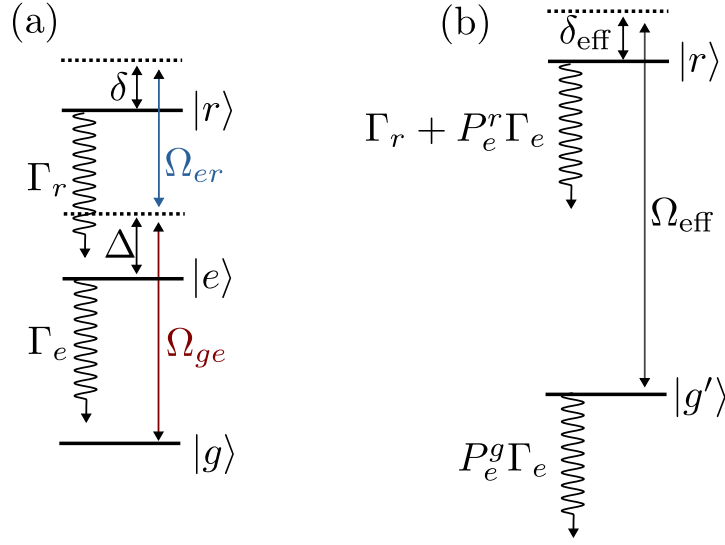


Figure 2.5: (a) Three level system typical of two-photon Rydberg excitation schemes. (b) Effective two-level system after adiabatically reducing the system in (a) in the limit of a large intermediate state detuning.

does not include the polarisability of the ionic core, which also contributes to the overall polarisability of the atom [154]. This correction is of the order of a few percent for transitions from the ground state in caesium [155], and it was not considered in the calculations carried out in this thesis.

### 2.3.8 Two-Photon Transitions

Two-photon transitions are used in the experiment when exciting atoms to a Rydberg state. The two-photon approach is currently the preferred method for Rydberg excitation because it allows for the partial cancellation of the photon momentum kick by using two counter-propagating beams, and it avoids the problems of static charge build-up and limited power availability associated with using a single photon excitation scheme which requires ultraviolet light. A schematic representation of the three-level ladder-type system typical of such Rydberg atom experiments is shown in Fig. 2.5(a).

In this configuration the first laser beam, typically in the visible range, drives a transition between a ground state,  $|g\rangle$ , and an intermediate excited state,  $|e\rangle$ , with a Rabi frequency  $\Omega_{eg}$  and a single-photon detuning  $\Delta$ . The second laser, usually in the infrared, couples the excited state to a Rydberg state,  $|r\rangle$ , with a two-photon detuning  $\delta$ . By applying the dipole and rotating wave approximations, we can write down the system Hamiltonian as [156]

$$\hat{H} = \hbar \begin{pmatrix} 0 & \Omega_{eg}/2 & 0 \\ \Omega_{eg}/2 & -\Delta & \Omega_{er}/2 \\ 0 & \Omega_{er}/2 & -\Delta - \delta \end{pmatrix}. \quad (2.48)$$

In order to include the dissipative effects of spontaneous emission, we can use the density matrix formalism and the Lindblad master equation. The excited and Rydberg state decay rates,  $\Gamma_e$  and  $\Gamma_r$  respectively, are used to define collapse operators [157]

$$c_e = \sqrt{\Gamma_e}|g\rangle\langle e|, \quad (2.49a)$$

$$c_r = \sqrt{\Gamma_r}|e\rangle\langle r|. \quad (2.49b)$$

By inserting the collapse operators into equation (2.29) we can obtain a Lindblad superoperator and describe the system dynamics using the master equation. In order to minimise scattering off the state  $|e\rangle$ , two-photon Rydberg excitations are typically performed with a large intermediate state detuning such that  $|\Delta| \gg \Omega_{eg}, \Omega_{er}$ . In this limit, one can adiabatically eliminate the intermediate state and obtain an effective two-level system as shown in Fig. 2.5(b). Here we have defined the effective Rabi frequency and effective detuning as [158]

$$\Omega_{\text{eff}} = \frac{\Omega_{eg}\Omega_{er}}{2\Delta}, \quad (2.50a)$$

$$\delta_{\text{eff}} = \delta + \Delta_g - \Delta_r, \quad (2.50b)$$

where  $\Delta_g$  and  $\Delta_r$  are the resonant AC Stark shifts of states  $|g\rangle$  and  $|r\rangle$  given by equations (2.51).

$$\Delta_g = \frac{\Omega_{eg}^2}{4\Delta}, \quad (2.51a)$$

$$\Delta_r = \frac{\Omega_{er}^2}{4\Delta}, \quad (2.51b)$$

Finally, we need to transform the three-level system dissipation terms due to spontaneous emission into their weighted equivalents for a two-level system. To achieve this, we calculate the population of the intermediate state using equation (2.52) following the method outlined in [159] which includes a contribution from the ground state,  $P_e^g$ , and the Rydberg state,  $P_e^r$ .

$$P_e = \frac{\Omega_{eg}^2 + \Omega_{er}^2}{4\Delta^2} = P_e^g + P_e^r, \quad (2.52)$$

where  $P_e^g = \Omega_{eg}^2/4\Delta^2$  and  $P_e^r = \Omega_{er}^2/4\Delta^2$ . Using these transformations, we can write down the effective Hamiltonian including dissipation for the effective two level system as [159]

$$\hat{H}_{\text{eff}} = \hbar \begin{pmatrix} \Delta_g - i\frac{P_e^g\Gamma_e}{2} & \frac{\Omega_{\text{eff}}}{2} \\ \frac{\Omega_{\text{eff}}}{2} & (\Delta_r - \delta) - \frac{i}{2}(\Gamma_r + P_e^r\Gamma_e) \end{pmatrix} \quad (2.53)$$

One important thing to note at this stage is that the phase accumulation due to a  $2\pi$  pulse is not guaranteed to be  $e^{i\pi} = -1$  in the case of a two-photon transition. This was observed in [160] and expressions were derived for the phase accumulated during a  $2\pi$  rotation as a function of the resonant and non-resonant AC Stark shifts. A resonant AC Stark shift is the shift produced

by the driving field laser on the transition it is targeting defined as shown in equations (2.51), for example. All other shifts are referred to as non-resonant shifts and have to be calculated using equation (2.46) and the respective electric field amplitudes and frequencies for two laser fields. The simplest case considered in reference [160] was a three level system where the hyperfine splitting of the intermediate state can be neglected and the intermediate detuning  $\Delta \gg \Gamma_e$ . The final result for the total phase accumulation during a two-photon  $2\pi$  pulse in this simple case is

$$\phi_{2\pi} = \pi - (\Delta_g + \Delta_{\Omega_{eg}}^{\text{nr}} + \Delta_{\Omega_{er}}^{\text{nr}})2t_\pi, \quad (2.54)$$

where  $\Delta_g$  is the resonant AC Stark shift on the ground state from equation (2.51a),  $\Delta_{\Omega_{eg}}^{\text{nr}}$  and  $\Delta_{\Omega_{er}}^{\text{nr}}$  are the non-resonant shifts on the ground state produced by the laser fields that drive transitions with Rabi frequencies  $\Omega_{eg}$  and  $\Omega_{er}$  respectively. This simple model is accurate to within 90%. A more accurate derivation which also considers the Zeeman-resolved hyperfine structure of the intermediate state is included in Appendix A of reference [160].

## 2.4 Rydberg Dipole-Dipole Interactions

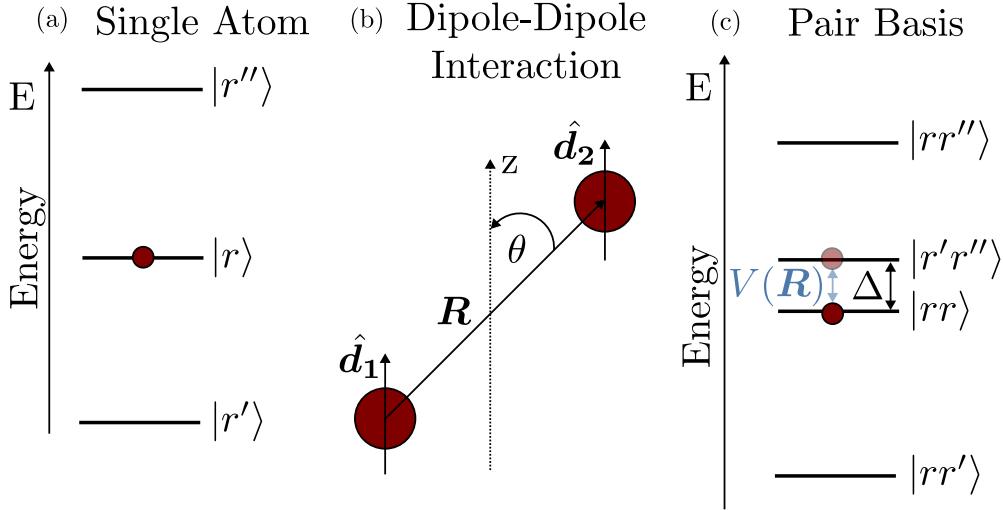


Figure 2.6: (a) Energy level diagram of a single Rydberg atom in state  $|r\rangle$  and the two states closest in energy to which it has a dipole coupling. (b) Schematic representation of the dipole-dipole interaction between two atoms separated by a distance  $R$  at an angle  $\theta$  to the quantisation axis. (c) Energy level diagram in the pair basis used to describe the dipole-dipole interaction,  $V(\mathbf{R})$ , which couples the doubly-resonant state,  $|rr\rangle$ , and the pair state nearest in energy,  $|r'r''\rangle$ , separated by an energy defect,  $\Delta$ .

A key ingredient for realising a quantum computer is the ability to generate entanglement between qubits which requires them to interact in a controllable way. In quantum computing based on neutral atom arrays, these interactions are realised using dipole-dipole interactions between atoms in Rydberg states. In order to understand the physics of this fundamental ingredient for our hardware platform, let us consider the simplest mathematical description of two interacting Rydberg atoms.

Equation (2.55) describes the energy associated with a dipole-dipole interaction between two atoms initially in the same Rydberg state,  $|r\rangle$ , with dipole moments  $\hat{d}_1$  and  $\hat{d}_2$  coupling them to the Rydberg states nearest in energy to  $|r\rangle$ , denoted as  $|r'\rangle$  and  $|r''\rangle$  as shown in Fig. 2.6(a).

$$V(\mathbf{R}) = \frac{\hat{\mathbf{d}}_1 \cdot \hat{\mathbf{d}}_2}{R^3} - \frac{3(\hat{\mathbf{d}}_1 \cdot \mathbf{R})(\hat{\mathbf{d}}_2 \cdot \mathbf{R})}{R^5}. \quad (2.55)$$

The vector  $\mathbf{R}$  describes the spatial separation between the nuclei of the two atoms. The orientation of  $\mathbf{R}$  is defined with respect to the quantisation axis as shown in Fig. 2.6 (b). We will consider the two atoms to be identical, so it does not matter energetically which dipole moment is associated with which atom.

The effect of the dipole-dipole interaction,  $V(\mathbf{R})$ , can be understood if we consider the combined energy of the two atoms as our system of interest, rather than the individual energies of the single atoms. This is referred to as transforming to the pair basis [135] whose energy landscape is shown in Fig. 2.6(c). By considering the different combinations of states to which a single atom in  $|r\rangle$  has an electric dipole coupling to, we can see that there exist a pair state  $|r'r''\rangle$  which has the smallest energy difference relative to the starting state  $|rr\rangle$ . This energy difference is referred to as the energy defect,  $\Delta$ , given by

$$\Delta = E_{|r'\rangle} + E_{|r''\rangle} - 2E_{|r\rangle}. \quad (2.56)$$

The energy defect is a function of the atomic species and the choice of Rydberg state and it plays an important role in defining the character of the dipole-dipole interaction.

In the limit of  $R \rightarrow \infty$  the dipole-dipole interaction between the two atoms is vanishing. If we now ask what happens when we take two atoms initially in  $|r\rangle$  and start moving the atoms closer together, we must consider the energy contribution from the dipole-dipole interaction which can couple the pair states  $|rr\rangle$  and  $|r'r''\rangle$ . The interaction Hamiltonian in the pair basis is

$$\hat{H} = \begin{pmatrix} 0 & V(\mathbf{R}) \\ V(\mathbf{R}) & \Delta \end{pmatrix}, \quad (2.57)$$

and its eigenvalues are

$$\Delta E_{\pm} = \frac{\Delta \pm \sqrt{\Delta^2 + 4V(\mathbf{R})^2}}{2}. \quad (2.58)$$

When we consider the eigenvalues of this Hamiltonian, we can see that the effect of  $V(\mathbf{R})$  is to shift the energies of the pair states as function of the separation between them. In the limit of  $|\mathbf{R}| \rightarrow \infty$ , we recover the energy defect as the energy difference between the eigenenergies of the Hamiltonian, while for non-zero values of the dipole-dipole interaction, we can consider two limiting cases to gain an understanding of the functional form of the spatial dependence.

### Van der Waals Regime

The van der Waals regime refers to the case when  $V(\mathbf{R}) \ll \Delta$  and we can use a second order Taylor expansion of the square root term in equation (2.58) to find the energy separation,  $\Delta E$ , between the eigenstates of the Hamiltonian. The resulting expression is [135]

$$\Delta E = -\frac{V(\mathbf{R})^2}{\Delta} = -\frac{C_6}{R^6}. \quad (2.59)$$

It is important to note that in this regime, the sign of the interaction depends on the sign of the energy defect which is determined by the choice of Rydberg state. By convention the strength of the interaction is expressed using the van der Waals coefficient,  $C_6$ , which contains all the information about the specific atomic energy levels being considered and scales as  $\propto n^{11}$ . This scaling comes from the fact that the dipole-dipole interaction in the van der

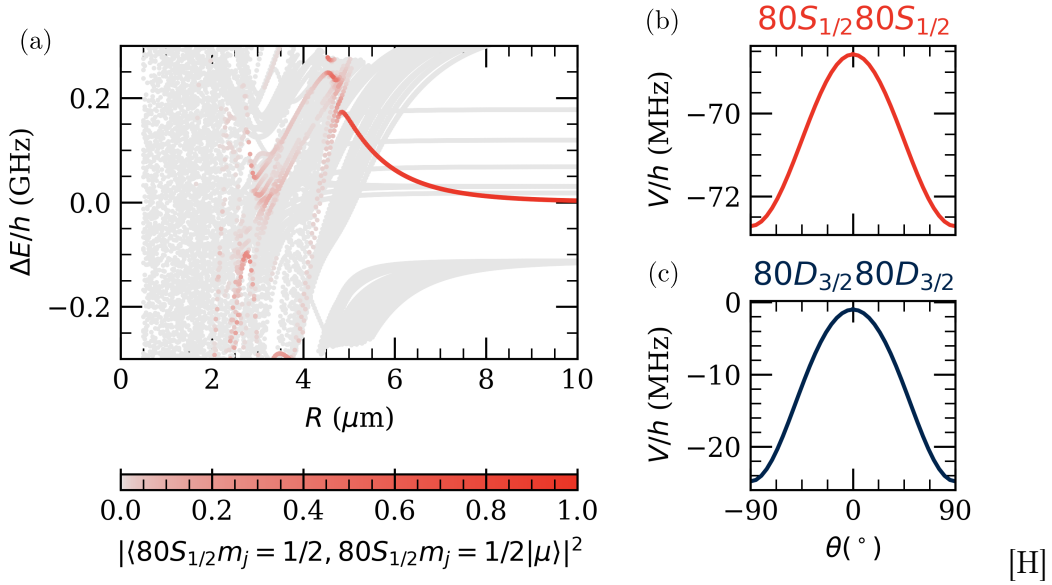


Figure 2.7: Simulations performed using the ARC package for Python [115]. (a) Results of direct diagonalization solution for the pair potential of the  $|80S_{1/2}m_j = 1/2, 80S_{1/2}m_j = 1/2\rangle$  Rydberg state as a function of distance. The simulations considered states with maximum  $\Delta n$  and  $\Delta l$  of 5 and a maximum energy defect of 25 GHz. The colours represent the overlap of the molecular potential eigenstates,  $|\mu\rangle$ , of the pair interaction Hamiltonian with the pair state at infinite separation. (b) and (c) Simulations of the angular dependence of pair interaction potential,  $V$ , at a separation of 6  $\mu\text{m}$  for two different Rydberg state pairs. Here  $\theta$  is the angle that the radial vector of the pair,  $\mathbf{R}$ , makes with the quantisation axis. For the  $nS$  Rydberg states, the interaction is almost isotropic, but for Rydberg states with higher orbital angular momentum the interaction energy varies significantly with  $\theta$ .

Waals regime is a second-order perturbation and the term  $\Delta$  scales as  $n^{-3}$  and  $V(R) \propto d^2 \propto n^4$  [135]. The values for  $C_6$  for alkali atoms can be obtained from the ARC software package which uses second order perturbation theory to calculate them by considering multiple pair states within a finite energy defect range specified by the user [115].

### Resonant Dipole Regime

The other limiting case occurs when  $V(\mathbf{R}) \gg \Delta$ . The interaction energy between the atoms in the pair is then given by

$$\Delta E = \pm V(\mathbf{R}) = \pm \frac{C_3}{R^3}. \quad (2.60)$$

In this regime the scaling with the principal quantum number is now reduced to  $\propto (n^*)^4$  and, due to the weaker scaling with  $R$ , one has to consider the interaction with all surrounding atoms as discussed in [161]. This is not the case in the van der Waals regime where the nearest-neighbour interactions dominate. Since  $V(\mathbf{R})$  is large, the coefficient  $C_3$  has to be calculated using direct matrix diagonalization as perturbative treatment is no longer valid. An example of such a pair interaction calculation for the  $|80S_{1/2}m_j = 1/2, 80S_{1/2}m_j = 1/2\rangle$  pair state is shown in Fig.2.7(a) using the ARC simulation package in Python [115]. The splitting of the potential for separations just above 4  $\mu\text{m}$  is due to the admixture of pair states which are not dipole coupled to the pair state at infinite separation, but experience quadrupole and higher-order couplings with increasing Rydberg interaction strengths. For atomic separations  $< 4 \mu\text{m}$ , the potential landscape becomes even more complex due to this strong mixing between energy levels resulting in what is referred to as the ‘spaghetti’ region which can be seen in Fig. 2.7(a). We do not operate in this regime in our experiments, but further information on the subject can be found in reference [162].

### Interaction Strength as a Function of Angle

If we return to equation (2.55) and evaluate the scalar product terms in the spherical basis as shown in [163], we can see that the dipole-dipole interaction energy is anisotropic and there is a dependence on the angle  $\theta$  with respect to the quantisation axis. This dependence on  $\theta$  is weak for states with  $l = 0$  such as the  $80S_{1/2}$  states used in the experiment. This is because the dipole-dipole interaction does not conserve the total angular momentum of the pair state when  $\theta \neq 0$ . The anisotropy is still non-zero for  $S_{1/2}$  states however, because the nearest energy pair state for an  $S$  state would be a  $P$  state with  $l = 1$ .

This effect is illustrated in Fig.2.7(b) and (c) which compare the anisotropy of the interactions between caesium atom pairs in the  $80S_{1/2}m_j = 1/2$  and  $80D_{3/2}m_j = 3/2$  states at an atomic separation of 6  $\mu\text{m}$ . For the  $80S_{1/2}$  Rydberg state the maximum variation in the  $C_6$  coefficient as a function of  $\theta$  amounts to 6%, while for the  $80D_{3/2}$  state the variation is 96 %. See Chapter 3 of reference [135] for an in-depth discussion on this topic.

## Dipole Blockade

Rydberg dipole blockade is the physical mechanism underpinning the majority of the state-of-the-art Rydberg atom quantum computing and quantum simulation experiments. To understand the dipole blockade mechanism, let us consider the behaviour of a pair of atoms in the presence of a driving electromagnetic field which couples a single atom in the ground state,  $|g\rangle$ , to a Rydberg state,  $|r\rangle$ . At infinite interatomic separation, the process is fully described by the discussion of light-matter interactions in Section 2.3.8 and we can observe Rabi oscillations between the  $|gg\rangle$  and  $|rr\rangle$  pair states. If we now start to reduce the separation between the atoms, the dipole-dipole interaction of the Rydberg states begins to shift the energy of the doubly-excited state  $|rr\rangle$  out of resonance with the driving field until such a point where the energy shift exceeds the power-broadened linewidth of the driving laser field<sup>11</sup>. At this point, we have reached the dipole blockade condition  $V(|\mathbf{R}| = R_b) = \hbar\Omega$ , where  $R_b$  is the blockade radius given by equation(2.61) and  $\Omega$  is the driving field Rabi frequency.

$$R_b = \sqrt[6]{\frac{C_6}{\Omega}}. \quad (2.61)$$

This process is illustrated schematically in Fig. 2.8. Assuming a strict blockade condition has been achieved, then for  $N$  atoms contained within  $R_b$ , only a single atom can be excited to the Rydberg state at a given time. However

<sup>11</sup> In other words, dipole blockade is achieved when  $V(\mathbf{R}) > \hbar \times \max(\Gamma, \Omega)$ .

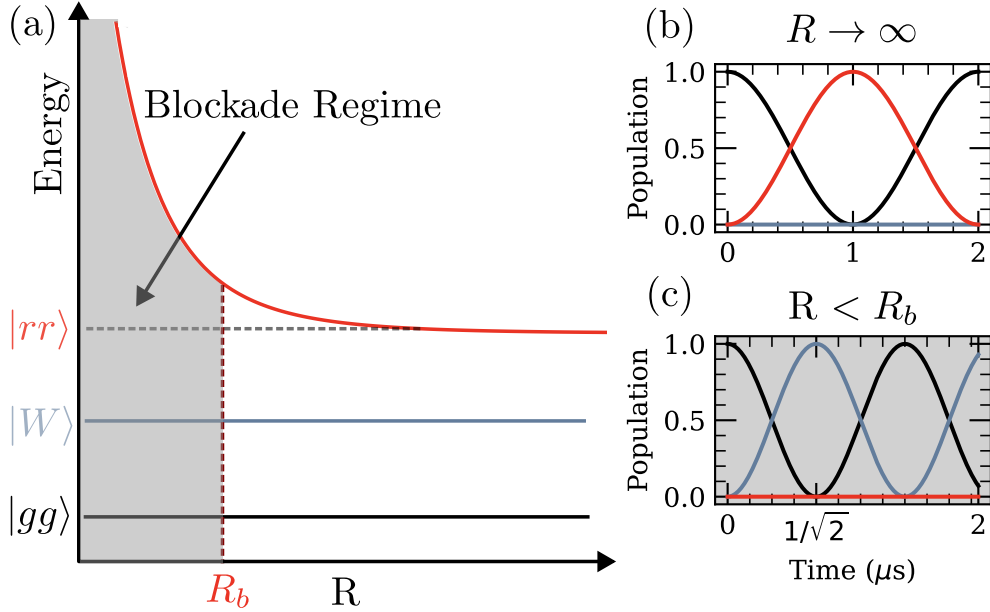


Figure 2.8: (a) Schematic of dipole-dipole interaction energy shift as a function of the radial distance between two Rydberg atoms (b) Rabi oscillation outside of the blockade radius for the Rydberg state  $80S_{1/2}$ . The pair state oscillates between  $|gg\rangle$  and  $|rr\rangle$  with Rabi frequency  $\Omega = 2\pi \times 1$  MHz. (c) Rabi oscillation within the blockade region defined as  $R < R_b = 6.6 \mu\text{m}$  for the specified parameters. The interatomic separation is  $5 \mu\text{m}$  and the interaction energy is  $V/h = 205$  MHz. Excitation to  $|rr\rangle$  is suppressed and the pair state populations oscillate between  $|gg\rangle$  and  $|W\rangle = \frac{1}{\sqrt{2}}(|gr\rangle + |rg\rangle)$  at an enhanced Rabi frequency of  $\Omega/2\pi = \sqrt{2} \times 1$  MHz.

there are  $N$  different permutations of realising this condition which gives rise to an entangled collective state of the  $W$  type<sup>12</sup> :

$$|W_N\rangle = \frac{1}{\sqrt{N}} \sum_{i=1}^N |g_1 g_2 g_3 \dots r_i \dots g_N\rangle. \quad (2.62)$$

Because there are now  $N$  different excitation pathways, the effective Rabi frequency is collectively enhanced by a factor of  $\sqrt{N}$ .

<sup>12</sup> The  $W$  state is named after Wolfgang Dür who first reported it and drew a distinction between inequivalent entangled states of three particles [164].

## Chapter 3

# Experimental Set Up

The realisation of a neutral atom quantum computer requires a complex set of optical, mechanical and electronic components. The overall footprint of the device spans two  $1.5 \text{ m} \times 3 \text{ m}$  optical tables just for the lasers and optics with an equivalent footprint required for the various electronics in the form of laser controllers, power supplies and chillers. In order to present a structured overview of the entire experimental set up, this chapter covers a single sub-system at a time in the following order. We begin by reviewing the ultra-high vacuum (UHV) system used to protect our qubits from collisions with the background gases present in the atmosphere. We then examine the lasers and optics required to obtain a cloud of cold atoms which is the starting point for all single atom experiments. Then, in Section 3.3, the 1064 nm tweezer array system is presented, which generates the optical potential used to confine our single atom qubits. The state read out and initialisation procedures are then described, before concluding the chapter with a description of the microwave and Rydberg systems used to control the internal states of our qubits and to generate entanglement between them. The final Section 3.8 gives a brief overview of the computer control system used to integrate all of these sub-systems into a single device capable of performing useful experiments. Certain aspects of the experimental set up such as the Raman

system for single qubit rotations and the 800 nm trapping system have been omitted because they are not directly relevant to the author’s individual contribution to the project which is the focus of this document. The 1039 nm moving tweezer trap used for atom sorting is only briefly covered in Section 3.3.3 because it was used to set up the 1D atom chains discussed in Chapter 6. Further details on these systems will be available in the thesis of Elliot Diamond-Hitchcock [165].

### 3.1 Vacuum Chamber

A new vacuum system was designed and assembled for the SQuAre project. It is made up of an octagonal main vacuum chamber connected to a 2D MOT section using a differential pumping tube. A 3D CAD rendering of the full vacuum assembly is shown in Fig. 3.1 with the key elements indicated with arrows to serve as a visual aid for the description given in the remainder of this section.

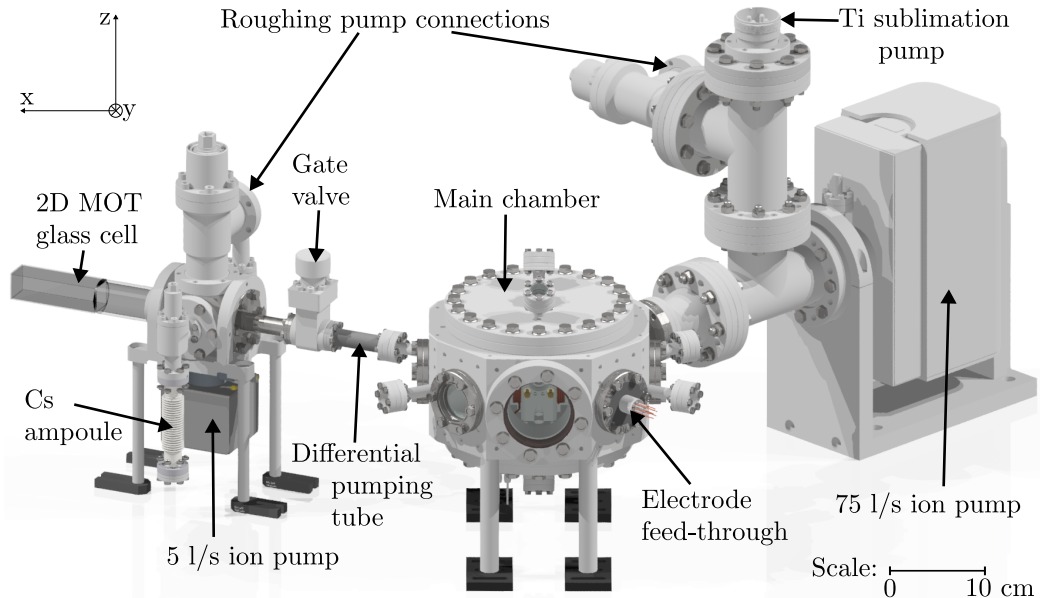


Figure 3.1: Annotated SQuAre experiment vacuum chamber with lab coordinate reference frame.

The metal components of the main chamber are made from 316LN stainless steel which has been shown to have lower outgassing of water and hydrogen compared to the lower-cost 304 alloy [166]. In addition, 316LN has lower magnetic permeability than other common alloys such as 304 or 316L which is an important consideration for minimising magnetic field noise in the experiment.

### **Main Chamber**

The main chamber is where the single atom physics take place. It is maintained at ultra-high vacuum (UHV) pressures by a 75 l/s Gamma Vacuum ion pump running continuously. A pressure reading of  $5 \times 10^{-11}$  Torr was obtained from the ion current to pressure conversion performed by the Gamma Vacuum pump controller. This pressure reading was not calibrated against an ionisation gauge or a MOT lifetime measurement as implemented in [167] or [168]. In addition to the ion pump, there is a titanium sublimation pump installed in the setup which can be switched on in single bursts as required. Its function is to sputter titanium which coats the inside walls of the vacuum chamber and is highly reactive with oxygen, nitrogen and hydrogen. The titanium coating can be depleted with time, but in the three years of system runtime at the time of writing the titanium sublimation pump has only been activated during the initial ultra-high vacuum preparation. The initial UHV pressure recorded after commissioning the system was  $1.3 \times 10^{-11}$  Torr and it has gradually increased since then at a rate of  $2 \times 10^{-11}$  Torr / year. This slow increase in pressure was not found to have a significant impact on the trap lifetimes, so it is likely that this was caused by ion pump leakage current [169]. The decision was made to delay a repeated firing of the titanium sublimation pump because of the associated risks such as introducing methane outgassing as discussed in reference [170].

## 2D MOT Section

The 2D MOT section of the vacuum assembly is used as a high-pressure cold atom source to the main experiment. The initial source of caesium is a glass ampoule placed inside a steel bellows and exposed to an air-conditioned temperature environment at 20° C. A shut-off valve is used to control the flow of atoms from the ampoule into the rest of the set up. Once the ampoule has been cracked, and the shut-off valve opened, the atoms can sublimate<sup>13</sup> into a 6-way cube which has connections to the 5 l/s ion pump at the bottom and the 2D MOT glass cell on the left. The remaining cube connections are to another Cs ampoule on the opposite side, a UHV all-metal valve used to make a temporary connection to an external roughing pump, and a connection to the differential pumping tube. The atoms migrating into the cube make their way into the glass cell through molecular diffusion where they are cooled into a 2D MOT as described in Subsection 3.2.2.

The pressure measured in the 2D MOT cell after the initial bake was  $8 \times 10^{-9}$  Torr inferred from the 5 l/s ion pump current. This was independently verified using the method from [171] by building a temporary 3D MOT in the 2D glass cell and recording a series of MOT load curves while the Cs partial pressure was decaying over several hours. To engineer this scenario, the Cs ampoule shut-off valve, which is normally closed, was opened for a period of one hour and then closed just before the start of the measurement. The measurement results are summarised in Fig. 3.2 and were fitted with

$$N_{eq} = \frac{\alpha}{\beta}(1 - \gamma\tau), \quad (3.1)$$

where  $N_{eq}$  is the equilibrium atom number in the MOT,  $\tau$  is the  $1/e$  loading time,  $\frac{\alpha}{\beta}$  is a ratio representing the maximum atom number that can be ob-

---

<sup>13</sup>Cs is in the solid phase at the lab ambient temperature of 19° C. Its melting point is 28.5° C.

tained in the system and  $\gamma$  is the loss rate from the MOT due to collisions with background particles. The values of  $\tau$  and  $N_{eq}$  were obtained using exponential rise curve fits to each recorded MOT load curve.

Using the estimated loss coefficient for Cs of  $4.9 \text{ Torr}^{-1} \text{ s}^{-1}$  from [167] and the fitted value for  $\gamma$  obtained from a fit with equation (3.1), a background gas pressure of  $6.8(2) \times 10^{-9} \text{ Torr}$  was obtained showing good agreement with the ion pump pressure reading. The deviation from a straight line fit is due to the violation of the assumption that the non-Cs background pressure in our chamber remains constant during the measurement. The assumption was good in the case of reference [171] because they used in-vacuum dispensers controlled by an electric current. The Cs in our experiment is released from an ampoule which is typically shut-off from the vacuum system. While in this state, the Cs ampoule is effectively isolated from the 2D MOT ion pump and the background pressure inside it increases with time due to ingress of particles at higher atmospheric pressure outside the ampoule assembly. When the Cs ampoule was opened at the start of the measurement, other background gases were also introduced into the vacuum system. Therefore, in our experiment both the background and the Cs partial pressures changed as a response to opening the valve and were pumped down to equilibrium at different rates by the ion pump.

This measurement was taken because the 2D MOT ion pump was malfunctioning shortly after the system was commissioned. Its pressure reading would increase to readings as high as  $6.97 \times 10^{-6} \text{ Torr}$  over the course of a few days. Briefly applying a voltage of 7.5 kV to the ion pump (high-potting) instead of the usual 4 kV would temporarily decrease the pressure reading, but it would creep up again after a few days. The pump was replaced once, but the same issue re-occurred suggesting that the ion pump placement in the 2D MOT system is sub-optimal and would need to be addressed in future experimental iterations. The failure mode hypothesis is that the ion pump

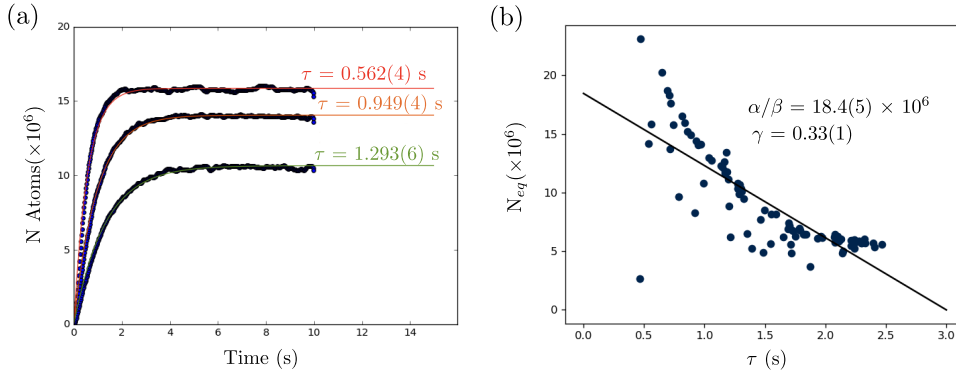


Figure 3.2: Independent vacuum pressure measurement in 2D MOT glass cell using a temporary 3D MOT. (a) A sample of three MOT load curves taken over several hours as the Cs partial pressure in the system decreases after closing the valve. (b) Plot of 3D MOT 1/e load time,  $\tau$ , vs equilibrium atom number,  $N_{eq}$ , with one hundred load curves taken over 8 hours. The data was fitted with equation 3.1 to obtain the values for  $\gamma$  and  $\alpha/\beta$ .

was mounted in close proximity to the Cs dispensers which resulted in a high vapour density that resulted in a significantly reduced pump lifetime. By installing the pump closer to the 2D MOT glass cell and further away from the dispensers, we expect that the pump lifecycle can be improved.

After a few months of unreliable operation, the 2D MOT ion pump was switched off, but this did not significantly affect the main chamber pressure. The reason for this was the differential pumping tube which connects the two areas of the vacuum system. Its intended benefit is to allow us to operate a high pressure 2D MOT with a large atom number for fast array loading, whilst maintaining up to three orders of magnitude lower Cs background pressure in the main chamber to minimise Cs-Cs collisions for an improved trap lifetime. The 10 cm long differential pumping tube with its narrow 3 mm inner diameter acts as a velocity filter for an atomic beam produced by shining a 2D push beam through the 2D MOT cloud. The conductance of the differential pumping tube,  $C$ , is a function of its geometry and is given by the approximate expression  $C \sim 12d^3/L$  where  $d$  is the inner diameter of the tube and  $L$  is its length. Then for a given pump rate,  $S$ , in 1/s the differential pressure ratio is given by

$$\frac{P_2}{P_1} = \frac{C}{C + S}. \quad (3.2)$$

which evaluates to  $8.1 \times 10^{-4}$  using our experimental parameters without accounting for the 75 l/s ion pump conductance.

### In Vacuum Lens Assembly

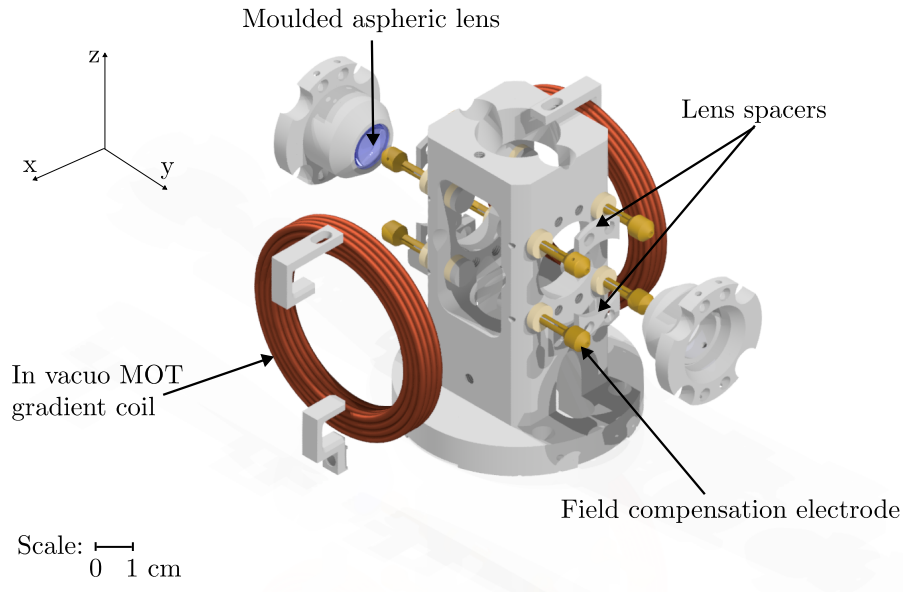


Figure 3.3: SQuAre experiment in-vacuum lens assembly showing lens mounts, electrodes for stray field cancellation and MOT bias coils.

The centre piece of the SQuAre experiment vacuum chamber is the lens assembly shown in Fig. 3.3. It is based on previous designs which employ in-vacuum high numerical aperture (NA) lenses for focussing the tweezer beams at the diffraction limit and for collecting the atomic fluorescence signal from single atoms as described in [146, 172, 173]. This approach eliminates the significant aberrations that result from tightly focussing a beam through a glass cell wall using a microscope objective [172], which is the other commonly used approach in single atom physics experiments. Microscope objectives for such applications often need to be manufactured at great expense based on custom designs to achieve a compatible working distance

that allows enough room to place other components around the glass cell such as magnetic field coils and electrodes for field stabilisation. Placing the lenses in vacuum makes it possible to achieve a high collection efficiency by working with a single moulded aspheric lens which typically has a working distance of a few millimetres. In our case, we use a Geltech 355561 lens [172] with a focal length,  $f = 10$  mm, and a working distance of 7 mm to achieve  $\text{NA} = 0.45$  at 852 nm. In terms of NA, microscope objectives outperform in-vacuum lenses with typical  $\text{NA} > 0.5$  [81, 84]. Alternative designs which employ an ex vacuo compound objective lens with an effective working distance  $> 35$  mm required to operate outside a stainless steel vacuum chamber have been demonstrated [174, 175], but their performance in terms of light collection efficiency has typically been worse. When operating with in vacuo lenses it is important to minimise the build-up of any electrostatic charge on their surface because they are in close proximity to the atoms which are extremely sensitive to any electric fields when excited to a Rydberg state [173]. To mitigate these effects, we use lenses which have a coating of indium tin oxide (ITO). This material is conductive and transparent, but reaching higher conductivity and therefore faster charge dissipation requires thicker deposition layers and thus reduced optical transmission. In our case, we operate with a 200 nm thick coating which gives  $> 90\%$  transmission at our target wavelengths and a 250  $\Omega$ /square sheet resistance. To cancel out any residual static electric fields inside the vacuum chamber, the SQuAre lens assembly has four electrodes per lens as shown in Fig. 3.3. The precise separation between the two lenses inside the assembly was calibrated in an iterative procedure before the system was put under vacuum. The lens assembly was put together ex vacuo and the beam collimation measured with a beam profiler over a distance of six meters. The lens spacers were then progressively machined down in 10  $\mu\text{m}$  increments and beam profiles re-taken at every iteration to maximise the distance away from the lens assembly at which a waist is formed. Once an optimal separation had been reached, the

in-vacuo MOT gradient coils were mounted onto the assembly and installed in the centre of the main chamber. They use low-outgassing Kapton coated wire with 1.8 mm conductor diameter and 0.2 mm of coating with a design axial field gradient of 10 G/cm.

## 3.2 Magneto Optical Traps (MOTs) & Sub-Doppler Cooling

### 3.2.1 Cooling Laser System

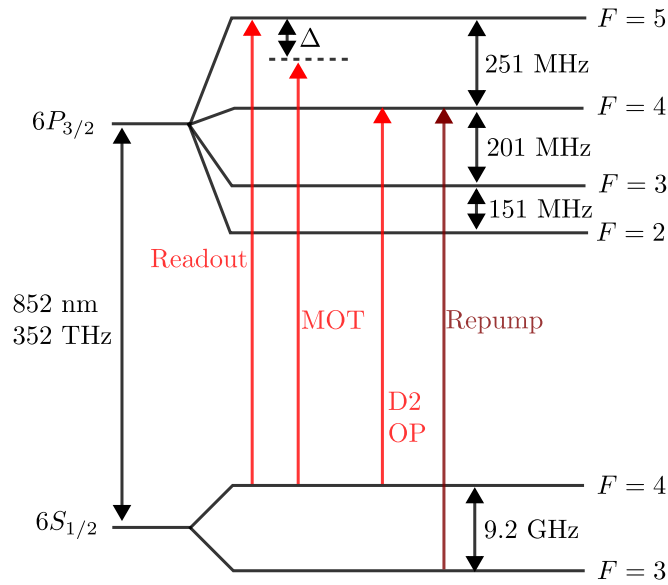


Figure 3.4: Summary of the laser frequencies on the caesium D2-line required for forming a MOT, optical pumping (D2 OP) and readout.  $\Delta$  represents the detuning of the MOT beams from resonance, typically around  $-3\Gamma$ , where  $\Gamma$  is the excited state linewidth.

The relevant laser frequencies on the D2-line of caesium are summarised in Fig. 3.4. Due to the large ground state hyperfine splitting of 9.2 GHz, we use two Toptica DL-PRO 852 nm lasers for cooling and repump. Alternatively, this could have been achieved with a single laser and an electro-optic

modulator (EOM) at the cost of reduced power efficiency. Because we also perform optical pumping and state detection (readout) on the D2 line, the cooling laser system also provides the light for these processes. They will be discussed in detail in Section 3.5.

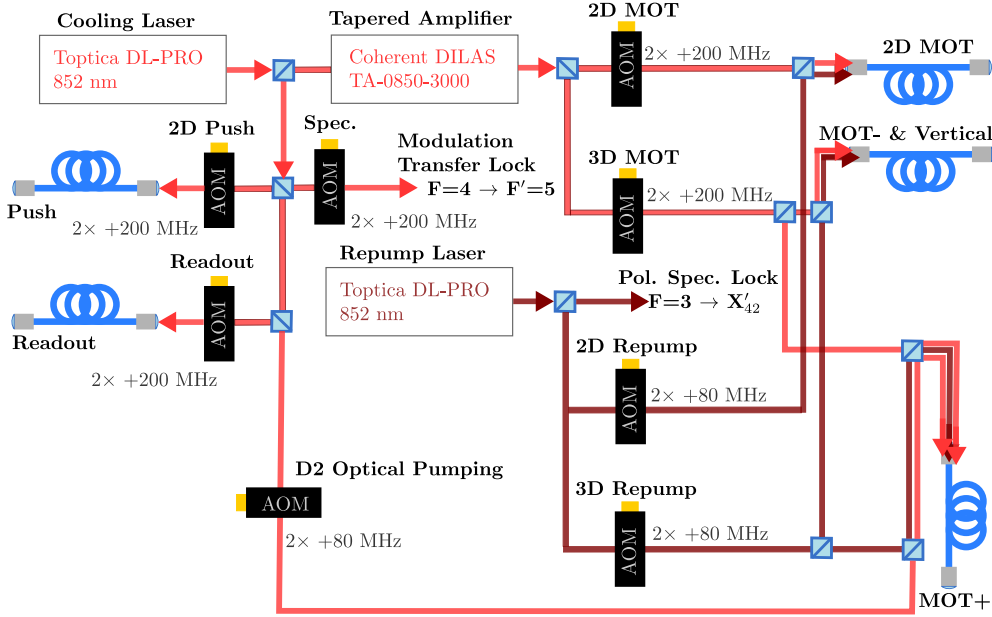


Figure 3.5: Schematic diagram of the 852 nm cooling laser system used for the 2D and 3D MOT. Spec. stands for spectroscopy and Pol. Spec. stands for polarisation spectroscopy.

A schematic diagram of the cooling laser system is shown in Fig. 3.5. The Toptica lasers can output up to 80 mW of light at maximum current. Approximately 20 mW of the 852 nm cooling laser output power is used to seed a Coherent DILAS TA-0850-3000 tapered amplifier (TA) which outputs 1.5 W of 852 nm light when driven with a 3 A current. The beam out of the TA has an elliptical profile which requires re-shaping into a Gaussian spot using a combination of cylindrical and spherical lenses for optimal performance in the acousto-optic modulators (AOMs). All AOMs are operated in double-pass configuration to access a larger frequency tuning range and the light is focussed into the AOM crystal for faster switching times at the cost

of reduced diffraction efficiency<sup>14</sup>. The remaining 60 mW of cooling light are distributed between the laser lock spectroscopy, the 2D push beam used to transport atoms through the differential pumping tube, the readout beam and the D2 OP pumping beam. We also split the repump laser into a 2D and a 3D beam path to allow for independent switching, because we want to switch off the 2D MOT light once we have loaded an array to minimise background light counts on our single atom imaging camera. The cooling laser set up is built on a separate optical table from the main experiment, so after passing through the AOMs, the light is coupled into single-mode, polarisation maintaining optical fibres and transported to the chamber optical table. The MOT+ fibre contains light at three frequencies: cooling light ( $F = 4 \rightarrow F' = 5$ ), repump light ( $F = 3 \rightarrow F' = 4$ ), and optical pumping light ( $F = 4 \rightarrow F' = 4$ ).

We employ different techniques to lock the cooling and repump lasers. For the cooling laser, we use a modulation transfer spectroscopy lock (MT lock) to perform sub-Doppler spectroscopy and lock the laser to the  $F = 4 \rightarrow F' = 5$  transition on the D2 line [176]. The MT lock set up is shown in Fig. 3.6 (a). Using counter propagating pump and probe beams of similar intensity, this locking technique creates a four-wave mixing process between the two pump beam sidebands generated by the EOM and the unmodulated probe beam to create a fourth wave in the form of a sideband for the probe beam which can be detected and de-modulated at the EOM frequency to obtain a sub-Doppler absorption spectrum [177, 178]. This resonance condition is only achieved for a specific atomic velocity class and the resulting lock signal is therefore insensitive to fluctuations in intensity, temperature or polarisation. It is implemented using a commercial EOM<sup>15</sup> modulated at 5 MHz and a Toptica Pound Drever Hall (PDH) Module to demodulate the signal from the transmission photodiode and obtain the error signal shown in Fig. 3.6(c).

<sup>14</sup> Typical double-pass diffraction efficiencies measured in our set up are  $\sim 50\%$  and typical AOM risetimes are of the order of 20 ns.

<sup>15</sup> EOM-02-5-V from Photonic Technologies.

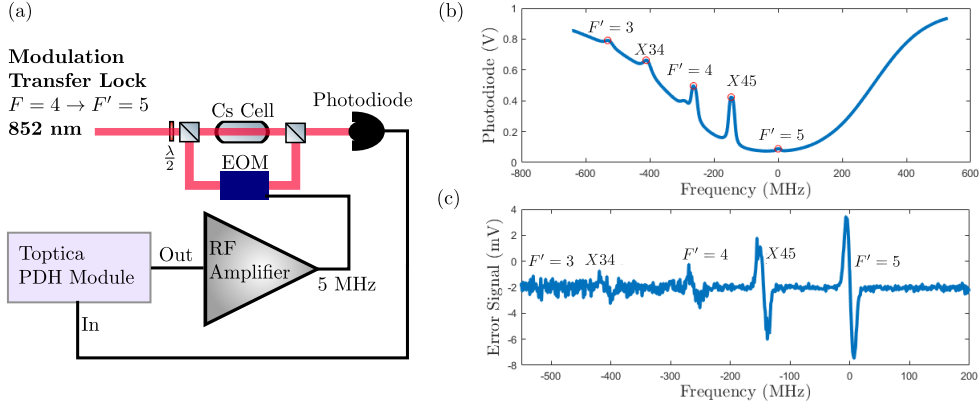


Figure 3.6: (a) Schematic diagram of the modulation transfer (MT) lock set up used to lock the 852 nm cooling laser. (b) Photodiode signal from MT lock showing sub-Doppler features. (c) Error signal after PDH demodulation used to lock the laser.

Another benefit of this type of lock is that the error signal is centred at zero offset which eliminates offset drift and results in improved long-term lock stability.

The 852 nm light out of the repump laser is locked to the  $F = 3 \rightarrow X'_{42}$  crossover transition using the standard polarisation spectroscopy method described in [179] without passing through an AOM. The repump light is then shifted into resonance with the  $F = 3 \rightarrow F' = 4$  at the atoms using double-passed 80 MHz AOMs<sup>16</sup>.

### 3.2.2 2D MOT

The 2D MOT is a modified version of the design presented in [180] which uses permanent magnets to produce the magnetic field gradient required to form a MOT. The orientation of the bar magnets was optimised for uniformity to achieve a 16(1) G/cm magnetic field gradient using the equations provided in [181]. An annotated 3D CAD rendering of the 2D MOT assembly is shown in

<sup>16</sup> The AOMs are actually operated at 88 MHz because the  $X'_{42}$  transition frequency is half-way between the transition frequencies from  $F = 3$  to  $F' = 2$  and  $F' = 4$ . See Section 8.3.2 in [117] for explanation.

Fig. 3.7(a). It consists of a metal cage which slides over the vacuum chamber glass cell and attaches to the CF40 cube of the 2D MOT. The permanent bar magnets are attached to two rectangular metal plates tilted at  $45^\circ$  to the z-axis which run along the length of the glass cell. Four 3D-printed shim coil formers attach to the cage. Each shim coil is wound with 11 m of 1-mm diameter wire to produce a 2.87 G/A field at the atoms. Along each of the two confinement axes of the 2D MOT there is one 3D-printed optics mount and one retroreflective mirror assembly with three compact mirrors from Thorlabs. Their orientation is shown in Fig. 3.7(b) for the horizontal 2D MOT axis. An identical arrangement is used for the vertical axis. Each 3D-printed optics mount houses two nonpolarizing beam splitters (NPBS) and a right-angle (RA) prism to provide three trapping regions in the glass cell. The first NPBS is a 30:70 and the second one is 50:50 to give approximately equal light intensities across the three trapping regions. Six quarter waveplates (QWP) per axis are required to achieve the correct circular polarisation for a MOT. The QWPs are inserted into circular slots cut into the metal frame of the cage.

We operate the 2D MOT with a  $1/e^2$  beam waist,  $w_0$ , of 10 mm to realise a large trapping volume. The MOT is operated with cooling light at a detuning of  $-3\Gamma = -2\pi \times 15.7$  MHz and resonant repump light. We use a total of 200 mW of cooling light and 7 mW of repump light split across the three trapping regions which gives a saturation parameter,  $s = 12$ , when referenced to the isotropic saturation intensity value for the  $F = 4 \rightarrow F' = 5$  transition taken from [128]. A linearly-polarised 2D push beam is applied with its k-vector along the cell length to direct the atoms from the 2D MOT region to the 3D MOT region in the main chamber via the differential pumping tube<sup>17</sup>. It has a waist of 0.8 mm and is typically operated with 100  $\mu$ W of optical power. In our design the final push beam mirror is mounted on the optical table using a long 30 cm post, so it is very sensitive to alignment drift

<sup>17</sup>The original design in [180] used a circularly polarised push beam.

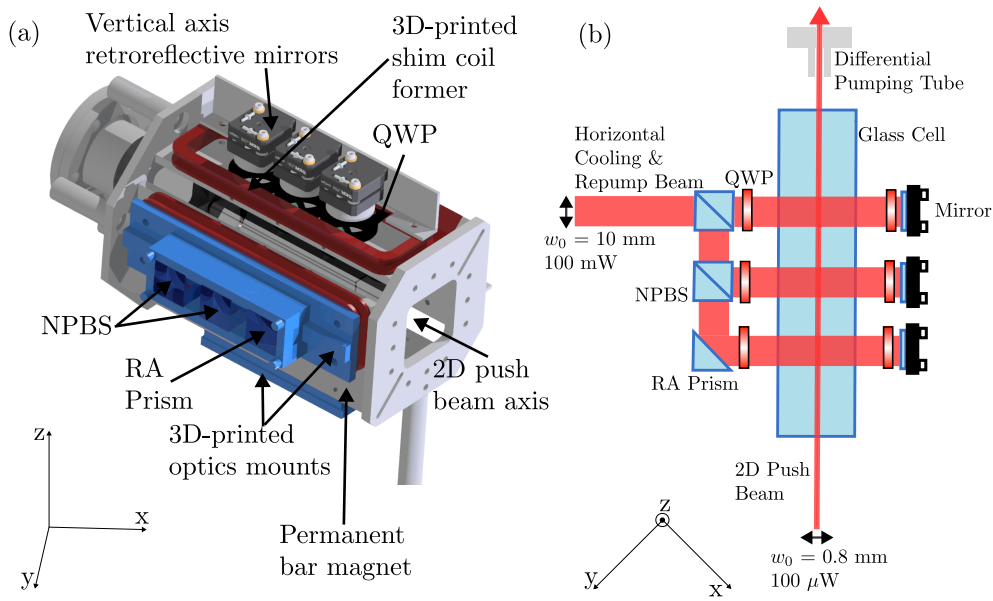


Figure 3.7: (a) Annotated 3D CAD rendering of the 2D MOT assembly. (b) Schematic representation of the 2D MOT beam paths in the horizontal plane. An identical set up is used to form the vertical 2D MOT confinement along the  $z$  axis. Abbreviations: QWP - quarter waveplate, RA prism - right-angle prism, NPBS - non-polarising beam splitter.

which manifests as slower 3D MOT loading. The original design in [180] circumvented this issue by having the 2D push mirrors attached directly to the cage. As part of regular experimental maintenance procedure, we find that we need to align the push beam using the 3D MOT signal on a 2 second load cycle to optimise performance. Because the push beam has an independent AOM to control its frequency and amplitude, we also tune these parameters to achieve the fastest 3D MOT load time possible and maintain a fast experimental repetition rate.

### 3.2.3 3D MOT

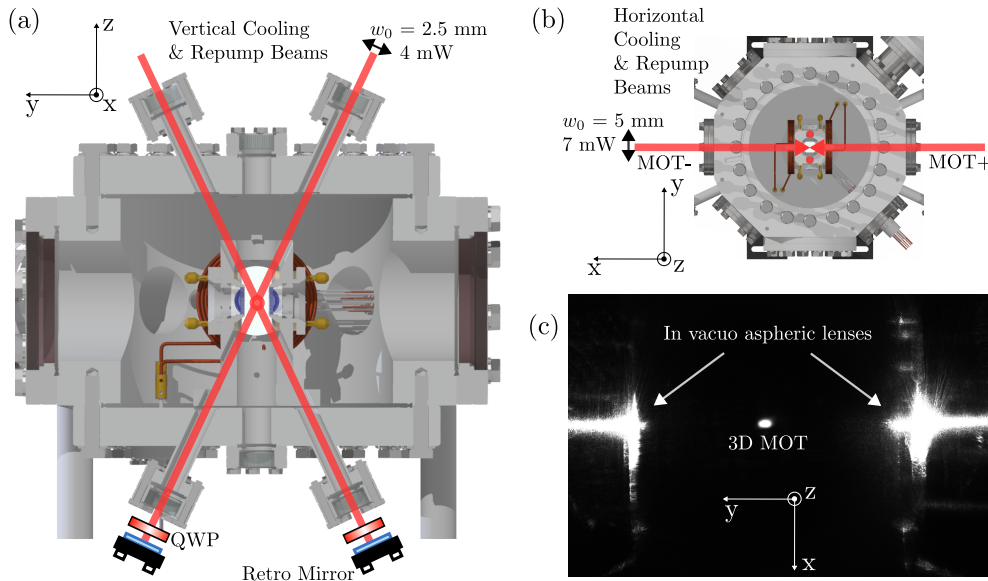


Figure 3.8: (a) Section through a CAD rendering of the main experimental vacuum chamber showing the vertical MOT beam configuration. The chamber geometry and the machined holes in the lens assembly constrain the beam size and the alignment angle of the vertical MOT beams. Both vertical MOT beams contain cooling and repump light. (b) Top-down view of the main chamber showing the two counter-propagating horizontal 3D MOT beams. The beam labelled as MOT+ contains cooling, repump and D2 optical pumping light. The other horizontal beam only carries cooling light. (c) Chameleon3 camera image of the 3D MOT cloud atomic fluorescence taken along the  $z$ -axis. Notice the light scattered from the in vacuo lens assembly.

In the experiment the 3D MOT is used as a source of single atoms for loading the holographic arrays. The atomic beam generated by the 2D push laser is directed from the 2D MOT glass cell towards the centre of the main chamber. This is where the 3D MOT is created using the in-vacuo coils that generate the quadrupole magnetic field required to form a MOT. Typically, the coils are driven with a current of 7 A during the MOT load sequence to reach a magnetic field gradient of 12 G/cm. If left on for extended periods of time, such as when aligning the 3D MOT mirrors, for example, the in-vacuo coils can cause heating in the chamber and lead to an increase in the ion pump

pressure reading. Such long periods of continuously running high current inside the chamber coils are to be avoided when possible.

The orientation of the six laser beams required to form a MOT is shown in Fig. 3.8. All the cooling light used to form the 3D MOT is controlled by a single AOM as shown in Fig. 3.5. A mechanical shutter can be used to block the vertical MOT beams before they are fibre-coupled to the chamber table. This is necessary during the polarisation-sensitive non-destructive readout (NDRO) procedure (see Section 5.1) because the circularly polarised vertical MOT beams do not have a well-defined polarisation along the x-axis which is our quantisation axis. Due to the geometric constraints set by the viewports and the in-vacuum lens assembly, we found that we need to install a 1/2" aperture on the output fibre collimator to reduce the diameter of vertical MOT beams to  $\sim 4$  mm. In addition, 3D-printed caps were fitted on the viewports through which the vertical beams enter the chamber to minimise the background light scattering inside the chamber. These additions to the set up led to significantly lower background camera counts in our single atom images. The waists shown in Fig. 3.8 are the unapertured Gaussian waists of the beams. The vertical MOT beams are retroreflected using mirrors attached to the viewports at the bottom of the chamber using a custom-machined cage mount. The cage mounts also have a space for installing a quarter waveplate. After observing interference fringes in our 3D MOT, we installed Piezo actuators<sup>18</sup> on the back of our retro-reflecting mirrors which improved the quality of our MOT, especially at the short 200 ms load times used when loading an array of single atoms. On the horizontal MOT axis, we operate with two counter-propagating beams instead of a retroreflected configuration. This was an important design consideration necessary for implementing NDRO because it allows us to toggle between a  $\sigma^-$  and  $\sigma^+$  polarised beam on the MOT- side for loading a MOT and NDRO respectively. The NDRO process is explained in more detail in Chapter 5. To

---

<sup>18</sup> PK25LA2P2 from Thorlabs

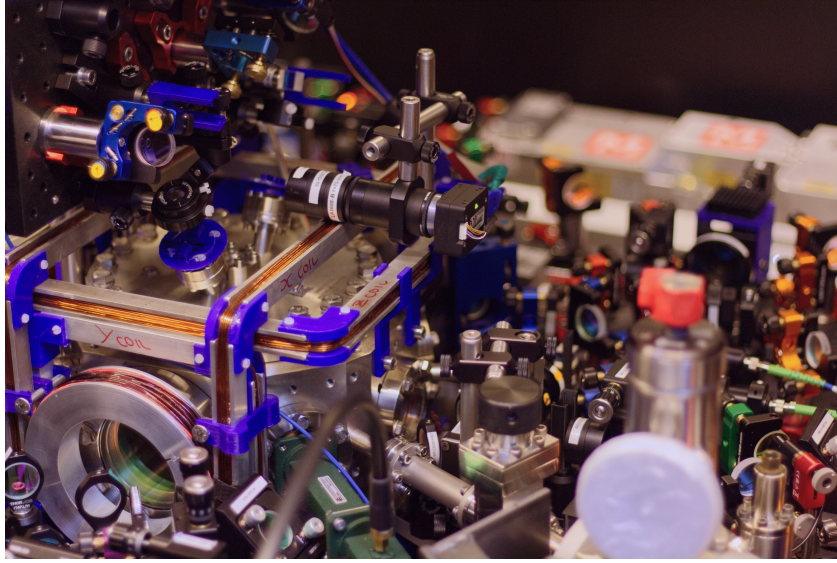


Figure 3.9: Photo of the experiment main chamber showing external shim coils and Chameleon3 camera used to image the MOT.

reduce the light scattered inside the chamber by the horizontal MOT beams, 8 mm diameter metal rings were installed in the output fibre collimators to aperture the beams. Even with these measures in place, we could still observe significant light scattering from the lens assembly as shown in the image in Fig 3.8(c), which was taken with a Chameleon3 USB camera we use to monitor the MOT fluorescence.

In order to have precise control of the magnetic field inside the chamber, external 3D MOT shim coils were installed using aluminium bars and 3D-printed corner sections to form the rectangular coil formers shown in Fig. 3.9. The coils were wound with 1 mm diameter copper wire and have different geometries for each axis. We use the shim coil along the  $x$ -axis to define our quantisation axis, so it has the largest area and can produce a magnetic field of 3.81 G/A at the atoms. Home-built coil drivers are connected to our experimental control system and allow for automated scanning of the magnetic field along each axis. This can be used to move the position of the zero-gradient point of the quadrupole magnetic field and therefore control the position of the 3D MOT in space.

As we operate with two independent horizontal MOT beams, rather than a retroreflected configuration, we observed that a power imbalance between the two cooling beams can also significantly shift the MOT position along the x-axis. Typically, we operate with 7 mW of cooling light in the horizontal beams and 4 mW in the vertical beams to give a saturation parameter of 8.3. The cooling beams have a detuning of  $-4\Gamma = -2\pi \times 20.9$  MHz from resonance on the  $F = 4 \rightarrow F' = 5$  transition on the caesium D2 line. The vertical beams also contain 0.6 mW of resonant repump light, while the MOT+ horizontal beam has 0.35 mW of repump. The relatively low efficiencies of repump power at the atoms compared to the repump laser output power is due to combining the repump beams and cooling beams into the same fibre using non-polarising beam splitters. Improving this will likely result in faster MOT loading times, but even with this limitation we can use our MOT to load an array with 225 sites in 0.25 s with  $>50\%$  single atom load efficiency. A typical 3D MOT load curve is shown in Fig. 3.10. Other state of the art experiments report MOT load times of the order of 100 ms, but the majority of them use UV-light-enhanced loading as outlined in [182] to achieve this. With our experimental set up, installing this would be impractical due to lack of easy optical access for the UV light source. In future experiments, it would be beneficial to make the 2D and 3D MOT beam sizes larger which is expected to improve the loading speed and maximum atom number in our set up [183].

### 3.2.4 Polarisation Gradient Cooling

Tweezer array experiments do not typically load atoms directly from a MOT. Since we are aiming to load single atoms into our tweezers, and we want to build large scalable arrays of 100s to 1000s of atoms with finite laser power, it is desirable to load colder atoms into a shallower potential so we can make more trap sites for a fixed laser power. In the SQuAre experiment we use the

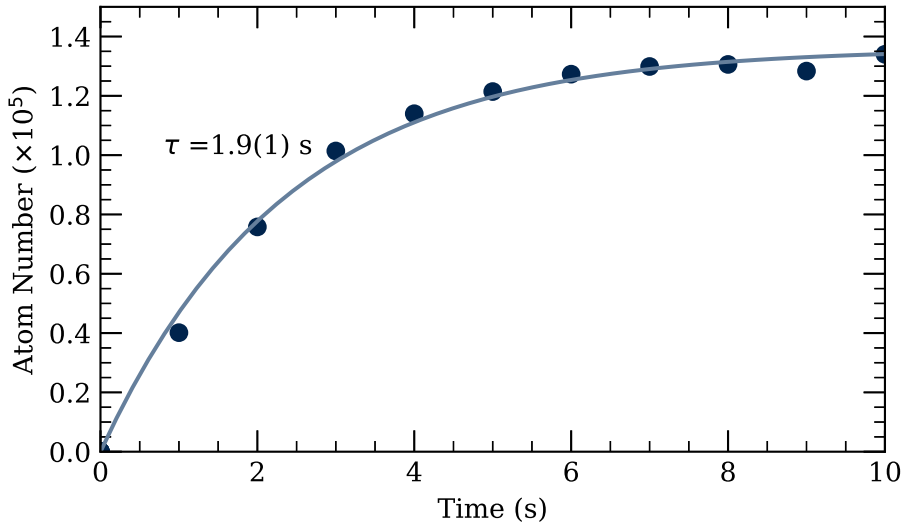


Figure 3.10: Typical 3D MOT load curve taken by converting Chameleon3 camera pixel intensity counts to atom number.

$\sigma+\sigma-$  polarisation gradient cooling (PGC) method<sup>19</sup> to achieve sub-Doppler temperatures before attempting to load atoms into the tweezer arrays. As the name implies, the effect is due to the polarisation gradients which are present in an electric field generated by counter-propagating laser beams. If the atom traverses these gradients at a rate faster than the decay rate of the excited state, then there is a coupling between its internal energy and its kinetic energy that can be exploited to achieve sub-Doppler temperatures. Note that in a three-dimensional trapping configuration this polarisation gradient is always present regardless of the chosen beam polarisations. However, the name PGC is somewhat misleading because the theoretical framework provided in the seminal works on the subject of sub-Doppler cooling considers a combination of AC Stark shifts, optical pumping effects and polarisation gradients to explain the observed experimental results [184, 185]<sup>20</sup>. In any case, regardless of the exact physical effects which underpin the cooling process, the practical implementation of sub-Doppler cooling always entails the following. After loading a MOT, the quadrupole coils are switched off, the

<sup>19</sup> This process is also referred to as Sisyphus cooling in the literature.

<sup>20</sup> A good summary of the ideas outlined in these seminal papers is given in [186].

cooling light detuning is increased and its intensity reduced. Careful zeroing of the magnetic field is necessary to achieve balanced light scattering from the atoms from all directions, otherwise the atomic cloud shoots off in a direction along the axis of the field imbalance as shown in Fig. 3.11(a).

To achieve optimal performance we optimise the cooling light intensity and detuning and then take a release recapture measurement to estimate the atomic temperature following the method outlined in [187]. We chose to use this method instead of the more-commonly used time of flight measurements, because the only optical access point available for our MOT camera was above the chamber. This would have skewed the results of the time of flight measurement because the expanding atom cloud would have been falling away from the camera focal plane under gravity. The high-performance, sCMOS single atom imaging camera described in Section 3.4 is viewing the 3D MOT from the side, so it could have been used in principle, but its narrow field of view designed for imaging microscopic single atom arrays made it impractical to observe the expansion of the relatively large MOT cloud over any meaningful time scales. The method we used entails forming a MOT, switching off the quadrupole magnetic field, applying PGC for a finite amount of time, and then switching off the lasers before recapturing the atoms in a MOT again. By monitoring the fraction of atoms recaptured after a given time in the dark, we can estimate the atom cloud temperature using

$$f_r = -\frac{2e^{-\frac{v_c^2}{v_T^2}} v_c}{\sqrt{\pi} v_T} + \operatorname{erf} \left[ \frac{v_c}{v_T} \right], \quad (3.3)$$

where  $v_c = R_c/\Delta t_{\text{dark}}$  and  $R_c$  is the estimated radius of the MOT cloud which we approximated as the size of our smallest MOT beam (2 mm radius). Using this method we recorded a temperature of the MOT as 251(1)  $\mu\text{K}$  as shown in 3.11(b). The subsequent PGC optimisation process revealed that

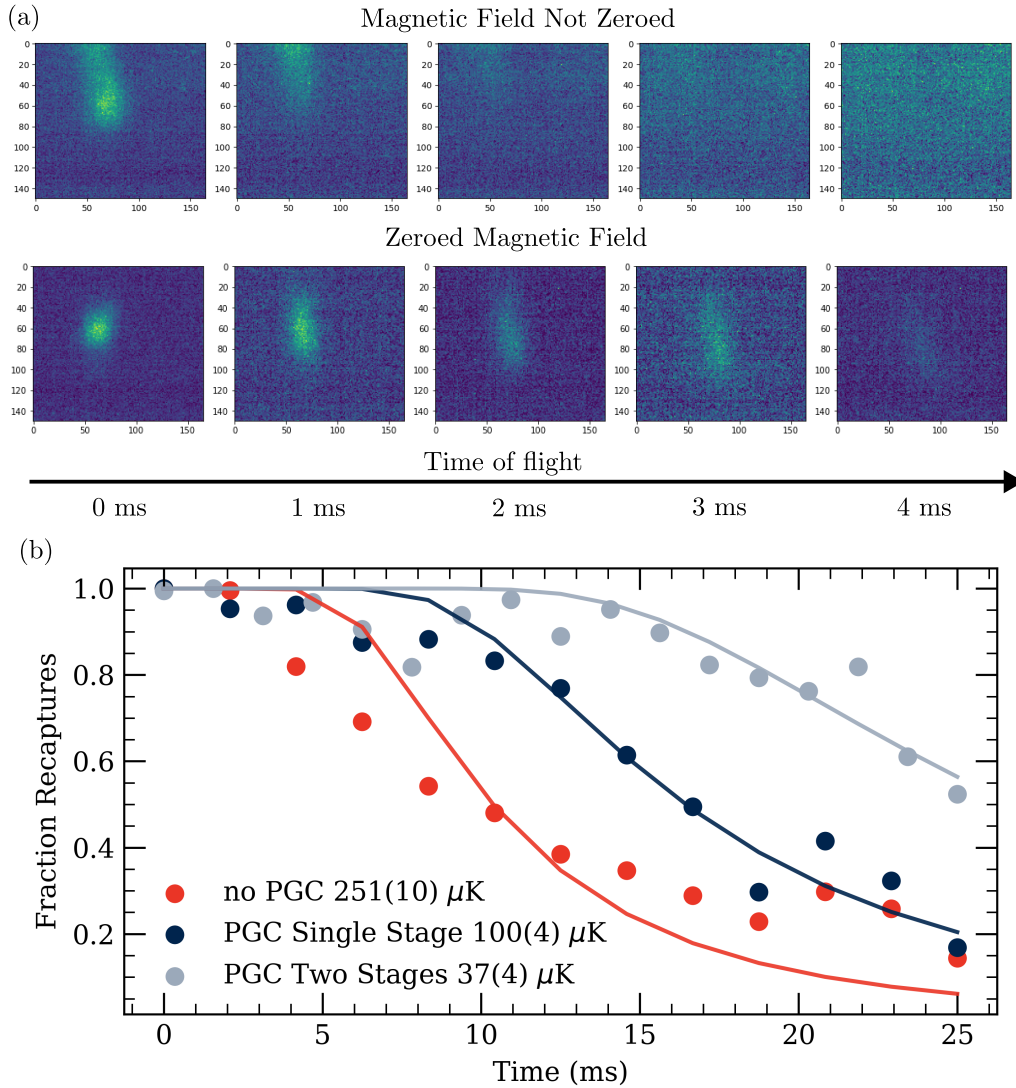


Figure 3.11: (a) Zeroing of magnetic field inside chamber. Top row of images show atom cloud dispersing in the vertical direction due to a field imbalance. Bottom row shows the results after zeroing the field using the 3D MOT shim coils. The atom cloud is still visible 4 ms after switching off the MOT gradient coils. (b) Atom cloud temperature measurements using the method from [187] showing improvements after sequentially introducing two-stages of PGC.

the optimal configuration requires two stages of PGC. Stage 1 is operated at a detuning of  $-5.8\Gamma$  for 3 ms and  $s = 1$ . For stage two we increased the detuning to  $-8\Gamma$ , reduced the powers to obtain  $s = 0.5$  and reduced the duration to 2 ms. The coldest temperature recorded with this method was  $37(4)\ \mu\text{K}$ , which was good enough to load our arrays, but it is more than ten times hotter than the coldest temperatures achieved with caesium atoms using PGC [188, 189]. Notably, the temperatures in [188, 189] were measured using the conventional time of flight technique. Therefore, we attribute the hotter temperature estimated from our data to the method we chose to employ, which was originally developed for a MOT generated by an optical nanofibre which has a spherical shape. Since our MOT is cigar shaped based on our beam geometry, this spherically-shaped MOT approximation is no longer valid resulting in a systematic uncertainty in our fit parameters. Because this temperature did not limit our ability to load the holographic trap arrays with single atoms, which is the focus of this work, we did not investigate the atom cloud temperature any further.

### 3.3 Holographic Atom Arrays

#### 3.3.1 Confining Atoms with Light

The aim of this section is to explain the methods by which we confine atoms with light in order to explore single-atom physics. The key physical principle that underpins optical dipole traps is the AC Stark shift discussed in Section 2.3.7. By using tightly focused light far-off-resonant from any atomic transitions, we use the AC Stark shift to engineer a trapping potential for atomic populations in specific energy levels. In the context of dipole trapping of neutral atoms, the AC Stark shift induced by a laser field,  $E_q$ , with angular frequency,  $\omega$ , is often expressed in terms of the real part of a complex-valued dynamic polarizability,  $\alpha(\omega)$ , [56] as

$$\Delta E_{\text{AC}} = -\frac{\text{Re}[\alpha(\omega)]E_q^2}{4}. \quad (3.4)$$

The polarizability term captures the information from the full multi-level expression for the AC Stark shift provided in eq. (2.46) and its sign determines the sign of the energy shift<sup>21</sup>. As a result of this, a dipole trap of a given wavelength may be trapping for some states and repulsive for others, because  $\alpha(\omega)$  can have a different sign for excited and ground states.

By remembering that the force is defined as the gradient of a potential and considering equation 3.4, we can see that the electric field of a far off-resonant laser will give rise to a spatially-varying force as

$$\mathbf{F} = -\nabla U_{\text{dipole}}(\mathbf{r}). \quad (3.5)$$

If we use the form of the AC Stark shift from eq. (3.4), and use the relation between the field intensity and the electric field amplitude<sup>22</sup>, we can express the trapping potential created by a Gaussian beam as

$$U_{\text{dipole}}(r, z) = -\frac{\alpha(\omega)}{2\epsilon_0 c} I(r, z). \quad (3.6)$$

We can then use the formula for the spatial intensity profile of a TEM<sub>00</sub> Gaussian beam in cylindrical coordinates to express the trapping potential in terms of a trapping potential amplitude,  $U_0$ , a Rayleigh range,  $z_R = \pi\omega_0^2/\lambda$ , and the  $1/e^2$  beam intensity radius,  $w(z) = w_0\sqrt{1 + (z/z_R)^2}$  as

$$U_{\text{dipole}}(r, z) = \frac{U_0}{1 + (z/z_R)^2} \exp\left(\frac{-2r^2}{w(z)^2}\right). \quad (3.7)$$

Writing down this form of the trapping potential is useful for seeing that

<sup>21</sup> The dynamic polarisability can be expanded in terms of scalar, vector (axial) and tensor polarizability components as discussed in reference [190]. Only circularly polarised light induces a non-zero vector polarizability which lifts the degeneracy of the  $m_F$  levels.

<sup>22</sup>  $I_{\text{peak}} = \frac{1}{2}\epsilon_0 c |E_{\text{rms}}|^2$ .

the radial trap profile is Gaussian, while the axial beam profile is Lorentzian. Since the Rayleigh range is larger than the beam waist, the confinement along the radial direction is stronger than along the axial direction<sup>23</sup>. The term  $U_0$  is a function of the polarizabilities of all the energy levels and sublevels to which the caesium ground state has a dipole coupling to, but a reasonable approximation can be obtained for the ground state by only considering the D1 and D2 lines in the case where the trapping light is linearly polarised with a detuning from resonance much larger than the hyperfine splitting of the ground states<sup>24</sup> as [153]

$$U_0 = \frac{\hbar\Gamma^2 I_0}{8I_{\text{sat}}} \left( \frac{1}{3\Delta_{\text{D1}}} + \frac{2}{3\Delta_{\text{D2}}} \right), \quad (3.8)$$

where  $I_0$  is the Gaussian beam intensity of the trap laser<sup>25</sup>,  $\Gamma$  is the excited state linewidth of the  $6\text{P}_{3/2}$  state, and  $I_{\text{sat}}$  is the saturation intensity of the cycling transition<sup>26</sup>,  $I_{\text{sat}} = 1.1 \text{ mW/cm}^2$ . If the thermal energy of the atoms,  $k_B T$ , is  $\ll U_0$ , then the atoms only explore the bottom of the trap potential. In this case we can approximate the motion of an atom confined inside the trap as a harmonic oscillator and write down equations 3.9 to describe the angular trap frequencies along the radial and axial directions as [56]

$$\omega_r = \sqrt{\frac{4U_0}{mw_0^2}}, \quad (3.9a)$$

$$\omega_z = \sqrt{\frac{2U_0}{mz_R^2}}. \quad (3.9b)$$

<sup>23</sup> This is why dipole traps are typically propagated along the horizontal axis such that the stronger radial confinement is acting against gravity.

<sup>24</sup> This is the case for our experiment where the detunings of the 1064 nm trap laser from the D1 and D2 lines are  $-2\pi \times 53.2 \text{ THz}$  and  $-2\pi \times 70.15 \text{ THz}$  respectively. Both of them are  $\gg 2\pi \times 9.192 \text{ GHz}$ , the hyperfine splitting of the  $6\text{S}_{1/2}$  ground state.

<sup>25</sup> The intensity of a Gaussian beam is expressed in terms of the measured beam power,  $P$ , and waist,  $w_0$ , as  $I_0 = \frac{2P}{\pi w_0^2}$ .

<sup>26</sup> In principle one should consider the difference in the trapping laser detuning for atoms in  $F = 3$  and  $F = 4$  hyperfine ground states, but the difference in  $U_0$  amounts to less than 1%.

## Scaling To Larger Numbers of Traps

The first optical dipole trap was demonstrated by Chu *et al.* [191] in 1986 for an ensemble of 500 sodium atoms and has since then been used to trap and manipulate molecules [192] and even bacteria [193]. Today, our challenge is to make very large numbers of these traps in two and even three dimensions and use them to trap single atoms. A number of different methods to achieve this scaling of the dipole trapping technique are used in current state-of-the-art experiments which have their own advantages and disadvantages. These include using passive optics such as micro lens arrays [62] or amplitude masks [57], multi-tone driving of an acousto-optic deflector (AOD) using an arbitrary waveform generator (AWG) [59, 194] and using holographic techniques, usually in the form of phase-modulating spatial light modulators (SLMs) [60, 61, 195]. The benefit of the AWG and SLM methods is that they are re-configurable unlike the static methods using passive optical elements, which are more efficient in terms of laser power and do not introduce additional noise. The AWG method is dynamically re-configurable on a microsecond timescale, while the SLM method requires hundreds of milliseconds to a few seconds in order to update the holographic trap pattern. Hybrid methods that combine an AOD with a partitioned SLM showing multiple holograms have been recently proposed in [111] as a way of getting the best of both worlds. The benefit of the SLM method is that it gives more flexibility for shaping the trapping potentials beyond the standard TEM<sub>00</sub> Gaussian spot traps used to trap ground state atoms in most large scale neutral atom quantum computing demonstrations to date. In our project we have opted to pursue the SLM approach using the set up described in the following section.

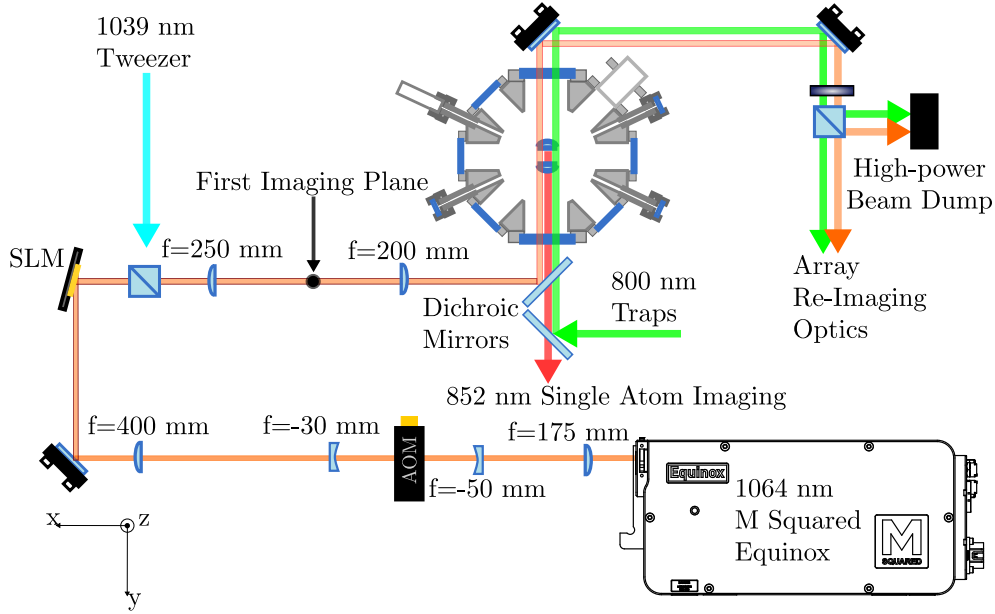


Figure 3.12: Schematic diagram of the 1064 nm trapping laser used to generate arrays of red-detuned holographic dipole traps using an SLM.

### 3.3.2 Red-Detuned Traps

#### 1064 nm Trapping Laser Set Up

We use a bespoke 1064 nm Equinox diode laser from M Squared Lasers with a maximum output power of 20 W in continuous wave (CW) operation to generate our red-detuned traps. This wavelength was chosen because it is far detuned from resonance to minimise off-resonant scattering and there are high-power 1064 nm lasers readily available to allow for scaling to large atom numbers. A schematic representation of the laser set up is shown in Fig. 3.12.

The 1064 nm light is switched on and off at the atoms using a single-passed AOM<sup>27</sup>. We chop the 1064 nm laser out-of-phase of with the 852 nm cooling and imaging light to reduce atom heating due to populations in anti-trapped excited states and to suppress the tensor AC Stark shifts on the  $6P_{3/2}$  state due to the 1064 nm light, which is linearly-polarised along the  $x$ -axis in the

<sup>27</sup> G&H AOMO 3110-197.

lab frame. A 1 MHz square waveform generated by a field-programmable gate array (FPGA) is applied to the AOM TTL control port to achieve this. The AOM is also used to implement amplitude ramps to adiabatically lower the trapping potential after imaging the atoms and thus reduce the temperature<sup>28</sup> of the atoms inside the traps during gate operations [197]. A typical ramping schedule is shown in Fig. 3.14(a). After passing through the AOM, the 1064 nm beam is expanded to a waist of 6.7 mm with a telescope and then apertured down to 12 mm diameter in order to fill the sensor of a liquid-crystal spatial light modulator (SLM)<sup>29</sup> with dimensions 12 mm x 15.8 mm following the method outlined in [198]. By filling the SLM sensor with light, we maximise our phase-modulation resolution because the beam intensity is distributed over the largest number of pixels. The SLM holograms are generated using the adaptive weighted Gerchberg-Saxton (WGS) algorithm from [199], and applied on top of a flatness-corrected blazed grating to separate the array from the zeroth order beam. After the SLM, a telescope is used to image the array as diffraction limited spots inside the chamber. The first imaging plane before the chamber was used for initial feedback in setting up the SLM hologram. For this initial feedback, a camera was placed in the telescope focal plane and the intensity of the individual trap spots was optimised for uniformity using an iterative procedure. The 1064 nm hologram is passed through a dichroic mirror to combine it with the 800 nm blue-detuned trapping light and the 852 nm fluorescence collection for our single atom imaging. After passing through the two in-vacuum lenses, the majority of the trapping light is safely dumped with a few mW of light directed towards an iDS uEye 2D re-imaging camera used to provide feedback during alignment of the 1064 nm arrays.

<sup>28</sup>The adiabatic lowering of the trap depth does not alter the occupation probabilities of the vibrational modes of the atom inside the trap modelled as a quantum harmonic oscillator [196]. This results in  $T/\sqrt{U_0}$  being a conserved quantity.

<sup>29</sup>Hamamatsu X13138-WR

### **Trap Loading Procedure**

With the holographic trap array overlapped with the centre of the 3D MOT, we apply chopped 1064 nm trapping light during the MOT load and PGC phases and then switch off the cooling light and give the MOT cloud 100 ms to disperse with the trapping light on continuously. The typical trap depth during the MOT load stage is 3 mK, but because the traps are chopped out of phase with the cooling light with a duty cycle of 50%, the effective trap depth is 1.5 mK. At this point, each trap could contain multiple atoms, so to ensure we are left with single atoms in each trap site we use red-detuned light-assisted collisions (LAC) to engineer atom-atom interactions which eject all atoms in sites with multiple occupancy [200]. Typical LAC durations in our experiment are  $\sim 50$  ms. At the end of the process we are left with a single atom in  $> 50\%$  of the traps. Typical loading rates in our experiment are 51(2)% for a 225-site array. Higher loading rates of up to 57(3) % have been achieved on smaller arrays. Alternative techniques for LAC using blue-detuned light have been demonstrated with single atom load probabilities of up to 90 % [64, 201], but we have not attempted to implement them in our current set up due to time constraints. A typical experimental sequence including the steps required to load the traps is shown in Fig. 3.13.

### **Trap Characterisation**

Once we have obtained an atomic fluorescence signal as described in Section 3.4, we are able to calibrate the trap parameters. We first record a trap lifetime measurement by loading single atoms into the traps, taking a first image of the occupied sites and then scanning the time spent in the traps with all other light sources switched off before re-imaging to check for atom loss. The atoms can be lost from the traps due to background gas collisions, heating from off-resonant scattering of the 1064 nm trapping light or interactions with leakage resonant light from the MOT or other laser sources. To

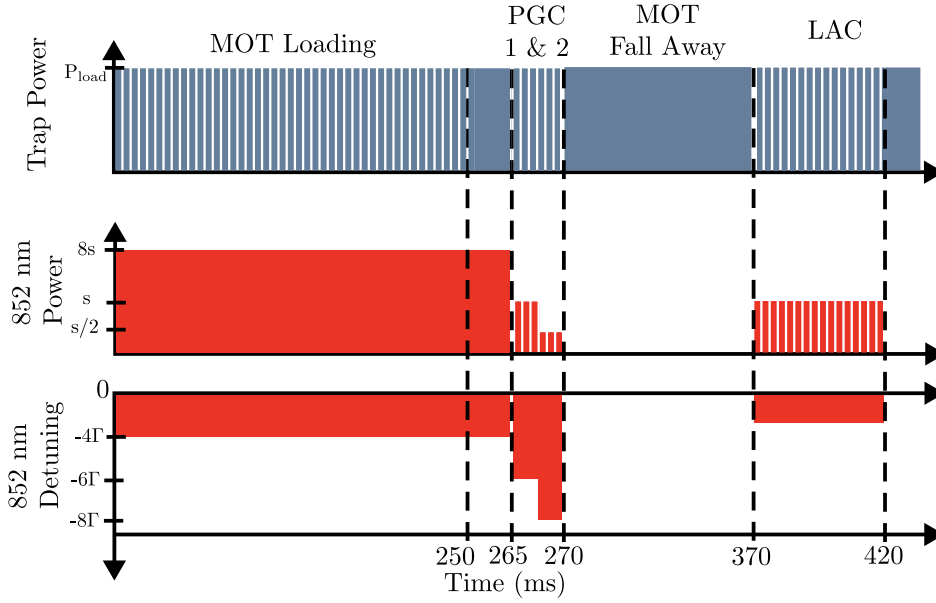


Figure 3.13: Timing diagram of the procedure required to load single caesium atoms into our 1064 nm red-detuned traps. The beam power is expressed in terms of the saturation parameter  $s$  defined in Section 2.3.3.

eliminate the latter loss source, we use home-built laser shutters described in Section 3.5 to physically block any leakage light from reaching the atoms. To account for the other two effects, we follow the method from [202] to fit our measurement results with the expression

$$P_{\text{total}}(t) = P_{\text{collision}}(t) \times P_{\text{heat}}(t), \quad (3.10)$$

where the two constituent terms are given by

$$P_{\text{collision}}(t) = e^{-t/\tau}, \quad (3.11a)$$

$$P_{\text{heat}}(t) = 1 - \exp\left(-\frac{U_0}{k_B(T_0 + \alpha t)}\right) \left(1 + \frac{U_0}{k_B(T_0 + \alpha t)} + \frac{U_0^2}{2k_B^2(T_0 + \alpha t)^2}\right), \quad (3.11b)$$

where  $T_0$  is the initial temperature of the atoms and  $\alpha$  is the heating rate. The temperature  $T_0$  was obtained from a trap release and recapture measurement performed at the same trap depth,  $P_{\text{expt}}$ , as the lifetime measurement. The experimental data from a release recapture measurement is shown in 3.14(b) and the red curve is a fit performed with a Monte Carlo simulation of the atomic trajectories with velocities sampled from a thermal Boltzmann distribution [203].

The results of a trap lifetime measurement are shown in Fig. 3.14(c). By fitting the data with equation (3.10), we obtain a trap lifetime of 12(1) s with a heating rate of 0.19(6)  $\mu\text{K}/\text{s}$  due to the 1064 nm light for a starting temperature,  $T_0 = 1.1(5)$   $\mu\text{K}$ , and  $U_0 = 30$   $\mu\text{K}$  for atoms held in the  $P_{\text{expt}}$  stage of our trap ramping schedule without toggling the trapping light on and off in order to avoid additional heating. The fitted heating rate is an order of magnitude higher than the predicted value of 0.02  $\mu\text{K}/\text{s}$  calculated using

$$\alpha = \frac{T_{\text{rec}}}{3} \Gamma_{\text{sc}} \quad (3.12)$$

from reference [204] with a caesium D2-line recoil temperature  $T_{\text{rec}} = 180$  nK and a 1064 nm photon scattering rate,  $\Gamma_{\text{sc}}$ , of 0.32 1/s for a 30  $\mu\text{K}$  deep trap obtained from reference [147]. A similar disagreement was observed with  $^{87}\text{Rb}$  atoms in reference [205] and attributed to residual 780 nm leakage light. Since we have mechanical shutters blocking the 852 nm resonant light in our set up, a more likely explanation would be 1064 nm laser intensity noise or pointing instability as reported in [206]. An alternative explanation would be insufficient data points to accurately perform the fit to extract such a low heating rate. If we fit the available data using only equation (3.11a) as shown in red in Fig. 3.14(c) thereby effectively neglecting the heating rate, we obtain a lifetime of 11.3(4) s with a smaller fit error suggesting that the trap heating effects are being over-estimated when fitting with the full

expression. To more accurately measure this low heating rate, we would have to extend the measurement time further to longer release times and check which fit provides better agreement, but such measurements are very costly in terms of experimental time and have been left as possible future work. The measured trap lifetimes provides a good estimate of the baseline survival probability of the atoms in our experiment. Typically the atoms spend 160 ms in the traps between the end of the first and the start of the second image, and using the 12 s lifetime we estimate a baseline survival probability of 0.9867(1), in good agreement with our experimental results.

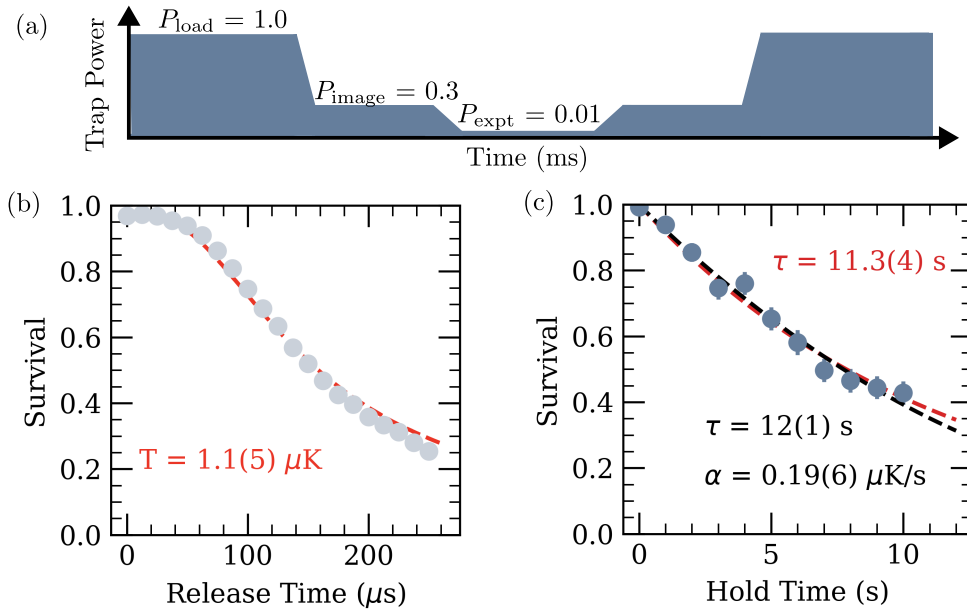


Figure 3.14: (a) Typical trap amplitude ramping schedule for the trap characterisation experiments. The trap temperature and trap lifetime measurements were both taken at the experiment trap amplitude value,  $P_{\text{expt}}$ , which is set to be 1% of the maximum trap amplitude used during loading. (b) Results from a release and recapture temperature measurement where the atoms have been released from the  $P_{\text{expt}}$  trap depth. The fit is obtained using a Monte Carlo simulation of the atomic trajectories. (c) Results from a trap lifetime measurement taken at  $P_{\text{expt}}$ . The fit shown in black was obtained with equations (3.11). The red curve is a simpler fit using only equation (3.11a) that shows better agreement with the data.

Finally, we measure the radial trapping frequencies as a function of the applied 1064 nm power for a rectangular array of 13 x 13 traps as shown in

Fig. 3.14 following the method from Section 2.3.3 in reference [205]. In this method, the trap light is switched off for two time periods,  $t_1$  and  $t_2$ , separated by a variable hold time in the trap,  $t_{\text{hold}}$ . The exact values of  $t_1$  and  $t_2$  depend on the temperature of the atoms in the traps and the trap depth, but they are typically of the order of a few  $\mu\text{s}$ . To make an informed guess for what durations to use, we run a Monte Carlo simulation seeded with the measured atom temperatures and an approximate trap depth. When the trap is modulated on resonance with the atomic motion, this leads to atom loss at twice the radial trap frequency because the atom can be ejected from the trap at either end of the harmonic trapping potential. We typically use a power of 44 mW/trap while loading atoms from the MOT and then ramp down as shown in Fig. 3.14(a). By taking a series of measurements over a range of powers, we can use equation (3.9a) to obtain a fit for the trap waist for each trap site. Using this method we arrive at a weighted average trap waist of  $1.48(5) \mu\text{m}$ , where the quoted error represents the standard error of the mean based on the distribution of fitted trap waists across the 169 site array.

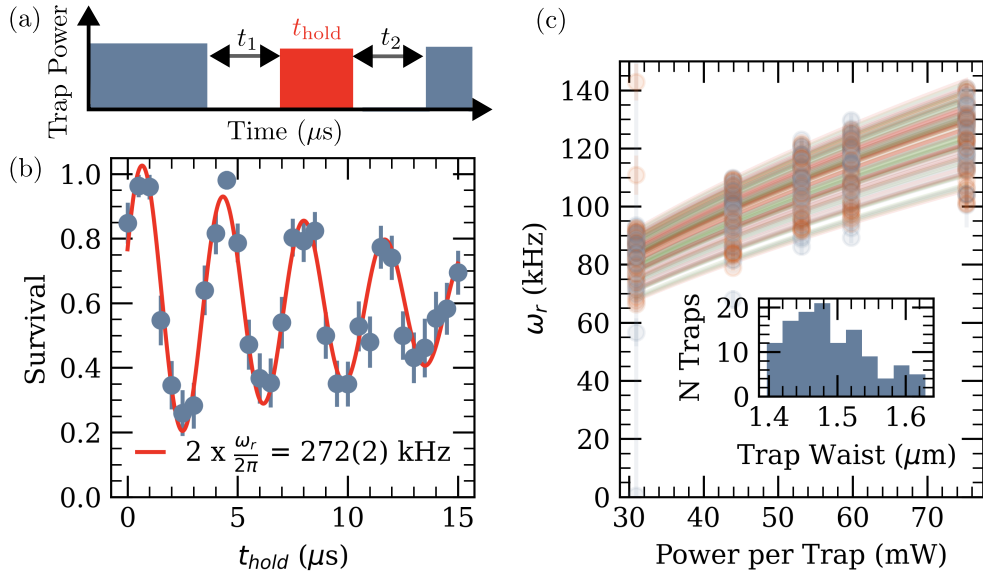


Figure 3.15: (a) Experimental sequence for trap frequency measurement adapted from [205]. The trap is switched off for two time periods,  $t_1$  and  $t_2$ , with a variable hold time in between them of  $t_{\text{hold}}$  to excite the radial motional mode of the trapped atom. When this is done on resonance with the atom's motion, the atom is lost from the trap. (b) Single trap data from a trap frequency measurement at a power of 74 mW/trap. The likelihood of the atom surviving the process without being lost from the trap oscillates at twice the radial trapping frequency,  $\omega_r$ . The solid line was fit using a damped sine wave. (c) Radial trap frequency measurements for a range of different powers used to estimate the trap waists for 169 traps inside the chamber. The fit of the trap waists was obtained using equation (3.9a).

This measurement technique is less suited for measuring the axial trapping frequency, because it is expected to be several times smaller than the radial trapping frequency as can be seen from the definitions in equations (3.9).

Using the relation

$$\omega_z = \frac{\lambda}{\sqrt{2\pi}w_0}\omega_r \quad (3.13)$$

we estimate that our axial trapping frequency amounts to 16.5 % of the radial trapping frequency for a given trap depth. This means that the hold and release times would need to be proportionally longer which would result in reduced signal level due to atoms escaping the trapping region during release.

An alternative technique, parametric excitation, can be used to measure the radial and axial frequencies by modulating a trap parameter such as power or position and scanning the modulation frequency until atom loss is induced on resonance with either trapping frequency [207, 208].

For specific arrays such as the 49-site array used for non-destructive read-out and the 225-site array used for randomised benchmarking, we also apply adaptive intensity feedback using atomic signal on the D1 resonance to modify the trap intensity weightings and achieve improved trap uniformity. The D1 line was chosen because it experiences a scalar AC Stark shift due to the 1064 nm light, unlike the D2 line which sees a tensor shift. By applying 1  $\mu$ W of laser power in our 895 nm D1 optical pumping beam, described in Section 3.5, for 3 ms we perform spectroscopy on the D1 line in the presence of a deep 1064 nm trap. We use the distribution of resonant frequencies to feedback to our hologram generation algorithm in order to maximise the mean AC Stark shift and minimise the variation in the resonant frequencies across the array. Figure 3.16 shows the improvement after 5 iterations of this process when applied to an array of 225 atoms spaced by 8  $\mu$ m which was used for randomised benchmarking in Section 4.5. The standard deviation of AC Stark shift distribution across the array was reduced from 2.83 MHz (11 %) to 0.864 MHz (3 %). This translates directly to improved 1064 nm trap depth homogeneity because of the linear relationship between the two. Our feedback method assumes that all the atoms have the same temperature and sample the trap intensity in the same way. This assumption may not be true for a single experimental realisation, but each data point was based on 100 experimental runs and the distribution of atomic velocities can be reasonably expected to converge to a common mean across traps for this number of samples. Ideally the trap frequency measurements from Fig. 3.15 would have been repeated on the corrected array to verify that this feedback procedure translated to improved uniformity of the trapping frequencies, but this was not done at the time due to time constraints.

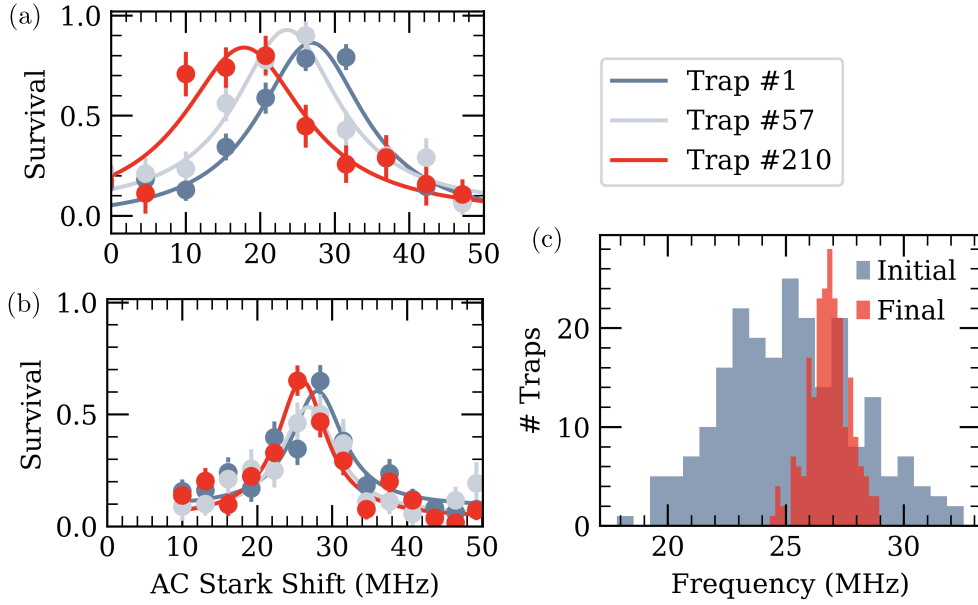


Figure 3.16: (a) Example D1 line resonances in the presence of 1064 nm light shown here for three out of 225 sites before intensity feedback. (b) D1 resonances for the same traps after 5 rounds of intensity feedback. (c) Histogram of initial and final distributions of AC Stark shifts induced by 1064 nm on 225 trap sites demonstrating improved uniformity due to the intensity feedback procedure.

### 3.3.3 Moving Tweezer Trap

The 1039 nm light for the moving tweezer trap is sourced from the same laser as the one used for our two-photon Rydberg excitation scheme described in Section 3.7. The tweezer beam path contains a single-passed AOM for switching and a crossed XY acousto-optic deflector (AOD)<sup>30</sup> which is used for steering the beam to individual trap sites on the array. After taking an initial image of the atoms loaded into the array, the computer control system generates atom sorting commands which are sent to the serial port of a Teensy microcontroller. The Teensy converts these move commands to voltage signals using a pre-calibrated lookup table. The Teensy outputs are sent to a dedicated Analog Devices AD5686 digital-to-analogue converter (DAC) through a low-pass RC filter to suppress noise peaks close to the typical trap

<sup>30</sup> DTSXY-400 2-axis by AA Opto-Electronics.

frequencies in the range 10-100 kHz similarly to the design described in [209]. The filtered signal is then amplified to match the range of the frequency to voltage converters of the XY AOM driver board. The Teensy is interfaced with our computer control system via USB so it can receive instructions on atom sorting steps with a high bandwidth such that the limits on the sorting speed are only imposed by the physics of the atom in the trap. Typical execution times are 3 ms per move. This is limited by the amplitude ramping rate when picking up and releasing atoms which was observed to cause atom loss if too fast. The 1039 nm moving tweezer trap is focused to a  $1.53(8) \mu\text{m}$  spot and operated with 50 mW of optical power at the atoms giving a trap depth of 4 K. Best performance is achieved with a high ratio of moving tweezer to static tweezer trap depth, so the 1064 nm traps are operated at reduced amplitude close to  $P_{image}$  in Fig. 3.14(a) to give a trap depth of 1 mK. Using a custom sorting algorithm that aims to avoid moving atoms across filled sites, we achieve a 10% defect-free rate with a single round of sorting and a 40% defect-free rate with three rounds of sorting when deterministically filling 49 sites from an underlying two-dimensional rectangular array of 121 stochastically-loading static traps. This is competitive with the state-of-the-art defect-free probabilities for 2D array sorting where they have been reported in the literature [66, 210]<sup>31</sup>. The limiting factor for the success probability as the array size increases is the finite lifetime of the atoms in the traps which leads to loss of sorted atoms as the duration of the sorting sequence increases. Further details on the moving tweezer traps and custom algorithm implemented in our experiment are available in [165].

<sup>31</sup> Not all publications include the defect-free array probability as a metric. Higher defect-free probabilities have been reported for one-dimensional arrays in the original set up using multi-tone driving of an AOD [59], but newer publications from this group have omitted this parameter.

### 3.4 Fluorescence Imaging of Single Atoms

To extract the information from our experiment we take fluorescence images of the single atoms inside our dipole traps. We use a Prime BSI sCMOS camera from Teledyne Photometrics with a quantum efficiency of 47% at 852 nm to detect our single atom signal. The camera is mounted in a custom cage attached to a translation stage for precise focus adjustment. The optical system used to collect the single atom fluorescence is shown in Fig. 3.17. It is designed to give diffraction limited performance up to an object offset of 40  $\mu\text{m}$  with a magnification of 7.47, which translates to a field of view (FOV) of 80  $\mu\text{m}$  at the focal plane inside the chamber, enough to fit a square lattice of 400 atoms with a 4  $\mu\text{m}$  spacing. A stack of two optical filters are installed in the camera telescope to achieve a narrow bandpass filter centred at 852 nm for minimising background noise levels.

The in-vacuum lens light collection efficiency for an isotropic photon emission pattern is 5.4% based on a numerical aperture (NA) of 0.45. We estimate a transmission of 70 % through all the imaging optics with the most significant losses coming from the two filters and the two dichroic mirrors<sup>32</sup>. Based on these parameters and the camera quantum efficiency, we arrive at an overall photon collection efficiency of 1.76% for our system. During non-destructive readout (NDRO) all beams illuminating the atoms have a well-defined circular polarisation. In this case, the overall light collection efficiency of the system is calculated using the method from [211] which accounts for the non-isotropic emission pattern of an atom emitting a circularly polarised photon. Based on this method and the 90° collection angle in our system with respect to the quantisation axis, we arrive at an in-vacuum lens light collection efficiency of 7.6% during NDRO, resulting in an overall imaging system collection efficiency of 2.5 %. For these estimates we have assumed that we have defined a sufficiently large region of interest for each atom in

<sup>32</sup> The calculation does not account for the astigmatism of any angled dichroics or filters.

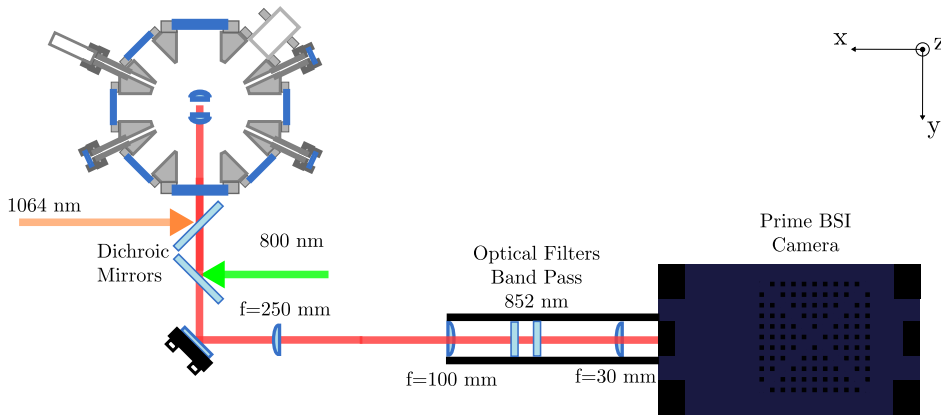


Figure 3.17: Schematic representation of the experiment single atom imaging system.

terms of number of pixels, such that all fluorescence from it is captured in our camera counts.

The fluorescence signal is obtained by shining cooling and repump light from the 3D MOT beams onto the atoms with powers and detuning similar to the ones used during the PGC stages, but optimised for balanced performance between minimal atom loss and highest separation between signal and background. Notably, this imaging process cannot determine if the atoms are in the ground state hyperfine  $F = 4$  or  $F = 3$  levels as atoms in both manifolds fluoresce. The imaging light is applied for 40 ms, but we expose the camera for 50 ms to allow time for the rolling shutter to initialise the full range of pixel rows used for imaging the atoms. Once trained on the atom positions, the camera only communicates the pixel intensity sums in the identified regions of interest (ROIs) for faster data transfer to the experimental control system instead of sending the full images. The training process entails saving fluorescence images of the atoms and identifying the high-intensity pixels in a 100-shot averaged image. These high intensity regions correspond to trap sites and their pixel co-ordinates are approximated using a simple thresholding procedure in the first instance. Then we iterate over the identified trap sites and select the  $n$  brightest pixels in a region of radius  $dx$  around the brightest spot as shown in Fig. 3.18(b). We usually work with  $n = 10$  and

$dx = 7$ , but the value of  $dx$  needs to be reduced for array spacing smaller than  $6 \mu\text{m}$  to avoid pixel cross-talk from adjacent traps<sup>33</sup>. We then produce histograms such as the ones shown in 3.18(c) by considering the distribution of pixel intensity sums for the identified ROI across 100 camera images. The distribution on the left represents background fluorescence counts, i.e. the absence of an atom in the trap site during a given camera image, and the distribution on the right represents the atom fluorescence signal, i.e. there was an atom in the trap during that image. A binomial distribution is trained on the histogram to obtain a threshold which minimises the infidelity defined as the average of the false positive and false negative counts. Typical discriminator fidelities in our experiment are  $> 0.999$ . The process is repeated for all trap sites to produce a full set of thresholds as shown in 3.18(d). Using these thresholds, we can convert the atomic fluorescence signal into binary information about the presence or absence of atoms in different images at different times in the experimental sequence. In addition, the information about the atoms' locations in space is used to train the moving tweezer so it can convert image co-ordinates to voltages output from the Teesny DACs and address single atoms in specific trap sites.

In a typical experiment we take multiple images, and after every image except the final one we apply an additional stage of polarisation gradient cooling (PGC). We refer to this stage as PGC3 and its parameters are optimised on a release and recapture measurement of the type shown in Fig. 3.14(b). The typical PGC3 duration is  $\sim 5$  ms with a detuning of  $-8\Gamma$  and saturation parameter,  $s = 1$ . The most basic experimental sequence uses two images. The first one is used to determine which sites were loaded with a single atom and the second image is applied at the end of the experiment to check which atoms had survived the particular experimental sequence. Additional images are inserted when atom sorting is used in the experiment. The atom sorting sequence requires information about which sites contain an atom at

<sup>33</sup> The optical system target magnification gives a  $1 \times 1 \mu\text{m}$  pixel size.

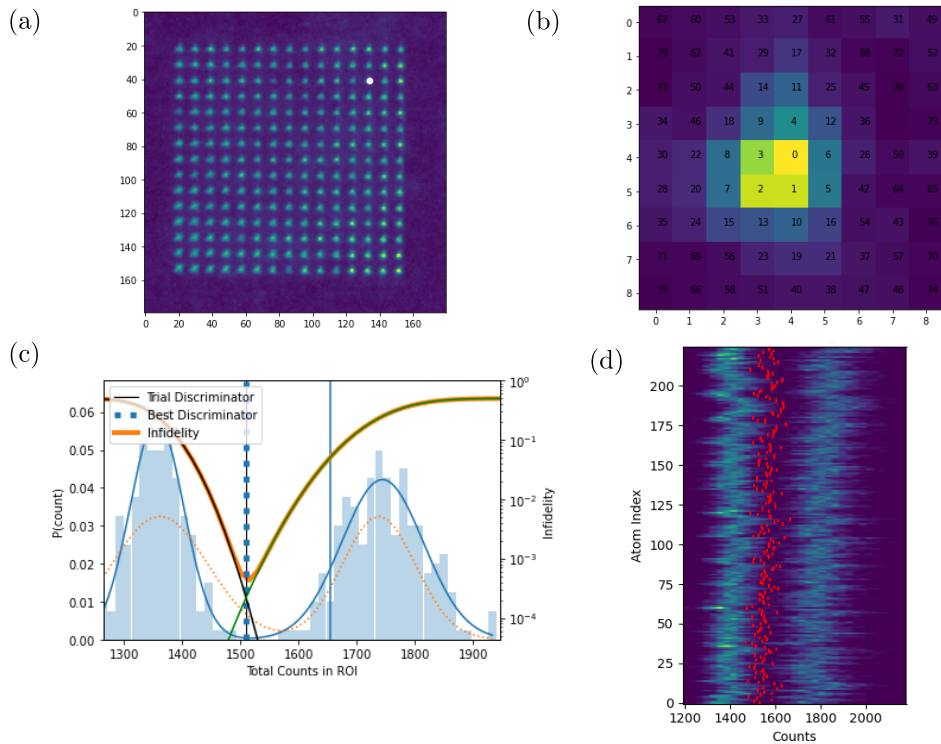


Figure 3.18: Brief summary of the process used to count single atoms in fluorescence images obtained using our sCMOS camera. (a) Averaged atom fluorescence signal across 100 camera images. The highlighted atom is the one used to obtain the data in (b) and (c). (b) After identifying a rough region of interest for a single atom on our averaged image, the ten brightest single pixels in the region are selected to produce a histogram. (c) Histogram of pixel intensity counts from the region shown in (b) based on 100 images. The data is fitted with a binomial distribution which minimises the infidelity resulting from either false positive or false negative atom detection events. (d) Final result of the discriminator training procedure for a 225 site array in the form of a 2D histogram. The red lines are the thresholds and the colour brightness represents the number of data points with a given ROI pixel count showing two distinct groupings at 1400 and 1800 counts representing the background and the atomic signal respectively.

the start of the experiment. If multiple stages of sorting are used, then each stage requires an image in order to obtain knowledge of the current trap occupancy. Finally, we may wish to insert a non-destructive image which uses the same analysis framework, but a different laser light configuration and underlying physical processes outlined in Chapter 5.

## 3.5 State Preparation & Detection

One of the DiVincenzo criteria for quantum computation is the ability to deterministically initialise the atoms in a well-defined qubit state at the beginning of the experiment [28]. In our experiment we have the ability to initialise the atoms into two different internal states of the Zeeman-resolved hyperfine ground state manifold. Both methods use incoherent light scattering to accumulate atomic populations in a single  $m_F$  sublevel of the ground state  $6S_{1/2}|F = 4\rangle$ . This is why we refer to our state preparation as optical pumping (OP). We shall look at each method in turn, starting with optical pumping into the clock state using the D1 line.

### 3.5.1 Optical Pumping

#### D1 Optical Pumping

Our implementation of D1 optical pumping uses 895 nm light produced by a Toptica DL-PRO diode laser. Before it reaches the atoms, the light is double-passed through a 200 MHz AOM for frequency control and fast switching. It is then coupled into a single-mode polarisation-maintaining fibre transporting it to the main chamber table. Similarly to the repump laser set up described in Section 3.2.1, the D1 OP laser lock uses a polarisation spectroscopy frequency locking technique. However, unlike the repump beam, the spectroscopy arm of the 895 nm laser is double-passed through a 200 MHz

AOM such that the laser can be directly locked to the  $F = 4 \rightarrow F' = 4$  resonance on the D1 line that we use for optical pumping. Passing the spectroscopy light through an AOM allows for greater frequency tuneability of the laser lock. This was useful when performing the 1064 nm intensity feedback on the D1 line, for example, where at times the AC-Stark-shifted resonance could exceed the dynamic range of the D1 OP AOM. By shifting the spectroscopy AOM detuning, we could shift the available dynamic range in frequency space.

As shown in Fig. 3.19(a), the beam is incident on the atoms from above with a linear polarisation vector directed along the quantisation axis (x-axis in the lab frame). We apply a 6.0 G bias magnetic field to lift the degeneracy of the Zeeman sublevels. Note that this value is slightly different to the 5.7 G used for optical pumping on the D2 line. We chose to operate like this because the fidelity of the D1 OP responded to the magnitude of the quantisation axis field and we found optimal performance at 6.0 G. This is somewhat counter-intuitive because we already use the shim coils along the y- and z-axes to align the polarisation vector of the optical pumping light with the bias magnetic field vector, but this alone was not enough to achieve optimal fidelity. We attribute this to the 3D MOT shim coil mounts which are not perfectly rigid and were mounted with some finite error in alignment, such that the x-axis shim coil had some finite components along the y- and z-axes which we were not able to compensate the smaller y- and z-shim coils alone. To ensure high polarisation purity we use a Glan-Taylor polariser with a higher extinction ratio than standard polarisation optics<sup>34</sup>. This is an important consideration for achieving optimal optical pumping fidelity as will be explained in the next paragraph. The beam waist at the atoms is  $w_0 = 800 \mu\text{m}$  and we typically operate it with 50  $\mu\text{W}$  of optical power which gives a saturation parameter  $s = 0.8$ . Our typical D1 optical pumping pulse

<sup>34</sup>The extinction of Glan-Taylor polariser is 100,000:1. Standard broadband polarising beam splitters have extinction ratios of 1000:1.

duration is 1 ms.

The physical principle of D1 optical pumping is rooted in the hyperfine structure selection rule that prohibits transitions with both  $\Delta F = 0$  and  $\Delta m_F = 0$ . Figure 3.19(b) illustrates how this can be utilised to accumulate atomic populations in the  $6S_{1/2}|F = 4, m_F = 0\rangle$  state. Upon applying a bias magnetic field, we start with our atoms randomly distributed amongst the different  $m_F$  sublevels in the ground state hyperfine manifold. When we apply a pulse of  $\pi$ -polarised D1 OP light, we drive transitions from all  $m_F$  sublevels except the  $m_F=0$  state because of the aforementioned selection rule. Over time, this leads to accumulation of populations in the upper clock state ( $|F = 4, m_F = 0\rangle$ ), provided that we have a high-enough polarisation purity to minimise population leakage to the  $m'_F = \pm 1$  states. We also need to apply a repump beam to re-introduce populations that have decayed into the  $F = 3$  manifold back into the optical pumping cycle. In our case, we found that using the vertical repump beams, which are randomly-polarised with respect to the quantisation axis<sup>35</sup>, gives best results. The same scheme could work on the D2 line with 852 nm light, but the main benefit of using the D1 line is that the nearest (and only) other hyperfine state is separated in energy by 1.167 GHz. This gives a four-times larger detuning from the nearest off-resonant state than using an equivalent clock state optical pumping configuration on the D2 line. In this case we would use the  $F = 4$  to  $F'=5$  transitions for optical pumping, whose energy difference from the  $F' = 4$  manifold is only 250 MHz. The larger the detuning, the greater the suppression of off-resonant scattering which, along with polarisation impurities, is one of the major contributors to reduced optical pumping fidelity.

To characterise our D1 OP performance we record an optical pumping time constant,  $\tau_{\text{OP}}$ , and a depumping time constant,  $\tau_{\text{Depump}}$ , as shown in Fig. 3.19(c) and (d). For the former, we image the atoms, apply the bias magnetic

<sup>35</sup> The beams have circular polarisation but because their  $k$ -vector is not colinear with the quantisation axis, the effective polarisation of the beams as seen by the atoms is not well defined.

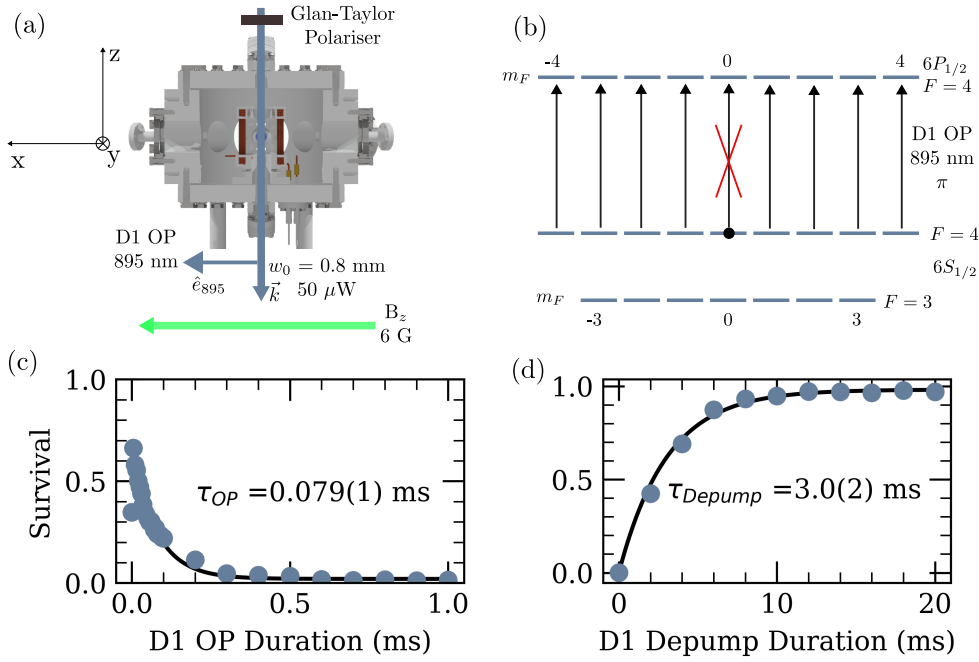


Figure 3.19: D1 optical pumping into clock state. (a) Schematic diagram of the D1 OP laser beam entering the main experimental chamber. The quantisation magnetic field is along the x-axis in the lab coordinate frame, parallel to the D1 OP beam polarisation vector,  $\hat{e}_{895}$ . (b) Schematic illustration of the D1 optical pumping process with  $\pi$ -polarised light. The repump beam coupling the  $F = 3$  manifold to the  $F = 4$  manifold on the D2 line is not shown. (c) Measurement of D1 optical pumping time constant. The fit is an exponential decay. (d) Measurement of the depumping rate out of the clock state as a function of the duration of the D1 OP pulse. The atoms start this measurement optimally prepared in the clock state. The fit in (d) is a rising exponential. Based on the fits in (c) and (d) we infer a maximum optical pumping fidelity of 0.974(3).

field and then scan the duration of a D1 OP pulse. Following that, we apply a destructive blow away beam to heat out atoms in  $F=4$  out of their traps as described in Section 3.5.2 before imaging the atoms a second time. This measurement does not discriminate between different  $m_F$  levels in the  $F = 4$  manifold, but we can infer this information from the maximum contrast of our microwave hyperfine ground state Rabi oscillations as described in Section 3.6. By fitting the data with a decaying exponential, we obtain an optical pumping time constant of 0.079(1) ms. The second measurement is done after the D1 optical pumping stage. We switch off the repump light and

only apply 895 nm optical pumping light with a variable duration. The rate of increase in the  $F = 3$  population is an indicator of our optical pumping infidelity because the atoms initially prepared in the  $|F = 4, m_F = 0\rangle$  state by the optical pumping light begin to leak out into the  $F = 3$  manifold due to polarisation impurity and off-resonant scattering. We record a depumping time constant of 3.0(2) ms. Using these two values, we can estimate the maximum achievable optical pumping fidelity in our system using equation [212]

$$F_{\text{OP}} = 1 - \frac{1}{\tau_{\text{Depump}}/\tau_{\text{OP}}}. \quad (3.14)$$

The result is a maximum fidelity of 0.974(3). The optical pumping fidelity could not be improved any further with simple scanning of experimental parameters such as D1 OP and repump detunings, shim coil and bias field values during optical pumping. A Raman-enhanced optical pumping method similar to what was implemented in [75, 81] could be used to improve this further. The most recent paper from the same group reported that this Raman-enhanced optical pumping method was causing significant heating due to the many cycles required to achieve full transfer and implemented a revised scheme outlined in [78]. The alternative scheme uses decohered stretched state optical pumping into the  $|F = 2, m_F = 2\rangle$  state of  $^{87}\text{Rb}$  followed by composite Raman pulses to coherently transfer atomic populations to the clock states. This improved scheme could be implemented in our experiment, but the larger number of hyperfine sublevels in  $^{133}\text{Cs}$  compared to  $^{87}\text{Rb}$  would make the transfer sequence longer and thus more challenging to realise experimentally. Optically pumping into the  $F = 3, m_F = 0$  state instead might improve this by reducing the number of hyperfine states in the manifold by two thus reducing the number of scattering events required.

## D2 Optical Pumping

As described in Section 3.2.1, the D2 optical pumping light is derived from the same 852 nm laser as the MOT light, but locked near resonance to the  $6S_{1/2}|F = 4\rangle \rightarrow 6P_{3/2}|F' = 4\rangle$  transition using an 80 MHz AOM. Figure 3.20(a) shows a schematic representation of the beam's orientation with respect to the experimental chamber and the quantisation axis. In this case we are implementing stretched state optical pumping which uses  $\sigma+$  polarised light in the presence of repump to incoherently transfer the atoms across to the stretched state as shown in Fig. 3.20(b). High polarisation purity was achieved by using a combination of a quarter- and a half-waveplate before the beams enter the chamber. Because the OP light passes through a dichroic mirror, the polarisation was optimised to high-purity  $\sigma+$  using a free-space polarimeter<sup>36</sup>. We used the signal on the opposite side of the chamber for optimising the polarisation purity. This was necessary because passing through the dichroic mirror affects the light's polarisation [213]. The beam is operated with 80  $\mu$ W of power and a  $1/e^2$  waist,  $w_0 = 5$  mm, apertured down to 4 mm to suppress background light scattering. This amounts to a saturation parameter,  $s = 0.1$ . A 5.7 G bias magnetic field was applied along the x-axis in the lab frame to lift the degeneracy of the  $m_F$  hyperfine sublevels. Using this configuration, we obtained a D2 OP fidelity,  $F = 0.993(7)$ , using the method described in the previous section. The measurements used to obtain the time constants required to calculate the optical pumping fidelity are shown in Fig. 3.20(c) and (d). We attribute the higher D2 OP fidelity to the higher Clebsch-Gordan coefficients near the stretched as compared to the  $m_F$  states near the clock state. This is evidenced by the fact that the recorded values for  $\tau_{\text{OP}}$  are an order of magnitude shorter for stretched state optical pumping compared to clock state pumping.

the fact that stretched state optical pumping is less sensitive to polarisation

---

<sup>36</sup> Schäfter & Kirchhoff SK10PA.

impurities because for atomic populations in  $|F' = 5, m'_{F'} = 5\rangle$  there are simply no leakage states to couple to, even in the presence of  $\sigma$ - and  $\pi$  polarisation impurities in the optical pumping beam.

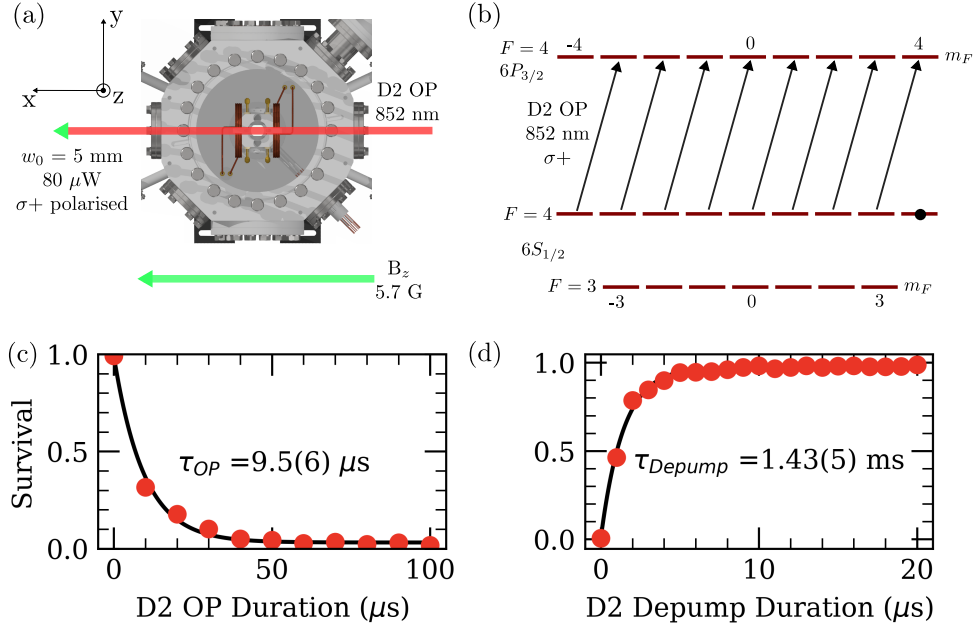


Figure 3.20: D2 optical pumping into stretched state. (a) Schematic diagram of the D2 OP laser beam entering the main experimental chamber. The quantisation magnetic field is along the x-axis in the lab coordinate frame. (b) Schematic illustration of the D2 optical pumping process with  $\sigma+$ -polarised light. The repump beam coupling the  $F = 3$  manifold to the  $F = 4$  manifold on the D2 line is not shown. (c) Measurement of D2 optical pumping time constant. Fit is an exponential decay. (d) Measurement of the depumping rate out of the stretched state as a function of the duration of the D2 OP pulse. The atoms start this measurement optimally prepared in the stretched state. The fit in (d) is a rising exponential. Based on the fits in (c) and (d) we infer a maximum optical pumping fidelity of  $0.993(7)$ .

### 3.5.2 State Detection

#### Ground State Blow Away

Conventional fluorescence imaging techniques for neutral atoms cannot discriminate the qubit state, so any atom present in the trap array would appear in a camera image. The conventional detection technique is to apply a

strong, near-resonant beam referred to as the push-out or blow-away (BA) beam which heats out atoms in one of the two hyperfine ground state manifolds [147] before taking a final camera image to check for trap occupancy. In heavy alkali atoms, the hyperfine splitting is of the order of GHz. This means that if we tune our push-out beam to be resonant with the transition from the  $F = 4$  manifold, there is negligible interaction with atoms in the  $F = 3$  manifold. In our specific case, we apply light resonant with the  $6S_{1/2}|F = 4\rangle \rightarrow 6P_{3/2}|F' = 5\rangle$  transition on the caesium D2 line to achieve this. We use a 852 nm beam with  $\sigma+$  polarisation and a  $1/e^2$  waist,  $w_0 = 5$  mm, apertured down to a 4 mm radius using a metal ring. The same beam is also used as one of the two non-destructive read out beams and it shares an optical path with the MOT- beam as shown in Fig. 3.21.

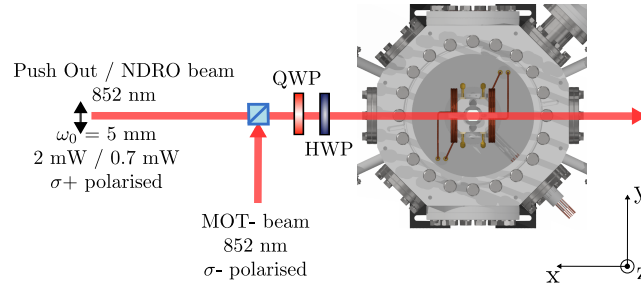


Figure 3.21: Schematic representation of the orientation of the 852 nm beam used for destructive state detection. The same beam also serves as one of two non-destructive read out beams.

The typical blow away pulse duration in our set up is 5 ms with typical operating powers of 2 mW (saturation parameter,  $s = 12.7$ ). The push out beam is operated with a 50% duty cycle out of phase with the 1064 nm trapping light during the blow away sequence. We operate the traps at the  $P_{\text{image}}$  depth of 1 mK during blow away. The power and detuning of the beam were tuned to achieve minimal off-resonant scattering loss from the  $F = 3$  manifold with the fastest achievable heating rate for atoms in  $F = 4$ . To quantify the performance of the blow away beam, we apply our optimal D1 optical pumping sequence followed by an additional 100  $\mu\text{s}$

of repump. The purpose of the additional repump pulse is to transfer any leakage populations out of the  $F = 3$  manifold and into the  $F = 4$  manifold where they can interact with the push out beam. This eliminates some of the effects of imperfect state preparation to give a better estimate of the true blow away detection fidelity. Using this procedure, we obtain a false-positive error of 0.5(2) % which is the probability for atoms in  $F = 4$  to survive the blow away sequence. This error is likely due to population leakage into the  $F = 3$  manifold during the blow away pulse and can be suppressed by using shorter, more intense BA pulses. To measure the probability of atoms in  $F = 3$  being pushed out of the traps by the blow away beam (false negative), we use a 20 ms pulse of repump light to transfer all population into the  $F = 3$  manifold before we execute the detection sequence. We obtained a 1.0(1)% false negative error probability in our system which we attribute to off-resonant scattering events.

### **Non-destructive Readout**

The non-destructive read out sequence described in Chapter 5 uses one of the horizontal 3D MOT beams<sup>37</sup> and the push-out beam. In this way, the atoms see  $\sigma+$  polarised light from both beams as required for the scheme to work. Only the basic parameters of the NDRO set up are stated here for quick reference with further details reserved for the relevant chapter in this thesis. The beams are operated with a detuning of  $-0.75\Gamma$  from the  $|F = 4, m_F = 4\rangle \rightarrow |F' = 5, m'_F = 5\rangle$  transition. We introduce a 600 kHz differential detuning between the two beams to suppress the formation of standing waves formed by the two counter-propagating beams of the same polarisation. The beam dimensions are the same as the MOT beams, a waist of 5 mm apertured down to a 4 mm radius, with an optical power of 0.7 mW/beam. We therefore operate near the transition saturation intensity

<sup>37</sup>The MOT+ beam shown in Fig. 3.8.

of  $1.1 \text{ mW}/\text{cm}^2$ . The NDRO beams are chopped out of phase with the 1064 nm trapping light with a 50% duty cycle and the trap depth is ramped up to 13 mK during NDRO to minimise atom loss due to heating.

### 3.5.3 Laser Shutters

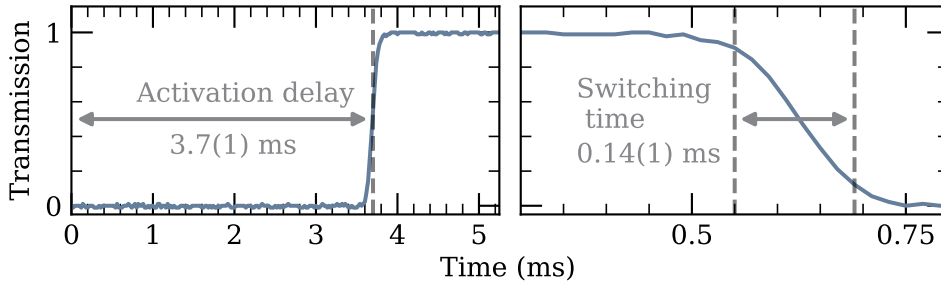


Figure 3.22: Response times of home-built laser shutter. (a) Activation delay from receiving TTL control signal to 50% transmission. (b) 90 – 10% switching time of the home-built shutter. The errors in the values shown are the standard deviations of 50 test measurements.

An important consideration for achieving high state preparation fidelities is preventing leakage light from reaching the main experimental chamber. Even though all laser beams in our experiment are switched using AOMs, there is still a possibility of coupling a few nW of 0<sup>th</sup> order leakage light into one of the optical fibres that lead to the main experimental chamber. To prevent this, we use nine home-built mechanical laser shutters driven by custom electronics which physically block beams that are not actively being used in a specific part of the experimental sequence. Our design is based on the work of G. Zhang *et al.* in [214] that introduced a simple 3D-printer friendly design for high-speed laser shutters. However the original design for the electronic circuit used to drive the DC motors inside the shutters was based on an obsolete integrated circuit chip. We modified the design to use a readily-available DRV8838 DC Motor driver chip and changed the RC circuit passive component values to set the desired shutter closing speed and force. A single circuit driver PCB has four channels and is powered by

a 5 V, 6 A external power supply. A typical response time and switching time for the shutters when driven by our PCB are shown in Fig. 3.22. The response delay from receiving a TTL signal was measured at 3.7(1) ms and the 90–10% switching time was 0.14(1) ms. For this test the bottom aperture of the shutter was used with an 852 nm beam focussed down to a  $1/e^2$  waist,  $w_0 = 40 \mu\text{m}$ . The maximum switching speed for the shutter is 100 Hz. Some frequency jitter was observed when using the shutters due to the vibrations caused by the closing action when the blade hits the rubber stop. This was minimised by placing Sorbothane sheets between the shutter mount and the surface of the optical table and slightly loosening the shutter post screw to reduce vibrational coupling.

## 3.6 Microwave System

The purpose of this section is to describe the microwave (MW) system used to drive single qubit rotations in our experiment. At the heart of this system is a Phase Locked Dielectric Resonator Oscillator<sup>38</sup> (PLDRO) operating at 8.95 GHz which serves as the ‘master clock’ of our experiment to which all qubit operations are referenced. The master clock defines the co-rotating frame in the resonant wave approximation and sets the co-ordinate system of the Bloch sphere for a single qubit.

A primary consideration in selecting this device as our MW source was the requirement for very low phase noise. This is important because the phase noise sets an upper bound on the maximum achievable gate operation fidelity [215]. Figure 3.23(a) shows a plot of the typical single-sideband phase noise values from the manufacturer’s specification. Linear interpolation was used to convert this to a continuous spectrum,  $\tilde{\mathcal{L}}(\omega)$ . Following the method from [215], we can convert this to a unilateral dephasing power spectral density

<sup>38</sup> Polaris Wave Single Loop PLDRO SPLDRO-RE10-8950-P13-2P.

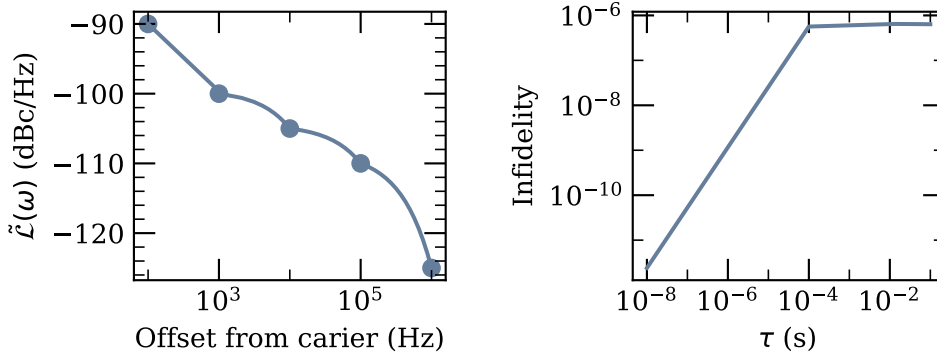


Figure 3.23: (a) Plot of the single sideband phase noise,  $\tilde{\mathcal{L}}(\omega)$ , of the master oscillator used in the experiment. The curve is a linear interpolation between the data points provided by the manufacturer's specification sheet. (b) Estimated fidelity limits due to master oscillator phase noise for different interrogation times,  $\tau$ , for a simple Ramsey fringe sequence based on the method described in [215].

(PSD) using

$$S_z^{(1)}(\omega) = \frac{1}{2}\omega^2 10^{\tilde{\mathcal{L}}(\omega)/10}. \quad (3.15)$$

The unilateral dephasing PSD can then be used to calculate an error integral,  $\chi(\tau)$  defined as

$$\chi(\tau) = \left(\frac{1}{\pi}\right) \int_0^\infty \frac{d\omega}{\omega^2} S_z^{(1)}(\omega) \sum_{I \in x,y,z} G_{z,I}(\omega, \tau), \quad (3.16)$$

where the set  $G_{z,I}(\omega, \tau)$  with  $I \in x, y, z$  is made up of filter transfer functions specific to the gate operation being performed. Such filter transfer functions are used in the development of dynamical decoupling pulse sequences as outlined in [216, 217]. To get a simple estimate of the expected performance, we use the filter function definition for an identity operation, representative of the coherence loss rate of a qubit during a Ramsey fringe due to master oscillator phase noise. Specifically, we use the filter function definition for free induction decay from reference [218] represented by a single value of  $G_z(\omega, \tau) = \sin(\omega\tau)^2/2$ . With this filter function definition, we can obtain

an estimate for the average fidelity of our qubit as a function of the Ramsey fringe duration using

$$\mathcal{F}_{\text{av}}(\tau) \approx \frac{1}{2} \left( 1 + e^{-\chi(\tau)} \right). \quad (3.17)$$

The result of this calculation, plotted in Fig. 3.23(b), shows that the infidelity resulting from the phase noise of our reference oscillator in the absence of external sources of decoherence is of order  $10^{-6}$  even for Ramsey interrogation times of 100s of milliseconds. This value is two-orders of magnitude below the current state of the art in neutral atom single gate fidelities. Therefore, we do not expect to reach an operating point where the phase noise of our master oscillator is limiting our operation fidelity because external decoherence sources such as magnetic field noise, differential AC Stark shift fluctuations and finite atom temperatures in the traps are expected to dominate [147].

To ensure long-term frequency stability we use the lock input of our master oscillator to connect an external 10 MHz GPS clock hosted in one of the atomic clock labs in our department. The output signal of the PLDRO is then conditioned as shown in Fig. 3.24(a). We first split the signal so half of it can be used to define the phase relation between our two Raman lasers which will provide an alternative way to implement single qubit rotations<sup>39</sup>. As the reader may have already noted, the oscillator frequency of our master oscillator does not match the transition frequency of our qubits defined by the 9.2 GHz hyperfine splitting of the caesium ground state. The PLDRO has a fixed frequency, but we want to have the ability to tune the frequency of our MW in order to address different transitions within the  $6S_{1/2}$  hyperfine manifolds. To achieve this, we use a Minicircuits ZMX-10G+ mixer to combine the output of the PLDRO with a frequency-tuneable source in the form of a 14-bit AD9910 direct digital synthesiser (DDS) which is directly

<sup>39</sup> The microwave splitter is an Atlantic Microwave Ltd COM02K4P-290005-S5S5.

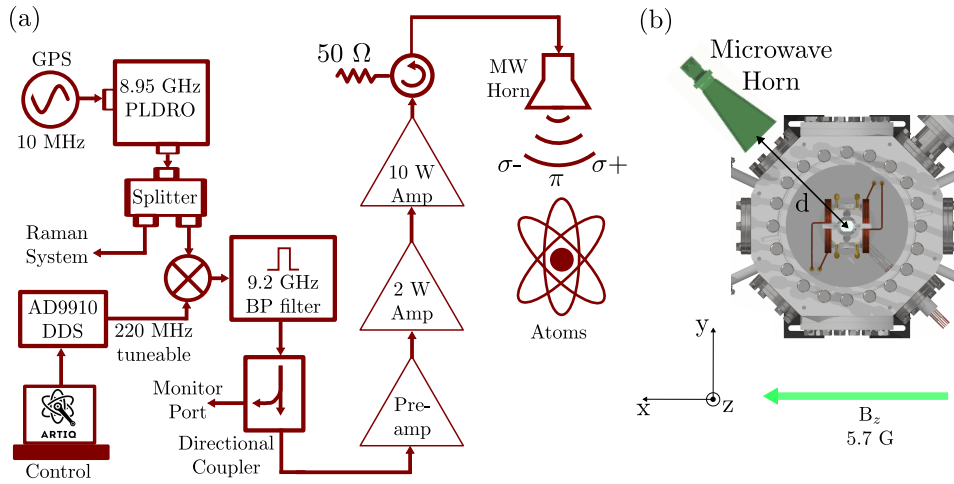


Figure 3.24: (a) Schematic diagram of the microwave system used to drive single qubit rotations in our experiment. (b) Orientation of the microwave horn with respect to the quantisation axis and distance to the atoms.

interfaced with our experimental control system<sup>40</sup>. It has a timing resolution of 1 GSPS and can output signals in the 80-400 MHz frequency range with a frequency resolution  $\leq 0.23$  Hz. The DDS has a lower phase noise than our master oscillator. To minimise the variability of the electric and magnetic field noise from shot to shot, all pulses are synchronised to be out of phase with the 50 Hz mains line electricity supply using a home-built line-trigger system<sup>41</sup>. We could not quantify the benefit provided by the AC mains trigger alone because the temperature stability of the experiment was the limiting factor for microwave qubit coherence and the attempted measurements with and without the AC mains trigger did not have a reproducible temperature environment.

We pass the mixed signal through a 9.2 GHz bandpass filter with a  $\pm 50$  MHz passband<sup>42</sup> to attenuate the difference frequency output of the mixer. A di-

<sup>40</sup> The DDS was not referenced to the 10 MHz GPS source during the experiments presented in this work.

<sup>41</sup> The trigger is constructed using an AC to AC converter to step down the 230 V mains voltage to 9 V so it can be applied to an analogue input pin of an Arduino Mega 2560 microcontroller. The Arduino outputs a continuous train of TTL pulses synced to the mains line with a user-defined phase delay which feeds into our experimental control system.

<sup>42</sup> APC Technology AT22F-WT349-AF.  $< 1$  dB pass band insertion loss. 20 dB attenua-

rectional coupler<sup>43</sup> is used to provide a monitoring port before amplifying the signal in three stages. The first stage is a low-noise pre-amplifier<sup>44</sup> with 20.5 dB gain at 9.2 GHz, followed by two high-power amplifiers. The 2 W amplifier is a Kuhne X-Band KU PA 9001250-2A and the 10 W amplifier is a Kuhne X-Band KU PA 10001050-8B. The signal is then passed through a circulator<sup>45</sup> with one port terminated with a high-power 50  $\Omega$  terminator for protection against back reflection and the other port connected to a microwave horn<sup>46</sup> using a low-loss coaxial cable rated for operation at 9.2 GHz. The microwave horn is aimed at a viewport of the main experimental vacuum chamber and is at a distance,  $d$ , of 15 cm away from the atoms as shown in Fig. 3.24(b). Because of the arbitrary angle of the horn with respect to the quantisation axis, the polarisation of the radiation it emits into the chamber is not well defined in the atoms' frame of reference. The magnitude of the output magnetic field as a function of distance for a half-wave dipole antenna across all three polarisation components is given by [205]

$$B_0 = \frac{Z_0 I_0}{2\pi c d}, \quad (3.18)$$

where  $Z_0=376.73 \Omega$  is the free space impedance in vacuum, and  $I_0$  is the intensity of the microwave electric field given by  $I_0 = \sqrt{2P_{\text{out}}/R}$ .  $P_{\text{out}}$  is the 10 W output of the final amplifier stage and  $R$  is the 50  $\Omega$  impedance of the horn waveguide. To estimate the correct amplitude of the B-field at the atoms, we must also consider the gain of the waveguide given by

$$G = \frac{4\pi A}{\lambda^2} e_A, \quad (3.19)$$

where  $A$  is the area of the waveguide,  $\lambda$  is the wavelength of the microwave radiation in the stop band.

<sup>43</sup> Minicircuits ZX30-14-972HP+.

<sup>44</sup> Minicircuits ZX60-05113LN+.

<sup>45</sup> Atlantic Microwave Ltd CIRK4-760010-S5S5S5

<sup>46</sup> Flann Microwave 16441 WR90/WG10.

diation and  $e_A$  is the antenna's aperture efficiency which can have a maximum value of 0.8. By taking the product of equations (3.18) and (3.19) and using the  $232.2 \text{ mm}^2$  area of our waveguide with a best-case antenna aperture efficiency, we arrive at a value,  $B_0 = 18.5 \text{ mG}$ , for the magnitude of our 9.2 GHz magnetic field inside the chamber across all polarisation components. From Rabi frequency measurements on hyperfine ground state transitions between different  $m_F$  levels, we infer the ratio of magnetic field amplitudes across polarisation components ( $\sigma+$ ,  $\pi$ ,  $\sigma-$ ) as (0.46, 0.27, 0.27) respectively. The imbalance between polarisation components is attributed to the arbitrary angle of the horn with respect to the quantisation axis as well as the standing wave patterns forming inside the chamber due to reflections from the metal surfaces. This shows good agreement with the clock state Rabi frequency of  $2\pi \times 8.2 \text{ kHz}$  recorded at the time, which corresponds to a driving MW field amplitude of 5.6 mG or 32 % of total estimated 18.5 mG across all polarisations.

Using the MW system described above, we are able to drive MW transitions between any two magnetic-dipole-coupled states in the  $F = 3$  and  $F = 4$  hyperfine manifolds of the  $6S_{1/2}$  ground state of caesium. Even though every MW pulse contains a mix of polarisations, we are able to target specific transitions by controlling the frequency of the output signal. We apply a 5.7 G bias magnetic field which induces differential Zeeman shifts of the order of a few MHz on all but the clock state transition which is insensitive to first order Zeeman shifts. Because the linewidth of a typical power-broadened MW resonance is of the order of 10s of kHz, we are able to achieve excellent selectivity in the transitions we address as shown in Fig. 3.25. The obtained resonances are in good agreement with theoretical calculations using the Breit-Rabi formula and a bias field of 5.73 G. The resonances with a target state in the  $F = 3$  manifold are associated with an increase in the survival, while the resonances for transfer in the  $F = 4$  manifold experience maximum atom loss when we apply our blow away detection beam. We are

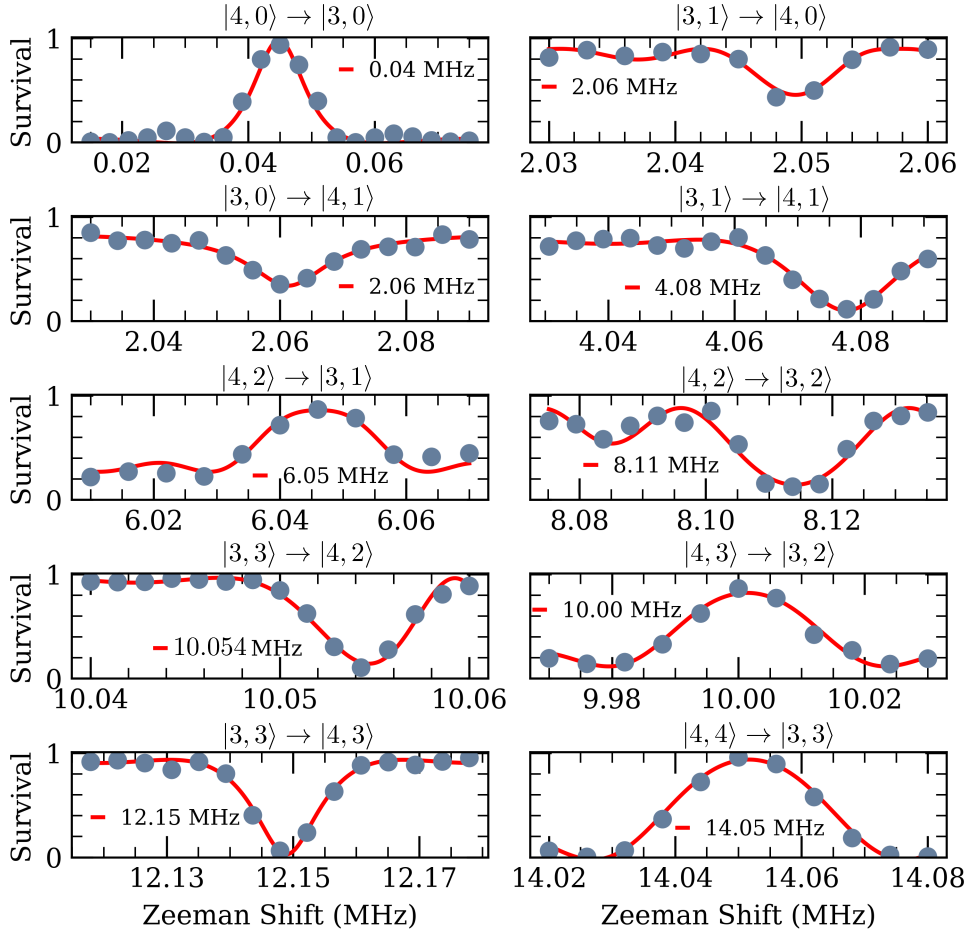


Figure 3.25: Microwave spectroscopy of the caesium hyperfine ground states. All transitions which do not include the states into which we can optically pump ( $|4, 4\rangle$  or  $|4, 0\rangle$ ) were accessed with sequential MW pulses. See main text for details. The resonances for each transition are fitted with a sinc function and each plot is labelled with the fitted differential Zeeman shift of the transition relative to the zero-field splitting of the caesium hyperfine ground states. The fit errors for the shift are of the order  $10^{-4}$  MHz, while the deviation from the predicted differential Zeeman shift using the Breit-Rabi formula for a bias field of 5.73 G is of the order  $10^{-2}$  MHz. The observed deviation from theory is attributed to errors in the voltage to Gauss calibration of the coil driver electronics.

only able to optically pump in either the  $|4, 4\rangle$  or the  $|4, 0\rangle$  state, so all other resonances were found by starting in one of these two states and applying multiple MW pulses of different frequencies to transfer populations across. This explains some of the loss of contrast. All resonances except for the clock state resonance were obtained by starting in the stretched state. The intention behind these resonance frequency calibration steps is explained in Section 5.2, but in the end we concluded that the transfer sequence is not necessary in order to implement NDRO.

The system was mainly used for driving single qubit rotations on the clock state transition for our randomised benchmarking results. A typical resonance and Rabi frequency calibration are shown in Fig. 3.26 for a 225 site array and a 49 site array, both spaced at  $8\ \mu\text{m}$ . After the MW drive, we apply a blow away pulse to record the population in  $F = 3$  as a function of the MW pulse duration. The Rabi flops in Fig. 3.26(a) and (d) are the array averages across all trap sites. The data set with 225 trap sites has a lower Rabi frequency because of a loose SMA connection to one of the amplifiers which was later fixed for the 49 site run. The damping in the 225 site averaged oscillation is not due to qubit decoherence, but a result of the averaging process across multiple trap sites. Figure 3.26(c) shows that there is a 3% inhomogeneity in the Rabi frequencies across the spatial extent of the array which leads to this effect. The 49 site array data in Fig. 3.26(f) shows the same gradient in Rabi frequency across the array, but the amplitude of the variation is halved in proportion to the ratio of the spatial extents of the two arrays. This issue was addressed with BB1 composite pulses as described in Section 4.2. Our optimal clock state Rabi frequency is  $\Omega/2\pi = 9.60(1)\ \text{kHz}$  corresponding to a  $52\ \mu\text{s}\ \pi$  pulse duration on the clock state qubit.

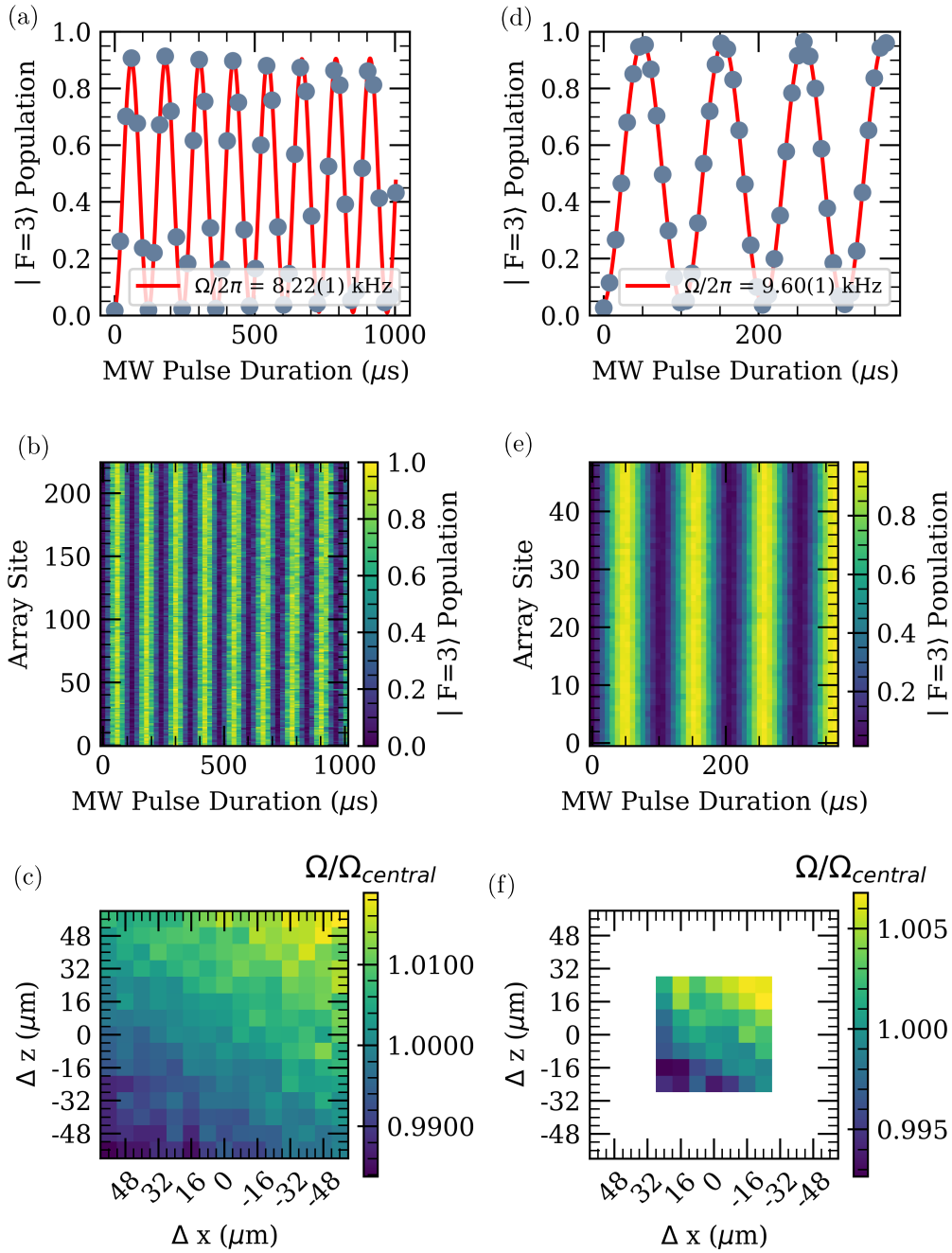


Figure 3.26: Rabi frequency calibration of the clock state qubit for two array sizes. (a) Averaged Rabi flop across a 225 site array. What appears as damping is in fact a result of the inhomogeneity of the Rabi frequency across the array. The lower Rabi frequency in (a) compared to (d) was due to a loose connection in the MW electronics chain. (b) 2D colormap plot of the clock state Rabi oscillations inside all 225 traps. (c) 2D spatial map of the variation in  $\Omega$  across the 225 site array. (d) Average Rabi flop across a 49 site array. Notice the improved contrast in the averaged oscillation due to the smaller spatial extent of the array which reduces the variation in Rabi frequencies. (e) 2D colormap plot of the clock state Rabi oscillations for a 49 site array. (f) 2D spatial map of the variation in  $\Omega$  across the 49 site array. The intensity uniformity of both 1064 nm arrays was optimised using feedback from an atomic signal as described in Section 3.3.2.

## 3.7 Rydberg System

### 3.7.1 Lasers

#### Rydberg Excitation Scheme

The design of the Rydberg laser system was motivated by our choice of Rydberg excitation pathways. The most direct way of exciting a ground state atom to a Rydberg state is by using a single photon in the ultraviolet (UV) wavelength range. In the case of caesium, this corresponds to a wavelength of 318 nm which has been used to perform spectroscopy [219] and demonstrate Rydberg blockade [220]. The main advantage of this approach is that it eliminates the off-resonant scattering from the intermediate state present in a two-photon excitation process which is a major source of fidelity loss [78]. However, the weak dipole matrix elements for direct excitation from an alkali ground state to the Rydberg manifold combined with the limited availability of high-power lasers at UV wavelengths make this approach unfavourable for scaling up to larger system sizes. There are also additional experimental challenges associated with the UV wavelength such as the build-up of static electrical charges on optical surfaces due to the photoelectric effect which can affect the stability and coherence of the highly-sensitive large dipole moment Rydberg states. Finally, at UV wavelengths there is also a more severe motional dephasing effect associated with the finite velocity of the atoms during Rydberg excitation which scales as  $\propto 1/k$ , where  $k$  is the wavevector of the light [221].

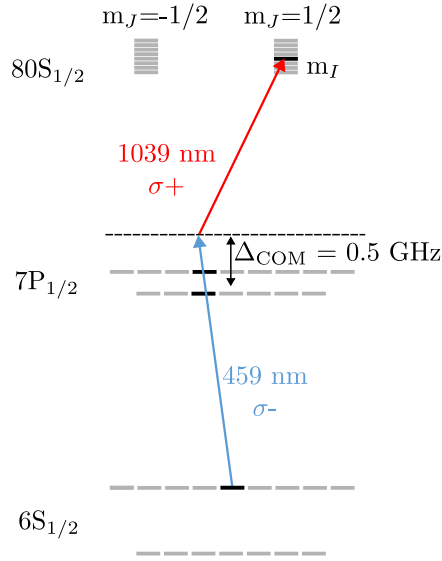


Figure 3.27: Rydberg excitation scheme used in this work. After optically pumping the atoms into the  $6S_{1/2}|F = 4, m_F = 0\rangle$  state, we apply a pulse of  $\sigma^-$  polarised 459 nm light to off resonantly couple to the intermediate  $7P_{1/2}$  state via both the  $|F = 4, m_F = -1\rangle$  and the  $|F = 3, m_F = -1\rangle$  channels. The detuning of the 459 nm light from the centre of mass (COM) energy of the intermediate state is,  $\Delta = +0.5$  GHz. The second leg of the transitions is driven by a 1039 nm laser with  $\sigma^+$  polarisation which resonantly couples to the  $n_{1/2}|m_J = +1/2, m_I = -1/2\rangle$  Rydberg state. We typically operate with  $n = 80$ .

For the reasons outlined so far, the more commonly used approach is a two-photon excitation process into the Rydberg manifold. The two broad categories are the standard two-photon excitation scheme which uses an IR photon on either the D1 or D2 line in combination with a visible laser wavelength<sup>47</sup> or the inverted excitation scheme which uses visible light to excite to the intermediate state and infrared light for coupling the intermediate state to the Rydberg state<sup>48</sup>. Both of these methods have the advantage of being able to drive excitations to both  $nS$  and  $nD$  Rydberg states, while the single-photon UV method is limited to  $nP$  states in alkalis due to the  $\Delta l = \pm 1$

<sup>47</sup> These are 495 nm or 509 nm for caesium in combination with the D1 and D2 lines respectively.

<sup>48</sup> For caesium the wavelength combinations are either 459 nm + 1039 nm via  $7P_{1/2}$  or 456 nm + 1059 nm via  $7P_{3/2}$

selection rule for electric dipole transitions. This is less favourable because  $P$  and  $D$  states have a more complex level structure, sensitivity to external perturbation and spatially anisotropic dipole-dipole interactions not present in  $S$  states [222]. The two-photon approach also provides some Doppler-dephasing cancellation when using two counterpropagating beams as is usually done in most experiments. In the end, we opted for the inverted excitation scheme because of the five-times smaller linewidth of the intermediate state combined with having access to higher laser powers in the IR range for driving the Rydberg coupling with its weaker matrix element. Our excitation scheme is shown in Fig. 3.27. Specifically, we opted for the 459 nm + 1039 nm combination exciting through the  $7P_{1/2}$  intermediate state because it has a narrower linewidth than the  $7P_{3/2}$  state resulting in higher expected gate fidelity, even though the coupling to the  $7P_{3/2}$  state requires 4 times less power in the visible range. In addition, by avoiding the  $7P_{3/2}$  state, we avoid the possibility of also coupling to the  $nS_{1/2}|m_J = -1/2\rangle$  Rydberg states, as was the case in reference [223]. The selection rule that explains this is  $\Delta m_J = +1$  for fine structure electric dipole transitions driven by light with  $\sigma+$  polarisation. For the Rydberg state in the transition from  $7P_{1/2}$  to  $80S_{1/2}$  we are operating in the Paschen-Back high magnetic field regime, even with the low amplitude 6.0 G quantisation magnetic field we apply, because the magnetic field interaction is stronger than the hyperfine splitting of the highly-excited Rydberg state [223]. However, for the intermediate state this is not the case. It is in the low-field regime and  $m_J$  is not a good quantum number. Therefore all the  $7P_{1/2}$  states which have  $m_I + m_J = m_F = -1$  can couple to the Rydberg state. In our case there are two states:  $|m_J = -1/2, m_I = -1/2\rangle$  and  $|m_J = 1/2, m_I = -3/2\rangle$ , but since there is no  $m_J = 3/2$  Rydberg state to couple to, only the  $|m_J = -1/2, m_I = -1/2\rangle$  state couples to the  $80S_{1/2}|m_J = +1/2, m_I = -1/2\rangle$  state when driven by light with  $\sigma+$  polarisation.

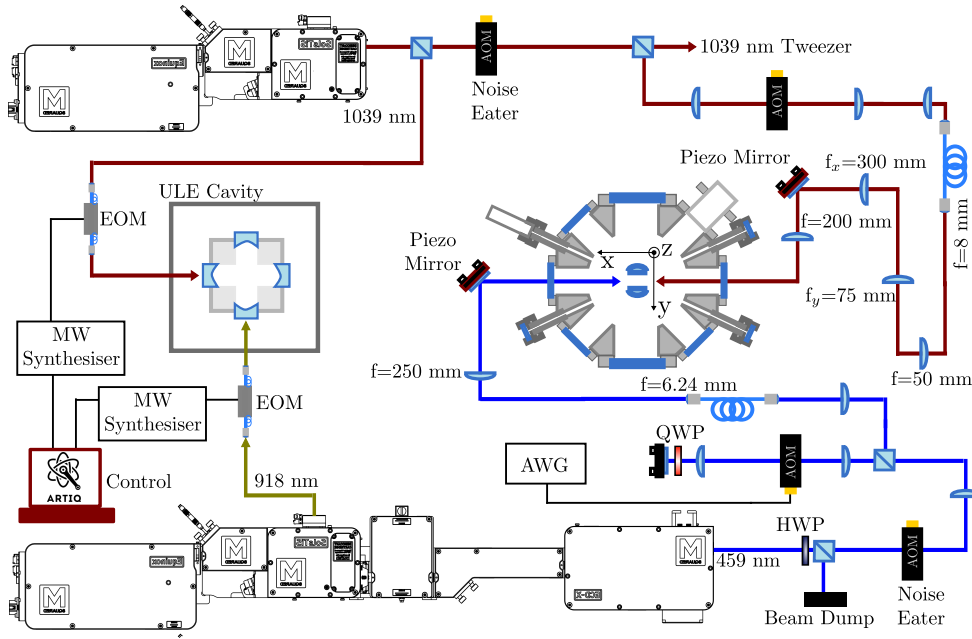


Figure 3.28: Schematic diagram of the Rydberg laser system. To avoid crowding the schematic, only the focal lengths affecting the beam size at the atoms have been shown.

### Rydberg Laser Set Up

Our system uses two M Squared Ltd. lasers as shown in Fig. 3.28. The 459 nm light is produced by frequency-doubling a 918 nm SolsTiS Ti:Sapphire laser using a second harmonic generation (SHG) process inside an ECD-F module with an enhancement cavity to boost the SHG efficiency. The laser outputs 0.8 W of 459 nm light when operated at full power and some of it is safely dumped at the output because of the power handling limitations of other optical components in the system. The system comes with a 918 nm pick off which we use for the ultra-low expansion (ULE) cavity lock described in Section 3.7.2. After passing through a noise eating (NE) AOM, the 459 nm is frequency shifted using a double-passed AOM before being fibre-coupled into a single-mode polarisation maintaining fibre for transporting it to the atoms. The laser is already installed on the main experimental table, but by fibre coupling it we are guaranteed a  $TEM_{00}$  mode at the atoms and we avoid having excessively long free space beam paths which would be subject

to pointing instability. The double-passed switching AOM for the 459 nm is driven by an arbitrary waveform generator (AWG)<sup>49</sup> which allows us to vary the amplitude, frequency and phase of the signal on  $\mu\text{s}$  timescales as required for the analogue optimisation experiments discussed in Chapter 6. After the fibre output we have a polarising beam splitter to clean up the polarisation and a pick-off for feeding back to the noise eater AOM before focusing the beam to a waist of  $w_0 = 90 \mu\text{m}$  at the atoms using a  $f = 250 \text{ mm}$  achromatic lens. The beam size was independently calibrated using a signal from the atoms as described in Section 3.7.4. We typically operate with 45 mW of 459 nm light at the atoms including the 10% reduction in power required to apply noise eating. This power is limited by the damage threshold of the  $\text{TeO}_2$  AOM crystal which prevents us from using the full available laser output power.

The 1039 nm system is a SolsTiS Ti:Sapphire laser with a maximum power output of 1.4 W. We pick off a small amount of light at the laser output for the ULE cavity lock and pass the rest through a noise eating AOM. The signal is split into a local and global beam path which correspond to the beams used for the 1039 nm sorting tweezer and global Rydberg excitation respectively. We omit the specifics of the 1039 nm tweezer path in this work because further details are available in the thesis of Elliot Diamond-Hitchcock [165] who was responsible for maintaining it. We use a single-passed AOM for switching the 1039 nm Rydberg excitation light and we couple the output of the AOM into a high-power single-mode polarisation maintaining fibre for the same reasons outlined in the previous paragraph about the 459 nm system. We perform some beam shaping after the fibre output to obtain a cylindrical beam which is narrow along the  $y$ -axis and broader along the  $z$ -axis to maximise the light intensity seen by the atoms in the array, which is situated in the  $x - z$  plane of the lab coordinate reference frame. The 1039 nm effective beam waist was calibrated by adjusting the position of the

---

<sup>49</sup> Spectrum M4i6631-x8

final lens along the light's  $k$ -vector to achieve the highest-possible Rydberg Rabi frequency when exciting to the  $50S_{1/2}$  state. The final result gives an effective beam waist of  $w_0 = 47 \mu\text{m}$  at the atoms as outlined in Section 3.7.4. The noise eating pick-off for this system is on the other side of the chamber, where most of the light is safely dumped and a small amount picked off for feedback to the noise eater AOM. Both Rydberg beam paths have a remote-controlled piezo mirror installed which we use to align the beams onto the atoms with  $\mu\text{m}$  precision by minimising survival after applying a pulse of area  $0.7\pi$  on the Rydberg transition and expelling excited atoms using the detection method from Section 3.7.3.

### 3.7.2 Narrow-Linewidth Laser Locking

In order to ensure long-term frequency stability and achieve a narrow linewidth for our Rydberg lasers, we use a temperature-stabilised ultra-low expansion (ULE) cavity with a free spectral range (FSR) of 3 GHz as an external frequency reference. The ULE cavity was provided by M Squared Lasers and it is based on a dual-axis cubic cavity design with two orthogonal axes [224]. The cavity is operated under a vacuum pressure of  $5 \times 10^{-6}$  Torr. Each laser could be locked to either axis, but we operate with the two lasers locked to orthogonal axes of the cavity. The expected finesse values based on the specified cavity mirror reflectivities are  $\mathcal{F}=40,000$  (71,000) for a 918 nm (1039 nm) wavelength. These were independently calibrated using cavity ring-down measurements by recording the decay rate of the light intensity transmitted through the cavity after rapidly extinguishing the input beam [225] as shown in Fig. 3.29(a) using the 918 nm system. The corresponding measurement for the 1039 nm laser yielded an abnormally high finesse because the available photodiodes experienced afterpulsing effects [226] which manifested in unrealistically slow decay during the ringdown measurement. Instead, the cavity finesse was calibrated by splitting the 1039 nm laser into

two paths. One was used to lock the laser to cavity axis 1 and the second beam path was passed through another electrooptic modulator (EOM) which was used to measure the cavity transmission peak as a function of the sideband frequency as shown in Fig. 3.29(b). From the recorded full-width half-maximum (FWHM) of 120 kHz we can infer a 1039 nm cavity finesse value  $\mathcal{F}=25,000$  by taking the ratio of the FSR to the measured Lorentzian resonance linewidth.

We use a Pound-Drever-Hall (PDH) locking method with an electronic sideband modulation scheme [227] to stabilise the laser to the cavity resonance. In this method a phase-modulated fibre-coupled EOM is used in each beam path before the respective cavity input mirror. The EOMs are driven by a mixed signal which contains two components as shown in Fig. 3.29(d). The first component is sourced from a MW synthesiser<sup>50</sup> directly connected to our ARTIQ experimental control system. Scanning the frequency of this signal,  $\nu_{\text{offset}}$ , allows us to vary the sideband offset from the cavity carrier resonance peaks separated by the 3 GHz cavity FSR. By locking to one of the two EOM sidebands we now have a means to freely tune the laser lock point whilst still using the cavity as a reference. We usually operate with the 918 nm EOM frequency fixed and scan the offset of the 1039 nm laser when performing Rydberg spectroscopy. The second signal input into the EOM is obtained from an arbitrary function generator<sup>51</sup> which provides the PDH modulation signal. The arbitrary function generator signal is mixed with the cavity reflection signal captured on a fast photodiode and fed into a MOGLABS FSC PID controller with parallel fast and slow control loops to generate the laser feedback signal. A cavity transmission photodiode is currently only used to monitor the quality of the laser lock, but in the future this could be used to implement a filter cavity set-up as formulated in [228] for reduced phase noise at frequencies near the effective two-photon Rydberg

<sup>50</sup> An M-Labs Sinara Mirny synthesiser based on ADF5356 chips.

<sup>51</sup> Multicomp MP750513

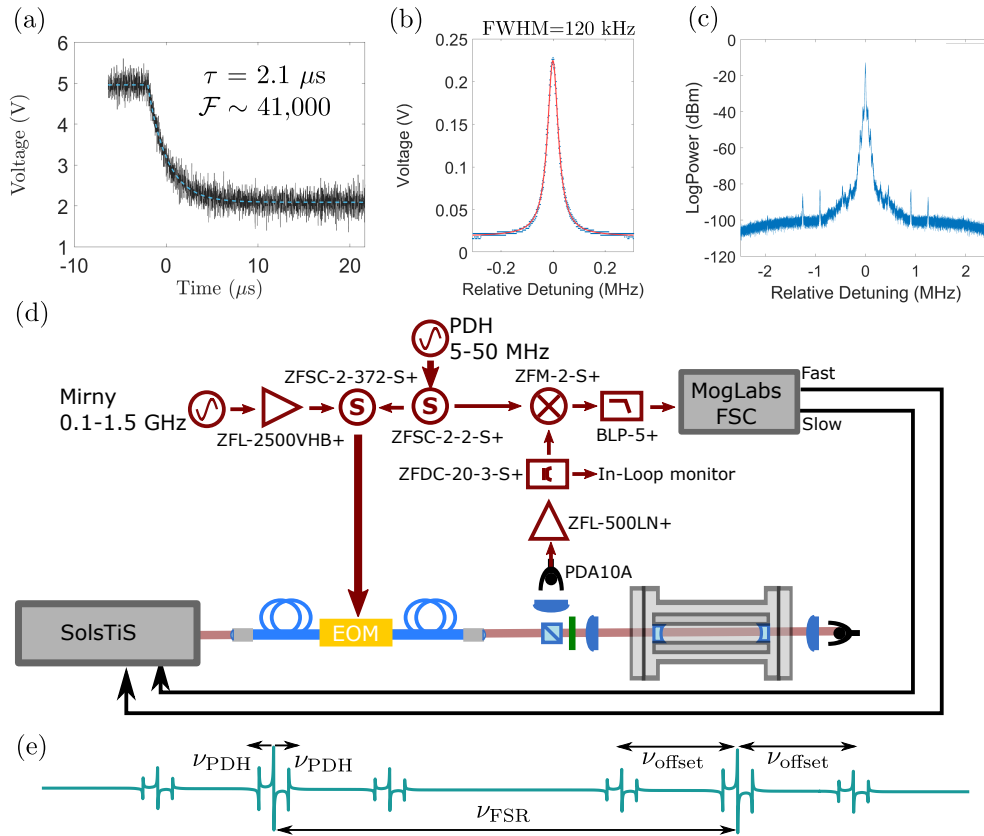


Figure 3.29: (a) Cavity ringdown measurement using 918 nm light showing good agreement with design specification. (b) Alternative measurement results used to determine the 1039 nm cavity finesse by locking laser and scanning EOM sideband frequency on the second cavity axis to obtain a resonance linewidth of 120 kHz. (c) Beat note measurement using two identical M Squared 1039 nm systems showing absence of servo bumps around 1 MHz. The FWHM of the beat note feature is 7 kHz when measured over 165 ms with 50 averages. (d) RF electronics diagram of PDH laser lock system used to stabilise Rydberg lasers to ULE cavity. (e) Schematic representation showing a theoretical error signal for the carrier, PDH and sideband lock.

Rabi frequency<sup>52</sup> as discussed in [77, 229]. To assess the level of phase noise present in our existing set up we performed a beat note measurement using an identical 1039 nm laser. The resulting feature is shown in Fig. 3.29(c) obtained from averaging 50 measurements with 200 Hz resolution bandwidth and a measurement time of 165 ms. It shows no evidence of servo bumps near frequencies close to the Rydberg Rabi frequency due the low phase noise of the M Squared SolsTiS platform and its proprietary PID control electronics [94]. This informed the decision to not implement a filter cavity set up at the time.

### 3.7.3 Rydberg State Detection

A typical experimental sequence which contains Rydberg excitation is shown in Fig. 3.30. The timing diagram starts after the first camera image has been taken. We apply a 1 ms pulse of D1 optical pumping (OP) to prepare the atoms in the  $6S_{1/2}|F = 4, m_F = 0\rangle$  state with 95% fidelity. After this the 1064 nm traps are adiabatically ramped down to an amplitude  $P_{\text{expt}}=0.01P_{\text{load}}$  in order to lower the atoms' temperature before switching off the 1064 nm light altogether. This is necessary because the 1064 nm potential is repulsive to Rydberg atoms. The excitation process begins with an 8  $\mu\text{s}$  pulse of 1039 nm light immediately after switching the traps off. This is the minimum pulse duration set by the time our experimental control system requires to update the analogue control voltage which sets the 1064 nm amplitude to a higher value for expelling the Rydberg atoms. This time could be reduced by using two analogue channels and a fast switch, but this was not a limiting factor at the time so it was not addressed. At this point of the experiment, no Rydberg excitations has taken place yet. The excitation happens only when we apply a pulse of 459 nm light which overlaps in time with the 1039 nm light. The duration of this pulse is scanned as shown in

<sup>52</sup> In our experiment the effective Rydberg Rabi Frequency is typically around  $2\pi \times 2$  MHz for excitation to  $80S_{1/2}$ .

Fig. 3.30 to record Rabi oscillations and the 1039 nm pulse duration is extended beyond 8  $\mu$ s if required. Within 250 ns of completing the excitation pulse, the 1064 nm traps are pulsed on at a high amplitude to expel atoms in the Rydberg state and re-capture ground state atoms. The amplitude of this pulse,  $P_{\text{expel}}$ , was optimised for optimal Rydberg oscillation contrast and minimal ground state atom loss. After this stage, a second camera image is taken to check for atom loss. The typical detection fidelity inferred from the maximum atom loss observed after an optimised  $\pi$ -pulse on the Rydberg transition is 0.95(2) without scaling for imperfect state preparation. If we account for the optical pumping fidelity of 0.957(9), this results in a Rydberg state detection fidelity of 0.99(3) limited by the finite Rydberg state lifetime. We also recorded a 1.8(2)% false positive probability of detecting an atom in the Rydberg state. This was done by executing the Rydberg excitation experiment with the 459 nm and 1039 nm beams physically blocked and recording the probability of atom loss. This error can be reduced by improved cooling allowing for longer release times from the 1064 nm traps without atom loss or by using a trapping potential which does not need to be switched off during Rydberg excitation such as a blue-detuned bottle beam trap [95, 230, 231].

### 3.7.4 Rydberg System Calibration

#### Rydberg Spectroscopy

The first step in the Rydberg calibration process is to perform spectroscopy on the  $7P_{1/2}$  state using 459 nm light. After preparing the atoms in the  $6S_{1/2}|F = 4, m_F = 0\rangle$  state using D1 OP, we apply a heavily attenuated 459 nm pulse (5  $\mu$ W of power) to scatter photons on the  $6_{1/2} \rightarrow 7P_{1/2}$  transition. The atoms have a chance of decaying to the  $F = 3$  manifold of the ground state during this process. After applying a fixed 459 nm pulse duration, we apply a push out pulse to heat atoms in  $F = 4$  out of the traps

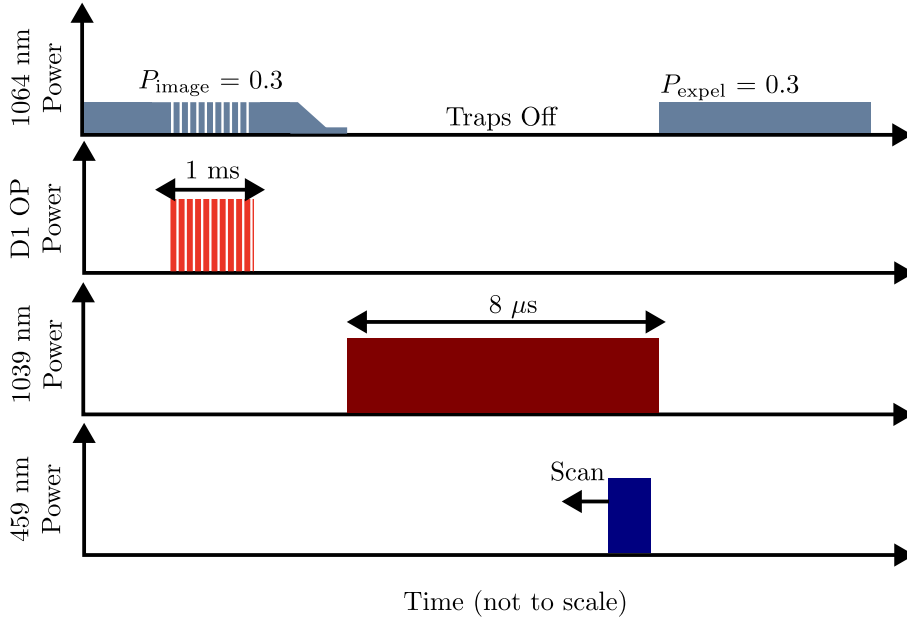


Figure 3.30: Timing diagram for Rydberg excitation experiments.

and take an image to record survival. By scanning the frequency of the 459 nm light we obtain resonant features corresponding to the transitions to the  $7P_{1/2}|F = 4, m_F = -1\rangle$  and  $7P_{1/2}|F = 3, m_F = -1\rangle$  states. Because the 918 nm signal that serves as the source of the 459 nm light is monitored on a High Finesse WS-7 wave meter, we have a high precision frequency reference accurate to within 10s of MHz to compare against available spectroscopic data [232]. In this way can ensure that we are operating at the target detuning of +0.5 GHz from the centre of mass frequency of the  $7P_{1/2}$  state. To find the resonance frequency of a transition to a target Rydberg state we start by calculating a theoretical estimate using the ARC software package [115]. As explained in the previous paragraph, the 459 nm side band offset frequency remains fixed at the value which gives the target 0.5 GHz intermediate state detuning. We employ two methods to perform spectroscopy on the Rydberg resonance. The first method used for low-precision spectroscopy is to apply a  $\pi$  pulse on the Rydberg transition and scan the 1039 nm sideband offset frequency. The result of such a measurement for the  $80S_{1/2}$  transition is shown in Fig. 3.31(a) for a single trap.

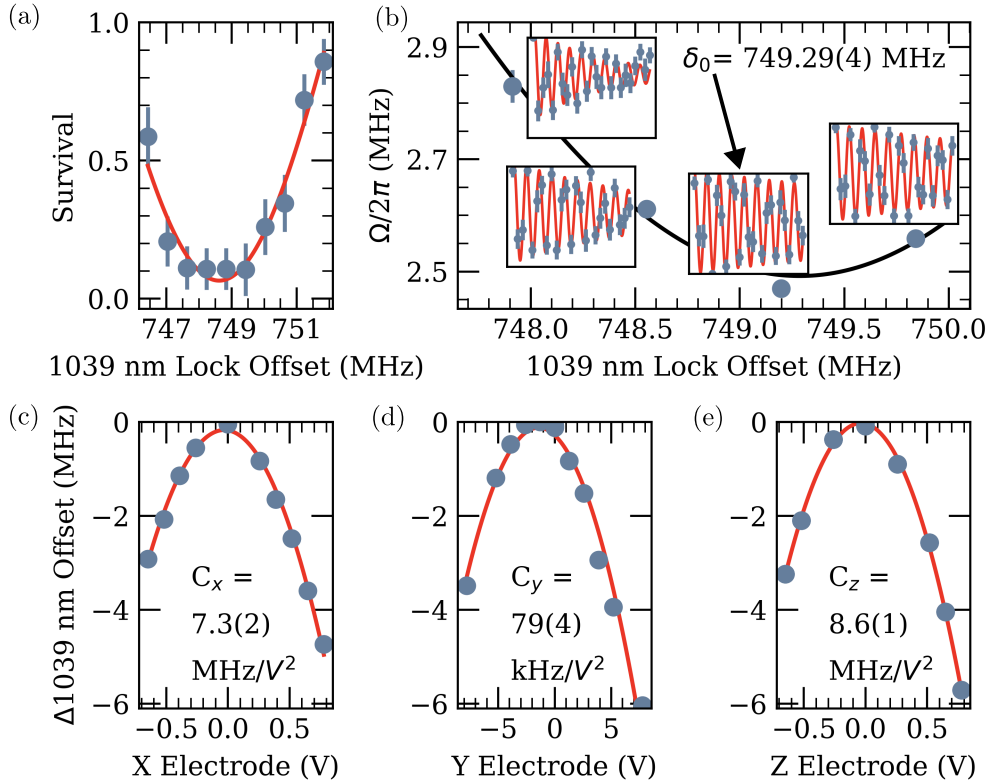


Figure 3.31: (a) Simple Rydberg resonance calibration method for the transition to the  $80S_{1/2}$  state using a  $\pi$  pulse. The data shown here is for a single trap in an array of 25 atoms spaced by  $20\ \mu\text{m}$  to avoid dipole-dipole interactions. (b) More precise resonance calibration method for the same trap and the same transition. The true resonance,  $\delta_0$ , was obtained by recording Rabi flops at multiple frequencies within the FWHM of the coarse resonance and fitting  $\Omega' = \sqrt{\Omega^2 + \Delta^2}$  to find the frequency for which  $\Delta = 0$ . (c), (d), (e) Electric field scans performed on the  $80S_{1/2}$  state to null stray DC electric fields inside the main chamber.

Once we have obtained a reasonable estimate of the resonance frequency, we follow the approach from [223] to obtain the true resonance frequency by taking multiple Rabi flops at several 1039 nm laser frequencies within the expected FWHM of the initial resonance and fit their Rabi oscillation frequency over a few cycles. By fitting the relation  $\Omega' = \sqrt{\Omega^2 + \delta^2}$  to the resulting Rabi frequencies we can obtain the true resonance frequency at the minimum of the curve as shown in Fig. 3.31(b). Note that the measurement was performed for the same trap in (a) and (b), but the recorded resonance

frequency is different using the two different methods. This occurs because the effective pulse area at short pulse durations is reduced due to the finite risetime of the 459 nm AOM which gives us a reduced AC Stark shift for very short pulse durations. If not calibrated using the more advanced method described here, this calibration inaccuracy manifests in what appears as rapid decoherence of the Rydberg Rabi flop.

### Stray Field Cancellation

Because of the large dipole moments of Rydberg states their polarizability scales as  $\propto n^7$  which makes them extremely sensitive to fluctuations in the background electric field inside the chamber. To suppress some of these effects we use the chamber electrodes described in Section 3.1 and apply a static electric field to null any background fields inside the chamber. This is done by recording the Rydberg resonance frequency at a range of different voltages and obtaining the zero field resonance following the process described in [205]. The results of such a scan performed at  $n=80$  is shown in Fig. 3.31(c),(d), and (e) for the  $x$ ,  $y$ , and  $z$  axis electrodes respectively. Notably the compensation field along the  $y$ -axis needs to be an order of magnitude larger because of the dielectric properties<sup>53</sup> of the plastic spacers installed in the in vacuo lens assembly, similarly to other experiments which use this in-vacuo lens design[205, 233]. Fits were performed using

$$\Delta 1039 \text{ nm Offset} = \delta_0 - C_i(\Delta V_i - \Delta V_{i_0})^2. \quad (3.20)$$

to extract the constant  $C_i$  for each axis,  $i$ , which quantifies the DC Stark shift on the atoms as a function of the applied chamber electrode voltage. By evaluating  $l_{eff} = \sqrt{\alpha/(2C_i)}$ , where  $\alpha=1526.9 \text{ MHz}/(\text{V}^2 \text{ cm}^2)$  is the static polarisability of the  $80S_{1/2}$  state calculated using ARC [115], we obtain the effective field length of the stray electric field inside our chamber which allows

<sup>53</sup>The lens spacers are made out of PEEK plastic with  $\epsilon_r = 3.5$ .

Table 3.1: Effective length of the background DC electric field inside the main experimental chamber. The large disagreement with simulation along the  $y$ -axis is because the simulation did not take into account the capacitance of the plastic in-vacuum lens spacer.

Axis	$C_i$ (MHz/V <sup>2</sup> )	Simulation Effective Field Length (cm)	Fitted Effective Field Length (cm)
$x$	$C_x = 7.3(2)$	8.06	10.94(5)
$y$	$C_y = 0.079(4)$	12.66	98(4)
$z$	$C_z = 8.6(1)$	8.06	9.42(2)

us to convert the applied electrode voltages to Cartesian components of the electric field amplitude at the atoms,  $F_i$ , using  $F_i = \Delta V_i / l_{\text{eff}}$  [198]. The obtained effective field lengths for each axis,  $i$ , are shown in Table 3.1.

### Rabi Frequency Calibration

A typical Rabi oscillation at  $80S_{1/2}$  obtained after these calibration steps is shown in Fig. 3.32(a) for a single trap. We achieve a Rabi frequency,  $\Omega/2\pi = 2.468(4)$  MHz using 45 mW in the 459 nm beam and 740 mW in the 1039 nm beam. At the time of writing we do not use advanced beam-shaping techniques for our Rydberg excitation beams. As a result there is a significant variation in the observed Rabi frequencies across different rows of atoms in the array as can be seen in Fig. 3.32(b). This can be improved at the cost of power loss by converting the Gaussian intensity profile of the beams into a top-hat profile through the use of either passive optical elements [234] or holographic methods with an SLM or digital micromirror device (DMD) [235]. Because the Rayleigh ranges of our Rydberg beams are much larger than the span of the largest array of atoms we could generate in our system<sup>54</sup>, there is <0.3% variation in the Rydberg Rabi frequency along a single row of atoms. Typical Rydberg coherence times recorded on the central row of atoms in our experiment, at the peak laser intensity, are of the order of  $T_{\text{decay}}$

<sup>54</sup> The Rayleigh ranges of our Rydberg beams are 55.4 mm and 6.68 mm for the 459 nm and 1039 nm beam respectively

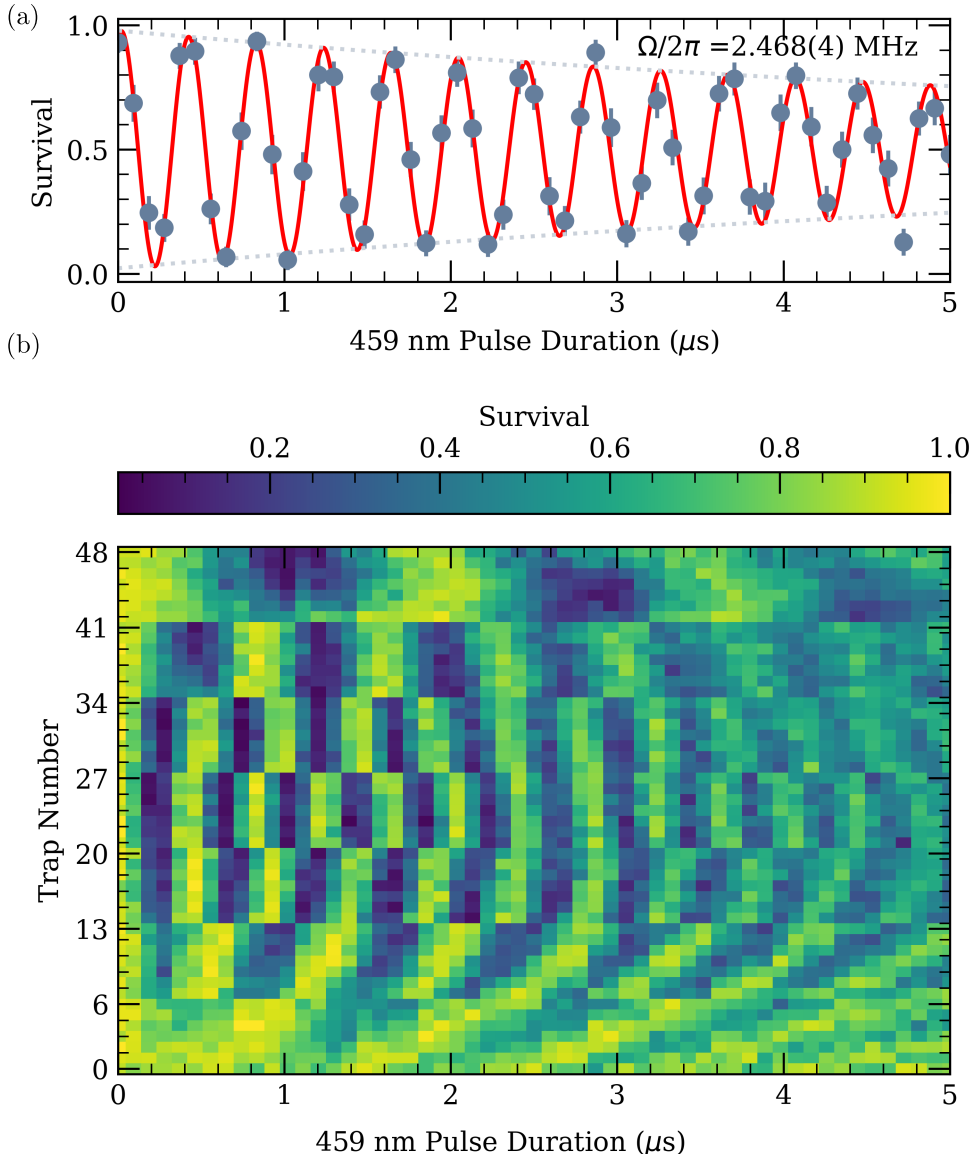


Figure 3.32: (a) Single trap Rabi oscillation for transition to the  $80S_{1/2}$  Rydberg state with a Rabi frequency,  $\Omega/2\pi = 2.468(4)$  MHz. The dotted lines are a decaying exponential fit to obtain a coherence decay time constant,  $T_{\text{decay}} = 8(1)$   $\mu\text{s}$ . (b) Colormap plot of the Rabi oscillations of the full 49-site array showing inhomogeneity in the Rabi frequency due to the spatially-non-uniform intensity distribution of the 1039 nm and 459 nm Rydberg laser beams.

$= 8(1)$   $\mu\text{s}$  as indicated with the dotted line shown in Fig. 3.32(a). The dotted line is a decaying exponential fit to the data.

To calibrate the Rydberg beam waists at the atoms we use a two-stage process. First, we measure the 459 nm beam waist using microwave (MW)

Ramsey spectroscopy on the clock state transition. We operate with resonant microwave pulses, but we shine the 459 nm light to induce a differential AC Stark shift on the clock state transition during the Ramsey interrogation time that causes MHz-scale oscillations. The Ramsey fringe oscillation frequency is then a direct measure of the magnitude of the AC Stark shift due to the 459 nm laser. A typical Ramsey fringe for a single trap obtained in this way is shown in Fig. 3.33(a) using 27.9 mW of 459 nm light. By performing this fit on every site of the array, we obtain a spatial map of the single site AC Stark shifts. We then fit the data with the equation for the radial intensity profile of a Gaussian beam waist,  $w(r) = w_0 \exp(\frac{-2r^2}{w(z)^2})$ , we obtain a value for the 459 nm laser waist,  $w_0 = 93(1) \mu\text{m}$ . Using this value for the 459 nm beam waist and the experimentally-measured Rydberg Rabi frequency and laser powers, we can infer the effective beam waist of the 1039 nm beam required to match what we measured to a theoretical calculation. This gives a 1039 nm effective beam waist of 47  $\mu\text{m}$ .

### 3.7.5 Rydberg Laser Noise Eating

To stabilise the amplitude of our Rydberg excitation pulses, we use a noise-eating (NE) AOM in each beam path. The PID servo feeding back to the NE AOMs is based on a design by Preuschoff *et al.* [236] which employs a RedPitaya microcontroller. A custom PCB design was created by the author with some added functionality relative to the original. The modification is an added multiplexer (MUX) at the output of the PID which allows the user to bypass the control loop entirely and provide an external control signal. This was done to eliminate the need to disconnect cables when switching between PID control of the noise eater acousto-optic modulator and manual control. The key feature of this PID control system is the ability to sample and hold the feedback signal. This is necessary, because typical Rydberg pulses are shorter than 1  $\mu\text{s}$  and therefore very challenging to stabilise because they

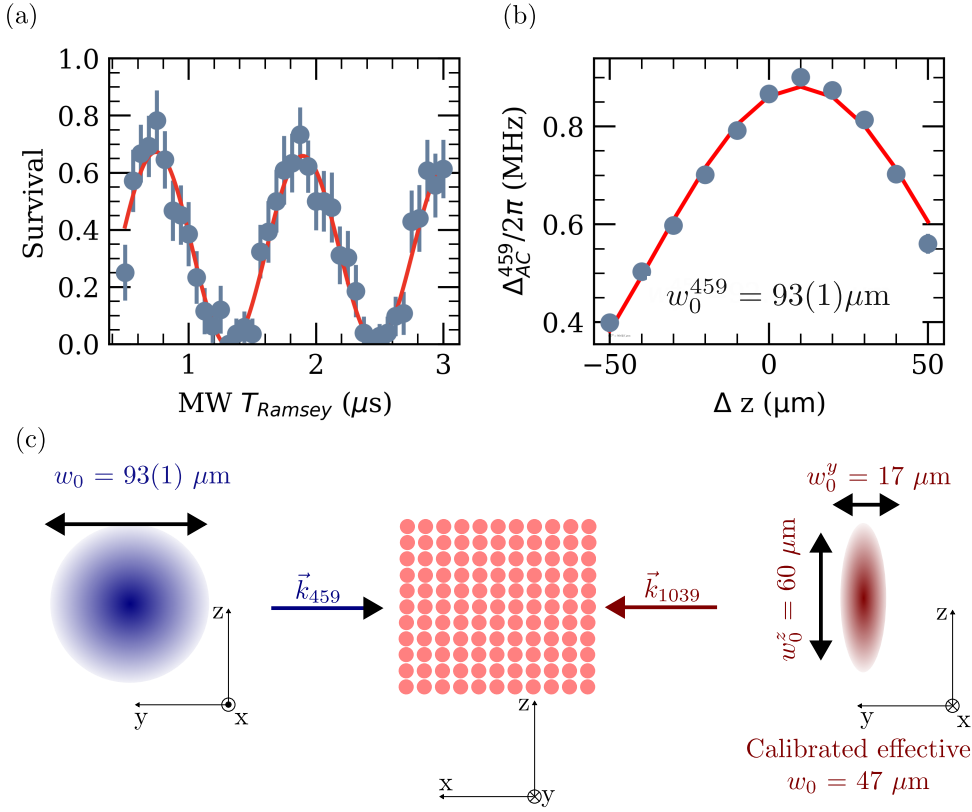


Figure 3.33: (a) Microwave (MW) Ramsey fringe measurement using 459 nm light to induce Ramsey fringe oscillations. The fringe oscillation frequency is a direct measurement of the AC Stark shift induced by the 459 nm beam. (b) Spatial distribution of the induced 459 nm AC Stark shifts across the array fitted with the equation for the Gaussian beam radial intensity distribution. This gives a value for the 459 nm Rydberg beam waist of  $93(1)\mu\text{m}$ . (c) Visual representation of the beam profiles of the two Rydberg beams and their waists. The 1039 nm  $x$  and  $y$  waists were measured with a beam profiler before the final optic and re-scaled based on the design magnification of the final lens. The calibrated effective waist is the waist required to match the measured experimental Rabi frequency to the simulated value when using the precisely-calibrated 459 nm waist size and laser powers.

would require PID bandwidths  $> 2$  MHz according to the Nyquist theorem. By using the sample and hold method, we apply a significantly longer "sampling" pulse on the order of tens of milliseconds which is used for intensity feedback. At the end of this sampling pulse, the final values of the proportional, integral and derivative gain of the control loop are saved in the digital memory of the microcontroller and held static at these values during the actual, short Rydberg pulse, applied a few milliseconds later. This method is unable to compensate for high-frequency intensity fluctuations that could happen during the hold stage, but it can achieve good long-term laser amplitude stability and minimise shot-to-shot variation in our Rydberg pulse areas. Initially, we attempted to place the noise-eating signal pick-off immediately after the NE AOM, but we found that there was no correlation in the noise measured by an out-of-loop photodiode placed before the chamber and the in-loop photodiode. This can be explained by the additional noise introduced along the optical beam path after the NE AOM by the switching AOMs, the periscope pointing instability, and polarisation intensity noise at the fibre output which need to be accounted for. To this end, we installed the pick off for the 459 nm system after the fibre output and used one of our home-built shutters to block the light from reaching the atoms during the sampling stage. Our home-built 3D-printed laser shutters were unable to withstand the power in the 1039 nm beam, so to test the system we chose to shine the 1039 nm light on the atoms during the atom loading stage of the experiment and switch it off before the optical pumping stage to avoid undesirable AC Stark shifts due to the high-intensity 1039 nm light. In this configuration, we were able to achieve significant suppression in the Rydberg laser pulse amplitude variation as shown in Fig. 3.34. The use of the Red-Pitaya noise eating system for amplitude stabilisation reduced the spread of observed pulse areas from 3% to less than 1% based on this 100-shot comparison. In the future, the same system can also be used to stabilise the amplitude of the 1064 nm and 800 nm trapping lasers, as well as the Raman

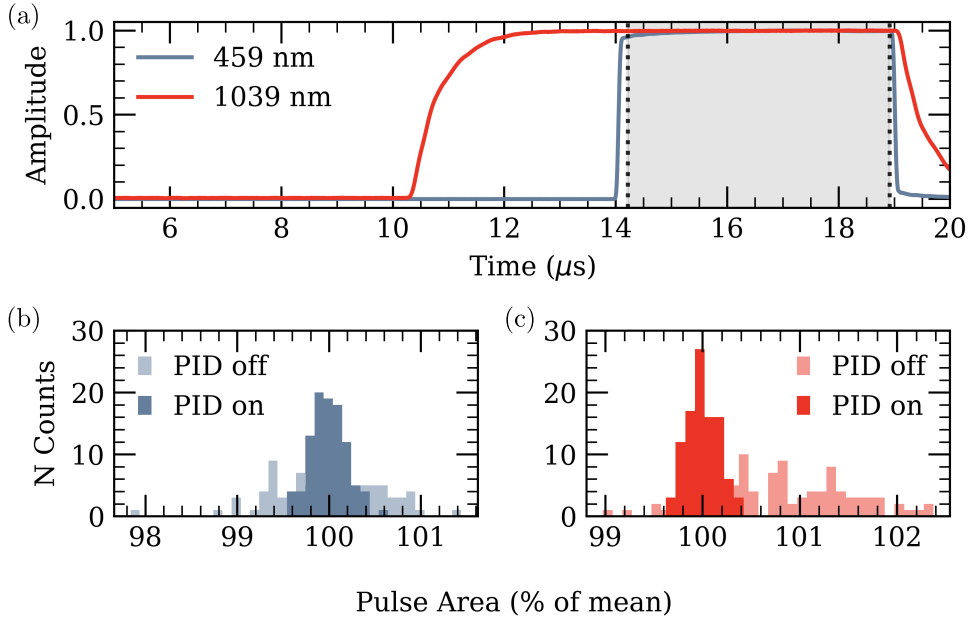


Figure 3.34: (a) Example Rydberg pulse logging for intensity stabilisation using a 5  $\mu\text{s}$  pulse of 459 nm light overlaid with an 8  $\mu\text{s}$  pulse of 1039 nm light. The gray-shaded region is used to calculate pulse area statistics across 100 shots with and without the noise eating PID. (b) and (c) Results showing improvement from the use of the RedPitaya noise eating system with the 459 nm and 1039 nm laser system respectively. The lighter colours represents the distribution of pulse areas without the noise eating PID and darker colours show the narrowing of the pulse area distribution due to the PID feedback. The spread of areas is reduced from 3% to less than 1% of the mean using this technique.

laser system.

### 3.8 Experimental Control System

Our experimental control system is based on the ARTIQ ecosystem by M-Labs [237]. The ecosystem consists of the modular Sinara hardware stacks which include a Kasli master module based on an Artix-7 FPGA, TTL input and output modules, Zotino 16-bit DAC analogue output cards and the Mirny and Urukul frequency synthesisers mentioned in the sections on microwave and Rydberg qubit operations. A key feature of the system is that

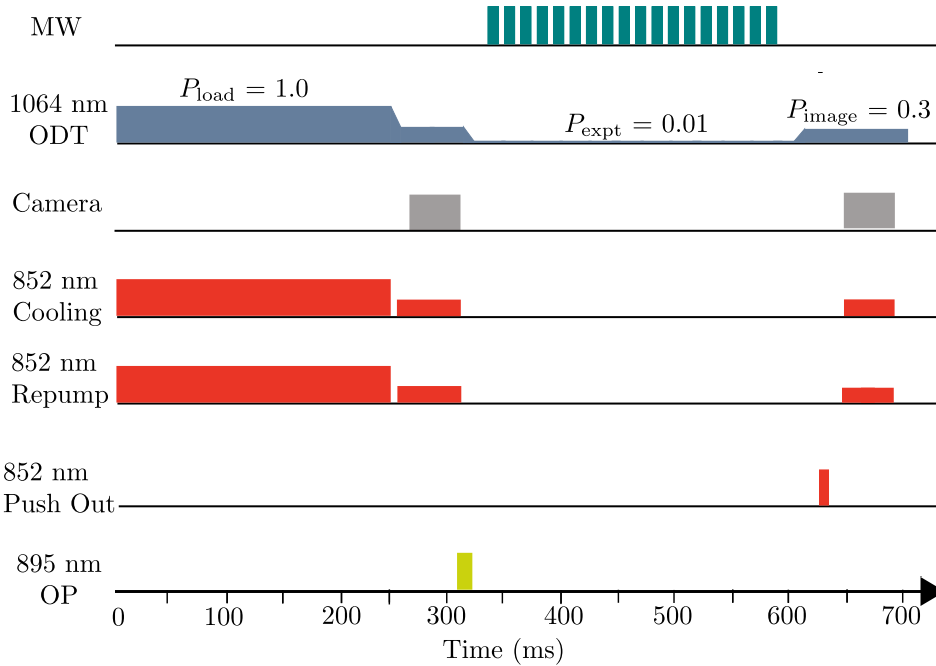


Figure 3.35: Typical experimental timing diagram showing the key stages in the experiment. In this instance a sequence of MW pulses has been shown as one example of the coherent manipulations of the qubits’ internal state. Alternative experiments using the Rydberg system have been shown in previous sections.

it offers deterministic real time control of the experiment with a timing resolution of 4 ns set by the base clock of the Kasli master module. At the time of writing, the Kasli master module was not referenced to the 10 MHz GPS reference used for the microwave master oscillator. The entire hardware stack is controlled using high-level Python-based scripts written in the ARTIQ open-source language developed by M-Labs. ARTIQ is used to update TTL logic levels, control microwave synthesiser output frequencies and phases, and output analogue voltages controlling AOMs all in the correct deterministic timing steps required to execute the various experimental sequences used in this work. A typical sequence is shown in Figure 3.35. In it, the ARTIQ control system sends TTL signals to switch the 852 nm and 895 nm light on and off as required, it outputs the analogue control voltages used to implement the 1064 nm ODT amplitude ramps and controls

the microwave (MW) pulse timing, phase and amplitude via an Urukul DDS directly interfaced with a Kasli crate.

The control system is equipped with a graphical user interface (GUI) accessible over the network from any lab PC, but for all but the most basic experiments we choose to operate it using Python scripts which allow the user to call a specific experimental sequence and update individual parameters as required using temporary parameter overwrites referred to as injections. We also use the ARTIQ user interface framework to operate and maintain a database of experimental parameters such as MOT shim coil voltages, AOM control voltages and frequencies and standard pulse durations for processes such as MOT loading, Rydberg pulse durations etc. In addition, we have integrated a live camera feed from the single atom imaging camera into the ARTIQ GUI for basic experimental monitoring. By looking at the number of atoms surviving the experimental sequence on each image and comparing to the expected behaviour we can spot obvious faults and errors in the experiment such as lasers unlocking. We operate a total of three Kasli crates: a single master crate and two satellite crates which currently communicate over the lab local area network when the instructions are not time-critical. For real-time synchronisation, we apply TTL trigger signals sent from the master crate to the two satellite crates. In principle the devices could communicate over a fast DRTIO<sup>55</sup> transfer system using a high speed duplex serial line connection in copper or via optical fibre. This method for networking Kasli crates was found to be unreliable so the choice was made to use TTL trigger signals instead at the cost of adding data transfer delays of up to several seconds at the start of each experiment. The reliability issues may be due to the fact that we are using the now obsolete ARTIQ version 6. Various other hardware such as the arbitrary waveform generator (AWG) used for 459 nm pulse shaping, the single atom imaging camera and the Teensy controller used to operate the moving tweezer beam are integrated

---

<sup>55</sup> Distributed Real Time Input/Output

into the ARTIQ control system. The integration is achieved using remote procedure calls (RPC) on the local area network within the network device support package (NDSP) infrastructure included in ARTIQ. This is also the mechanism used to achieve integration with the Machine-Learning Online Optimization Package (M-LOOP) package [238] used in the closed-loop optimisation of our adiabatic ramps discussed in Chapter 6. All experimental results in the form of single atom ROI pixel counts and the parameters used to obtain them are saved in HDF5 files at the end of each experiment and analysed using Python scripts.

## Chapter 4

# Microwave Single Qubit Gates

The aim of this chapter is to summarise the work done to characterise the coherence of our qubits and measure the global single qubit gate fidelities in our system using microwave operations. Section 4.1 covers the measurement of the reversible and irreversible dephasing times of our qubits, along with a discussion of the factors that limit these times in our current system. What follows is an outline of how composite BB1 pulses were implemented in order to reduce sensitivity to Rabi frequency inhomogeneities. The concept of Clifford Group randomised benchmarking (RB) is introduced in Section 4.4. In the final section of this chapter, RB is used to experimentally measure the average gate fidelity for global single qubit rotations and the state preparation and measurement (SPAM) errors in our set up.

## 4.1 Characterising Qubit Coherence with MWs

The starting point for characterising the quality of our qubits is measuring their coherence time, which, along with the average gate duration, sets a limit on the maximum circuit depth we could execute on our hardware platform. Therefore, this is one of the key metrics used to describe the performance of a quantum computer. In a more fundamental sense, the ability to maintain a coherent phase relation between the two basis states in our computational basis is a necessary step to recording truly quantum statistics as opposed to statistical mixtures of states which could be described classically [239].

The coherence time is limited by interactions with the environment, and while we cannot fully isolate our qubits from it, we can take steps to limit and understand these interactions. They can come in the form of environmental noise sources such as background magnetic and electric field noise, or they can be a result of noise in the trapping laser field or in the control fields used to manipulate the qubit degrees of freedom such as the phase noise of the master oscillator described in Section 3.6 [147]. Even if we could eliminate all of these sources of dephasing, we would still need to consider finite temperature effects which mean that the atoms we load into our traps can have a slightly different velocity distribution in each experimental iteration. This arises from the fact that the atomic velocity in the dipole traps is described by a statistical distribution very close to a Boltzmann distribution<sup>56</sup>, which has a finite spread at non-zero temperatures [203]. The combined result of all of these effects for a given quantum system can be quantified with a total transverse decay time,  $T_2$ , described in Section 2.3.4, which is a function of the reversible and irreversible dephasing times,  $T_2^*$  and  $T_2'$ . The purpose of this section is to describe how we measured these two parameters in our

---

<sup>56</sup> The Maxwell-Boltzmann distribution was originally defined for an ideal gas made up of many particles in thermal equilibrium, but in references [197, 203] it was experimentally demonstrated that this description also holds true for single atoms confined in harmonic trapping potentials.

experiment.

### MW Ramsey Fringes

Ramsey interferometry is the method that was used to measure the  $T_2^*$  reversible dephasing time constant of our qubits [240]. It is a ubiquitous method in the field of atomic clocks since they were first demonstrated by Essen and Parry in 1955 [241] which uses two  $\pi/2$  pulses separated by a fixed time interval  $T$ . By applying this sequence and scanning the driving field frequency offset,  $\delta$ , one can measure fringes in the atomic populations which oscillate as  $P \propto \cos^2(\delta T/2)$  [117]. Since the central fringe width in terms of a full-width half maximum can be shown to scale as  $\Delta f = 1/2T$ , this technique makes it possible to measure the resonant frequency of an atomic clock transition with very high precision if the scan is taken at long interrogation times<sup>57</sup>. Ramsey fringes rely on maintaining coherence between the clock states, so by modifying the sequence it can be used for measuring the qubit coherence times instead of the resonance frequency. This is done by adding an intentional fixed detuning,  $\delta$ , to the source oscillator and scanning the duration of the interrogation time,  $T$ . The key idea is summarised in Fig. 4.1.

The method amounts to preparing the qubit in an equal superposition of the  $|0\rangle$  and  $|1\rangle$  states along the equator of the Bloch sphere where the atom is maximally sensitive to dephasing effects. This is achieved by applying a MW pulse with an effective area corresponding to a  $\pi/2$  rotation around the x-axis of the Bloch sphere (a  $\pi/2$  pulse). In order to observe Ramsey oscillations we detune the MW pulse frequency by  $\delta/2\pi = 0.4$  kHz from the experimentally measured clock state resonance and scan the Ramsey interrogation time,  $T_{\text{Ramsey}}$ . We then apply a final  $\pi/2$  pulse followed by a pulse from our push

<sup>57</sup> The process usually entails starting with a short interrogation time and then gradually increasing it so one can keep track of the central fringe which corresponds to the true resonance. See Section 5.5 of reference [138] for a detailed explanation.

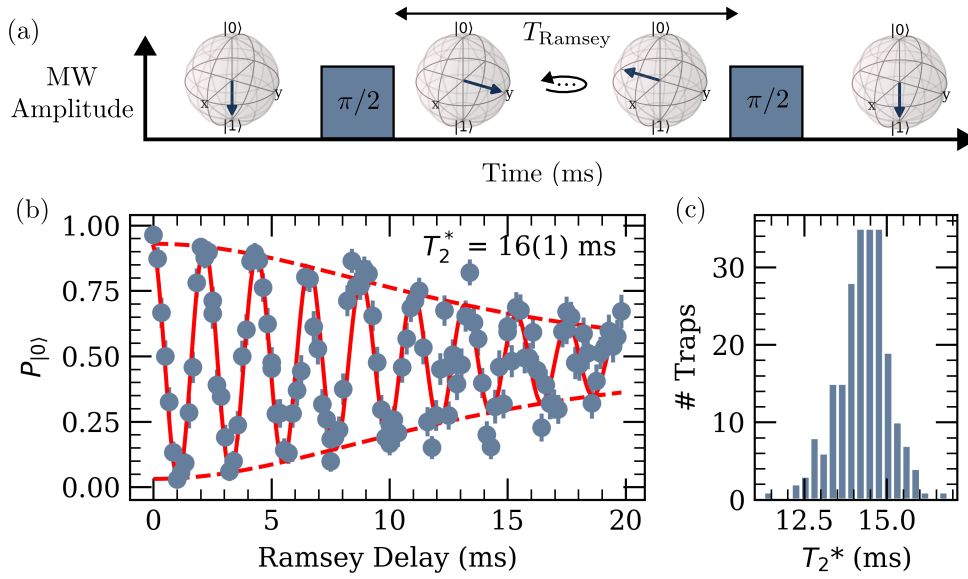


Figure 4.1: (a) Schematic representation of a Ramsey sequence using Bloch sphere visualisation. A  $\pi/2$  pulse puts the Bloch vector along the equator where it precesses around the z-axis with a frequency equal to an intentional MW detuning of a few kHz. This detuning sets the frequency of the oscillation in (b). By scanning the Ramsey interrogation time,  $T_{\text{Ramsey}}$ , before applying a second  $\pi/2$  pulse a Ramsey fringe can be obtained. In (b) a Ramsey fringe obtained in this way for a single trap in a 225 site array is shown. A fit was performed on the data using equation 4.1. (c) Histogram of the  $T_2^*$  times obtained for the full 225 site array centered around a mean value of 14 ms with a standard deviation of 0.8 ms.

out beam to heat atoms in the  $|1\rangle$  state out of the traps before taking a final image. Following the analysis in Kuhr *et al.* [147], which takes into account the finite atomic velocity inside the traps, we fit the resulting oscillations with

$$P_{|0\rangle} = B + \alpha(t, T_2^*) \cos[\delta' t + \kappa(t, T_2^*) + \phi], \quad (4.1)$$

where the term  $\delta'$  is the effective detuning from the clock state resonance which includes the intentional detuning plus the effect of any external factors. The decay parameter,  $\alpha$ , and the phase shift,  $\kappa$ , are given by

$$\alpha(t, T_2^*) = \left[ 1 + 0.95 \frac{t^2}{T_2^{*2}} \right]^{-3/2}, \quad (4.2a)$$

$$\kappa(t, T_2^*) = -3 \times \arctan\left( 0.97 \frac{t}{T_2^*} \right). \quad (4.2b)$$

The constant factors of 0.95 and 0.97 in the definitions of these parameters arise from the averaging over the distribution of light shifts experienced by an atom with a temperature described by a Boltzmann distribution inside a dipole trapping potential [147]. In fact, the phase shift,  $\kappa$ , results from the fact that hotter atoms in the tails of these thermal distributions dephase faster than cold atoms.

The resulting fit using equation (4.1) is shown in Fig. 4.1(b) for a single trap in a 225 site array with a reversible dephasing time,  $T_2^* = 16(1)$  ms. The distribution of  $T_2^*$  times obtained in this way for the full 225 site array is shown in Fig. 4.1(c) with a mean value of 14 ms and a standard deviation of 0.8 ms. It should be noted that longer array-averaged  $T_2^*$  times of 21.1(4) ms have been observed in our experiment using the same sequence and array size. The data shown here was chosen because it is most representative of the state of the system during the randomised benchmarking work discussed

later in this chapter. The reasons for this variability in the recorded  $T_2^*$  times will be discussed later in this section.

The finite temperature of the atoms inside our 1064 nm traps plays a major role in setting a limit on the reversible dephasing time of our qubits. It results in a different effective differential light shift due to the 1064 nm trapping light for hot and cold atoms<sup>58</sup>. Therefore the reversible dephasing time is inversely proportional to the atom temperature as [147]

$$T_2^* = 0.97 \frac{2\hbar}{\eta k_B T}, \quad (4.3)$$

where

$$\eta = \frac{\omega_{\text{hfs}}}{\Delta_{\text{eff}}} = 1.45 \times 10^{-4} \quad (4.4)$$

is a scaling factor given by the ratio of the hyperfine splitting of the caesium ground state,  $\omega_{\text{hfs}}$ , divided by an effective detuning of the trapping laser from the manifold of  $m_F$  states,  $\Delta_{\text{eff}}$ , which takes weighted contributions from the D1 and D2 lines into account [242]. We can infer the average atomic temperature of the atoms in our array from the fitted  $T_2^*$  values. Using this method, we estimate an average atomic temperature of 7  $\mu\text{K}$  based on a 14 ms Ramsey fringe decay time. This result suggests that our atoms are hotter during the Ramsey fringe than the  $\sim 1 \mu\text{K}$  temperature inferred from the release and recapture measurement in Section 29. A temperature of 1  $\mu\text{K}$  would correspond to a  $T_2^*$  time of  $\sim 90$  ms in the absence of other decoherence mechanisms<sup>59</sup>. We investigated this by repeating the release and recapture measurement, but this time we also applied a D1 optical pumping pulse before releasing the atoms to quantify the heating effect due to the

<sup>58</sup> What is meant by hot and cold here is the mean value of a Boltzmann velocity distribution associated with a given atom temperature.

<sup>59</sup> Convention dictates that dephasing is the term used to refer to information loss due to reversible effects and decoherence is used in the case of irreversible processes [243].

incoherent state preparation process used to prepare the qubits in the  $|1\rangle$  state at the start of the Ramsey measurement. The resulting temperature fit was  $\sim 6 \mu\text{K}$  which would correspond to a reversible dephasing time of  $\sim 17 \text{ ms}$ , much closer to the experimentally observed results. To minimise the heating rate during optical pumping, we would have to engineer a state preparation process that requires fewer photon scattering events. This could be achieved using stretched state optical pumping on the D2 line which was observed to occur on a faster timescale, followed by a series of coherent Raman or MW pulses to transfer population to the clock states as implemented in [78]. Alternatively, Raman sideband cooling could be implemented in our experiment to cool the atoms down to their motional ground state inside the dipole traps before D1 optical pumping is applied [244].

While recording the initial Ramsey fringe data, we observed a long term drift effect which resulted in discontinuities in our measurements as shown in Fig. 4.2(a). Our investigations led us to check the effect of the ambient temperature stability on the magnetic field produced by the external shim coils which are used to set the quantisation axis in our experiment. To test this, we repeated a single point from a Ramsey sequence at a fixed interrogation time of 2 ms 200 times while monitoring the optical pumping bias coil with a temperature sensor placed in close proximity to it. Each experimental run takes at least 50 s to obtain 25 data points required for meaningful error bars, but the temperature sensor logs every second. In order to obtain a Pearson correlation coefficient between  $T_{\text{Coil}}$  and  $P_{|0\rangle}$ , we interpolated between experimental data points to artificially match the number of observations. With this method, we obtain a correlation coefficient of -0.46 showing that there is some correlation between the two variables. The measurement is imperfect because of the interpolation that was performed, and because there is likely an offset error of up  $\pm 1$  minute in the matching of the two data sets. However, this hypothesis is also supported by the fact that the best array-average coherence time of 21.1(4) ms recorded in our experiment was achieved imme-

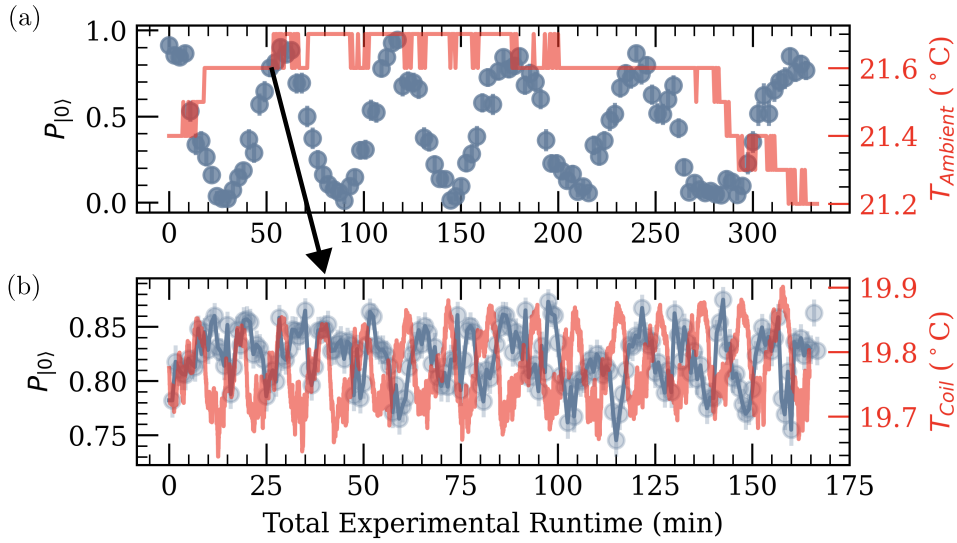


Figure 4.2: (a) A single trap Ramsey fringe measurement, where the x axis has been converted to units of total experimental run time. Phase discontinuities around 10 minutes and 300 minutes appear to be correlated to drifts in the lab ambient temperature. (b) Test measurement using a fixed Ramsey interrogation time of 2 ms repeated 200 times. The black arrow indicates the point in the Ramsey fringe that corresponds to 2 ms interrogation time. Each data point takes 50 s to record. The temperature sensor was placed in close proximity to the optical pumping bias coil for this measurement. By interpolating the experimental data to match the 1 s sampling rate of the temperature sensor, we obtain a Pearson correlation coefficient of -0.46 between  $T_{Coil}$  and  $P_{|0\rangle}$ .

diately after improving the air conditioning system performance by tuning the PID control loop to achieve a  $\pm 0.1$  °C temperature stability throughout the entire run. Unfortunately, this level of temperature stability cannot be maintained consistently with varying outside weather conditions and this has likely affected some of our randomised benchmarking runs as discussed in Section 4.5.

The hypothesised physical mechanism by which the clock state resonance responds to the temperature change is related to the quadratic differential Zeeman shift on the clock state. Firstly, the thermal expansion and contraction of the 3D MOT shim coil formers may result in changes in the magnetic field orientation effectively changing the OP bias field amplitude along the

x axis. A likely culprit are the ABS plastic 3D-printed corners of the coil formers which have a significantly higher coefficient of thermal expansion compared to the aluminium bars they hold together<sup>60</sup>. The coil driver is operated in constant current mode, which allows it to compensate for changes in the resistivity of the coil wires due to temperature fluctuations. However, the sense resistor used to implement this servo has some temperature sensitivity which could affect the current stability with changing lab ambient temperatures. Upgrading this resistor to one with a lower temperature coefficient for future experiments will likely result in improved performance. Based on our coil driver calibration, a 0.5 °C temperature change will result in an 8 mG drift of the optical pumping bias field. By taking the derivative of equation (2.9) with respect to  $B$  and substituting this value, we can estimate that the resulting change in the second order differential Zeeman shift of the clock state transition frequency amounts to 20 Hz on a 15 kHz FWHM resonance linewidth. The effect of such drifts on long experiments could be reduced by implementing a magnetic field servo system using the atomic signal as implemented in [138] for trapped  $^{43}\text{Ca}^+$  ions. The idea is to use a magnetically sensitive MW transition, which in our case would be the stretched state transition. After recording a resonance with a fixed  $\pi$  time, one detunes the microwave source by  $\pm \text{FWHM}/2$  of the transition linewidth and monitors the population transfer. Any deviation from the perfect 0.5 on either side is an indication that there has been a drift and the magnetic field which needs to be adjusted to balance it out. Alternatively, one could use a fluxgate magnetometer and feedback coils outside the vacuum chamber as was implemented in [70] for active field stabilisation. None of these two approaches have been implemented in our experiment yet, but they could be used to counteract the temperature drifts.

<sup>60</sup> The linear thermal expansion coefficient of ABS thermoplastic is 72-108  $\mu\text{m}/(\text{m } ^\circ\text{C})$ . The equivalent value for aluminium is 21 to 24  $\mu\text{m}/(\text{m } ^\circ\text{C})$  [245].

## Spin Echo Measurements

One positive aspect of the finite atom temperature effects on the qubit coherence is that they are reversible. This means that the temperature-induced dephasing can be undone through the use of sequences of dynamical decoupling pulses [246]. The original work by Hahn introduced the most basic decoupling technique in the form of the spin echo which was used to extend the coherence time in nuclear magnetic resonance experiments [247]. Also known as the Hahn echo, the technique introduces a  $\pi$ -area pulse in between the two  $\pi/2$  pulses used in Ramsey measurements as shown in Fig. 4.3(a). The effect of this  $\pi$  pulse is to re-focus the qubit dephasing by flipping the ensemble of state vectors on the Bloch sphere such that the faster-precessing vectors end up "behind" the slower precessing ones and there is a single point in time after the  $\pi$  pulse, where the second  $\pi/2$  pulse can be used to perfectly undo the effects of reversible dephasing. The decoherence due to time-asymmetric noise sources cannot be undone with the spin echo technique.

We used the spin echo technique in our experiment to measure the irreversible coherence time of our system,  $T_2'$ , and we implemented it in two different ways. The first method uses a varying phase on the second  $\pi/2$  microwave pulse to induce an oscillation in the observed atomic populations in the  $P_{|0\rangle}$  state as shown in Fig. 4.3(b) for 6 different Ramsey interrogation times,  $T_{\text{Ramsey}}$ <sup>61</sup>. This measurement was performed on an array of 32 sites because it was interleaved with other measurements being taken at the time which required this atom configuration. An alternative spin echo measurement was performed on the full 225 site array by introducing a time imbalance,  $\delta T$ , to the second part of the Ramsey interrogation sequence to produce revivals as shown in Fig. 4.3(c) for a single trap. The time imbalance,  $\delta T$ , is scanned

<sup>61</sup> If we were to apply a perfectly symmetric Hahn echo sequence we would simply observe a decay in the  $P_{|0\rangle}$  population instead. We introduce the imbalance in order to see oscillations in the atomic populations which is the most clear-cut evidence of coherence in our system.

between -10 ms and +10 ms for each interrogation time,  $T_{\text{Ramsey}}$ , in order to observe the revival fringes. The dashed red lines are fits using [147]

$$P_{|0\rangle} = B - \alpha(t - T_{\text{Ramsey}}, T_2^*) A \cos[\delta'(t - T_{\text{Ramsey}}) + \kappa(t - T_{\text{Ramsey}}, T_2^*) + \phi], \quad (4.5)$$

where the symbols have the same meanings as in equation 4.1. For both spin echo measurement methods, we extract the fringe visibility at each  $T_{\text{Ramsey}}$  and fit the resulting curve with

$$V(T_{\text{Ramsey}}) = C_0 \exp\left[-\frac{1}{2}(T_{\text{Ramsey}}/2)^2 \sigma_{\text{exp}}^2\right]. \quad (4.6)$$

An example fit is shown in Fig. 4.3(d) and used to obtain a value for the time-independent detuning fluctuation,  $\sigma_{\text{exp}}$ . The irreversible dephasing time is then given by  $T_2' = \sqrt{2}/\sigma_{\text{exp}}$  as derived in [147]. The array averaged results from the two methods are an irreversible decoherence time,  $T_2'$ , of 192(25) ms and 145(17) ms using methods one and two respectively. The quoted errors are the standard deviations of the distribution of  $T_2'$  times across the two arrays. The histogram for the 225 site array is shown in Fig. 4.3(e). The two measurements are in good agreement considering the fact that they are separated in time by three months and the installation of an additional laser on the main experimental table which has likely affected the background magnetic field noise levels. These results are very similar to the values obtained using ensembles of caesium atoms in 1064 nm traps from [147]. Our recorded  $T_2'$  times are lower than the state of the art in alkali atoms of 303(13) ms obtained with  $^{87}\text{Rb}$  in reference [223], but this experiment used a more complex dynamical decoupling sequence (XY16-256) that required 256  $\pi$ -pulses using a Raman laser [248].

To understand the limitations on our measured  $T_2'$  times, we can consider a range of irreversible decoherence mechanisms as outlined in [147]. First, we consider the intensity noise of our trapping laser. Any such noise would

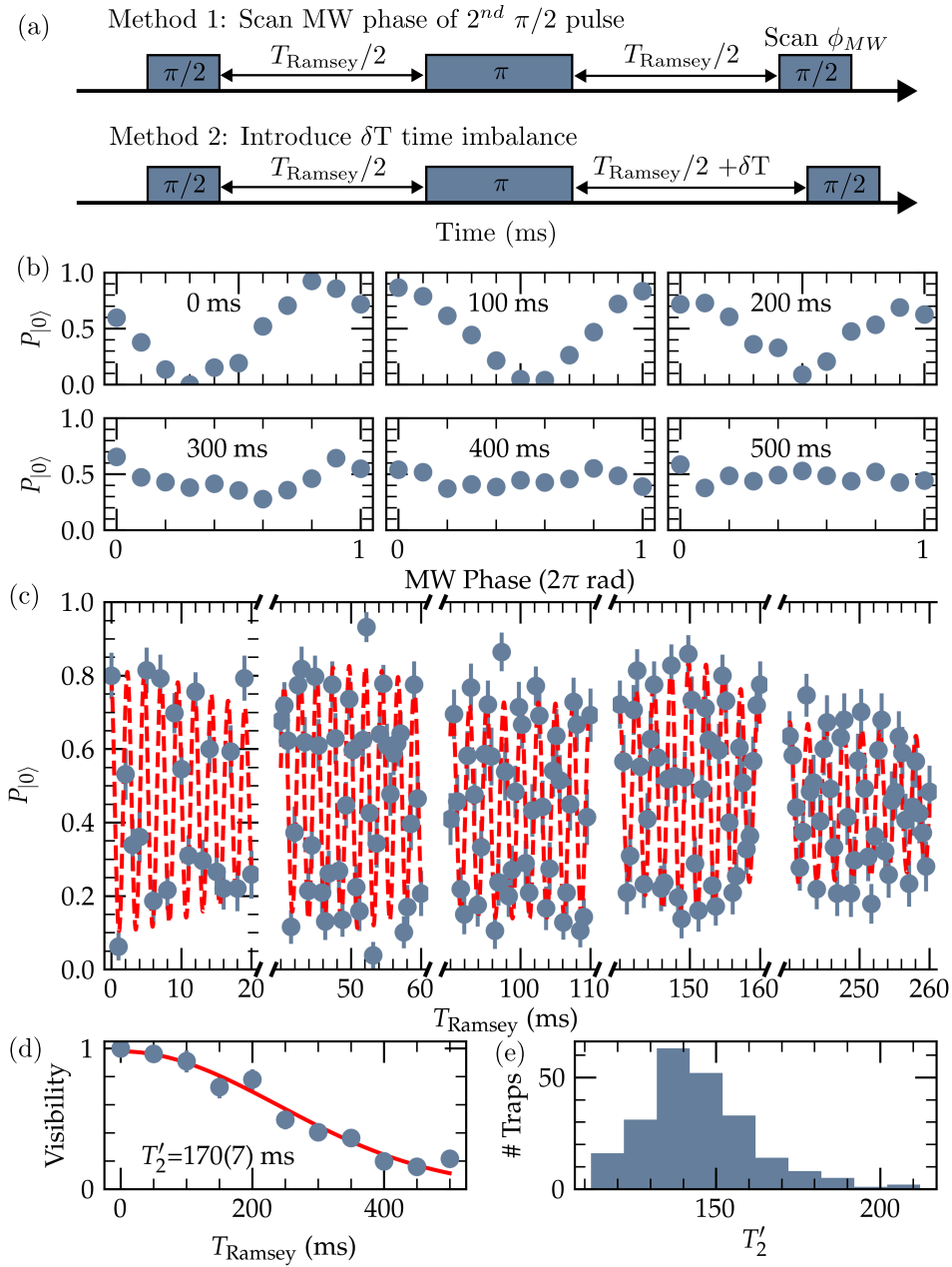


Figure 4.3: (a) Schematic representation of the two different methods used to measure the irreversible decoherence time,  $T'_2$ . (b) Single trap results from method 1 measurement using MW phase scan for second  $\pi/2$  pulse on a 32 site array. (c) Spin echo revival measurement (method 2) for a single trap on a 225-site array. Showing best trap with  $T'_2 = 212(21)$  ms. (d) Example fringe visibility fit for measurements shown in (b) fitted with equation (4.6). (e) Distribution of  $T'_2$  measurements on 225 site array with an average of 145 ms and a standard deviation of 17 ms.

result in a detuning instability due to the differential AC Stark shift induced on the clock state transitions by the 1064 nm laser. During MW operations we use a trap depth of 30  $\mu\text{K}$  which results in a differential shift of 91 Hz. We used a photodiode to record the 1064 nm laser intensity over 17.5 s with a sampling rate of 10,000 samples/s and calculated the Allan variance [249],  $\sigma_A^2$ , at a time  $\tau = 125 \text{ ms}$ <sup>62</sup> using

$$\sigma_A^2(\tau) = \frac{1}{m} \sum_{k=1}^m \frac{(\bar{x}_{\tau,k+1} - \bar{x}_{\tau,k})^2}{2}, \quad (4.7)$$

where  $\bar{x}_{\tau,k}$  is the average photodiode voltage of the  $k$ -th time interval of length  $\tau$  normalised to the average photodiode voltage of the entire data set. We arrive at a value of 0.28% for  $\sigma_A$  which is the magnitude of the relative intensity fluctuations of our 1064 nm trapping system on the timescales relevant to the spin echo measurement. We then convert this into a detuning error using  $\sigma(\tau) = \sqrt{2}\delta_0\sigma_A(\tau)$ , where the  $\sqrt{2}$  factor accounts for the fact that we are calculating the difference of the standard deviations of two detunings because this is a differential light shift. The resulting detuning fluctuation is 0.36 Hz which accounts for a significant portion of the total detuning error,  $\sigma_{\text{exp}}$ , of 1.6(2) Hz that corresponds to our 225-site average  $T'_2$  time of 145(17) ms. This error could be reduced by installing an intensity stabilisation system for our 1064 nm laser. The RedPitaya system designed for Rydberg laser noise eating is capable of doing this, but at the time no suitable mounting location near the main experimental chamber was available to install a feedback photodiode.

A related source of decoherence in our system is the 1064 nm laser pointing instability which would manifest as a larger effective trapping laser intensity fluctuation at the atoms. This was not measured in our set up on the millisecond timescales relevant to this experiment, but we have observed

<sup>62</sup> We chose 125 ms because it is the  $T_{\text{Ramsey}}/2$  time of the spin echo measurement with the longest interrogation time we recorded.

some day-to-day variation in the atomic positions identified on our fluorescence images. The array-averaged drift in the atomic position was 1.5 pixels based on two sets of 200 fluorescence images recorded 12 hours apart. This corresponds to approximately one beam waist of our 1064 nm traps when considering the camera magnification of  $\sim 1 \mu\text{m}$  per pixel. This variation is too large to be physical and is likely exaggerated by the fact that atom emission patterns are random and we allocate 10 pixels per atom. Therefore the location of the centre of mass of the atomic fluorescence signal could shift from image to image without the trap physically moving. In any case, we would need to consider a different method to capture the pointing instability on a more meaningful timescale because each fluorescence image in our experiment takes 40 ms. The simplest method would be to place a camera immediately before the chamber and use it to capture multiple images of the dipole trap Gaussian spots location with a fast  $< 1$  ms exposure time. This data was not available at the time of writing. Alternatively, a segmented photodiode could be used to independently measure both intensity fluctuations and pointing instability.

Atom heating inside the 1064 nm traps will also contribute to our qubit decoherence because the atoms in later stages of the Ramsey interrogation period are hotter than in the earlier stages giving rise to a time-asymmetric temperature-induced dephasing. In Section 29 we inferred a heating rate of  $0.19(7) \mu\text{K/s}$  from a trap lifetime measurement taken at the trap depth used in the spin echo experiments. We calculate the resulting detuning fluctuation error,  $\sigma_{\text{heat}}^{(3)}$ , using [147]

$$\sigma_{\text{heat}}^{(3)} = \frac{\eta k_B}{\hbar} \sqrt{\frac{3}{2} \dot{E} T_2' T}, \quad (4.8)$$

where the superscript represents the fact that we are considering a three-dimensional Gaussian momentum distribution when evaluating the atom energy,  $\dot{E}$  is the heating rate and  $\eta$  is the scaling factor introduced in equation

(4.3) which is specific to caesium at the 1064 nm trapping light. The resulting heating rate is  $\sigma_{\text{heat}}^{(3)} = 1.6$  Hz which alone would be enough to explain the observed decoherence rate in our spin echo measurements. Reference [206] showed that the heating rate has an exponential dependence on the trapping laser intensity noise and a linear dependence on the pointing instability. By reducing these noise sources, the heating effects on the atoms inside the traps will also be suppressed. Similarly, reference [197] found that noise present in the trapping laser signal that is near resonant with the dipole trap axial and radial frequencies will excite the motional modes of the atoms inside the traps. In our case the trapping frequencies at the ramped down trap amplitudes used during the microwave experiments are a few kHz. The most likely sources of noise at this frequency would be mechanical vibrations of the periscope through which the 1064 nm passes to reach the atoms.

An additional source of thermal decoherence due to the trapping light is photon recoil from off-resonant scattering. Using the Rayleigh scattering rate calculated in reference [147] for caesium in a 1 mK trap and scaling it down to our trapping depth of 30  $\mu\text{K}$ , we obtain a rate,  $\Gamma_s = 0.3 \text{ s}^{-1}$ . We can then use

$$\sigma_{\text{ph}}\left(\frac{T'_2}{2}\right) = \eta k \sqrt{\frac{3k_B T \Gamma_s T'_2}{m} \frac{T'_2}{2}} \exp\left(-\frac{\Gamma_s T'_2}{2} \frac{T'_2}{2}\right) \quad (4.9)$$

to calculate a detuning error due to 1064 nm photon scattering,  $\sigma_{\text{ph}}$ , of 0.73 Hz based on a starting atom temperature of 7  $\mu\text{K}$  as discussed in Section 5.6. As shown in [147], the rate of spin relaxation due to Raman scattering from the 1064 nm laser is sufficiently slow to be neglected on the timescales considered in our experiment. The Raman scattering rate is  $\Gamma_{\text{Raman}} = 0.12 \text{ s}^{-1}$  for a 1 mK deep trap which corresponds to a spontaneous decay time,  $T_1 = 1/\Gamma_{\text{Raman}} = 8.6$  s. This scales linearly with the trap depth and we operate with traps which are more than 33 times shallower which further reduces the likelihood of any Raman scattering events during the spin

echo measurements.

Next we consider the contribution from the differential quadratic Zeeman shift on the clock states due to the applied bias magnetic field. Any noise or drift present in this field will affect the qubit coherence. For the 6.0 G bias control used in our experiment, the differential quadratic Zeeman clock state shift calculated with equation (2.9) amounts to 15.38 kHz. A noise measurement of the bias field was performed before recording the spin echo measurements using a 3-axis HMC5883L magnetoresistive magnetometer with a bandwidth of 160 Hz and a 12-Bit AAC with a 2 mG resolution. The sensor was placed on top of the vacuum chamber and recorded the stability of the optical pumping bias field over the course of two minutes in continuous operation. Ideally, we would have monitored the bias field live during the experiment, but we did not have access to a magnetometer with a sufficient bandwidth to sample the fields on a sub 1 ms timescale required to do so. The recorded RMS noise level outside the chamber was of the order of the sensor resolution with peak values of 3 mG which would correspond to time-independent detuning fluctuations,  $\sigma_{\text{exp}}$ , of 15.5 Hz. This value is not consistent with the recorded average  $T_2'$  time of 145(17) ms which corresponds to a total combined  $\sigma_{\text{exp}}$  of 1.6(2) Hz. We conclude that the device used to measure the magnetic field noise did not have the resolution and bandwidth to accurately capture the magnetic field noise in our experiment. A fluxgate magnetometer such as the Bartington Mag710 would have been more suitable for the task with its 1 nG resolution and 1 kHz bandwidth, but the decision was made not to purchase one specifically for this measurement. Furthermore, the measured magnetic field noise includes contributions from the 50 Hz mains line which we have reduced in our experiment by virtue of an AC mains trigger which starts the microwave pulse sequence on the falling edge of the mains cycle waveform. This eliminates 50 Hz noise for the first 10 ms of the experiment and ensures that mains noise is sampled in a deterministic fashion for the remaining duration of the experiment.

Finally, short term shot-to-shot fluctuations of the microwave pulse power or the pulse duration would also manifest as reduced spin echo fringe coherence in our experiment. While we did observe significant 3% site-to-site variation in the microwave Rabi frequency as shown in Fig. 3.26, we have no indication to believe that there is significant shot-to-shot variation in the pulse area because we can record high-contrast Rabi oscillations captured over hour-long experimental runtime periods as shown in the same figure. In terms of pulse timing, the DDS that is triggered to apply the pulses has a 1 ns temporal resolution for pulses with a typical duration of 50  $\mu$ s for a  $\pi$  pulse. In principle, a measurement could be taken to verify this using a high sample rate oscilloscope which could be used to capture a large number of deterministically-triggered MW pulses and calculate their pulse area and timing errors (jitter).

In summary, the most likely limiting factors on our  $T'_2$  time are the 1064 nm laser intensity noise and the in-trap heating rate resulting from this intensity noise. Further suspected sources of decoherence with a significant impact on our measured  $T'_2$  times, which have not been quantified with sufficient accuracy at the time of writing are the 1064 nm laser pointing instability, along with the magnetic field noise. To improve and further understand the decoherence mechanisms in our system, these sources should be investigated further.

## 4.2 BB1 Composite Pulses

After calibrating the coherence times of our qubits, we intended to proceed with randomised benchmarking. However, the microwave Rabi frequency variation across the array discussed in Section 3.6 made it difficult to achieve the level of calibration required for state-of-the-art single qubit gate performance. We identified the BB1 composite pulse sequence as a relatively

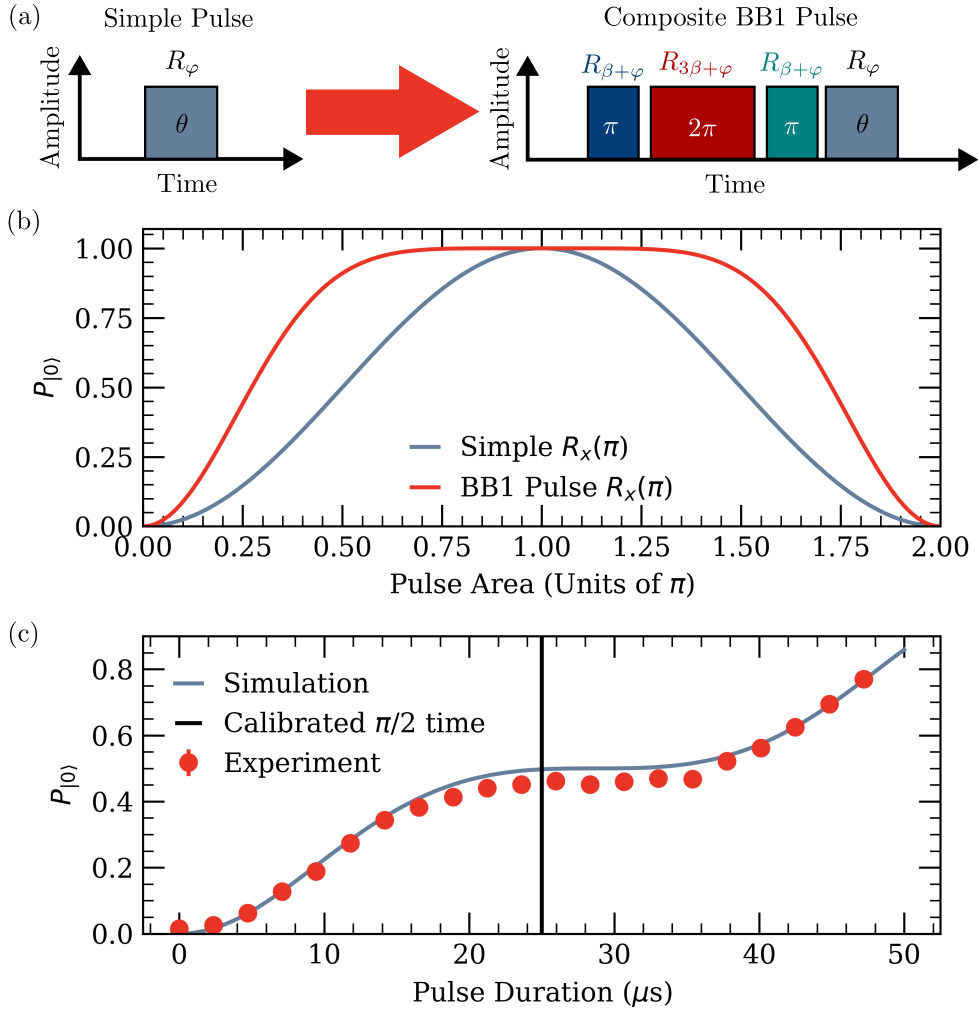


Figure 4.4: (a) Schematic representation of BB1 composite pulse method. A simple rectangular pulse of area  $\theta$  implementing a rotation around an axis  $\varphi$  on the Bloch sphere is converted into a series of four pulses. The parameter  $\beta$  is defined in equation 4.10. (b) Simulation demonstrating the significantly reduced sensitivity to pulse area errors of the equivalent BB1 pulse relative to a simple  $R_x(\pi)$ . (c) Experimental demonstration of an  $R_x(\pi/2)$  BB1 pulse showing reduced sensitivity to pulse area errors around the experimentally calibrated  $\pi/2$  time as intended. The red points are array-averaged values from a 225 site array. The error bars are smaller than the data points.

simple means of addressing this issue in order to achieve truly scalable operation on our platform. The BB1 sequence was first introduced by Wimperis *et al.* in the field of nuclear magnetic resonance imaging [250] and can be implemented as shown in Fig. 4.4(a). The notation  $R_\varphi(\theta)$  represents a qubit rotation of area  $\theta$  around an axis  $\varphi$  on the Bloch sphere. When applying this composite pulse sequence, a single pulse becomes a series of four pulses. The first three pulses always have the same fixed pulse area, but the axis around which they rotate the qubit on the Bloch sphere is a function of the target pulse parameters. The final pulse is the intended simple pulse we want to implement. The parameter  $\beta$  defined as

$$\beta = \cos^{-1}\left(\frac{\theta}{4\pi}\right). \quad (4.10)$$

is used to define the axis of rotation of the first three pulses in the sequence. The first three pulses act as a passband filter in amplitude space around a desired pulse area as shown in Fig. 4.4(b). In this simulation we compare the sensitivity to pulse area errors of a simple  $R_x(\pi)$  pulse and the equivalent BB1 composite pulse. In the simulation we are varying the area of all the BB1 pulses and modelling it as a constant percentage pulse area. The plateau around the target pulse area of  $\pi$  demonstrates the bandpass effect of this composite pulse sequence. It is also important to note that a specific BB1 pulse needs to be designed for each qubit gate. In Fig. 4.4(c) we show an experimental test of an  $R_x(\pi/2)$  pulse which now has a plateau around the calibrated  $\pi/2$  time as intended, in good agreement with a simulation using the experimental parameters. The deviation from perfect 50 % transfer is due to averaging across a large array and the finite trap lifetime. Changing the axis of rotation on the Bloch sphere is physically realised by changing the phase of the microwave source in our experiment. In general, the specific phases used for a given BB1 pulse will depend both on the target pulse area by virtue of the parameter  $\beta$ , but also on the intended pulse's axis of rotation.

It should be noted that the BB1 pulse sequence does not reduce the sensitivity of our qubits to errors in detuning, nor does it implement any spectral filtering in frequency space. The latter point could be addressed by changing the amplitude profile of our pulses from a simple rectangular profile into a Blackman-Harris profile [251] which would suppress the high-frequency components of a sharp-edged basic pulse. This was considered non-critical for our experiment because our trapping frequencies are of the order of kHz, so any high frequency components of our rectangular microwave pulses are unlikely to excite the motional modes of our atoms in the traps. In terms of reducing sensitivity to detuning errors, reference [252] has shown that using adiabatic rapid passage (ARP) microwave pulses can yield significant improvements compared to simple rectangular  $\pi$  pulses. The idea was first introduced in the field of nuclear magnetic resonance in reference [149] and requires implementing a shaped amplitude and frequency profile for the pulses which can make the population transfer in the system insensitive to detuning errors over a frequency range up to one half of the chirp rate. The limitations of our AD9910 DDS chip mean that we cannot simultaneously implement frequency, phase and amplitude control in RAM mode in order to test BB1 composite pulses with an ARP frequency and amplitude profile. This limitation can be overcome in the future by using our arbitrary waveform generator instead of the DDS to provide the dynamical signal mixed in with our static 8.85 GHz master oscillator. However, implementing ARP will come at the cost of significantly slowing down our average gate duration because the robustness of the ARP pulses to detuning errors improves as the pulses are made longer in time. Therefore, future work on improving single qubit gate fidelities and robustness will need to investigate if there exists an ARP pulse shape for our system which will result in an overall performance increase.

### 4.3 BB1 Pulse Calibration

The final stage of preparation before running our randomised benchmarking experiments is the calibration of the microwave pulses. In order to understand our calibration process, we need to briefly review how we program our microwave synthesiser.

The BB1 pulse sequence is implemented using the random-access memory (RAM) mode of an AD9910 DDS which is mixed with our 8.95 GHz master oscillator to drive the hyperfine ground state transitions as described in Section 3.6. This method of operation allowed us to achieve the fastest toggling between different phases and amplitudes from pulse to pulse as required for implementing the BB1 protocol. The theoretical BB1 implementation does not require shaped amplitude profiles, but our experimental implementation allows us to achieve two things. First, the gaps between the pulses can now be programmed into RAM as a single step with amplitude of zero to speed up playback. Second, we can now independently calibrate the DDS amplitude for different gates in order to compensate for timing discretisation errors. These errors arise from the fact that we can allocate a finite number of memory locations to a given pulse which introduces some small, but finite discretisation errors in our pulse timing<sup>63</sup>. In order to circumvent this, we also allow for the possibility to allocate a different amplitude for each pulse which we can scan in addition to calibrating the  $\pi$  and  $\pi/2$  times. In this way we have more precise control of the effective pulse area which is necessary for achieving high single qubit gate fidelities. The effective gap between our pulses within a BB1 sequence is set by the playback speed for a single memory block with amplitude zero which in our case is 2.1  $\mu\text{s}$ . To achieve the fastest playback speed, we pre-record a given random gate string to the system memory and then use direct memory access (DMA) to playback the

---

<sup>63</sup> The AD9910 RAM has 1024 memory locations. In our case we allocate 12 locations per  $\pi/2$  pulse area. This amounts to  $\sim 2.1 \mu\text{s}$  playback time for a memory block which is then discretised using the AD9910 base timing step of 4 ns to define a playback speed.

pulse sequence during the actual experimental run for faster performance. In this way, the gap between gates was reduced to only 0.5  $\mu\text{s}$  allowing us to fit more pulses in the finite qubit coherence time.

A typical calibration procedure for a large array of qubits consists of the following steps. We first calibrate the clock state microwave resonance using a simple rectangular  $\pi$  pulse. In principle much greater frequency precision could be achieved using a series of Ramsey fringes as implemented in reference [138] for a single ion qubit, for example. However, we found that in our case the spread of resonance frequencies across the 225 site array is 2.0(8) kHz, even when we have implemented adaptive intensity feedback to our 1064 nm arrays as outlined in Section 29. In this work, our objective was to achieve scaling to large system sizes so even if we could calibrate the resonance to a higher standard of accuracy on a single trap site using Ramsey fringes, this would not translate to improved global single qubit gate fidelities across the entire array. The variation pattern of clock state resonances across the array appears random without any discernible spatial gradients or trends as can be seen in Fig. 4.5. Going forward the uniformity of the resonances frequencies could be improved further by also implementing a feedback procedure to correct for aberrations in the 1064 nm trapping potential using the signal from the atoms as described in the supplementary materials of reference [87]. In future work, when local single qubit operations are implemented into our set up, this higher calibration overhead would have to be incurred.

The next calibration step is to record a Rabi oscillation fringe, again using simple rectangular pulses, to obtain the  $\pi$  time of the clock state transition. This  $\pi$  time is then used to define the playback speed of our BB1 pulses. The final calibration step is to apply increasing numbers of up to  $1001 \times R_x(\pi)$  and  $1006 \times R_x(\pi/2)$  BB1 pulses and scan the pulse amplitude to maximise transfer to the  $P_{|0\rangle}$  state. In order to have scanning range in both directions, we record the resonance and Rabi flop measurements with 80% of the avail-

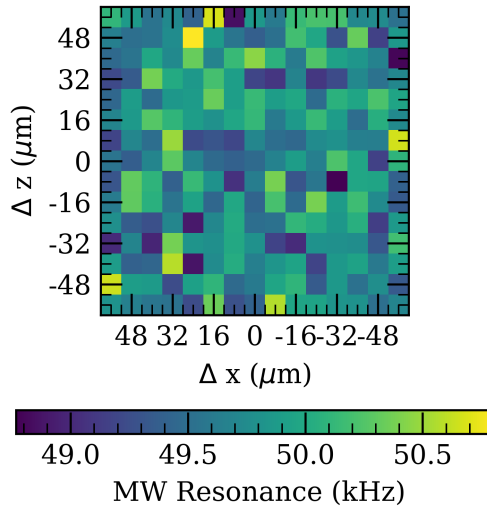


Figure 4.5: Spatial variation of the clock state microwave resonance across a 225 site array with an  $8\ \mu\text{m}$  spacing as used in our randomised benchmarking experiments. The microwave (MW) resonance is defined as a detuning from the unshifted caesium ground state hyperfine splitting.

able maximum amplitude. The reason we allow for different amplitudes for the BB1  $\pi$  and  $\pi/2$  pulses is to account for the effect of the finite risetime of our microwave source which means that the pulse areas do not scale exactly linearly with time.

## 4.4 Clifford Group Randomised Benchmarking

The method we chose for characterising our single qubit gate performance is Clifford group randomised benchmarking (RB). It was originally proposed by Emerson *et al.* in [253] and refined by Dankert *et al.* in [254] to the form implemented in this work. The first experimental realisation of the method was carried out by the Wineland group in NIST using a single trapped  ${}^9\text{Be}^+$  ion [255], but it was done in a modified form which led to the emergence of two slightly different implementations of Clifford group randomised benchmarking in the literature. The methods have been shown to differ by up to

a factor of three in the average gate fidelities they return in reference [256]. We focus our initial description on the method we used in our work, which is the standard Clifford group RB method, before returning briefly at the end of the section to outline the differences with the second method, referred to as the NIST RB method.

The idea of randomised benchmarking is to efficiently characterise the fidelity of an average gate operation (a single qubit gate in our case) by applying an increasing number of randomly sampled gates and recording the resulting depolarisation errors,  $d$ , as a function of the number of gates applied,  $N$ . In our case we uniformly sample our gates from the 24 unitary operations<sup>64</sup> that make up the single qubit Clifford gate set [14] realised as shown in Appendix A. Reference [254] demonstrated that sampling from this finite discrete gate set is sufficient for realising the RB protocol in practice. The specific way we realise the gates is summarised in Table 4.1. We define 9 basic rotation gates and program them into our AD9910 DDS. Notably, unlike reference [68] we chose to adopt the common practice of using virtual gates to realise our global  $R_z(\theta)$  rotations as first introduced in the NMR community [258], but it is also adopted in trapped ion [255] and superconducting qubit experiments [259]. A virtual  $R_z(\theta)$  gate is implemented by rotating the Bloch sphere co-ordinates for subsequent pulses instead of rotating the qubit state vector. In other words, the relative phases of subsequent  $R_x$  and  $R_y$  gates are shifted by an amount equivalent to the  $R_z$  pulse area. This is done almost instantaneously in software so in this way we reduce the total drive time required to achieve an effective rotation around the z-axis compared to the alternative which is to use composite  $R_x$  and  $R_y$  rotations to realise  $R_z$  gates as was done in [68]. When applying virtual  $R_z$  gates we still allocate a delay equivalent to the gate area to allow the qubit to sample any noise sources present in our system to avoid skewing the average gate results towards higher fidelities

---

<sup>64</sup>In general there are a total of 57 classes of Clifford gate sets depending on the gate operation being characterised. See reference [257] for additional information on these classes.

Table 4.1: Our implementation of the basic 9 gates in the single qubit Clifford group gate set. The remaining 14 gates in the set are composed of these basic gates as shown in Appendix A.

Gate Index	Gate	Pulse Area	Delay Area	DDS Phase Current Pulse	Phase Offset Next Pulse
0	$I$	0	$\pi/2$	0	0
1	$R_z(\pi/2)$	0	$\pi/2$	0	$\pi/2$
2	$R_z(\pi)$	0	$\pi$	0	$\pi$
3	$R_z(-\pi/2)$	0	$\pi/2$	0	$-\pi/2$
4	$R_y(\pi/2)$	$\pi/2$	0	$-\pi/2$	0
5	$R_y(\pi)$	$\pi$	0	$-\pi/2$	0
6	$R_y(-\pi/2)$	$\pi/2$	0	$\pi/2$	0
7	$R_x(\pi/2)$	$\pi/2$	0	0	0
8	$R_x(\pi)$	$\pi$	0	0	0
9	$R_x(-\pi/2)$	$-\pi/2$	0	$\pi$	0

when  $R_z$  gates are applied. For the same reason of fairness, we allocate a  $\pi/2$  pulse delay to the identity operation as adopted by the community. It should be noted that the computational cost of using this method when using single-site resolved single qubit gates would be significant, because we would be required to keep track of the  $R_z$  phase shifts on every individual qubit. Additionally, if a virtual  $R_z$  gate is not followed by an  $R_x$  or an  $R_y$  gate which implements a physical rotation of the qubit state vector on the Bloch sphere, then the qubit would not be in the correct state for other gate operations. So this is another complication that needs to be accounted for in the software control architecture when using virtual  $R_z$  rotations.

The typical procedure for randomised benchmarking used in our experiment has the following steps:

1. Generate a random string of  $l$  gates uniformly sampled from the Clifford group.
2. Truncate the sequence at some length  $N \leq l$  for each experimental iteration.
3. Using knowledge of the initial qubit state and the random gate string of length  $N$ , calculate the final single qubit rotation required to return the atomic population to the desired target state ( $|0\rangle$  in our case).
4. Run 300 repetitions of the experiment for a given value of  $N$  plus the specific final rotation required.
5. Repeat for a different value of  $N$  until  $N = l$ .

This NIST method only differs in step 1 because it does not sample uniformly from the full 24-gate Clifford group. Instead a random gate string is composed of alternating  $\pi/2$  pulses and  $\pi$  or identity pulses with a random sign and axis of rotation, so a typical section of a NIST RB gate string would have the form:  $R_x(-\pi/2)R_y(\pi)R_y(\pi/2)IR_y(\pi/2)R_x(\pi)\dots$ . In the NIST method, only the  $\pi/2$  pulses count towards the gate count [255]. This method is widely adopted in the trapped ion community for characterising single qubit gate performance [260, 261], but it does not generalise to multi-qubit gates [256]. We chose to use the conventional RB method to facilitate direct comparisons with other recent work on single qubit randomised benchmarking in neutral atom arrays [68, 70], and because it is closer in its implementation to the original proposal in [254] giving it a stronger theoretical backing. It should be noted that the NIST RB method has also been employed by the neutral atom community for single qubit randomised benchmarking in optical lattices [262], for example.

Regardless of the chosen method, the result of the measurement is a target state population curve exponentially decaying with the number of applied gates,  $N$ , which can be fitted with equation 4.11 to extract an average depolarisation per gate,  $d$ , and a depolarisation associated with state preparation and measurement errors, ( $d_{\text{SPAM}}$ ).

$$P_{|0\rangle} = \frac{1}{2} + \frac{1}{2}(1 - d_{\text{SPAM}})(1 - d)^N. \quad (4.11)$$

The corresponding curve obtained in our experiment for a 225 site array is shown in Fig. 4.6 in Section 4.5. From this fit, one can extract the average fidelity of a Clifford gate,  $F^2 = 1 - d/2$ , where the factor of 1/2 arises from the fact that depolarisation will result in the correct target state 50% of the time. The fidelity of two density matrices,  $\rho$  and  $\rho'$ , is defined as [4]

$$F(\rho, \rho') = \text{Tr} \left[ \sqrt{\sqrt{\rho}\rho'\sqrt{\rho}} \right]. \quad (4.12)$$

Before proceeding to discuss our RB results, we should consider the advantages and disadvantages of this method relative to other approaches for characterising single qubit gate performance. The first method developed for characterising quantum computer performance was quantum process tomography (QPT) [263, 264]. It requires preparing  $4^N$  input states and recording the output states after operating on them with the gate which is to be characterised. Here  $N$  is the number of qubits in an  $N$ -qubit gate. The extracted output states can then be processed to obtain  $16^N - 4^N$  independent gate parameters. Understandably, this method did not gain favour within the experimental physics community because of the increased complexity resulting from the larger number of gate parameters which need to be communicated and processed, and because it was shown to be very sensitive to SPAM errors [265]. The randomised benchmarking method was developed as a response to these shortcomings of QPT by decoupling SPAM errors from gate errors

and only returning two simple parameters to characterise gate performance. However the RB formalism is underpinned by the assumption that the dominant noise channels in the system are Markovian, i.e. uncorrelated, but in real-world experiments this assumption is often violated [266]. This means that RB can overestimate gate fidelities in the presence of correlated, non-Markovian, noise and lead to increased variance in the recorded fidelities as was shown in the work by Ball *et al.* [267]. The RB method would therefore ideally be complemented by another method such as robust phase estimation (RPE), for example, which is intended to specifically measure systematic errors in a quantum system [268]. The interested reader can find out more about these and other gate performance characterisation methods and their relative strengths and weaknesses in references [269, 270] or other work in the area of Quantum Characterisation, Verification, and Validation.

## 4.5 Randomised Benchmarking Results

We now present our randomised benchmarking results on a holographic array of 225 trap sites with 8  $\mu\text{m}$  separation between atoms. We applied up to 1000 global single qubit microwave rotations on our clock state qubits plus the final rotation that returns the qubits to the  $P_{|0\rangle}$  state. A fixed 375 ms hold time in the 1064 nm traps was allocated regardless of the number of gates applied in order to decouple atom loss due to the finite trap lifetime from the average gate fidelity. A total of 8 different random gate strings were uniformly sampled from the single qubit Clifford group gate set. Each data point is based on 300 experimental repetitions with stochastic atom loading, so not all sites were filled in all measurements. Similarly to reference [70], a single calibration was performed at the start of the data taking process without interspersing any calibration measurements in-between benchmarking runs as was done in [261], for example.

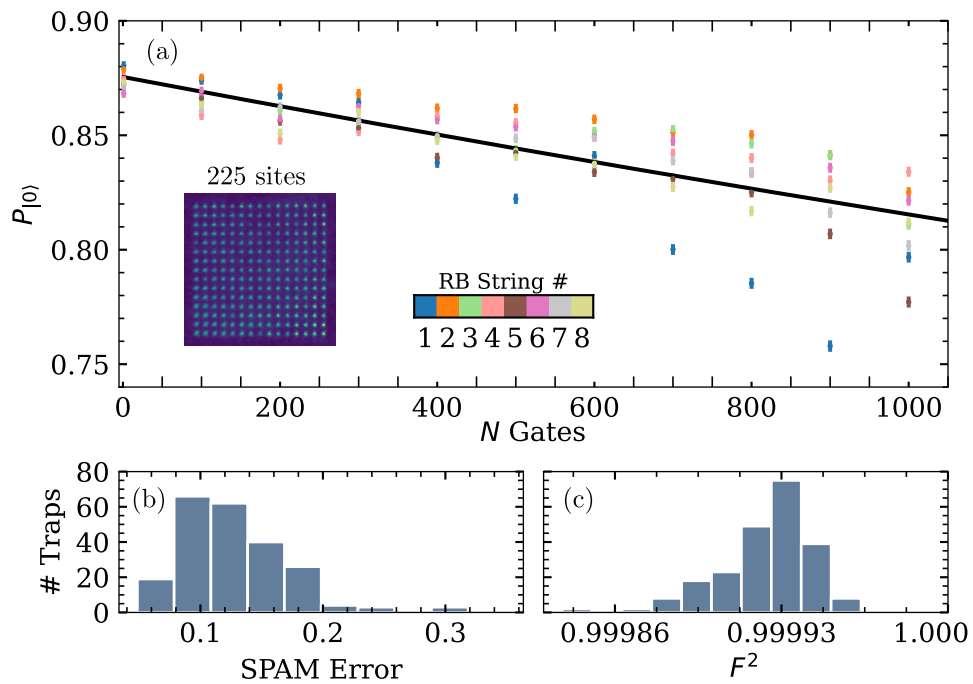


Figure 4.6: (a) Array-averaged randomised benchmarking results for the 225 site array shown in inset image. Eight different random gate strings were generated and a single fit was performed to the data points across all eight strings using equation 4.11. (b) Histogram of state preparation and measurement errors across the full 225 site array. (c) Histogram of average global single qubit gate fidelities on a per-trap basis. Errorbars represent one standard deviation.

The results of our benchmarking measurements are presented in Fig. 4.6(a). Each error bar represents one standard deviation. To extract the average gate depolarisation and SPAM depolarisation per trap site, we performed a single fit to the data from all eight random strings using equation 4.11. The value of  $P_{|0\rangle}$  was scaled by the 93(1)% probability of retaining the atoms in the traps during the 375 ms hold time limited by the finite trap lifetime of 9.7(8) s recorded at the time of the benchmarking run. The results are summarised in the histograms in Fig. 4.6(b) and (c). Using these methods, we achieved an average error per gate of  $7(2) \times 10^{-5}$  across the 225 site array, corresponding to a value of 0.99 993(2) for the average gate fidelity,  $F^2$ . These results are the highest averaged single qubit gate fidelities recorded in any platform with over 100 qubits at the time of writing. In the specific case of neutral atom tweezer arrays, only reference [70] has achieved lower average gate errors of  $4.7(1.1) \times 10^{-5}$  using magic trapping with circularly polarised 830 nm laser light propagating along the quantisation axis to eliminate the differential Stark shift on an array of 4x4 87 Rb atoms.

Our decision to allocate a fixed hold time in the traps regardless of the number of gates applied, along with the limitations of imperfect state preparation discussed in Section 3.5.1, resulted in a large average SPAM error of 0.119(1). This error can be suppressed by the use of non-destructive readout which is the subject of the next chapter of this thesis. In the peer review process of the publication that resulted from this work, the consensus was reached that the survival data used to perform the fit with equation (4.11) must be scaled as

$$P_{|0\rangle} = A \left[ \frac{1}{2} + \frac{1}{2}(1 - d_{\text{SPAM}})(1 - d)^N \right], \quad (4.13)$$

where  $A$  is a constant scaling factor that accounts for the baseline survival of the atoms in the array during the fixed 375 ms hold time used in the measurement. To determine the value of the scaling factor, we measured the

baseline survival probability for the full microwave sequence, but without applying a push out beam and obtained a value of  $A = 0.93(1)$ . This constant scaling factor does not significantly affect the fitted average gate fidelity, but it does result in a smaller reported SPAM error. All the values quoted in this section already include this scaling factor, and so does the data in Fig. 4.6.

The obtained randomised benchmarking results are in good agreement with the theoretical model from reference [68] which derives a relationship between the averaged gate fidelity  $F^2$  and the dephasing parameter  $\alpha$  from equation (4.2). This relationship is

$$\langle F^2 \rangle = 1 - \frac{\langle d \rangle}{2} = 1 - \left[ \frac{1 - \alpha(\langle t_{C_1} \rangle, T_2^*)}{2} \right], \quad (4.14)$$

where  $\langle t_{C_1} \rangle = \langle \theta_{C_1} \rangle / \Omega$  is the average gate duration, and the form of the  $\alpha$  parameter has been modified to  $\alpha(t, T_2^*) = 1/2 + 1/2[1 + 0.95(t/T_2^*)^2]^{-3/2}$ . In our case, the average area is increased to  $\theta_{C_1} = 2.95\pi$  because of our use of BB1 composite pulses. Using this value, a microwave Rabi frequency of  $\Omega/2\pi = 7.68(1)$  kHz<sup>65</sup> and the  $T_2^*$  time of 14.09(8) ms measured on the 225 site array after the benchmarking measurement, we calculate a theoretical average error per gate of  $6.6 \times 10^{-5}$  in good agreement with the measured average gate error of  $7(2) \times 10^{-5}$ .

Our results clearly show variation in the average gate fidelity from string to string. The initial suspicion was that the worst-performing string, String #1, would have a lower proportion of virtual  $R_z$  gates which have the lowest error because they are implemented as delays of area  $\theta$  and a phase jump in software for subsequent pulses. The distribution of Clifford gates per random string is shown in Fig. 4.7. In fact, String # 1 has a higher distribution of virtual  $R_z$  gates than the average, so this hypothesis does not explain the

<sup>65</sup> The base clock state microwave Rabi frequency in our system at full amplitude is actually  $\Omega/2\pi = 9.60(1)$  kHz, but as explained previously we operate around 0.8 of the maximum during the benchmarking sequence to have calibration range in either direction.

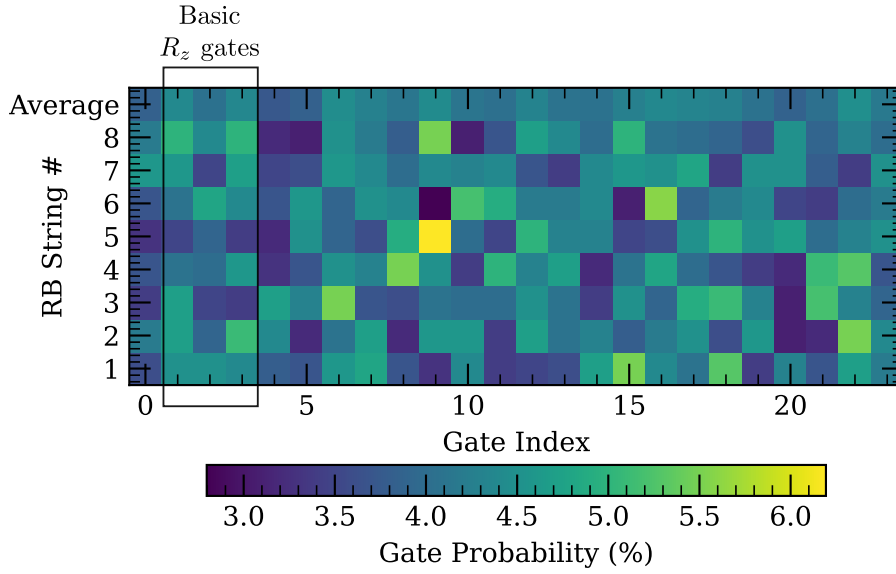


Figure 4.7: Distribution of random gates for each of the 8 strings that were used to obtain the results in Fig. 4.6. The horizontal axis represents the Clifford gate index from Table A.1. The vertical rows represent each random gate string. The top row shows the average distribution of gates across all eight strings which is very close to a uniform distribution. The colour represents the probability that a given gate features in a given gate string.

significant deviation.

To understand the behaviour of String # 1 a simulation model using propagators was developed. The model takes the specific sequence of gates into account, as well as the experimentally measured atom loss probability and optical pumping fidelity, as well as the average depolarisation per gate based on the  $\alpha$  parameter calculated using  $T_2^*$  of 14.09(8) ms and our average gate parameters. All  $R_x$  and  $R_y$  gates are modelled as BB1 pulses. Identity operations and  $R_z$  gates are modelled as perfect rotations independent of the Rabi frequency, but subject to detuning errors because of the fixed hold time in the traps allocated to them in our experimental script. Figure 4.8 shows the results of this simulation for strings #1 and #4 which are the worst- and best-performing random gate strings respectively. The solid black lines indicate the expected performance with perfect calibration and zero drift, but accounting for finite atom temperature in the traps and our SPAM errors.

The coloured points are the array average experimental results for the two strings. The top row in Fig. 4.8 represents the sensitivity of the specific gate string to errors in the pulse area, modelled as a constant pulse area error for simplicity. The bottom row represents the sensitivity to constant detuning errors in the driving field microwave frequency. The figure highlights two important features of our experiment. Firstly, as expected the sensitivity to pulse area errors is significantly suppressed due to our use of BB1 composite pulses. In order to observe fluctuations of the order observed in our experiment for String #1 we would have to experience pulse area variations of the order of +10% which is unrealistically high. On the other hand, our sensitivity to detuning errors is significantly stronger. The simulation shows that detuning errors within the order of magnitude commensurate with our calibration error and temperature-induced drift can lead to significant variation in the observed value of  $P_{|0\rangle}$ . Therefore, this is the more likely explanation for the worse performance observed with String #1. As discussed at the end of Section 56, we have already observed temperature variations causing resonance shifts of the order of 20 Hz in our lab. Whilst the output power stability of our MW amplifier has been observed to be stable to within 1% for multiple hours at a time after an initial 20-minute warm up period which we have built into our sequence.

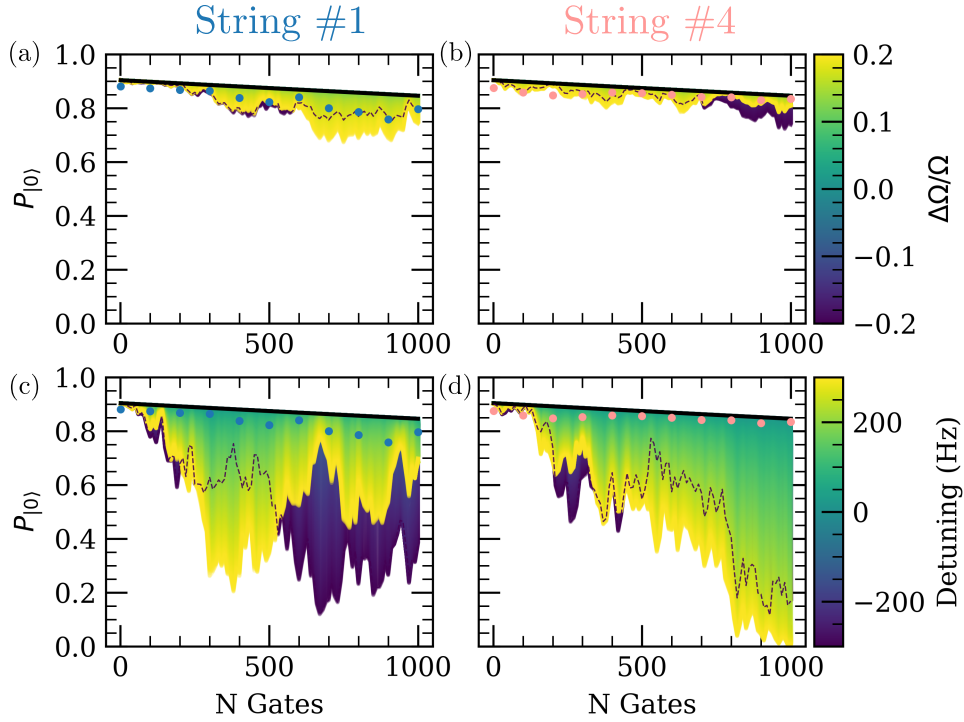


Figure 4.8: Randomised benchmarking simulations using Heisenberg propagators. The model accounts for SPAM errors and atom temperature effects. Pulses are simulated in a realistic way as implemented in our experiment. See main text for more details on simulation model. The solid black lines are the ideal simulation results for a perfectly calibrated system and a specific gate string. The coloured lines represent the system response to a static parameter error. The dashed lines are the envelopes of the negative parameter shift simulation results when they are obscured by the positive parameter shift results on the plot. The simulations shown much greater sensitivity to detuning errors. The solid dots are the array average experimental results for String #1 and String #4. The error bars are smaller than the points on this scale. The comparison highlights variation in the sensitivity from string to string.

From Fig. 4.8 it also becomes clear that the sensitivity of each gate string to parameter errors can be significantly different because of the gate randomisation process and the fact that different gates have different parameter sensitivities. Virtual  $R_z$  gates and identity gates are only susceptible to detuning errors because their physical implementation on the atoms is a simple delay. In sequences with more  $R_x$  and  $R_y$  gates, there is an additional sensitivity to pulse area errors. It is also worth noting that parameter errors of

the same amplitude, but different sign result in different measurement outcomes and can skew the fidelity towards lower values. This is evidence of the inability of the RB method to decouple systematic errors from stochastic errors due to noise.

## 4.6 Conclusion

With the work discussed in this chapter we have been able to characterise the performance of our qubits encoded in the hyperfine clock states of the  $6S_{1/2}$  manifold in  $^{133}\text{Cs}$ . We have recorded  $T_2^*$  times exceeding 14 ms on a large array of 225 trap sites and  $T_2'$  times  $> 140$  ms without composite pulses. While these numbers are within state-of-the-art performance, we have identified a range of areas for improvement. Improving the stability of our air conditioning system or implementing a magnetic field amplitude stabilisation servo to compensate for any slow magnetic field drifts would likely result in the largest performance improvement. In addition, installing an intensity stabilisation system on our 1064 nm trapping laser has also been identified as a priority in order to extend the irreversible decoherence time of our qubits. The analysis of irreversible dephasing mechanisms carried out in this work has highlighted the fact that more thorough noise source characterisation would be required to fully understand the limitations of our platform. Specifically, taking measurements of the 1064 nm laser pointing instability on short timescales and monitoring the magnetic field noise with a high bandwidth, high resolution magnetometer have been identified as key action points.

Using Clifford Group randomised benchmarking, we have recorded the highest global single qubit gate fidelity on a system of this scale ( $>100$  qubits) across all quantum computing platforms at the time of writing. In the process of analysing the results we have identified significant variation in the

resonance frequencies across the array which would negate the benefits of high-precision Ramsey fringe frequency calibrations. The width of the distribution of resonance frequencies, likely caused by 1064 nm intensity inhomogeneities, could potentially be narrowed down by implementing more sophisticated holographic feedback methods or by operating with magic wavelength traps with zero differential AC Stark shift on the clock state transitions. The sensitivity to such variations in detuning could be significantly reduced by implementing adiabatic rapid passage pulse profiles to our composite BB1 pulses. Further work must be done to confirm if this would result in a net increase in the average gate fidelity because the benefits ARP pulses provide will be partially offset by the fact that the average gate duration would be increased compared to using simple rectangular BB1 pulses. The simulations performed to understand the sensitivity of different random gate strings to parameter errors in our system has further highlighted the importance of suppressing detuning errors to reach better performance levels in the future. To fully understand the sensitivity of individual gates to parameter errors, a different method called interleaved benchmarking could be used to extract the depolarising parameter of a specific gate by interleaving it with a random gate string as suggested in [271].

## Chapter 5

# Non-Destructive Readout (NDRO)

An outstanding challenge in neutral atom quantum computing is improving the state detection procedure to make it compatible with the future requirements of fault-tolerant operation [14] based on error-correcting codes which require mid-circuit readout [272, 273]. Alternative routes to fault-tolerant operations, which do not require mid-circuit measurement, have been proposed [274–276], but they come with other disadvantages such as increased encoding overhead in terms of number of physical qubits required to implement a logical qubit. Additional benefits of implementing non-destructive measurements in a set up include the ability to access different forms of computation such as measurement-based quantum computing [277], semiclassical Fourier transform [278], preparing long-range entangled quantum matter [279] and suppressing state measurement and preparation errors [280] to name a few. The conventional method for reading out qubit states in experiments with alkali neutral atoms is clearly incompatible with these modes of computation because it relies on a push-out measurement, as described in Section 3.5.2, which results in the loss of all atoms in the  $F = 4$  manifold. In addition to requiring re-loading of atoms after every measurement, the conventional

readout method is usually relatively slow compared to the coherence times of alkali neutral atom systems. This is also incompatible with repetitive error-correcting codes where multiple mid-circuit measurements need to be performed per experimental cycle. More recent developments using two-valence electron atoms such as  $^{171}\text{Yb}$  have successfully demonstrated mid-circuit operations [281–283], but several different methods to achieve this have also been proposed and realised with alkali atoms in recent years. One approach is coupling the atom to a cavity in order to enhance fluorescence light collection [284, 285] or use the cavity transmission or reflection spectra to perform state detection [286, 287]. Another alternative applicable to qubits encoded in two Rydberg states is to use collective enhancement and electromagnetically induced transparency (EIT) to speed up readout and perform it without atom loss [103]. Finally, there is the non-destructive readout procedure based on a cycling transition implemented in the stretched state of alkali atoms which was originally introduced in [288] and is the subject of this chapter. For the remainder of this work, the term non-destructive readout (NDRO) will be used to refer to this specific method.

The basic principle of NDRO is explained in Section 5.1, followed by a discussion on the different approaches that were considered for transporting the atoms between the computational and NDRO readout hyperfine sublevels. The chapter concludes by presenting the final experimental results from our set up and discussing future improvements.

## 5.1 Principle of Operation of NDRO

The principle of NDRO is illustrated in Fig. 5.3. The method uses two counter-propagating beams, red-detuned from a stretched state transition on the D2 line with the same circular polarisation handedness in the atomic reference frame. In a typical cold atoms experiment, one of the two horizontal

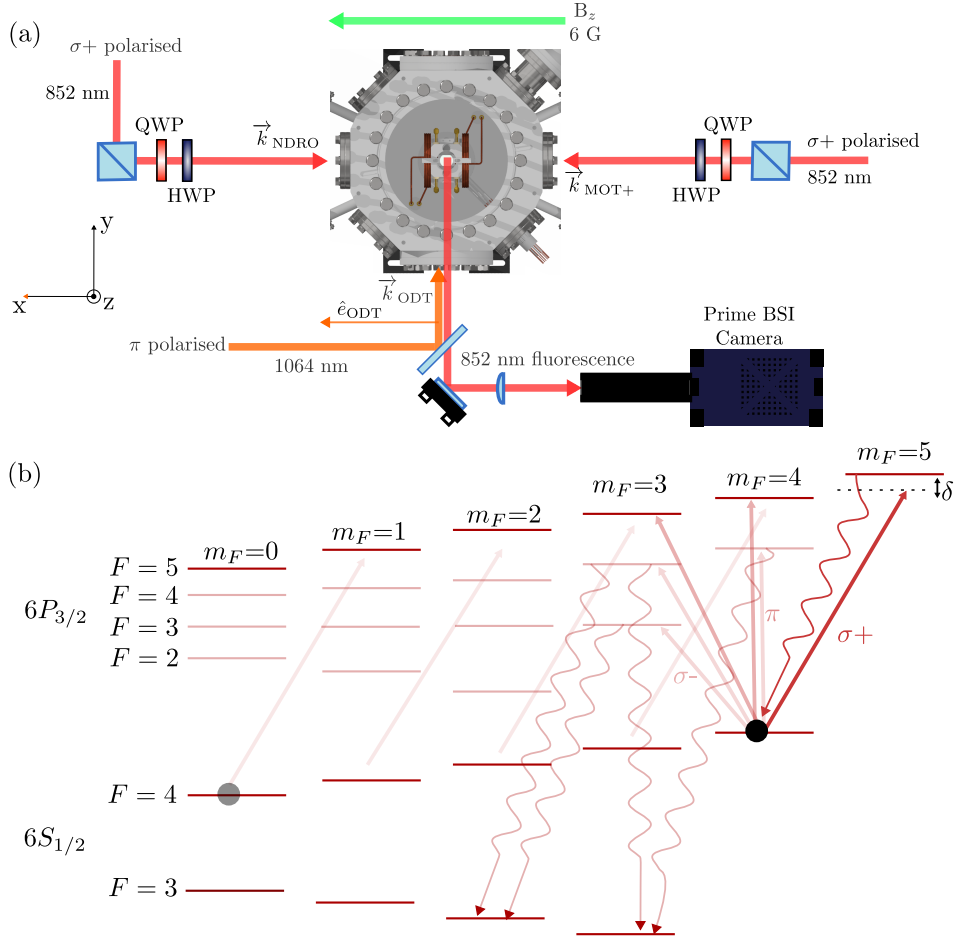


Figure 5.1: (a) Schematic diagram of the set up required to implement NDRO. Two horizontal beams with the same high-purity,  $\sigma+$  polarisation at the atoms are required. Their polarisations are defined with respect to a quantisation magnetic field,  $B_z$ , which lifts the degeneracy of the  $m_F$  levels. Aligning the polarisation of the 1064 nm trapping laser to be along the quantisation field axis is important for suppressing any circular polarisation components of the 1064 nm light at the atoms which could give rise to fictitious magnetic fields as observed in [211]. (b) Level diagram illustrating principle of operation of NDRO. Red-detuned, high-purity circularly polarised light on the D2 line is used to drive a stretched state cycling transition. Lighter-shaded arrows emanating from the  $|F = 4, m_F = 4\rangle$  state indicate polarisation impurities which, along with off-resonant Raman scattering, can lead to leakage errors into the  $F = 3$  manifold during NDRO.

3D MOT beams can be used as an NDRO beam. We chose to apply  $\sigma+$  polarised light to drive the  $|F = 4, m_F = 4\rangle \rightarrow |F' = 5, m'_F = 5\rangle$  transition, which means that we could use the MOT+ beam from our existing set up. Because the other horizontal MOT beam, MOT-, would have the opposite handedness at the atoms, we added an additional NDRO beam which was combined with the MOT- beam on a PBS. While not an essential requirement for implementing the NDRO technique, in reference [211] it was shown that having two counter-propagating beams is useful for cancelling out heating due to photon scattering and thus allowing more photon scattering events to take place before inducing atom loss from the traps. The original implementation in [288] used a single NDRO beam, but achieved lower detection fidelity. Using either a single or counterpropagating configuration of NDRO beams, one could optically pump the atomic populations in the  $F = 4$  manifold of the  $6S_{1/2}$  state to the stretched state, where upon the continued application of the same laser field the atoms will scatter photons on the cycling stretched state transition. By collecting this fluorescence signal on a camera, a state-selective detection procedure can be performed. A second important difference compared to our conventional atom imaging process is that no repump light is applied during NDRO. This is why the process is state selective. The populations in the  $F = 3$  manifold do not interact with the NDRO light due to the large hyperfine splitting in heavy alkalis of the order of several GHz. For this reason, the  $F = 4$  and  $F = 3$  manifolds are referred to as bright and dark states respectively. By correctly balancing the laser power, detuning and the duration used for NDRO, the process can be performed without inducing atom loss from the traps due to heating hence the name non-destructive readout. The specific parameters used and the practical limitations imposed on the minimal achievable atom loss during NDRO will be discussed in Section 5.3 of this chapter.

Figure 5.3(b) highlights another important consideration for minimising NDRO detection errors, namely minimising leakage into the  $F = 3$  manifold

which can manifest in false negative detection errors and atomic populations getting stuck outside of the computational basis during NDRO. In order to minimise the likelihood of these events, great care must be taken in ensuring that the NDRO beams have a well-defined circular polarisation with respect to the quantisation axis. This is achieved by aligning the  $\vec{k}_{\text{NDRO}}$  and  $\vec{k}_{\text{MOT+}}$  vectors to be colinear with the direction of the quantisation field  $B_z$  and adjusting the quarter- and half-waveplates installed in each beam path using a polarimeter to achieve the highest possible degree of polarisation purity. The two beams must also be counter-propagating to minimise heating due to photon scattering. Any imperfections will result in the 852 nm light acquiring  $\pi$  and  $\sigma$ - polarisation components which can drive transition that have a decay path to the  $F = 3$  manifold resulting in leakage errors. Additionally, if the polarisation unit vector,  $\hat{e}_{\text{ODT}}$ , of the 1064 nm light has some finite degree of misalignment with respect to the quantisation axis, this could give rise to fictitious magnetic fields as discussed in [211] where the degree of misalignment was  $\alpha=60^\circ$  due to the chamber geometry of that particular experiment. Such misalignment results in some degree of circular polarisation at the atoms even though the trapping laser is linearly-polarised in the lab frame. The experimental chamber used in this work was specifically designed to virtually eliminate such fictitious magnetic fields by having  $\alpha \sim 0^\circ$  limited only by our ability to align the 1064 nm laser polarisation vector with the quantisation axis.

## 5.2 Transfer Sequence for NDRO

### 5.2.1 MW Transfer Sequence Simulation

Part of the challenge with implementing NDRO in a practical demonstration lies in transferring atomic populations between the computational basis and the stretched state. As a reminder, we encode our qubits in the  $m_F = 0$  levels

of the hyperfine ground states to eliminate first-order sensitivity to magnetic field noise and drifts. The simplest way of achieving this population transfer is to use the same laser light that we use during NDRO to optically pump atoms from  $|F = 4, m_F = 0\rangle$  into  $|F = 4, m_F = 4\rangle$ . However, it was initially believed that the relatively large number of different  $m_F$  levels in the hyperfine ground state of  $^{133}\text{Cs}$  with its  $I = 7/2$  nuclear spin would result in poor performance due to the relatively large number of photon scattering events required. To address this, a microwave transfer scheme inspired by the techniques employed in trapped ion experiments using Zeeman-level-encoded  $^{40}\text{Ca}^+$  qubits [138] was simulated and tested in our experiment.

### Multi-Level Atoms

When we consider applying unpolarised microwave radiation to a Zeeman-resolved hyperfine ground state manifold, we must account for the multi-level structure because a single  $m_F$  state could couple to multiple  $m'_F$  states. In the case of Cs, we have a total of 16 hyperfine  $m_F$  states which results in a  $16 \times 16$  Hamiltonian for the problem. At the weak bias magnetic field used in the experiment, we are operating in the anomalous Zeeman splitting regime where there is no state mixing. The frequency separation between the different  $m_F$  states in this regime is of  $\sim$  MHz and the frequency of the driving microwave (MW) field is  $\sim$  GHz. Therefore, the rotating wave approximation (RWA) is valid. We do not consider higher order transitions due to magnetic quadrupole or higher order moments in the simulation. Under these approximations, a single  $m_F$  state can couple to a maximum of three other  $m'_F$  states, one for each component of polarisation of the radiation field ( $\sigma^-, \pi, \sigma^+$ ).

We now need to consider how to express the detuning terms in the Hamiltonian for this system. The MW frequency is defined relative to the zero magnetic field energy-splitting of the  $^{133}\text{Cs}$  hyperfine ground states,

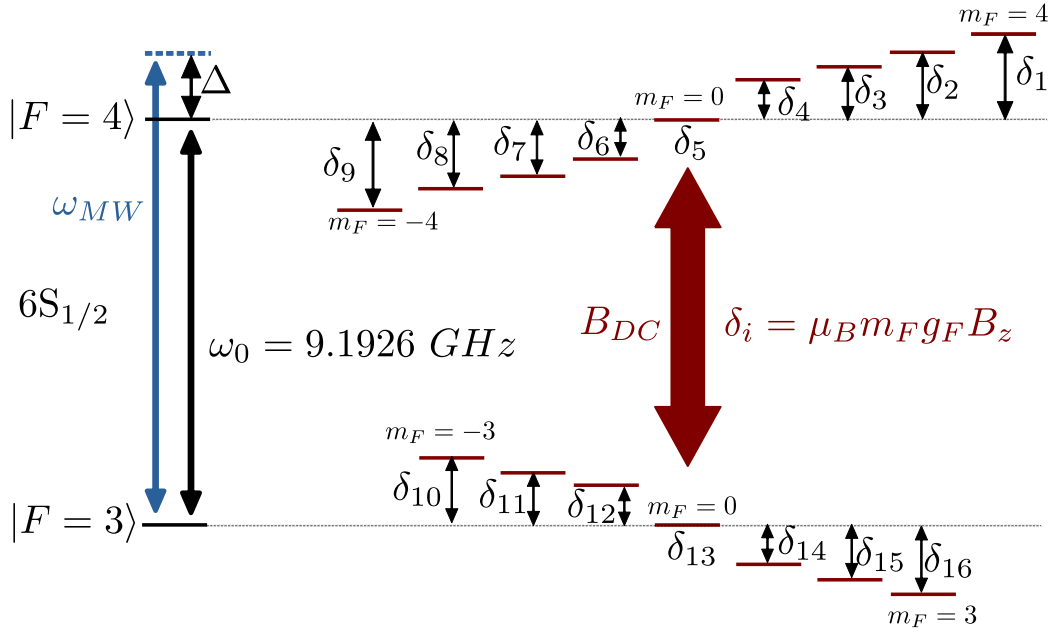


Figure 5.2: Schematic representation of the hyperfine ground state manifold of the Cs  $6S_{1/2}$  state with an applied bias magnetic field  $B_{DC}$  to lift the degeneracy of the  $m_F$  levels. The terms  $\delta_i$  are the Zeeman interaction energy shifts from the unshifted transition at 9.1926 GHz.

$\omega_0 = 9.1926$  GHz, and the MW detuning is expressed as  $\Delta = \omega_{MW} - \omega_0$ . The state labelling convention is shown schematically in Fig. 5.2, along with a representation of the problem state space.

Using this convention, we can now define the problem Hamiltonian as

$$\hat{H} = \hbar \begin{pmatrix} \Delta - \delta_1 & 0 & 0 & \dots & 0 & 0 & \frac{1}{2}\Omega_{1,16} \\ 0 & \Delta - \delta_2 & 0 & \dots & 0 & \frac{1}{2}\Omega_{2,15} & \frac{1}{2}\Omega_{2,16} \\ 0 & 0 & \Delta - \delta_3 & \dots & \frac{1}{2}\Omega_{3,14} & \frac{1}{2}\Omega_{3,15} & \frac{1}{2}\Omega_{3,16} \\ \vdots & & & \ddots & & & \vdots \\ 0 & 0 & \frac{1}{2}\Omega_{14,3} & \dots & -\delta_{14} & 0 & 0 \\ 0 & \frac{1}{2}\Omega_{15,2} & \frac{1}{2}\Omega_{15,3} & \dots & 0 & -\delta_{15} & 0 \\ \frac{1}{2}\Omega_{16,1} & \frac{1}{2}\Omega_{16,2} & \frac{1}{2}\Omega_{16,3} & \dots & 0 & 0 & -\delta_{16} \end{pmatrix} \quad (5.1)$$

This Hamiltonian was used in the numerical simulations for the population transfer between the stretched state  $|F = 4, m_F = 4\rangle$  and the clock state  $|F = 4, m_F = 0\rangle$  shown in the next section.

### Simulation Results

The initial idea was to use circularly polarised optical pumping on the D2 line to initialise our qubits in the  $|F = 4, m_F = 4\rangle$  state and then coherently transfer them to the clock states. A simulation was performed that included all of the  $m_F$  levels in the  $F = 4$  and  $F = 3$  hyperfine ground states using the Hamiltonian described in Section 5.2.1 and modelled with realistic parameters matching our experimental optical pumping bias field and microwave power. The results of the simulation are summarised in Fig. 5.3. Notably, the simulation indicates that using a transfer sequence with six pulses which avoids the weaker  $\sigma$ - transitions would achieve a faster overall transfer time than the most direct sequence which consists of four pulses. The predicted durations are 248  $\mu\text{s}$  and 232  $\mu\text{s}$  for the four- and six-pulse sequences respectively. While the reduction in time only amounts to 15  $\mu\text{s}$ , there is an additional gain in terms of reducing decoherence because the atoms are moved away from the most magnetically-sensitive states on a faster timescale using the six-pulse sequence. If one is willing to transfer populations from the stretched state to the  $|F = 3, m_F = 0\rangle$  clock state instead, there is an even faster pulse sequence of five pulses available with a total duration of 224  $\mu\text{s}$  which only circumvents the slowest  $\sigma$ - transition and takes the most direct route otherwise.

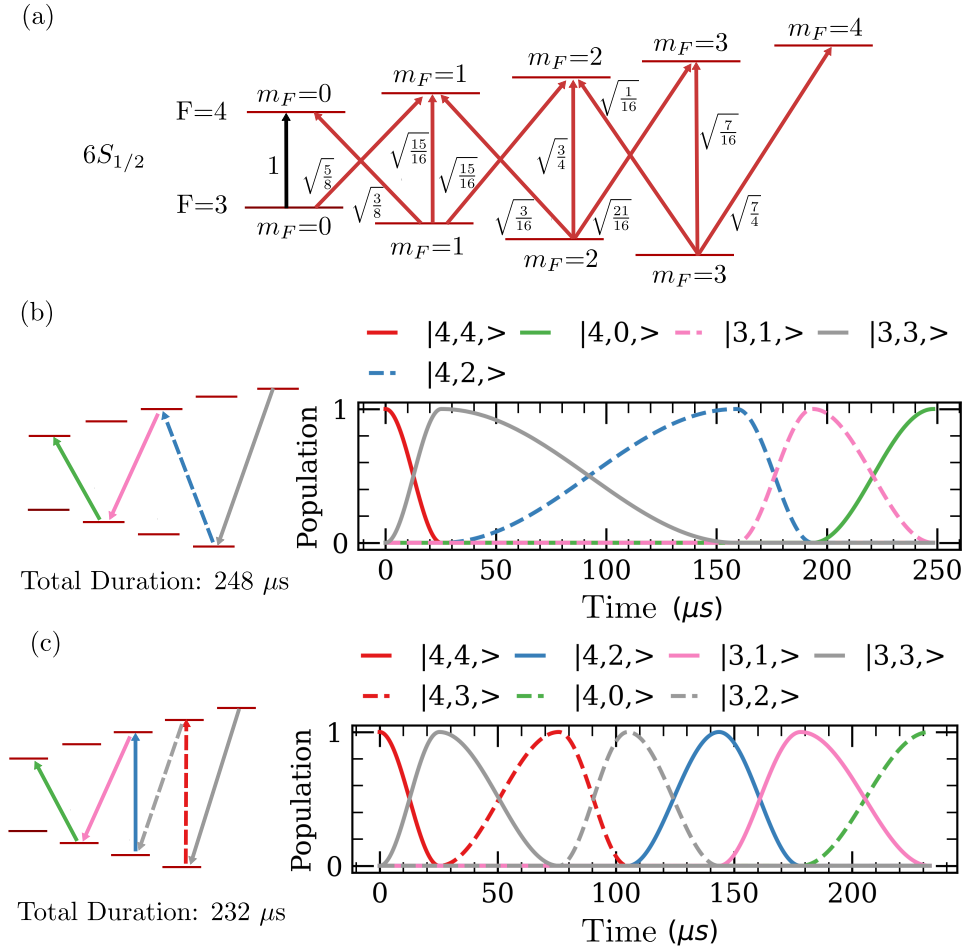


Figure 5.3: (a) Schematic diagram of the relevant magnetic dipole transition strengths in the hyperfine ground state manifold of  $^{133}\text{Cs}$  in units of  $\mu_B B_q / \hbar$  where the subscript  $q$  denotes the polarisation component of the driving  $B$  field. (b) Schematic diagram and simulation of the most direct transfer sequence from  $|F=4, m_F=4\rangle$  to the  $|F=4, m_F=0\rangle$  state using four MW pulses. (c) Alternative driving sequence which uses six pulses, but avoids the weaker  $\sigma$ -transitions to achieve a faster overall transfer time. The simulations do not include decoherence effects due to finite  $T_2$  times.

An implementation of the transfer sequence from the computational states to the stretched state for NDRO must also consider the following complication. The naive approach of using simple  $\pi$  pulses to achieve population transfer between hyperfine ground states has been found to be problematic in reference [289]. In this work it was observed that for an atom in a superposition of the  $|0\rangle$  and  $|1\rangle$  states, encoded in the clock states, a MW pulse that is

resonant with the  $|F = 4, m_F = 0\rangle \rightarrow |F = 3, m_F = 1\rangle$  transition would also be near resonant for the  $|F = 3, m_F = 0\rangle \rightarrow |F = 4, m_F = 1\rangle$  transition. This is incompatible with the NDRO method because after this initial pulse, one would end up with what were originally dark state populations now stuck in the bright  $F = 4$  manifold producing false positive counts in an NDRO image. This undesirable effect is illustrated in Fig. 5.4(a) using the simulation model described above. One way to circumvent this is to add a Ramsey delay during the first pulse in the sequence, with a delay timing optimised to ensure that the populations from  $|F = 3, m_F = 0\rangle$  that were partially transferred to  $|F = 4, m_F = 1\rangle$  evolve a differential phase which will result in them returning back upon the application of the second  $\pi/2$  pulse in the Ramsey sequence as implemented in [138] for  $^{40}\text{Ca}^+$  ions. Figure 5.4(b) is a simulation which illustrates how this would work in the case of our caesium neutral atom qubits with a 6.0 G bias field applied. Based on the derivation from reference [138], the required delay can be calculated using

$$T_{\text{Ramsey}} = \frac{2}{\delta} \tan^{-1} \left[ \frac{\Omega_{\text{eff}}}{\delta} \cot \left( \frac{\theta}{2} \right) \right], \quad (5.2)$$

where  $\Omega_{\text{eff}} = \sqrt{\delta^2 + \Omega^2}$  and  $\theta = \Omega_{\text{eff}} \frac{\tau_\pi}{2}$ .  $\Omega$ ,  $\delta$ , and  $\tau_\pi$  are the Rabi frequency of the target transition, the detuning of the undesirable transition from the target transition resonance, and the  $\pi$  pulse duration of the target transition respectively. Using equation (5.2) and our experimental parameters for the bias field and Rabi frequency, the required delay for our experiment is  $T_{\text{Ramsey}} = 41 \mu\text{s}$ . This additional cost in terms of coherence times is not unreasonable and can be partially offset by using the six-pulse transfer sequence discussed above which results in faster overall transfer.

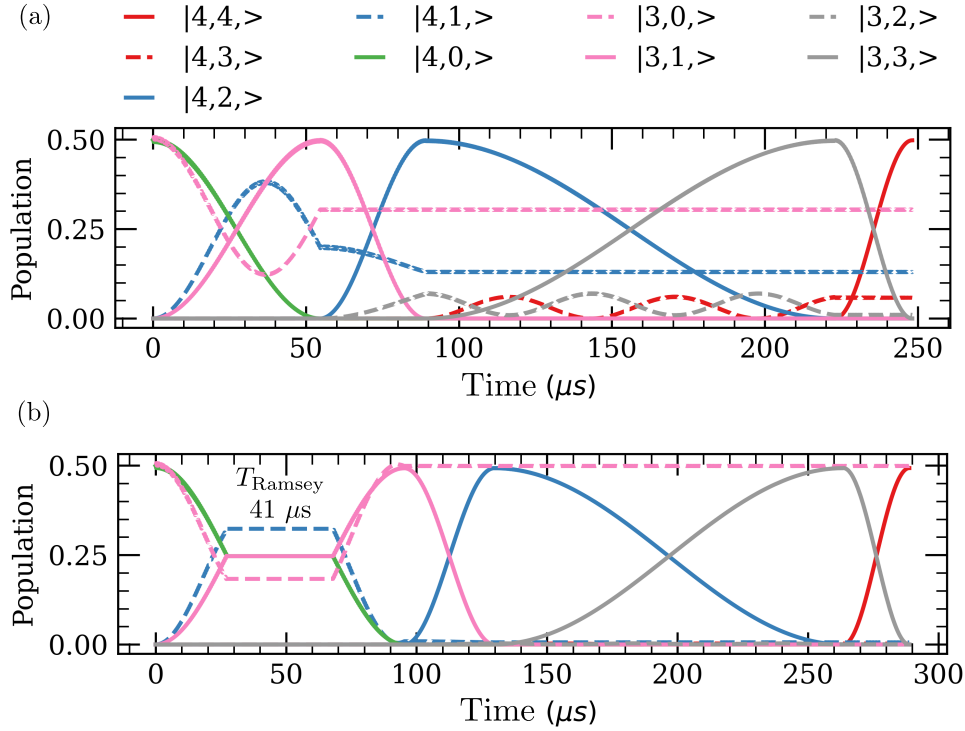


Figure 5.4: (a) Simulations of naive MW transfer sequence intended to achieve population transfer from  $|F = 4, m_F = 0\rangle$  to  $|F = 4, m_F = 4\rangle$ . If the qubit is in a superposition state as modelled here, there is an undesired population transfer away from  $|F = 3, m_F = 0\rangle$  resulting in population leakage. (b) Modified sequence which splits the first  $\pi$  pulse in the sequence into two  $\pi/2$  pulse and inserts a Ramsey delay between them. Its duration,  $T_{\text{Ramsey}}$ , is calculated to achieve a differential phase evolution between  $|F = 4, m_F = 0\rangle$  and  $|F = 3, m_F = 0\rangle$  which will return the leaked populations back to  $|F = 3, m_F = 0\rangle$  upon application of the second half of the pulse. The rest of the MW transfer sequence is then applied without any change from the naive implementation shown in (a). For our experimental parameters, this delay amounts to  $T_{\text{Ramsey}} = 41 \mu\text{s}$ .

## 5.2.2 MW Transfer Sequence Experiment

The MW pulse sequence for transfer between the stretched state and the clock states was tested in our experiment by preparing the atoms in the  $|F = 4, m_F = 4\rangle$  stretched state using D2 OP optical pumping as described in Section 35. With this as a starting point, successive microwave spectroscopy was performed by sequentially moving the population across from

the stretched state to the clock state  $|F = 4, m_F = 0\rangle$  using simple rectangular MW  $\pi$  pulses. At each stage, a MW resonance scan was performed and a short Rabi flop recorded to extract the transition  $\pi$  time. The results of the measurements are shown in Fig. 5.5. The most direct four-pulse transfer sequence was tested first. Very significant decay in the oscillation contrast of the clock state transition was observed. In an attempt to remedy this, a measurement was performed using the six-pulse sequence which avoids the slow  $\sigma$ - transitions and moves the atomic populations to the less-magnetically sensitive  $m_F$  states faster. The result was a significant improvement in the contrast of the clock state Rabi oscillations performed at the end of the transfer sequence, but the performance level was still not in-line with achieving competitive state preparation fidelities. The highest Rabi oscillation contrast experimentally recorded on the clock state transition after transporting the atoms with a MW transfer sequence was 0.79(4). This was calculated based on the data shown in the rightmost column of Fig. 5.5(c).

At the time of recording the MW transfer sequence data, BB1 pulses had not yet been implemented in our system. Some improvement can be expected by reducing our sensitivity to  $\pi$  pulse calibration errors. The Rabi frequency variation across the 25 site array at 8  $\mu\text{m}$  spacing is expected to be less than 1%, so it is unlikely that this is the limiting factor. The more likely source of error is the drift of the bias magnetic field discussed in Section 5.6. The available data does not show significant decoherence of the MW Rabi flops for any of the transitions except for the slowest  $|F = 3, m_F = 3\rangle \rightarrow |F = 4, m_F = 2\rangle$  transition. In hindsight, it would have been useful to record longer Rabi oscillations in order to be in a position to make a more conclusive statement about the rates of dephasing of different transitions. The suspected cause for the loss of contrast as the sequence progresses is likely due to calibration drift on a slow timescale of minutes to hours. The measurements shown here were taken overnight over the course of several hours. A log of  $|F = 4, m_F = 4\rangle \rightarrow |F = 3, m_F = 3\rangle$  transition resonance frequencies

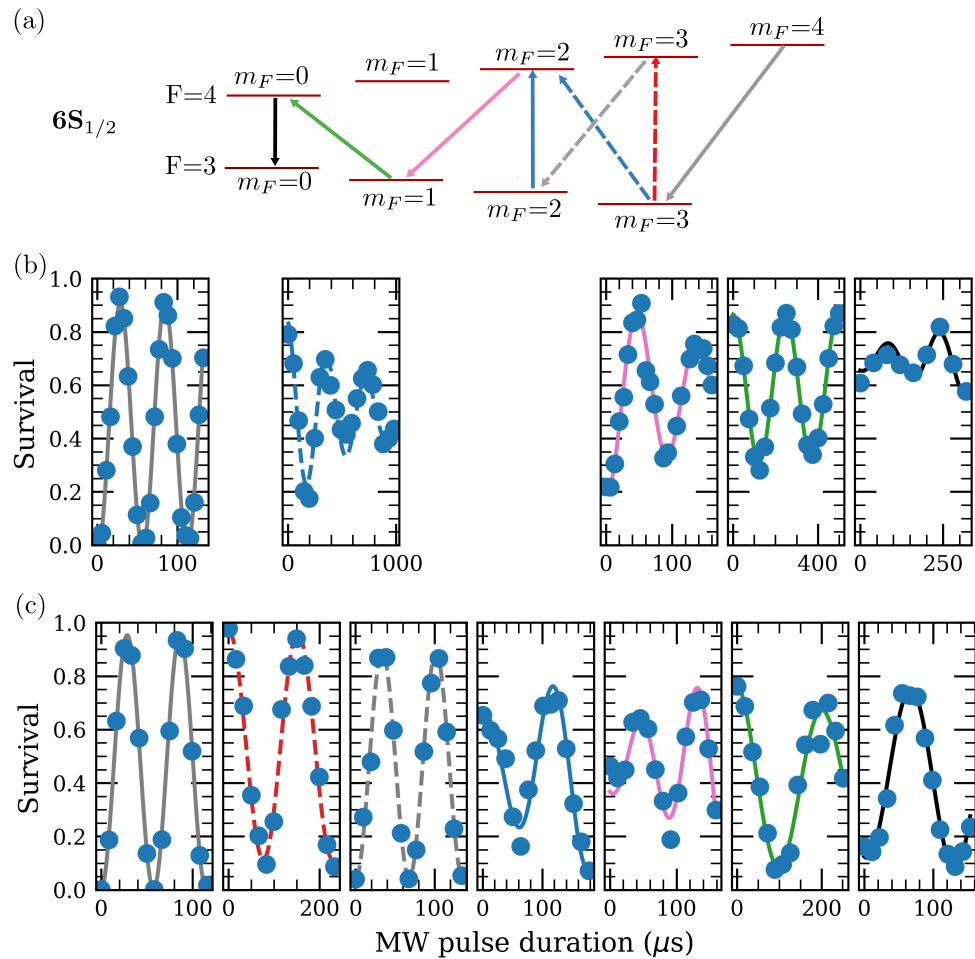


Figure 5.5: (a) Schematic representation of the two different pulse sequences tested in our experiment. The colour-coding and line style matches the data in (b) and (c). (b) Rabi oscillation contrast using four-pulse MW transfer sequence. (c) Six-pulse MW transfer sequence avoiding slower  $\sigma$ - transitions. The experimental data shown is an array average across 25 trap sites. The fits were performed using a sine function to guide the eye. What appears as an unphysical increase in coherence with longer MW drive times is attributed to the MW resonances drifting in and of resonance during the experimental run due to the limited temperature stability of the lab.

recorded over the course of two years shows typical daily drifts of the order of  $\sim 5$  kHz. On several occasions, the resonances were observed to drift by as much as 10 kHz over the course of two hours, but this is likely due to the fact that alignment work had been done on the experiment in that time. In any case, the performance of the transfer sequence in terms of contrast loss will most likely be significantly improved by implementing a more sophisticated calibration procedure, which records stretched state microwave resonances every few minutes and uses the known ratios of magnetic dipole moments to update the resonances on the other transitions. Alternatively, adiabatic rapid passage pulses as discussed in Section 4.2 could be used to reduce the sensitivity to detuning errors due to magnetic field drifts or noise. After observing these results, the decision was made not to pursue the MW sequence approach at this stage, because the current objective was not to implement mid-circuit measurement, but to use NDRO to suppress state preparation and measurement errors. As this technique does not require transferring the atoms back to the clock state after readout, it appeared that using incoherent optical pumping would yield better returns on the time invested.

### 5.2.3 NDRO Optical Pumping Simulation

In order to explore the feasibility of optically pumping atoms into the stretched state, a density matrix simulation model of this incoherent process was set up to estimate the expected transfer fidelity and the rate of transient depumping into the  $F = 3$  manifold using the Lindblad master equation. The model uses a reduced hyperfine manifold starting from  $|F, m_F = -1\rangle$  states and including all the levels up to the maximum  $m_F$  level for a given hyperfine state. This is a reasonable approximation for our purposes because we apply high-purity  $\sigma+$  polarised light during NDRO and this transfer process takes place after the atoms have been prepared in  $|F = 4, m_F = 0\rangle$  state with 0.957(9) fidelity. All magnetic sublevels in the  $F = 3$  manifold of

the  $6S_{1/2}$  ground state were grouped together into a single leakage channel that has no coherent couplings to other states, but only serves as a sink for populations decaying from the excited states. The model takes into account the  $6P_{3/2}$   $F'=4$  and  $F'=5$  excited states and their branching decay ratios were calculated with the ARC software package for Python [115]. Using typical values for the detuning and optical power per beam from previous work on NDRO in [211] as a starting point<sup>66</sup>, the simulation predicts better transfer performance when we move population across with incoherent optical pumping than what we achieved experimentally using the simple rectangular  $\pi$  pulse MW transfer sequence. The simulation results are shown in Fig. 5.6 for the 6.0 G bias magnetic field used in our experiment assuming perfect  $\sigma+$  polarisation. The predicted number of photon scattering events to reach steady state is  $\sim 140$ . One factor to consider for future work, especially if repeated transfers from the clock state to the stretched state and back are required, is the atom heating induced by this process. We can obtain a worst-case upper bound for the amount of heating,  $\Delta T_{\text{OP}}$ , introduced with each optical pumping cycle by using

$$\Delta T_{\text{OP}} = 2 \times N_{\text{scat}} \times T_{\text{recoil}}, \quad (5.3)$$

where  $T_{\text{recoil}} = 198.34$  nK for the caesium D2 line [128],  $N_{\text{scat}}$  is the number of photons scattered, and we have added a factor of two to account for the possibility of the momentum kicks upon absorption and re-emission having the same direction. This worst-case scenario predicts a temperature increase of 26  $\mu\text{K}$  due to each optical pumping cycle for 140 photon scattering events. This is an overestimate, because by operating with red-detuned light there is some amount of polarisation gradient cooling which counteracts this heating. For example, in reference [111] which also implemented NDRO optical pump-

<sup>66</sup>These values were a detuning of  $\Gamma/2$  and a combined intensity in both beams equal to the saturation intensity of the  $6S_{1/2}, F=4 \rightarrow 6P_{3/2}, F'=5$  transition.

ing with caesium atoms it was found that one transfer cycle heated the atoms by only 3  $\mu\text{K}$ . In the context of using NDRO for mid-circuit measurements with many transfer cycles, it would be preferable to use coherent transfer with shaped MW or Raman beams. In any case, for the purposes of our experiment we only require a single transfer from the clock state to the stretched state after which we image the atoms so the heating rate is not a primary concern. Importantly, the steady state population of the  $|F = 4, m_F = 4\rangle$  state predicted by the simulation is 0.93 and the leakage population into the  $F = 3$  manifold is 0.0021. The overall population transfer to  $|4, 4\rangle$  is actually better than this because once the optical pumping light is extinguished, the populations in the excited states have a large probability of decaying to the stretched state. By continuing the simulation with the OP light turned off, we estimate that within 250 ns the population in the excited states has fully decayed to give a predicted 99.8 % occupancy of the target state  $|4, 4\rangle$ . According to our model, the number of photon scattering events and the steady state populations are largely insensitive to polarisation impurities. An impurity as large as 10% would result in  $\sim 1\%$  change in the value of these parameters. Based on this simulation the decision was made to proceed with an experimental test of NDRO performance.

## 5.3 Experimental Realisation

### Obtaining an Initial NDRO Signal

When looking for the first signal, D2 optical pumping was used to prepare the atoms in the  $|F = 4, m_F = 4\rangle$  state before attempting NDRO. The first challenge in experimentally realising the technique was to reach an operational point where the atoms were not being heated out of the traps during the imaging process. In order to achieve this, the 1064 nm trap depth has to be increased significantly. In reference [211], where NDRO was realised with

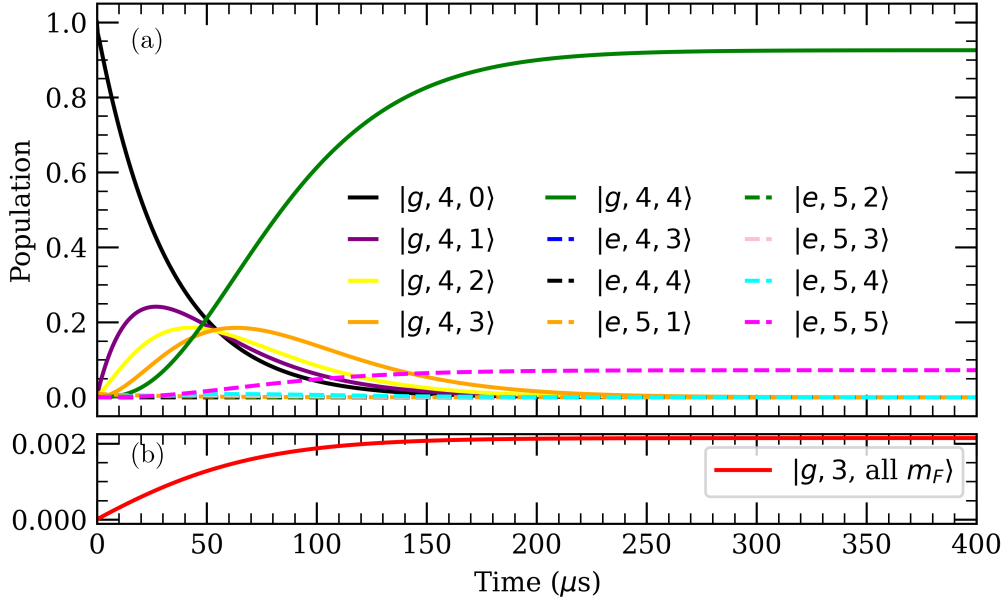


Figure 5.6: (a) Simulation results for incoherent state transfer from the state  $6S_{1/2}|F=4, m_F=0\rangle$  to  $6S_{1/2}|F=4, m_F=4\rangle$  using NDRO  $\sigma+$  polarised light in the absence of repump. The model is explained in the main text. (b) Zoomed-in view of the population leakage into the  $F=3$  manifold of the  $6S_{1/2}$  ( $|g\rangle$ ) state due to spontaneous decay from the  $6P_{3/2}$  ( $|e\rangle$ ) state.

five  $^{87}\text{Rb}$  atoms, the trap depth required was 10 mK. Similarly to this reference, we also apply our NDRO imaging beams out of phase with the trapping laser to avoid tensor light shifts that would cause additional heating. Our traps are operated at a depth of 13 mK for NDRO, but due to this chopping process the effective trap depth is reduced to 6.5 mK during imaging. This is the maximum trap depth we could achieve with our available 1064 nm laser power when operating with a  $7 \times 7$  array of trap sites separated by 8  $\mu\text{m}$ . At this point we achieve a good balance between scalability and minimal atom loss. We chose to operate at 8  $\mu\text{m}$  separation between trap sites, as this is a common spacing we use, but in principle this value is arbitrary and should not affect NDRO performance with the limiting factor being the 1  $\mu\text{m}$  resolution of our atom imaging system. Increasing the trap depth beyond 13 mK on a smaller  $5 \times 5$  array size resulted in only 1-2% increases in atom survival. Figure 5.7 shows example images from a typical experimental sequence which

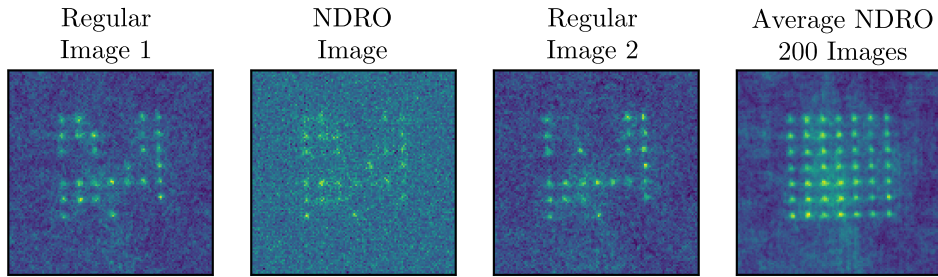


Figure 5.7: Example camera images from a typical experimental sequence which includes NDRO. An NDRO image is inserted between shots of the standard non-state selective imaging technique. The NDRO image has lower background counts because the vertical imaging beams are shuttered, but the overall signal-to-noise ratio is noticeably worse in the NDRO images because we can scatter fewer photons before losing the atoms. The image in the final column is an average across 200 NDRO images.

includes NDRO. The first image is taken with the conventional non-state-selective imaging process to check which sites have atoms loaded into them. The second image is a state-selective NDRO image to check for occupancy of the  $F = 4$  manifold of  $m_F$  levels. A lower background level is observed for NDRO images because the vertical MOT beams which scatter the most background light inside the chamber are switched off and shuttered during NDRO. The image in the third column in Fig. 5.7 is taken with conventional imaging again to check for atom loss without applying the push out beam. The image in the fourth column is a 200-shot average of NDRO images taken on the 49 site array.

### Experimental NDRO Transfer Sequence

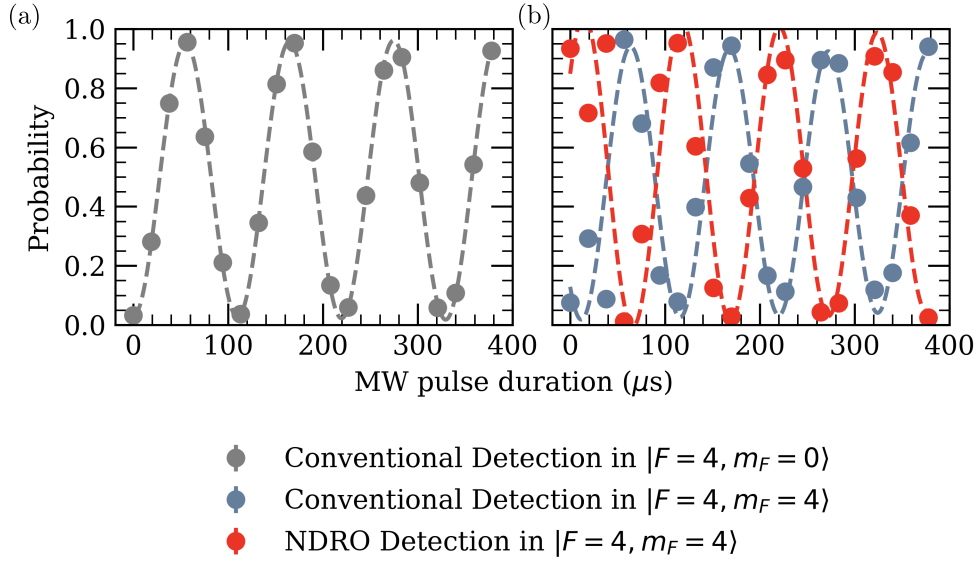


Figure 5.8: Array-averaged experimental results used to test the population transfer efficiency from the clock states to the stretched state using NDRO light. The atoms are initialised in  $|F = 4, m_F = 0\rangle$  with D1 optical pumping and a microwave pulse is used to drive a Rabi oscillation on the clock transition. (a) Results of a control measurement with conventional destructive read out only. (b) Results from a measurement where NDRO light was used to pump the atoms across to the stretched state where they were imaged non-destructively for 10 ms. Following the NDRO, a conventional destructive image was also taken to estimate the probability of leakage into  $F = 3$  during NDRO. The error bars are smaller than the data points. The Rabi oscillations fits are decaying sine curves and the fitted Rabi frequency was  $2\pi \times 9.2(3)$  kHz.

The next stage was to test if the optical pumping transfer fidelity from the clock states to the stretched states was in line with simulations. To do this, D1 optical pumping was applied to prepare the atoms in the  $|F = 4, m_F = 0\rangle$  state followed by a microwave pulse on the clock state transition with a variable length. The resulting Rabi flop on the clock state transition was read out in three different ways. Figure 5.8(a) shows the results of a control measurement where a conventional destructive measurement was performed to read out the state of the atoms. The resulting oscillation has a peak value of  $0.96(1)$  and a minimum of  $0.03(1)$ . This is in line with our optical pumping

fidelity estimate of 0.957(9) from Section 3.5.1. Next, the same preparation steps using D1 optical pumping and scanning the microwave pulse duration are performed, but this time an NDRO imaging sequence is inserted before applying the destructive conventional detection. The NDRO imaging light pumps only the atomic populations in the  $F = 4$  manifold across to the stretched state  $|F = 4, m_F = 4\rangle$ . The duration of this pumping pulse is extended to a total of 10 ms in order to collect the fluorescence from the cycling transition and record an NDRO image. After the NDRO image, we perform a conventional detection step with a push out beam to heat all atoms in  $F = 4$  out of the traps before imaging conventionally for 40 ms as in the control measurement. The results from this experiment are shown in Fig. 5.8(b). The oscillation maxima occur at 0.95(1) and 0.96(1) detection probability, while the minima occur at 0.011(8) and 0.08(1) for the NDRO and conventional detection processes respectively. From this we infer an NDRO optical pumping transfer efficiency of 99(2)%. The reduced contrast of the Rabi oscillation when read out with a conventional image after NDRO can be attributed to population leakage into the  $F = 3$  during NDRO.

### NDRO Parameter Optimisation

The final optimisations were performed by preparing the atoms in the clock state using D1 optical pumping and scanning parameters to obtain the best possible NDRO performance on our hardware. The data in Fig. 5.9 summarises the results of these optimisations performed on  $7 \times 7$  site array with 8  $\mu\text{m}$  separation. The optimal parameters were aimed at achieving a balance between high detection fidelity and minimal errors in the form of atom loss and population leakage into the  $F = 3$  manifold. These requirements are conflicting because the former benefits from more photon scattering events, while the latter is adversely impacted due to the recoil heating and non-zero leakage probability into  $F = 3$  associated with every

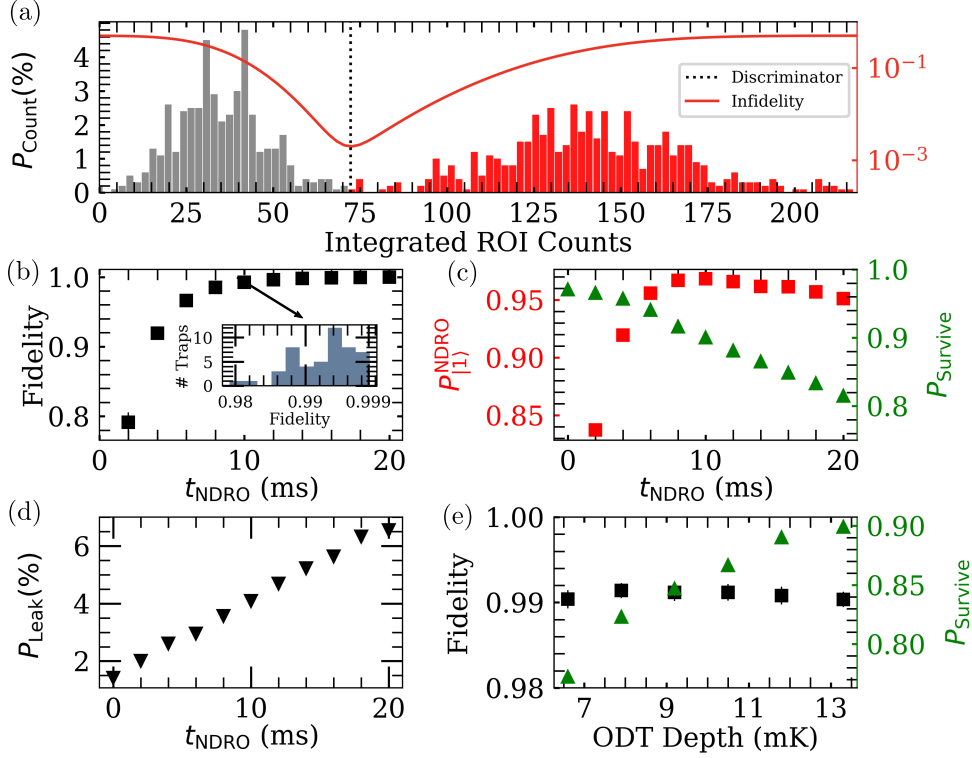


Figure 5.9: Characterising NDRO performance on a  $7 \times 7$  array of 13.3 mK traps separated by  $8 \mu\text{m}$ . A 10 ms imaging duration,  $t_{\text{NDRO}}$ , was found to be optimal based on the following scans. (a) Example histogram of the pixel intensity counts within a region of interest showing signal (red) and background (grey) counts for a single site typical of the 0.9926(6) average discriminator fidelity achieved in our set up. The dashed vertical line represents the best discriminator for this trap site. (b) Discriminator fidelity as a function of the NDRO imaging time. The inset shows the distribution of discriminator fidelities for the full 49 site array at  $t_{\text{NDRO}} = 10$  ms. (c) Detection ( $P_{|1}^{\text{NDRO}}$ ) and survival ( $P_{\text{Survive}}$ ) probabilities as a function of  $t_{\text{NDRO}}$ . (d) Probability of population leakage into the  $F = 3$  manifold,  $P_{\text{Leak}}$ , during NDRO. The observed leakage is an order of magnitude larger than predicted by the Lindblad master equation simulation from Section 5.2.3 which assumed perfect polarisation. The effect of polarisation impurities will be discussed in Section 5.3. (e) Atom survival and discriminator fidelity as a function of the trap depth demonstrating that the state discrimination fidelity remains approximately constant despite increasing atom loss at lower trap depths.

photon scattered. The optimal parameters for our system are a detuning from the  $|F = 4, m_F = 4\rangle \rightarrow |F' = 5, m'_F = 5\rangle$  transition of  $\delta = -0.75\Gamma$ , where  $\Gamma$  is the linewidth of the  $6P_{3/2}$  excited state, and a combined NDRO beam intensity equal to the saturation intensity,  $I_0 = 1.1 \text{ mW/cm}^2$ . Similarly to reference [211], we found a slight improvement in NDRO survival when operating with a 0.6 kHz relative detuning between the two NDRO beams to avoid standing wave formation. Using these parameters, we investigated the optimal imaging duration and found that 10 ms achieves the best balance between detection fidelity and atom survival. Increasing the NDRO duration leads to improved separation, but as can be seen in Fig. 5.9(b) and (c) this has an adverse effect on the probability to retain the atoms in the traps after NDRO,  $P_{\text{Survive}}$ , and the probability of observing a population leakage error into the  $F = 3$  manifold,  $P_{\text{Leak}}$ . The histogram in Fig. 5.9(a) shows the typical separation we can achieve between signal and background counts when applying NDRO for 10 ms with the optimal parameter values. After performing a binomial distribution fit to the two peaks following the image processing steps described in Section 3.4, we obtain an average discriminator fidelity of 0.9926(6). NDRO images require different thresholds compared to regular images because both the signal and the background counts are lower due to the reduced imaging duration, and the fact that the vertical-axis imaging beams are blocked during NDRO because they do not have a well-defined polarisation relative to the quantisation axis. Having trained our atom detection algorithm in this way, we record a raw probability of detecting an atom in  $F = 4$  using NDRO,  $P_{|1\rangle}^{\text{NDRO}}$ , of 0.968(1) limited by our D1 optical pumping fidelity. In this configuration, we record values of  $P_{\text{Survive}}=90.0(2) \%$  and  $P_{\text{Leak}}=4.1(1) \%$ . Finally, Fig. 5.9 shows the results of a test used to determine if the final optimised settings would allow operation at lower trap depths for improved scaling within our fixed 1064 nm power budget. No such improvement was found, but the experimental scan results show that one could still achieve good discrimination between signal

and background even at lower trap depths at the cost of higher atom loss. This means that if one were willing to operate with a reduced experimental repetition rate, the NDRO technique for post-selection could still be applied to larger arrays than the  $7 \times 7$  sites considered in this work.

### **Comparison to State of the Art**

The performance of our experimental realisation of NDRO as compared to previous results in the literature is summarised in Table 5.1. The work described in this thesis has implemented NDRO on the largest number of atoms to date. Our experiment's detection fidelity is competitive with previous methods, except for reference [290] where a single photon counting module (SPCM) with adaptive time-resolved feedback was used to achieve 99.91% fidelity. The time-resolved adaptive feedback entails imaging in  $5 \mu\text{s}$  increments and interrupting the process as soon as the detection threshold has been exceeded to reduce unnecessary scattering events and the associated errors and atom loss. However, this technique would be more difficult to scale to large array sizes, because it would require keeping track of every atom's photon counts whilst imaging. This increases the demands on the camera data transfer bandwidth. In addition, without the use of single-site imaging beams, it is not obvious how the detection process could be interrupted at earlier times for only some of the atoms in a large array without the loss of information from other atoms. The performance in our set up in terms of the probability to observe leakage into the  $F = 3$  manifold,  $P_{\text{Leak}}$ , and the atom survival probability,  $P_{\text{Survive}}$ , during NDRO needs to be improved in order to be in-line with the state of the art. The longer imaging times and the lower quantum efficiency of the sCMOS camera in our experiment compared to the detectors used in other experiments are a likely reason why we observe this level of performance. In reference [291] an additional image processing method using Bayesian statistics to find the region of interest pixels which

Table 5.1: Comparison to state of the art in NDRO.

Ref.	Fidelity	$P_{\text{Leak}}$	$P_{\text{Survive}}$	Duration (ms)	Detector	# Atoms
[288]	98.6%	-	> 98%	1.5	Avalanche Photodiode	1 x $^{87}\text{Rb}$
[211]	98.7%	2%	> 98%	5	EMCCD Camera	6 x $^{87}\text{Rb}$
[291]	>98%	2%	98.8%	10	EMCCD + Bayesian Inference	10 x $^{87}\text{Rb}$ Lattice
[290]	99.91%	-	99.1%	0.25	SPCM + Time-resolved Feedback	1 x $^{133}\text{Cs}$
This work [280]	99.1%	4%	90.1%	10	sCMOS Camera	49 x $^{133}\text{Cs}$

contain the most information about the state of the atom during NDRO were employed to improve the single-site detection fidelity in the context of optical lattices. Alternative techniques based on defining a point-spread function for the atomic fluorescence signal have been shown to improve detection fidelities at low signal-to-noise ratios [292] in optical lattice experiments and could be implemented in our set-up to allow us to operate with shorter imaging times for reduced atom loss and leakage without compromising detection fidelity.

### Understanding & Improving Performance

In order to understand the performance limitation of the NDRO procedure realised in our experiment, a simulation model was developed based on the analysis from the supplementary materials in reference [211]. The model takes into account the bias magnetic field, detuning and intensity of the

probe beams, the polarisation purity and the angular mis-alignment between the quantisation axis and the dipole trapping laser polarisation vector. The effects of the angular misalignment are implemented into the model using Wigner angular momentum rotation matrices [293] to work out how the polarisation of the 1064 nm laser appears at the atoms.

The first factor to consider is a calculation of the number of photons scattered in 10 ms using our experimental parameters. This scattering rate sets the base scaling for the heating rate and for the rate of leakage into the  $F = 3$  manifold. With a bias magnetic field of 6.0 G, detuning  $\delta = -0.75\Gamma$  and combined beam intensity equal to  $I_{\text{sat}}$  we arrive at a scattering rate of  $3.8 \times 10^6$  photons/s. As we operate the trapping light and the imaging light out of phase with a 50 % duty cycle, the effective illumination time during our NDRO images is actually 5 ms. An absolute worst-case scenario calculation using the number of photons scattered in 5 ms and a recoil temperature of 198.3 nK for the D2 line transition [128] predicts that the atoms will heat up to 7.65 mK during NDRO. This exceeds the 6.65 mK effective trap depth of our 13.3 mK deep 1064 nm traps when operated at a 50 % duty cycle. This recoil heating estimate is a gross overestimate because we operate with two counter-propagating beams and the momentum kicks they give to the atoms in our experiment upon absorption cancel out on the average provided the two beam intensities are well-matched and the beams are well-aligned. This leaves the heating effects from the momentum gained by the atom upon spontaneous emissions events which are random in direction and the fluctuations in the number of photons absorbed from each side per unit of time, both of which obey Poissonian statistics. Following the approach developed in Chapter 9 of reference [117] for the case of optical molasses in zero magnetic field, the mean square velocity along a single axis can be calculated using

$$\bar{v}_z^2 = (1 + 1/3)E_r \frac{2R_{\text{scatt}}}{\alpha}, \quad (5.4)$$

where  $E_r$  is the recoil energy and  $\alpha$  is the molasses damping constant given by

$$\alpha = 2\hbar k^2 \frac{-2\delta}{\delta^2 + \Gamma^2/4} R_{\text{scatt}}. \quad (5.5)$$

Here  $k$  is the photon momentum. Using these equations and our experimental parameters we arrive at an equilibrium temperature of 90  $\mu\text{K}$  after 10 ms of chopped NDRO for an isotropic emission pattern. However the atoms during NDRO have the emission pattern of a rotating dipole because they are driven by two circularly polarised beams of the same handedness [211]. If we account for this, there is additional undamped heating along  $x$ - and  $y$ -axes which results in an equilibrium temperature of 730  $\mu\text{K}$ . By defining a Maxwell-Boltzmann distribution based on this temperature, it can be shown that there is a 0.02% probability associated with atomic kinetic energies that exceed the trap depth. It should be noted that this model for optical molasses is not strictly valid in our case because we operate with a 6.0 G bias field which lifts the Zeeman degeneracy of the hyperfine levels. However, one could argue that it is not a bad approximation because we are interested in the temperature of an atomic population that has been prepared in the stretched state with high fidelity and a static bias magnetic field. Furthermore, the populations are being driven in a cycling transition which, provided the polarisation purity is high enough, closely resembles a two-level system. The presence of a magnetic field has been shown to affect laser cooling mechanism in references [294, 295] for the case of an applied magnetic field gradient as used in a magneto optical trap. In reference [296] a numerical simulation was carried out to show that a static, spatially uniform magnetic field can lead to loss of sub-Doppler cooling in an applied magnetic field of 4 G for  $^{87}\text{Rb}$  modelled

along one dimension in a  $\sigma+$   $\sigma-$  polarisation configuration. While relevant, none of these observations are directly applicable to NDRO because, unlike polarisation gradient cooling, the two beams being applied along a single axis have the same  $\sigma+$  polarisation at the atoms. Developing a theoretical model for the momentum exchange processes in this specific configuration is beyond the scope of this work. Using the Maxwell-Boltzmann distribution and asking the question, what temperature do the atoms need to have in order to have a 10 % probability of escaping our 6.65 mK deep traps (effective depth when considering 50 % duty cycle), we obtain a value of 2.9 mK. This prediction could be verified by taking a release and recapture measurement after NDRO or using an alternative technique as implemented in [197] which consists of adiabatically lowering the trap depth after NDRO and monitoring when the atoms start to escape the trap to infer their temperature. Other heating mechanisms such as the in-trap heating rate and the heating due to the chopping of the 1064 nm light at a rate of 1 MHz are also present, but their contribution is expected to be negligible compared to the heating due to photon scattering during NDRO.

Next, the factors contributing to the observed  $P_{\text{Leak}} = 4\%$  in our experiment will be considered. Firstly, there is the polarisation purity of our 852 nm NDRO imaging light. Any non- $\sigma+$  components of polarisation will break the cycling transition and introduce excitation pathways to states which can radiatively decay to the  $F = 3$  manifold. The polarisations of the two NDRO beams were set using zero order quarter- and half-waveplates adjusted based on the signal from a free-space polarimeter<sup>67</sup> after the beams had passed through any polarisation-altering optics such as dichroic mirrors. Based on the polarimeter reading, we have achieved polarisation purities  $> 99.9\%$  using this method. In reference [211] a home-built equivalent method implementing a rotating polarisation optic into the set up was used to extract a polarisation purity from the contrast of transmission fringes measured on a

<sup>67</sup> SK010PA from Schäfer + Kirchhoff.

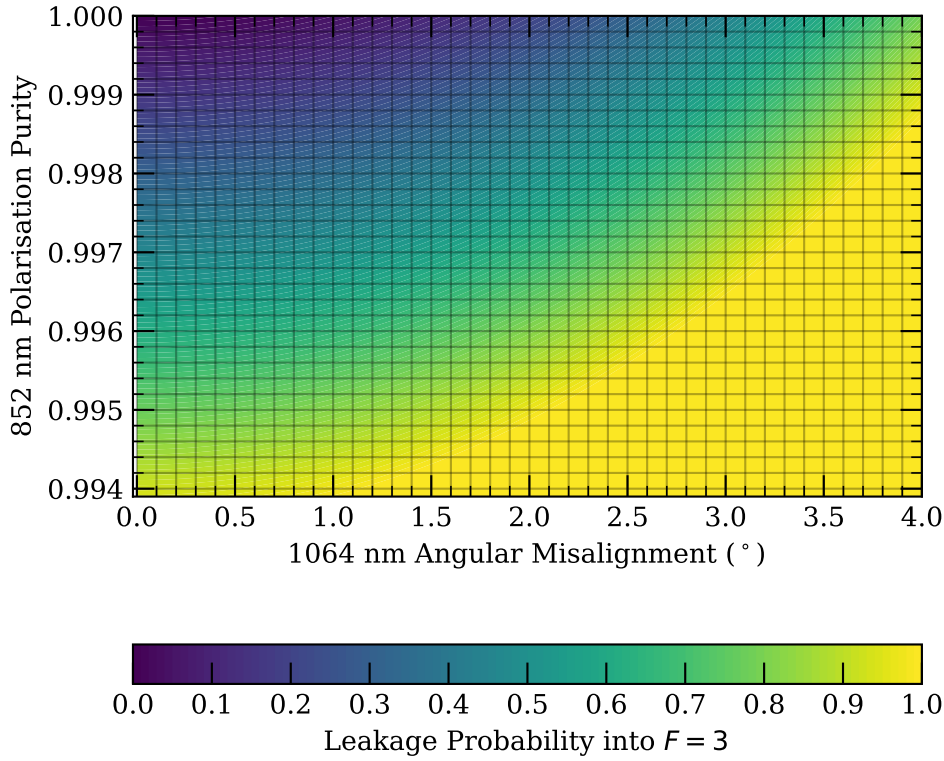


Figure 5.10: Contour plot of the NDRO leakage parameter sensitivity to the 852 nm NDRO beam polarisation purity and the angular misalignment of the 1064 nm trapping laser polarisation vector with respect to the quantisation axis. The simulation is based on the experimental parameters used in our experiment, outlined in the main text. The colours represent the probability of a leakage event into the  $F = 3$  manifold during the 10 ms NDRO procedure for a given set of parameter errors.

photodiode after the light had passed through a linear polariser. The polarisation of the beams in our set up was further optimised by rotating the pairs of quarter and half-waveplates installed in the set up to maximise the depumping time constant when applying NDRO light to a sample of atoms prepared in  $|F = 4, m_F = 4\rangle$ . The light was applied for long durations until the atomic populations were fully depumped into the  $F = 3$  manifold and an exponential fit was used to extract the value of the depumping time constant.

The same method of recoding the depump time was also used to scan the magnetic field shim coil currents to optimally align the bias field direction along the k-vector of the NDRO light similarly to what was implemented in [211].

Using the simulation model and the calculated photon scattering rate, the probability of a depumping event in our set up as a function of polarisation purity can be estimated. To begin with the assumption will be made that the alignment of the 1064 nm polarisation vector with the bias field and the k-vectors of the NDRO light is perfect. To fully explain the observed leakage probability of 4.1(1)%, the model predicts a polarisation impurity of  $2.7 \times 10^{-4}$  in our NDRO beams or a polarisation purity of 99.973 %. It should be noted that the polarisation purity as seen by the atoms is a function of both the beam's polarisation and the alignment of its k-vector along the quantisation axis, because any misalignment would introduce  $\pi$  and  $\sigma$ -polarisation components in the atomic frame of reference.

Allowing for some finite degree of misalignment between the dipole trapping laser and the quantisation axis and using the perfect polarisation purity initially, the simulation predicts that an angular misalignment  $\sim 1^\circ$  will be enough to explain the observed leakage rate of 4.1(1)%. Figure 5.10 shows a summary contour plot showing the sensitivity to polarisation purity and the angular misalignment of the 1064 nm beam based on our simulation. The 1064 nm could be aligned using the NDRO leakage probability as a cost function to minimise. By installing a piezo mirror in the 1064 nm beam path, this could be automated to run as an overnight measurement.

## 5.4 NDRO for SPAM Error Suppression

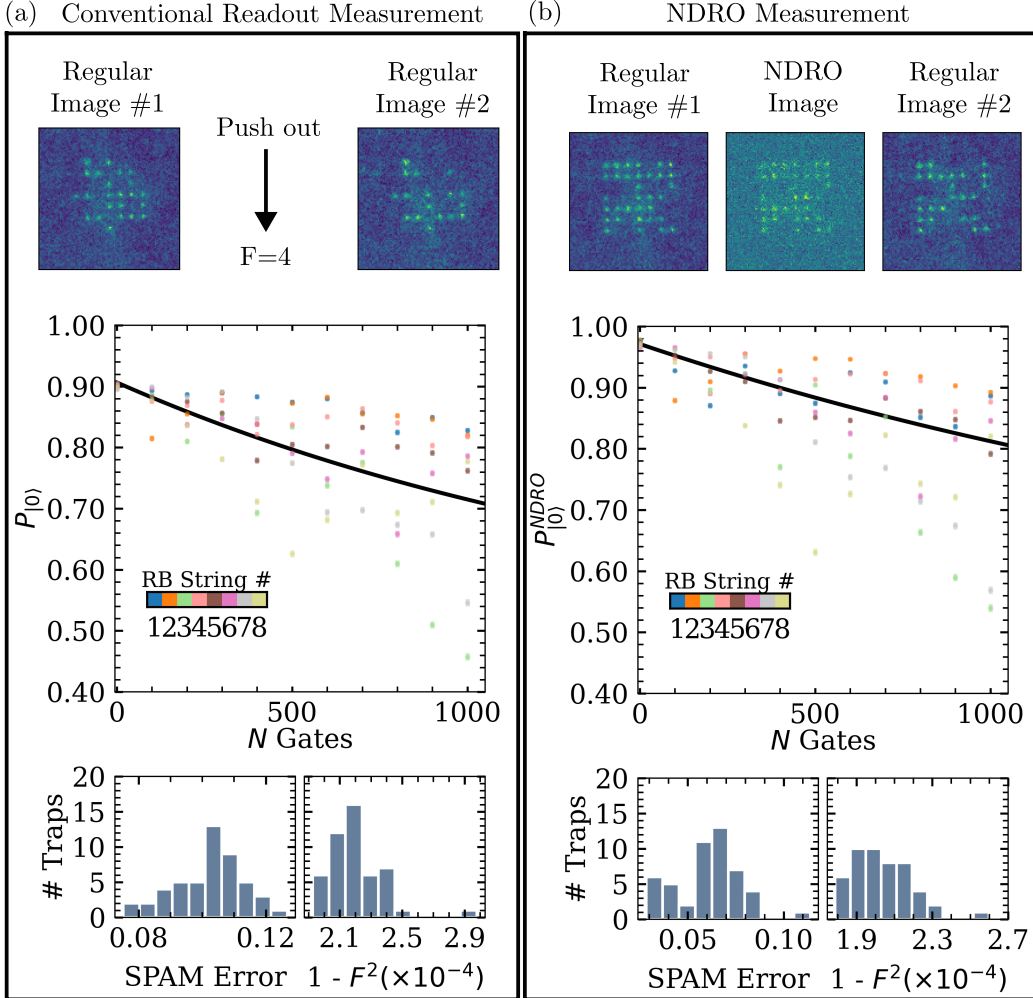


Figure 5.11: Randomised benchmarking measurements taken on a 49 site array with 8  $\mu\text{m}$  spacing. (a) Control measurement with regular state detection using push out beam. (b) Same measurement as in (a), but this time the state of the atoms was read out non-destructively for SPAM error suppression. This is implemented by inserting an NDRO image in between the two regular images instead of applying a push out beam. The final image now only checks for atom survival and the data is post-selected for zero atom loss between the initial and final image. In this way the contribution of the finite trap lifetime to the SPAM error is eliminated at the cost of a reduced data rate.

The ultimate objective of the work carried out in this chapter was to perform the first demonstration of a practical benefit from using NDRO. Specifically,

the intention was to use the technique to suppress the significant SPAM errors observed in our randomised benchmarking measurements by using NDRO as a way to implement post-selection based on atom survival. Figure 5.11 shows a side-by-side comparison of randomised benchmarking results read out conventionally (a) and non-destructively (b). A 49 site array with 8  $\mu\text{m}$  spacing was used instead of 225 sites because of the power limitations of our trapping laser outlined in Section 5.3. The same random gate strings were used as the ones for the larger array. As expected, the two measurements produced almost identical average gate fidelities with array-averages of 0.99978(9) and 0.99978(1) for the NDRO and conventional technique respectively. The reason that the recorded fidelity is worse compared to the 225-site-array results is the limited dynamic range of the acousto-optic modulator (AOM) controlling the 1064 nm trapping light. As explained in section 3.3.2, we use adiabatic ramping down of the trapping potential to lower the atom temperature for improved  $T_2^*$  coherence times. The same laser power is incident onto the AOM when performing an NDRO sequence with a 49 site array as the maximum power required to operate with 225 trap sites using conventional readout<sup>68</sup>. The AOM amplitude response as a function of the input control voltage has been calibrated to be approximately linear, and for the experimental ramping stage of the 1064 nm traps we operate at the bottom of that calibration range. This results in a situation where the same absolute laser power is being split across 49 sites instead of 225 sites resulting in deeper potentials and hotter atoms during the benchmarking sequence. Furthermore, the magnitude of the differential AC Stark shift on the clock states is increased from 39 Hz to 211 Hz further shortening the expected reversible dephasing time. This hypothesis was verified by recording a comparison of Ramsey fringes for the 225 site and 49 site arrays and extracting  $T_2^*$  coherence times of 14(0.8) ms and 12(0.6) ms respectively. The data is available in

<sup>68</sup> This power is the maximum available output power in our 1064 nm laser of 18 W, which reaches the atoms with approximately 50% efficiency when accounting for all the losses along the beam path.

the supplementary materials of the publication that resulted from this work [280]. Using  $T_2^* = 12$  ms in equation (4.14) which relates the average gate fidelity to the reversible dephasing time, the predicted average gate fidelity is still  $> 0.9999$ . A  $T_2^*$  time of 8 ms would be required to match the recorded gate fidelities on the small 49-site array. Similar discrepancies between the prediction obtained based on equation (4.14) and the measured average gate fidelities were observed in reference [68] and attributed to errors in pulse length and detuning. Unlike reference [68], composite BB1-pulses were used in our benchmarking experiments to reduce sensitivity to pulse area errors so the only plausible remaining explanations for the discrepancy are errors in the detuning. Ideally, comparative spin echo measurements would have been performed on the two arrays to confirm if the observed difference in fidelities is due to irreversible decoherence mechanisms. If the recorded  $T_2'$  times were significantly different, this would suggest that the 1064 nm laser amplitude fluctuations and pointing instabilities are the likely cause for observing worse performance on the smaller array. On the other hand, if the measurement returned similar  $T_2'$  times for the two arrays, then the remaining probable cause would be the noise and drift of the environmental conditions. It is possible that the background magnetic field noise and experimental temperature stability were worse during the smaller array measurements as compared to when the 225 site array data was being taken. The measurements were separated in time by several days.

Importantly, the comparative measurement was a success in terms of SPAM error suppression. The same scaling method was used for the conventional data as the one for the conventionally-readout 225 site array in Section 4.5, but the baseline survival on the 49-site array was higher 0.95(1) due to the increased trap depth during the microwave operations. This re-scaling ensures a fair test against the NDRO data which has been post-selected for atom survival in the final image. Even with this rescaling, the observed SPAM error with NDRO was suppressed by a factor of 1.7 compared to the control mea-

surement on the same array. This was achieved by using our NDRO instead of a push out beam to detect atoms in  $F = 4$ , which allows us to discriminate between atom loss and the presence of an atom in  $F = 4$ . In this way we are able to post-select our data for full atom survival in the final image which is a conventional image without a push out beam and should induce no loss. As discussed in Section 4.4, randomised benchmarking (RB) was developed to be insensitive to SPAM errors, but other techniques such as quantum state tomography (QST) have a large sensitivity to SPAM errors [265]. Therefore in the future the NDRO technique could be used in conjunction with QST to extract more information about the system performance than just using RB.

## 5.5 Conclusion

In conclusion, the work described in this chapter amounts to the largest scale demonstration of a practical benefit from the NDRO technique at the time of writing. The technique was used to suppress state preparation and measurement (SPAM) errors in a randomised benchmarking sequence by a factor of 1.7 compared to a control measurement with the same parameters but using conventional detection with a push out beam. Compared to smaller scale demonstrations, the NDRO performance in our system in terms of duration, survival and leakage probabilities needs to be improved. This could be achieved by using higher numerical aperture microscope objective lenses and an EMCCD camera with higher quantum efficiency at 852 nm to minimise the required number of scattered photons for good detection fidelity. In addition, magic wavelength traps [70] or blue-detuned traps for ground state atoms [230, 297, 298] could be used instead of our red-detuned 1064 nm traps to suppress differential AC Stark shifts and obviate the need to chop the imaging and trapping light out of phase which reduces the effective trap depth and adds some amount of heating. In addition, more advanced image-

processing techniques developed for optical lattices [292, 299] could be used to boost detection fidelity without the need to scatter more photons.

In terms of future work, the coherent microwave transfer sequence tested in the early stages of the project would need to be improved in order to progress towards using NDRO as a mid-circuit measurement. The reason why incoherent optical pumping methods are not likely to be good candidates for this is that they significantly increase the atom temperature with each transfer cycle. The existing sequence could be improved through the use of coherent adiabatic rapid passage pulses with microwaves or Raman lasers. Shortly after publishing the work described in this chapter, the first mid-circuit measurement using the NDRO technique was demonstrated in [111] where the transfer back to the clock states after readout was performed with composite microwave CORPSE pulses [300] which reduce sensitivity to MW resonance drifts, while dynamical decoupling pulses were being applied to the data qubits to maintain their coherence during readout. This work also proposed a re-cooling scheme for the ancilla qubits on the 685 nm quadrupole transition  $6S_{1/2}|F = 4\rangle \rightarrow 5D_{5/2}|F = 6\rangle$  as demonstrated in [301] to counteract the inevitable heating associated with NDRO population transfers. As mentioned in the chapter introduction, there have also been recent demonstrations of mid-circuit measurements on  $^{171}\text{Yb}$  atoms in references [281–283].

# Chapter 6

## Analogue Quantum Computation

The aim of this chapter is to summarise the early quantum simulation results obtained on our system as an initial benchmark of its current level of performance. The first section outlines the basics of the 1D quantum Ising spin model we used and how it can be mapped to an array of interacting Rydberg atoms. Section 6.2 describes how the presence of the Rydberg interactions was validated in our system and how the strength of the dipole-dipole interaction for different inter-atom separations was measured. The final section of this chapter presents some early experimental results for the quantum simulation of the Ising 1D spin chain problem in the regime where classical simulation of the system is still very much tractable. These results serve as an initial benchmark and a way of identifying what hardware improvements are required to achieve better agreement with theory before attempting more challenging problems.

### 6.1 Quantum Ising Model for 1D Spin Chains

The Ising model bears the surname of Ernst Ising who first solved it analytically for a one-dimensional chain of magnetic dipoles in an external magnetic field as part of his doctoral thesis [302]. The model was originally

developed to describe the behaviour of ferromagnetic materials in classical statistical mechanics. It explained why some materials can attain a degree of net magnetisation when cooled below a certain critical temperature even in the absence of an external magnetic field. In a magnetic material the magnetic dipole moments of the constituent particles are aligned along the same direction, while in a paramagnetic material their orientations are distributed randomly and average out to zero [303]. In the context of the Ising model, a transition from an ordered state to a disordered state and vice versa is called a phase transition. The total magnetisation (energy) of a system of  $N$  magnetic dipoles,  $\sigma_i$ , with nearest neighbour interactions,  $J_{ij}$ , under an applied external magnetic field,  $h$ , is described by the Hamiltonian [304]

$$H = - \sum_{i < j} J_{ij} \sigma^i \sigma^j - \sum_j h^j \sigma^j, \quad (6.1)$$

where  $\sigma \in \{-1, +1\}$  in units of the particle's magnetic dipole moment. In its classical form, the Ising model exhibits finite-temperature phase transitions only when considering systems with more than one dimension. However, if the particles are modelled as quantum-mechanical objects with spin angular momentum operators, i.e. Pauli matrices, describing their magnetic moments, then one can observe a quantum phase transition (QPT) in 1D. This can occur at zero temperature in the case of an applied external magnetic field,  $h_t$ , which is transverse to the quantisation axis set by the direction of a longitudinal field,  $h_l$ . The Hamiltonian describing this configuration is

$$H = - \sum_{i < j} J_{ij} \hat{\sigma}_z^i \hat{\sigma}_z^j - \sum_j h_l^j \hat{\sigma}_x^j - \sum_j h_t^j \hat{\sigma}_z^j. \quad (6.2)$$

The Pauli operators  $\hat{\sigma}_x$  and  $\hat{\sigma}_z$  used to describe the particles' magnetic moments along the two field components do not commute. This adds quantum mechanical fluctuations to the model which give rise to a continuous QPT from a disordered to an ordered phase as the value of the parameter  $h_t$  is

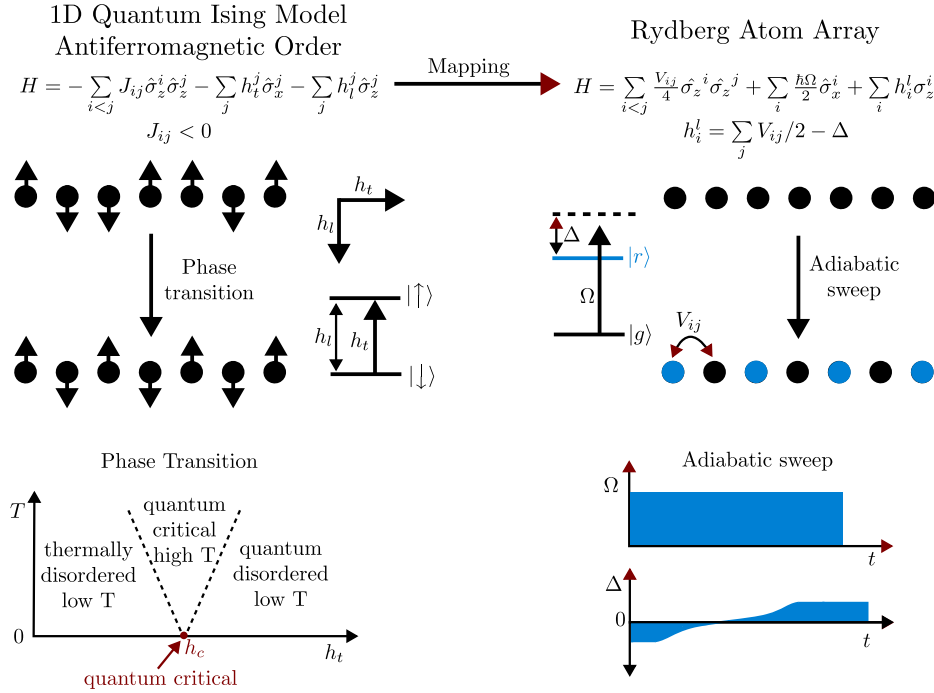


Figure 6.1: Illustration of how the quantum Ising model for a 1D spin chain with antiferromagnetic interactions,  $J_{ij} < 0$ , can be mapped to an array of Rydberg atoms. The longitudinal magnetic field  $h_l$  which lifts the spin energy degeneracy maps to a Rydberg laser detuning,  $\Delta$ , and an energy offset term,  $\sum_j V_{ij}/2$ . The transverse field  $h_t$  maps to the Rydberg excitation Rabi frequency,  $\Omega$ , and the interaction term,  $J_{ij}$ , maps to the van der Waals interaction energy,  $V_{ij}$ . An adiabatic sweep of the Rydberg laser detuning,  $\Delta$ , while driving Rydberg transitions with a laser frequency  $\Omega$  mimics the zero-temperature phase transition from a disordered to an ordered phase. This evolution explores the  $T=0$  line on the phase diagram, starting with  $h_t < h_c$  where the system is disordered and moving into the region  $h_t > h_c$  where the system is in an ordered phase.

scanned through some critical value,  $h_c$  [305]. A phase diagram of this continuous phase transitions is shown in Fig. 6.1. The sign of the interaction term  $J_{ij}$  sets whether the ordered phase is ferromagnetic or antiferromagnetic. For  $J_{ij} < 0$ , equation (6.2) describes an antiferromagnetic interaction because it is energetically favourable for neighbouring spins to align in the opposite directions.

As illustrated in Fig. 6.1, this type of model maps very easily and naturally onto the Hamiltonian of a Rydberg atom array. The idea was first proposed in

reference [306] for optical lattices. The atoms are initially prepared in their ground state,  $|g\rangle$ , with interatomic separations smaller than the Rydberg blockade radius. The Rydberg blockade radius is the distance,  $R_{ij}$ , for which the energy of the van der Waals interaction<sup>69</sup> between atoms  $i$  and  $j$  is equal to the driving field Rabi frequency [72]. The interactions  $V_{ij}$  are switched on when the atoms are coupled to an excited Rydberg state,  $|r\rangle$ , by a global laser field with Rabi frequency  $\Omega$  and detuning from resonance  $\Delta$ . The Hamiltonian of this system takes the form

$$H = \sum_i \frac{\hbar\Omega}{2} \hat{\sigma}_x^i + \sum_{i<j} V_{ij} \hat{n}^i \hat{n}^j - \sum_i \Delta_i \hat{n}^i, \quad (6.3)$$

where  $\hat{\sigma}_x = |g_i\rangle\langle r_i| + |r_i\rangle\langle g_i|$  and the operator  $\hat{n}_i = |r_i\rangle\langle r_i|$  counts if there is a Rydberg excitation on site  $i$ . By tuning the inter-atomic separation to introduce next-nearest interactions and beyond, an experiment can access different symmetries in the ordered phase as demonstrated in [194]. In this work only the nearest-neighbour interaction will be considered. The Hamiltonian from equation (6.3) can be re-written into a form that matches the quantum Ising model Hamiltonian from equation (6.2) to highlight the correspondence between the two systems [307]. The transformation required to achieve this is  $\hat{n}^i = (1 + \hat{\sigma}_z^i)/2$  and the final result up to a constant is

$$H = \sum_{i<j} \frac{V_{ij}}{4} \hat{\sigma}_z^i \hat{\sigma}_z^j + \sum_i \frac{\hbar\Omega}{2} \hat{\sigma}_x^i + \sum_i h_i^l \hat{\sigma}_z^i, \quad (6.4)$$

where the term  $h_i^l = \sum_j V_{ij}/2 - \Delta$  captures the effects of the laser detuning and the Rydberg interactions each atom experiences which act as an effective longitudinal field. The effects of this longitudinal field depend on the geometrical arrangement of the atoms. For a ring-type arrangement or in an idealised infinite lattice, this longitudinal field is the same for all atoms and

<sup>69</sup> As described in Section 2.4, the energy of the long-range, van der Waals interaction is given by  $V_{ij} = -C_6/R_{ij}^6$ .

can be eliminated by applying a global detuning, but for a system with open boundary conditions or with a finite length, the spins at the edges evolve differently than the bulk as shown in reference [308]. It is important to note the sign difference in the interaction terms of the Rydberg atom realisation of the Ising Hamiltonian. This difference is due to the fact that most Rydberg tweezer array experiments, including our experiment, typically couple to a Rydberg S state. For an S state the nearest state in energy is usually lower in energy and therefore the sign of the energy defect is negative for all principle quantum numbers  $n$ . As discussed in Section 2.4, the sign of the energy defect determines the sign of the  $V_{ij}$  interaction term in the van der Waals regime based on equation (2.59). Therefore the models realised with Rydberg atom arrays typically explore the antiferromagnetic ordered phase because  $\Delta E = V_{ij} > 0$ .

The quantum Ising model is exactly solvable in one and two dimensions [309] and experimental simulations of the model in 1D and 2D have been performed in a number of different platforms including trapped ions [310], superconducting qubits [311], optical lattices [308, 312] and tweezer arrays [86, 87, 194, 307]. However, the problem still serves as a convenient benchmarking tool for a new quantum simulation platform because as the number of atoms in the array grows, the energy gap between the ground states of the Hamiltonian gets exponentially smaller which makes it more taxing for the quantum hardware. This is the context for the work described in this chapter where the simplest case of a 1D spin chain was used as a test of the analogue simulation capabilities of our platform.

## 6.2 System Calibration

Before attempting to tackle an analogue optimisation problem, a range of calibration measurements were performed first to ensure th at dipole-dipole

interactions in our system are well-understood and behave as expected. The aim of this section is to summarise the results of these calibrations steps.

### 6.2.1 Rabi Frequency $\sqrt{N}$ Enhancement

The objective of the first test was to simply show that atoms placed inside a Rydberg blockade radius of each other are interacting. This was done by using stochastic array loading on an array of trimers shown in Fig. 6.2(a), such that within a single experimental run one could obtain data for three different scenarios: a single atom loaded in a trimer, two atoms loaded and all three atoms loaded. The expected behaviour was a  $\sqrt{N}$  enhancement in the Rabi frequency, where  $N$  is the number of interacting atoms within a Rydberg blockade radius of each other. As explained in Section 2.4, the Rydberg blockade condition dictates that only a single excitation can be present in the blockade volume at any time, but for  $N$  atoms contained inside that volume there are  $N$  different configurations which satisfy this condition giving rise to an entangled  $|W\rangle$  state with an enhanced coupling. In the specific array configuration used in our experiment, the groupings of three trap sites were spaced at  $6\ \mu\text{m}$  from each other, and each trimer was separated from all adjacent trimers by  $16\ \mu\text{m}$ . Given that the calculated Rydberg blockade radius for the  $80S_{1/2}$  state with a Rabi frequency of  $1\ \text{MHz}$  is  $R_b = 11\ \mu\text{m}$ , these spacing ensure that atoms within a trimer interact while interactions between different trimers are negligible due to the rapid  $1/R^6$  decay of the interaction strength in the van der Waals regime. The results of our experiment for  $N \in \{1, 2, 3\}$  are summarised in Fig.6.2 (b) - (d).

The resulting ratios of the enhanced Rabi frequencies relative to the reference frequency are  $1.42(3)$  and  $1.74(4)$  for  $N = 2$  and  $N = 3$  respectively, showing good agreement with theory. The fast timescales for dephasing observed in this data set are due to two factors. First, the data shown is an array average and due to trap-to-trap variations in the Rabi frequency, the averaged

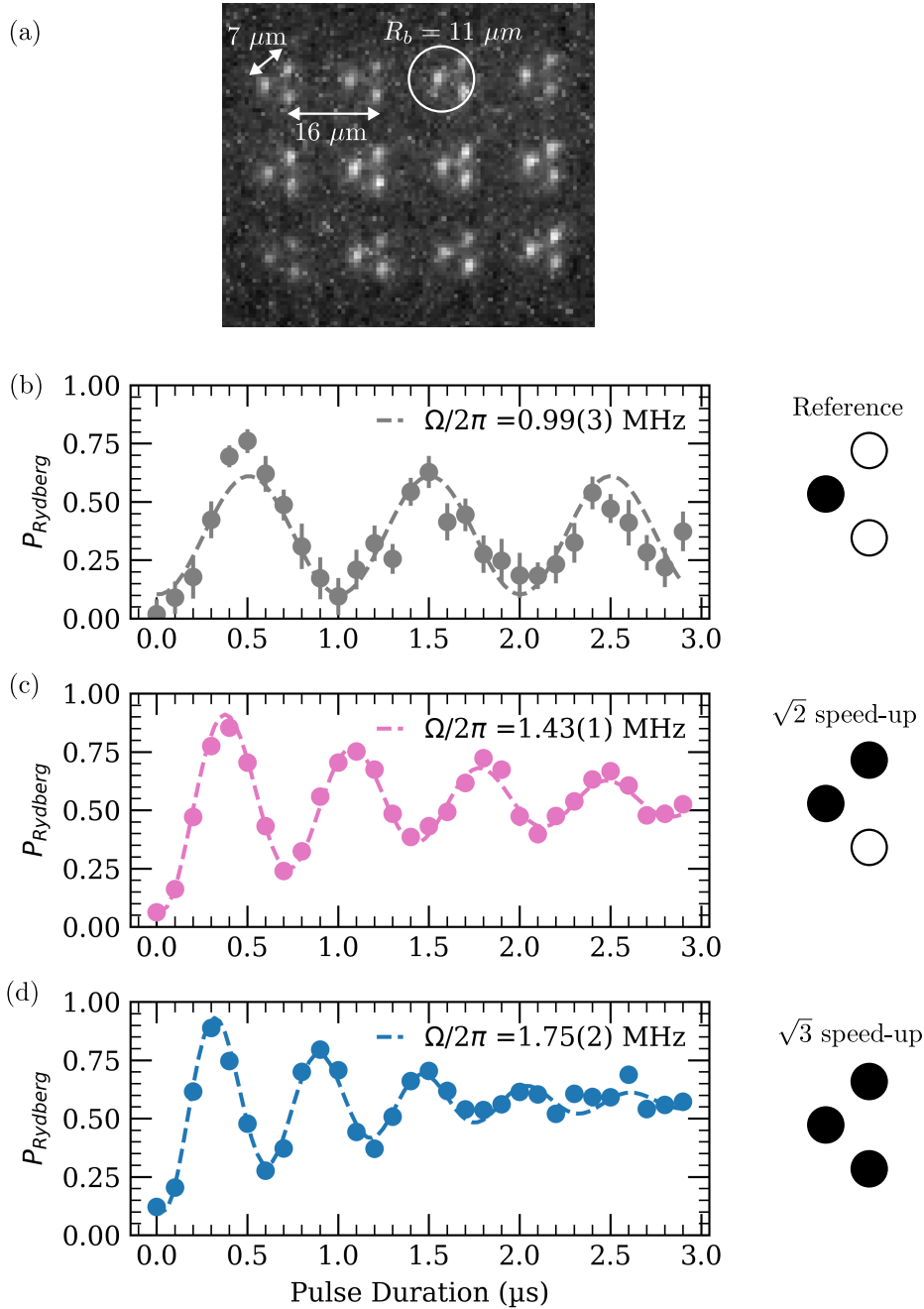


Figure 6.2: Measurements of the  $\sqrt{N}$  enhancement of the transition Rabi frequency due to Rydberg blockade. (a) Averaged image of an array of trimers showing the inter-atomic separations relative to the Rydberg blockade radius for the  $80S_{1/2}$  state and the measured  $1 \text{ MHz}$  Rabi frequency. (b) Reference Rabi oscillation when only a single atom loaded in the trimer. (b)  $\sqrt{2}$  enhancement of the Rabi frequency when any combination of two atoms was loaded into a trimer. (c)  $\sqrt{3}$  enhancement of the Rabi frequency when all three atoms were loaded in a given trimer. The collectively-enhanced Rabi oscillations experience a faster rate of decoherence because of the increased sensitivity to fluctuations in the atomic positions caused by the pointing instability of our trapping laser as explained in Section 6.2.2. All oscillations are averaged across the full array. The fit is a decaying sine function.

data appears to dephase faster than individual traps. The decision to work with array averaged data was made in order to speed up data taking and obtain smaller error bars with fewer measurements. Secondly, the Rydberg resonance was calibrated using a simple  $\pi$  pulse method which was later found to be inaccurate because of variations in the AC Stark shift due to the finite 459 nm AOM rise time. At the time of recording this data, the more sophisticated calibration procedure described in Section 3.7.4 had not yet been implemented. Finally, it should be noted that the Rabi oscillations in the blockade regime decay faster as the number of atoms participating in the interaction,  $N$ , increases. This is due to the strong dependence of the Van der Waals interaction on the interatomic separations,  $R$ , which can fluctuate from shot to shot due to the pointing instability of our trapping 1064 nm laser. The sensitivity of the interaction to such fluctuations as a function of  $R$  will be discussed in the next section, but with regards to this measurement it is important to note that it increases linearly with  $N$ .

## 6.2.2 Dipole-Dipole Interaction Energy Calibration

With clear evidence that the atoms in our array are interacting, the next calibration stage was to quantify the magnitude of the dipole-dipole interaction,  $V_{dd}$ . For this measurement, the atoms were arranged in groups of two as shown in the averaged image in Fig. 6.3(a). Atom sorting was used to improve the data rate for this experiment and the top two and bottom two rows of the array were used as a reservoir of atoms with which to fill the sub-array made up of 9 atom pairs. The measurement follows the method from reference [223], which uses two sequential pulses on the Rydberg transition with a varying frequency offset on the second pulse,  $\Delta$ , used to bridge the energy gap introduced by the dipole-dipole interaction. The applied pulses have a duration equal to the  $\pi$  time of the  $\sqrt{2}$ -enhanced Rabi frequency of the Rydberg transition and are separated in time by 0.2  $\mu\text{s}$  to ensure determin-

istic phase evolution between the two pulses. The experimental sequence is represented schematically in Fig. 6.3(b) and (c). Even though a two-photon transition is used in the actual experiment, for clarity of explanation a single driving laser field with angular frequency  $\omega$  will be considered<sup>70</sup>. For atoms located within a Rydberg blockade radius of each other, this laser field can only excite a single atom within the blockade volume, resulting in the entangled state  $|W\rangle$ . If a second pulse with the same frequency is applied, it does not have enough energy to couple to the doubly-excited pair state due to the  $V_{dd}$  interaction energy which is greater than the driving field Rabi frequency in the Rydberg blockade regime. Therefore the second pulse with frequency  $\omega$  serves to de-excite the atomic populations in  $|r\rangle$  down to  $|g\rangle$ . If however, the frequency of the second pulse is increased by an amount equal to  $V_{dd}$ , then the energy gap can be bridged and the doubly-excited state  $|r, r\rangle$  can be populated. This is illustrated in the energy diagram in Fig. 6.3(c).

The results of a measurement performed in our experiment for an atomic separation of  $R = 8 \mu\text{m}$  are shown in Fig.6.3(d). The target Rydberg state was  $80S_{1/2}$  with a  $C_6$  coefficient of  $2947 \text{ GHz } \mu\text{m}^6$  obtained using the *pairinteraction* software package [116]. In our experiment we observe ground state populations as atom survival and Rydberg populations as atom loss induced by the 1064 nm trapping potential which is repulsive to Rydberg atoms, but attractive to ground state atoms. The two peaks represent the single Rydberg excitation resonance coupling to the pair state  $|W\rangle$  in blue and the double Rydberg excitation in red. Experimentally we observe the  $|W\rangle$  state as the survival of both atoms,  $|g, g\rangle$ . The frequency separation between the peaks of these two Lorentzian line shapes is a direct measurement of the interaction energy,  $V_{dd}$ . Figure 6.3(e) summarises the array-averaged

<sup>70</sup> As was shown in Section 2.3.8, the intermediate state in a two photon transition can be adiabatically eliminated to obtain an effective single photon frequency and detuning. Therefore the explanation given is still valid for a two-photon transition with a large intermediate state detuning as is the case for our experiment. In our case, the frequency of the 1039 nm laser which couples the intermediate state  $7P_{1/2}$  to the Rydberg state  $80S_{1/2}$  is the one being scanned.

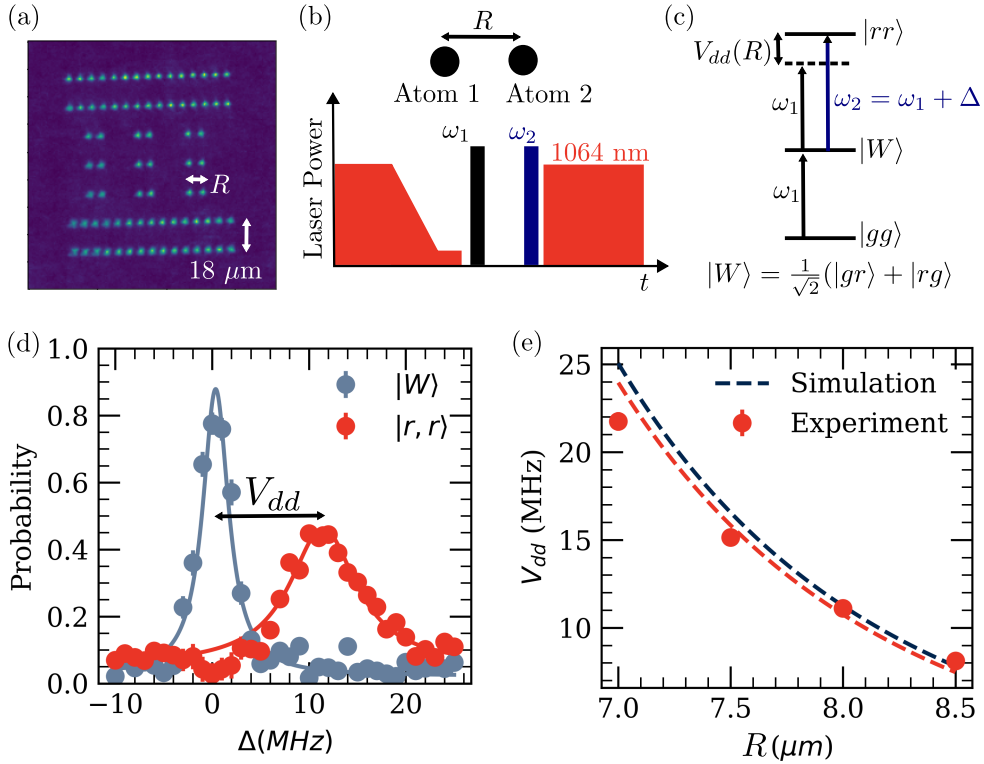


Figure 6.3: (a) Averaged image of atom geometry used to measure the magnitude of the dipole-dipole interaction,  $V_{dd}$ . The densely filled rows at the top and bottom serve as a reservoir for the moving tweezer used for atom sorting. (b) Schematic representation of the experimental sequence used for the measurement. Two pulses are applied on the Rydberg transition with a  $0.2 \mu\text{s}$  gap between them and the frequency of the second pulse is scanned. (c) Energy level diagram illustrating how by scanning the frequency of the second pulse to overcome the Rydberg blockade energy, the strength of the dipole-dipole interaction can be measured. (d) Results from a single measurement at  $R = 8 \mu\text{m}$  showing the frequency separation between the two Lorentzian line shapes corresponding to the  $|W\rangle$  and  $|r, r\rangle$  state resonances in the pair basis. (e) Summary plot showing good agreement with theory based on a  $C_6$  coefficient calculation with the *pairinteraction* software package [116]. The data has been fitted with equation (6.5) using a single fit parameter that accounts for a scaling error in the SLM hologram spacing.

results for four different interatomic separations in red and compares them to the theoretical prediction in blue. The data shows good agreement with theory. When fitted with

$$V_{dd} = -\frac{C_6}{(R \times s)^6}, \quad (6.5)$$

where the only free parameter is the SLM hologram scaling factor,  $s$ , the fit returns an SLM scaling factor of 1.0075. The experimental data for smaller values of  $R$  shows worse agreement with the theory and the fit applying the SLM scaling factor is unable to account for this discrepancy. By taking the derivative with respect to  $R$  of equation (6.5) it becomes clear that the sensitivity of the measured value of  $V_{dd}$  to position fluctuations in the atomic separation increases rapidly for smaller values of  $R$ . The scaling relation is

$$\delta V = \frac{6C_6\delta R}{R^7}, \quad (6.6)$$

where  $\delta V$  is the error in the interaction energy corresponding to a  $\delta R$  fluctuation in the interatomic separation. This was also observed in the atomic signal obtained from our measurement where the width of the resonance feature corresponding to  $|r, r\rangle$  was found to increase significantly for smaller values of  $R$ . In reference [223], the increased width of the double excitation resonance feature compared to the  $|W\rangle$  resonance was attributed to fluctuations in value of  $V_{dd}$  due to the finite temperature of the atoms inside the traps which can vary from shot to shot as described by a Maxwell-Boltzman distribution. The  $|W\rangle$  state resonance is insensitive to such fluctuations when operating in the Rydberg blockade regime. To improve the quality of our measurements, it would be necessary to reach lower atomic temperatures during Rydberg excitation by implementing Raman sideband cooling [313].

### 6.3 Rydberg Quantum Simulation Results

The intention of the work described in this chapter is to demonstrate that our experimental platform is capable of performing analogue quantum simulations. After calibrating the system as outlined in the previous sections, the decision was made to move on to the simplest problem that could be attempted as a benchmark for system performance: the 1D antiferromagnetic quantum Ising model described in Section 6.1 of this chapter. The specific problem geometry that would be simulated was informed by the parameters available in our experiment. Namely, the achievable Rydberg Rabi frequency and the principal quantum number of our target Rydberg state which set the interaction strength,  $V_{dd}$ . This in turn determines the interatomic separations required to operate in the strong dipole blockade regime. The maximum number of atoms that could be arranged in a 1D chain was limited by the imaging resolution of our camera and the field of the view of our in-vacuum aspheric lenses  $\sim 100 \mu\text{m}$ . As there was evidence to suggest that the coherence at relatively high Rydberg principal quantum numbers  $n = 75 - 80$  was good<sup>71</sup>, the decision was made to operate in this range. Since the strength of the van der Waals interaction scales as  $\propto n^{11}$ , this allowed us to operate at relatively large inter-atomic separations in the range of 6 to 8  $\mu\text{m}$  and still achieve interaction energies  $V_{dd}/\hbar$  in the range of 69 to 12 MHz respectively. Operating at smaller interatomic separations was found to be challenging in terms of imaging cross-talk between neighbouring sites due to the limited resolution of our single atom imaging system. The system was designed to give a 1  $\mu\text{m}$  resolution per camera pixel, but the atomic signal is spread out over multiple pixels in our single atom images, and using our simple binomial distribution thresholding algorithm we observe a reduction in the state detection fidelity for separations  $< 6 \mu\text{m}$ . Part of this smearing effect might be the result of the 1064 nm trapping laser pointing instability, which has

---

<sup>71</sup>This is referring to the Rydberg Rabi oscillation data in Section 3.7.4.

not yet been measured at the time of writing. In addition to diagnosing and reducing the severity of this pointing instability, the detection fidelity for small interatomic separations can be improved in the future by implementing a more sophisticated image processing algorithm such as the ones described in references [292, 314]. This current limitation precludes us from accessing the higher-order antiferromagnetic phases of matter simulated in reference [194] which used a microscope objective lens with higher collection efficiency to achieve inter-atomic separations as low as  $2.87 \mu\text{m}$  for the  $70S_{1/2}$  Rydberg state in  $^{87}\text{Rb}$ . Nonetheless, our experimental parameters still allow us to access the Rydberg blockade regime and perform a proof of principle demonstration on our hardware. As the system is not in its final state yet at the time of writing, the discussion will span a range of different configurations which were tested in the course of the work described in this thesis. An effort will be made to make it clear to the reader which configuration was being used at each point of the discussion.

### 6.3.1 Initial Guess for Ramp Parameters

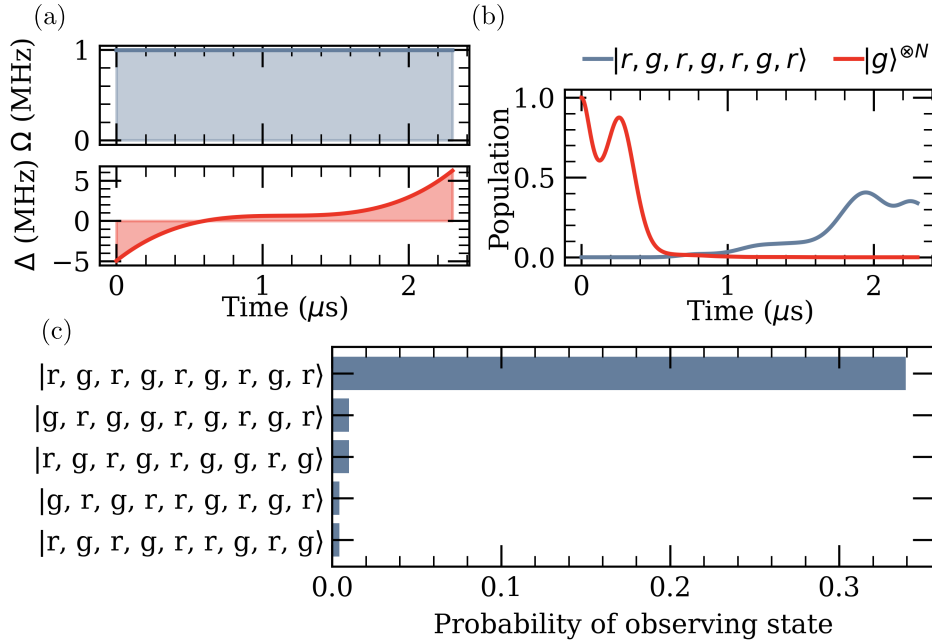


Figure 6.4: Classical computer simulation of the dynamics of a system of  $N = 9$  atoms evolving under an adiabatic detuning sweep. (a) Optimal cubic pulse profile based on differential evolution optimisation of the target state,  $|r, g, r, g, r, g, r, g, r\rangle$ , population. (b) Plot of the population dynamics of the initial ground state,  $|g, g, g, g, g, g, g, g, g\rangle$ , and target state during the optimal pulse from (a). (c) Distribution of state probabilities for the five most probable states at the end of the adiabatic sweep shown in (a). The predicted target state probability is 33.9%. The model includes contributions from the finite lifetimes of the intermediate and Rydberg states which are modelled as population loss into a dark state which represents all of the hyperfine ground states outside of the computational basis.

In order to realise the simulation experimentally, an adiabatic sweep of the Rydberg laser detuning must be performed which drives the simulated transition in phase space as illustrated in Fig. 6.1. An informed guess for the initial ramp parameters was obtained using a prediction based on a simulation model developed by our theory collaborator, Dr. Gerard Pelegri. The model uses the experimentally measured laser powers and waists to model the dynamics of the full  $N$ -atom chain with the exact geometric arrangement of atoms. The individual atom Hamiltonians use adiabatic elimination as out-

lined in reference [159] to create an effective two-level system with dissipation to a leakage state in order to simulate the effects of the finite intermediate state detuning and finite Rydberg state lifetime. The output of a typical simulation is shown in Fig. 6.4 for a chain of 9 atoms,  $\Omega/2\pi = 1$  MHz, 8  $\mu\text{m}$  inter-atomic separation and excitation to the Rydberg  $75S_{1/2}$  state. The reason for this lower Rydberg Rabi frequency compared to what was reported in previous sections is that the 459 nm optical set-up was rebuilt to use a focussed beam in the AOM crystal instead of the collimated beam used up to this point. The reasons behind this decision are described in more detail in Section 6.3.3, but the effect of the change was improved AOM bandwidth at the cost of reduced optical power due to the AOM damage threshold<sup>72</sup>. The choice of operating at the lower principal quantum number of  $n = 75$  was also informed by the AOM limitations in the sense that operating with a smaller  $V_{dd}$  reduced the frequency scan range of the simulated optimal detuning ramps. The theoretical optimal ramp shown in Fig. 6.4(a) is the final result of using the differential evolution optimisation algorithm implemented in the *SciPy* package for Python [315] following the method from [316]. The algorithm was set up to maximise the probability of reaching the known target many body state at the end of the ramp. The simulated ramp is a cubic detuning ramp parametrised as

$$\Delta(t) = at^3 + bt + c, \quad (6.7a)$$

$$a = 4s \frac{\Delta_f - \Delta_i}{(t_f - t_i)^3}, \quad (6.7b)$$

$$b = \frac{\Delta_f - \Delta_i}{t_f - t_i} - \frac{a}{4}(t_f - t_i)^2, \quad (6.7c)$$

$$c = \frac{\Delta_f - \Delta_i}{2}, \quad (6.7d)$$

where the subscripts  $i$  and  $f$  denote the initial and final value respectively,

<sup>72</sup> AA MT200-A0.5-VIS has a maximum optical power density of 5 W/mm<sup>2</sup>.

$\Delta$  is the 1039 nm Rydberg laser detuning from resonance, and  $s$  is a shape coefficient determining the curvature of the cubic ramp. Using this ramp, the simulation predicts that the target state  $|r, g, r, g, r, g, r, g, r\rangle$  should be obtained with 33.9 % probability, with the next-most-probable state having a probability of occurring of only 1.0 %. Figure 6.4(b) models the dynamics of the many-body state which corresponds to the most probable antiferromagnetic ordering at the end of the sweep. By inspection of the Rydberg Hamiltonian in equation (6.3) it becomes evident why only one of the two possible antiferromagnetic orderings is preferred. For an odd number of atoms, the state with more Rydberg excitations has lower energy because the term  $-\sum_i \Delta_i n_i$  which lowers the system energy for every excited atom when the detuning is positive.

### 6.3.2 Experimental Realisation

The simulated optimal ramp parameters did not produce the expected results. When using the simulated ramps, the target state could not be achieved with a probability  $> 5\%$  in our experiment. In order to efficiently explore the large parameter space that defines the adiabatic ramp, the decision was made to use closed-loop optimisation based on the idea of the Quantum Approximate Optimisation Algorithm (QAOA) introduced in [317]. QAOA is hybrid approach that uses a quantum processing unit to run (part of) a computation and then feeds the measurement results back to a classical optimiser in order to find an optimal parameter set that satisfies some target condition. In our case, the M-LOOP<sup>73</sup> package [238] was used as the classical optimiser with a cost function defined by  $1 - P_{\text{target}}$ , where  $P_{\text{target}}$  is the probability of the target antiferromagnetically-ordered state. Of course, this approach would not work for a general quantum simulation problem where the target state is not known ab initio. An example of how QAOA can be

<sup>73</sup> Machine-Learning Online Optimization Package

implemented in such a case is given in reference [318] for a MaxCut type optimisation problem implemented on an array of Rydberg atoms, where the cost function would be to minimise the energy of a known problem Hamiltonian. In our experiment, the M-LOOP optimiser was seeded with an initial guess based on the simulation and given access to all the parameters used to define a cubic ramp from equation (6.7). The data was taken on an array of atoms that included three independent rows of 9 atoms, but the discussion will focus on the middle row only which is the one that the measurement was calibrated for. The algorithm failed to converge to an optimal ramp, but in the explored parameter space a set of parameters was found which resulted in  $> 30\%$  probability of achieving the target state. The measurement results and the ramp used to obtain them are shown in Fig. 6.5.

While the probability of obtaining the target string with the adiabatic ramp from Fig. 6.5(a) is quite high at 34(4) %, there are a number of issues associated with this measurement. Firstly, all of the best-performing ramps turned off the laser power at very small positive detunings close to zero. In Section 6.2.2 the dipole-dipole interaction strength for an 8  $\mu\text{m}$  separation between the atoms was measured at 11.1(2) MHz for the  $80S_{1/2}$  state. For the  $75S_{1/2}$  state, the expected value would be 5.9 MHz. The optimal theoretical ramp prediction shown in Fig. 6.4(a) finished the detuning ramp at a positive 6.22 MHz, slightly above the expected van der Waals regime energy shift. This theoretical prediction also agrees with the simulations and experimental results from reference [194]. This discrepancy has also been observed in earlier experiments in our group using different AOM configurations, Rydberg Rabi frequencies and atom separations and some of the probable causes will be discussed in the next section. In addition, the algorithm showed a preference for linear ramps by setting the shape coefficient,  $s$ , to zero and effectively implementing a linear ramp. This suggested that AOM bandwidth effects are limiting the system performance as linear frequency ramps have fewer higher frequency components. To test this hypothesis, the ac-

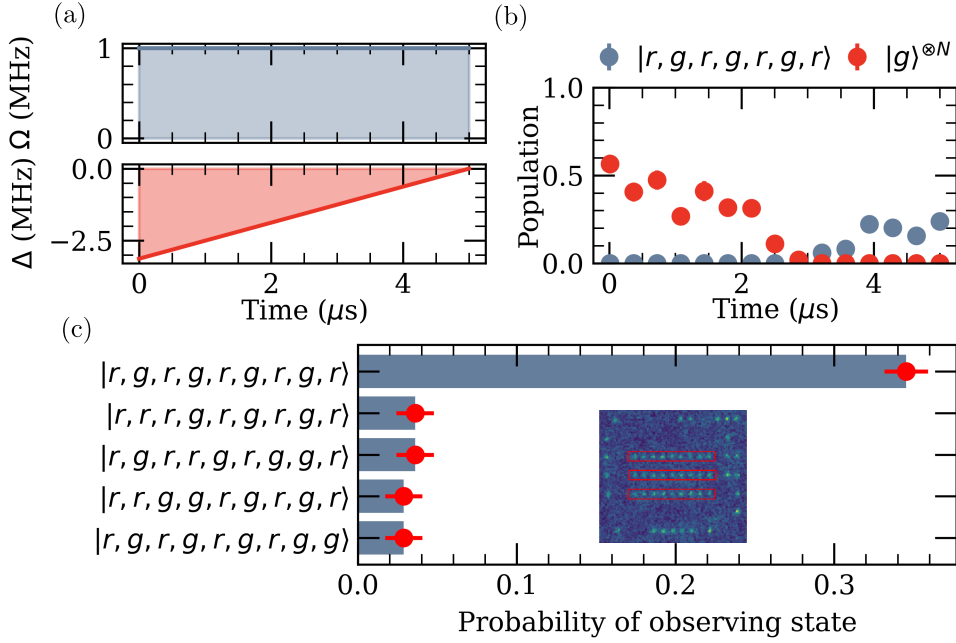


Figure 6.5: Experimental results for the dynamics of a system of  $N = 9$  atoms evolving under an adiabatic detuning sweep. (a) Pulse profile found by optimising the probability to observe the target state,  $|r, g, r, g, r, g, r, g, r\rangle$  with M-LOOP. (b) Experimental measurement of the population dynamics of the initial ground state  $|g, g, g, g, g, g, g, g, g\rangle$  and the target state during the pulse. The maximum target state probability reached at the end of the population dynamics scan was 24(4)%. (c) The top five most probable states measured experimentally using the adiabatic ramp from (a). The target state probability is 34(4)%. The error bars represent 68% Clopper-Pearson confidence intervals. The inset image is showing the array used to obtain the data. The data shown is for the middle row of 9 atoms.

tual frequency components introduced by the AOM frequency ramps could be measured by beating the light that has passed through the AOM with unshifted light on a fast photodiode. Secondly, the maximum target state probability reached at the end of the population dynamics scan shown in Fig. 6.5(b) was only 24(4)%. This measurement was taken 8 hours after the M-LOOP algorithm had recorded the optimal ramp in (a) and used it to obtain the results shown in (c). This was a clear indication that the target state probability is subject to experimental drift.

### 6.3.3 Experimental Imperfections

The aim of this section is to highlight some of the known and suspected experimental imperfections present in our set up at the time of writing.

#### Finite AOM Risetime & Bandwidth Effects

The detuning sweeps in our 1D atom chain simulations are implemented using an arbitrary waveform generator (AWG)<sup>74</sup> passed through a linear amplifier to drive our 459 nm laser AOM<sup>75</sup>. The measured pulse shapes on a fast 350 MHz photodiode provided clear evidence of finite-bandwidth effects as illustrated in Fig. 6.6. The blue trace, captured on a photodiode at the fibre output, as close as possible to the atoms, shows the amplitude response of our 459 nm system when operating with a collimated beam with a  $1/e^2$  waist  $w_0=250 \mu\text{m}$  in the AOM crystal. The AOM is set-up in a double-passed, cat eye retroreflector configuration to minimise beam steering of the doubly-diffracted beam at the fibre input collimator [319]. The overall system transfer function is set by the square of the Lorentzian AOM frequency response times the fibre coupling efficiency, which also varies as a function of AOM drive frequency due to beam steering. In order to improve the overall system bandwidth, the AOM optical path was re-built to operate with the 459 nm beam focussing into the AOM crystal with a  $1/e^2$  waist  $w_0 = 79 \mu\text{m}$  at the cost of reduced double-pass efficiency. One drawback of operating in this configuration was that the 459 nm beam power had to be reduced to not exceed the AOM crystal damage threshold as mentioned in the previous section.

As a result of these power limitations, the initial set up could only achieve a 1 MHz Rydberg Rabi frequency limited by the reduced 459 nm power when operating with a focussed beam. The final set up at the time of writing used

<sup>74</sup> Spectrum M4i6631-x8

<sup>75</sup> AA MT200-A0.5-VIS

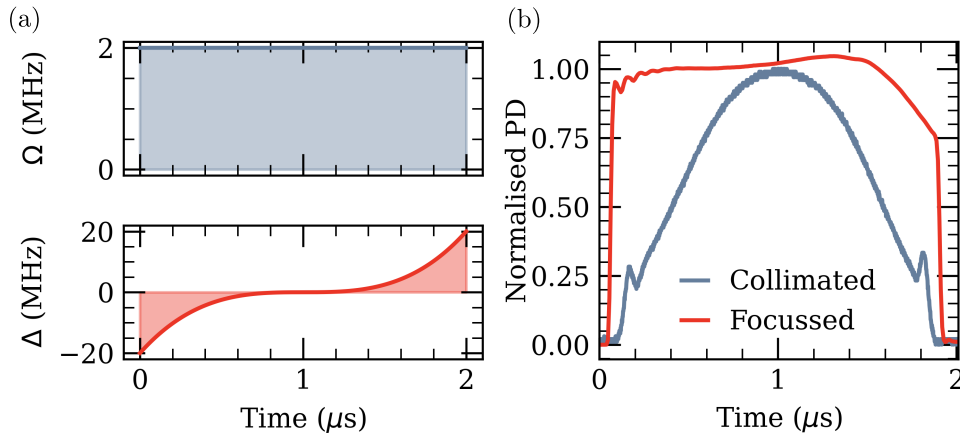


Figure 6.6: Improvement in AOM bandwidth for adiabatic sweeps when operating with a focussed instead of a collimated beam entering the AOM crystal. (a) Test cubic ramp shape with shape coefficient  $s=1$  and a detuning range from  $-20$  MHz to  $+20$  MHz. Note that due to the double-pass configuration, this corresponds to scanning the AOM frequency from  $-10$  MHz to  $+10$  MHz relative to its centre frequency. (b)  $459$  nm laser signal captured on a photodiode (PD) at the optical fibre output, as close as possible to the vacuum chamber. The signals have been normalised to the AOM centre frequency pulse amplitude without any chirping. The resulting amplitude variation captures both finite AOM bandwidth effects and fibre-coupling loss due to AOM beam steering. A significant improvement in the overall system bandwidth was observed.

an upgraded AOM<sup>76</sup> with a higher damage threshold and a faster switching time. The original AOM crystal was made from  $\text{TeO}_2$  while the upgraded version uses fused silica for improved power handling and has a faster switching speed due to a faster acoustic velocity in the material<sup>77</sup>. It should be noted that the diffraction efficiency of fused silica AOMs has a stronger dependence on the beam polarisation than  $\text{TeO}_2$  AOMs. In order to maintain high double-pass diffraction efficiency, the design was modified to use a Faraday rotator and half-waveplate before the AOM so the retroreflected light has the same polarisation in each pass. This requires the removal of the quarter waveplate typically used in these set ups.

Some preliminary data was taken using the new AOM with the full  $2$  MHz

<sup>76</sup> MQ180-A0,25-VIS

<sup>77</sup>  $4200$  m/s for  $\text{TeO}_2$  vs.  $5960$  m/s for fused silica

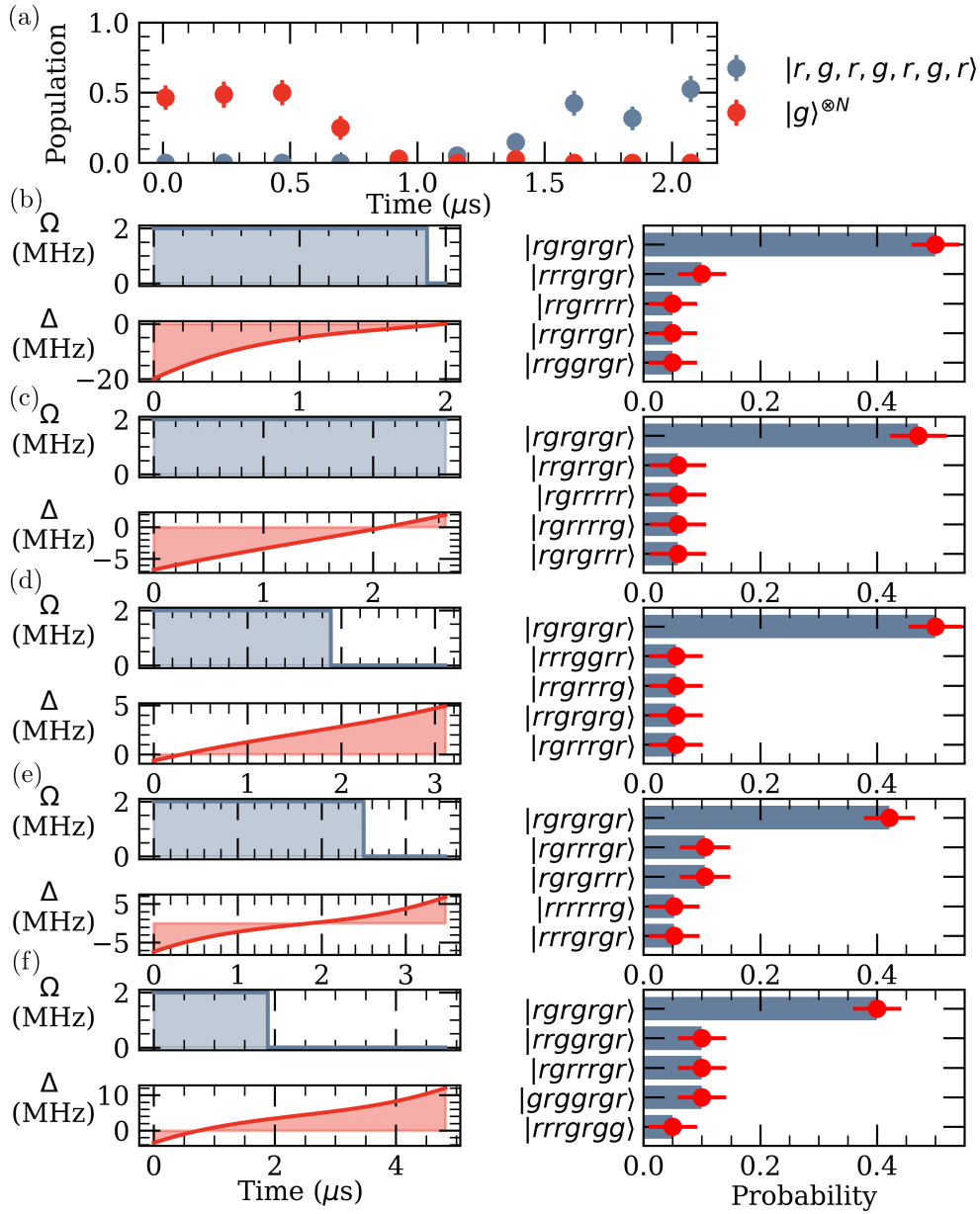


Figure 6.7: (a) Experimental results for the dynamics of a system of  $N = 7$  atoms evolving under an adiabatic detuning sweep using the upgraded AOM and the pulse profile from (b). (b) - (f) Summary plot showing the five best ramps found by the M-LOOP algorithm in a single optimisation run when operating with the new fused silica AOM in the set up. All ramps produced target string probabilities  $\sim 50\%$  with significantly different parameters. The error bars represent 68% Clopper-Pearson confidence intervals.

Rabi frequency, 8  $\mu\text{m}$  separation and a 1D chain of 7 atoms with excitation to the  $80S_{1/2}$  state. Unfortunately, the measurements are based on only 25 data points because of a power outage and air conditioning failure which disrupted further data acquisition. Nonetheless, the new AOM configuration was shown to perform well by achieving the target state with probabilities  $\sim 50\%$  when the optimal theoretical ramp predicts a maximum of 65%. A summary of the results is shown in Fig. 6.7. Even with the AOM upgrade, the theoretically-predicted detuning sweep profiles did not perform well in the experiment. The best-performing ramps found by the M-LOOP algorithm still switched off the laser power at detunings close to resonance, but the performance appeared to be more resilient to parameter variations with new set up as evidence by the fact that five different ramp profiles achieved target string probabilities  $\sim 50\%$ . Additionally, unlike the data shown in Fig. 6.5, the same target state probability was achieved in the time evolution scan as in the single measurement taken during the M-LOOP optimisation run the night before. Notably, our simulation predicted very low target state probabilities ( $< 10\%$ ) when using the optimal ramp parameters found empirically by M-LOOP highlighting the need to carry out further investigations. Work done on an external test set up also found that ramping the Rabi frequency at the beginning and end of the pulse, rather than abruptly turning it on or off, resulted in slightly improved AOM amplitude response. Similarly to reference [194], the tests suggested that this works best if the detuning profile is held constant while the AOM amplitude is being ramped. A direct benefit from using these types of ramps in terms of improved target state preparation or better agreement with theory has not yet been observed in the experiment at the time of writing.

In an attempt to better understand why the optimal ramps are truncated near resonance, the duration of the best pulse shown in Fig. 6.7(b) was extended beyond the optimal point near 0 MHz to record the corresponding population dynamics in the system. The measurement results are shown in

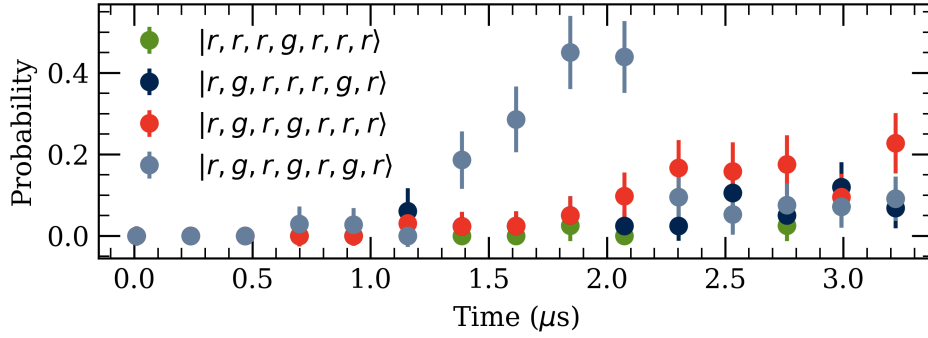


Figure 6.8: Scanning the duration of the adiabatic ramp from Fig. 6.7(b) beyond the optimal point near resonance reveals a symptom of poor frequency calibration in our system. The most probable states are the ones with a single Rydberg blockade condition violation indicative of the need for improved frequency calibration and AC Stark shift compensation in our system.

Fig.6.8. What we learned from the measurement is that the most probable states past resonance are the ones where there appears to have been a single Rydberg blockade violation. In its current form, our measurement cannot distinguish between atom loss and population in the Rydberg state because of our destructive detection scheme for Rydberg states. However, the room temperature state lifetime of the  $80S_{1/2}$  Rydberg state in caesium has been measured as  $191.4 \mu\text{s}$  [320], giving a probability of decay  $\sim 2\%$  in the longest  $4 \mu\text{s}$  ramp duration which cannot account for the observed population dynamics. Furthermore, based on our measured atom temperature after optical pumping of  $\sim 7 \mu\text{K}$  using release and recapture, we do not expect to experience more than  $0.1\%$  atom loss due to the finite temperature of the atoms. Similarly, the expected atom loss due to the finite trap lifetime is also negligible. The sharpness of the feature past resonance near the  $2 \mu\text{s}$  pulse duration point is also indicative of a blockade condition violation rather than an atom loss effect. Therefore, the most probable source of this behaviour are the imperfections in our experimental procedure which will be the subject of the next section.

## Further Improvements

**Improved Resonance Calibration Method** A number of further improvements have been identified, but not yet implemented at the time of writing. Firstly, all the data taken so far has suffered from an offset error in the Rydberg resonance frequency. This is due to the finite AOM risetime effects discussed in Section 3.7.4 that require a more time-consuming resonance calibration method. This effect amounted to an error  $\sim 1$  MHz when using the original TeO<sub>2</sub> AOM and has not yet been quantified for the new fused silica AOM. The near-resonant AC Stark shift due to the 459 nm light on the ground state transition is positive in our excitation scheme, which means that the transition from the intermediate state to the Rydberg state is shifted to shorter frequencies. This agrees with the hypothesis that the true Rydberg resonance is actually at negative detunings when measured with our imperfect  $\pi$  pulse calibration method. There is also a negative, far-off-resonant AC Stark shift due to the 459 nm light on the excited to Rydberg state transition, but its magnitude is much smaller.

**AC Stark Shift Compensation** Even with the upgraded AOM the amplitude response of the system shows significant variation across the required dynamic range of  $\pm 10$  MHz around the centre frequency. Based on the photodiode measurements in Section 6.6, the power loss is more severe for large positive detuning values. This is a concern because our measurement is most sensitive to this region of the ramp because this is when the dipole-dipole interactions take place. In reference [223], where similar AOM performance was reported, the effect was compensated for by implementing a feedback loop which adjusted the detuning ramp frequencies based on the AOM amplitude response to account for changes in the AC Stark shift. Initial attempts to implement this in our system by modifying the frequency profile of an existing working pulse or a theoretically predicted optimal pulse failed to converge.

In our system, when operating at full power with a 2 MHz Rabi frequency, the AC Stark shift due to the 459 nm light was measured  $\sim 1.5$  MHz while in reference [223] it amounted to  $\sim 5$  MHz. Because of this smaller effect, the decision was made to delay work on the AC Stark shift compensation algorithm for the future. Ideally, the pulse compensation would be incorporated in the M-LOOP optimisation run whereby every pulse proposed by the algorithm would be recorded on a photodiode first. This data would then be used to apply AC Stark shift compensation to the frequency profile before running the experiment on the atoms.

**Improved Ramp Optimisation Process** The classical optimisation algorithm was not constrained optimally in the parameter ranges it was allowed to explore. By examining the five best ramps found by the optimiser presented in Fig. 6.7, it can be seen that the parameter landscape contains many local optima which make the task harder. One alternative approach tested in our project was to constrain the algorithm to linear ramps<sup>78</sup> to simplify the parameter landscape. This approach did produce significant target state probabilities, but it did not achieve better agreement with theory as the algorithm still preferred small detuning ranges near resonance. An alternative approach was taken in reference [223] where an iterative ramp optimisation process was used instead of a machine learning algorithm. The cubic ramp parameters were optimised in the following order:  $c$ ,  $b$ ,  $\frac{\Delta_f}{\Delta_i}$ , and finally  $a$ . They found that several loops of this process resulted in optimal performance. This approach was not tested in our experiment. It should be noted that they used a different parametrisation of their cubic ramps as stated in reference [194].

---

<sup>78</sup> By hard-coding the value of the shape coefficient  $s$  to be zero.

## Effect of Detection Errors

In order to understand the effect that our state preparation and detection fidelity have on the probability of obtaining the target state, a maximum likelihood reconstruction protocol adapted from reference [223] was used. Using the parametric bootstrapping method from reference [321], the 68 % rectangular confidence intervals with skewness compensation,  $\sigma_k$ , were calculated for each of the observed states. Using the ground state and Rydberg state detection errors of our set-up described in Section 3.7.3, a transformation matrix,  $M$ , is constructed with elements  $M_{ij} = p(\text{reconstructed}|\text{guess})$ . The most likely reconstructed state can then be obtained by minimising the cost function

$$C(\mathbf{P}_{\text{expt}}, \mathbf{P}_{\text{guess}}) = \sum_k \frac{D_k^2}{\sigma_k}, \quad (6.8)$$

where  $\mathbf{D} = \mathbf{P}_{\text{expt}} - M\mathbf{P}_{\text{guess}}$  with the vector elements representing the state probabilities for each of the possible  $2^N$  states. The cost function was minimised using the Sequential Least Squares Programming (SLSQP) method implemented in *SciPy* [315]. The results of this reconstruction for the measurement presented in Section 6.3.2 are shown in Fig. 6.9. The available data set consisted of 139 measurements and the bootstrapping was performed with 6000 trials. The MLE predicts a slightly higher corrected probability of 36 % for obtaining the target state compared to the raw measurement data result of 34(4) % for a chain of 9 atoms.

## 6.4 Conclusion

The work described in this section constitutes the first demonstration of analogue optimisation using a neutral atom tweezer array in the United Kingdom. At the time of writing, the system is in an early stage of development

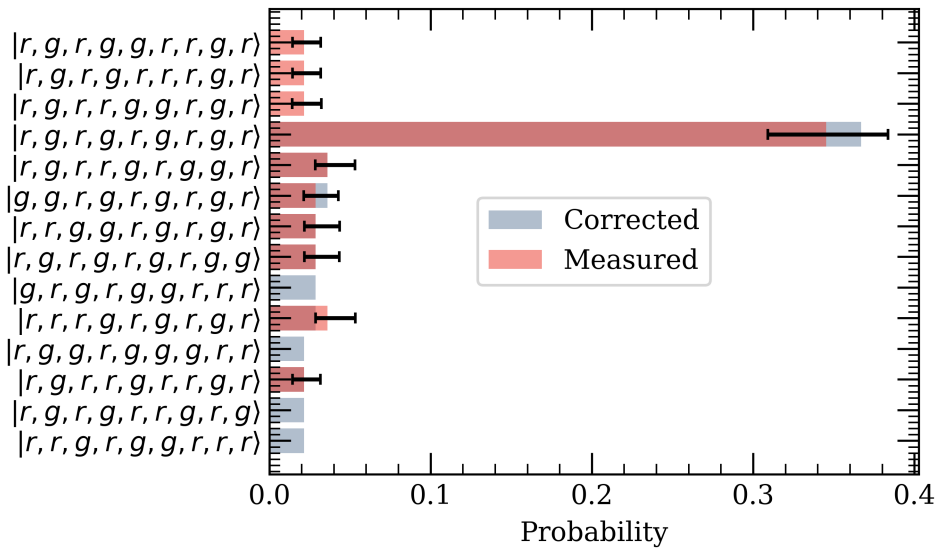


Figure 6.9: Ten most probable states using maximum likelihood (MLE) state reconstruction of the experimental results from section 6.3.2. The error bars represent 68% confidence intervals obtained using a parametric bootstrapping method. The raw measurement data is shown in red and the results of the MLE reconstruction are shown in blue.

and the 1D antiferromagnetic Ising problem was used as a simple benchmarking tool. While the classically-calculable target states were correctly identified as the most probable states by our device, there remain a number of issues and improvements which need to be addressed to make the system competitive with state-of-the-art simulation platforms. Firstly, the lack of agreement between our theoretically-simulated adiabatic ramp profiles and the empirically obtained optimal ramps would need to be understood and addressed. The improvements in our experimental methods and hardware discussed in the previous section will likely reduce the severity of the discrepancy between theory and experiment. In addition, the theoretical model has been modified to incorporate the measured amplitude response of the 459 nm AOM into the simulation and its effect on the Rydberg resonance via the AC Stark shift. There is ongoing work at the time of writing to explore the effects of these improvements in searching for better agreement between theory and experiment. Going forward, the Rydberg beams would

need to be re-shaped to improve the level of power uniformity in order to tackle more challenging two-dimensional problems in our experiment. This can be achieved by holographically shaping the beam into a flat-top profile as implemented in reference [78]. Currently, the Gaussian beam profiles of our Rydberg lasers result in significant variations of the calibrated resonance and resonance frequency across different rows of the array. Once all of these improvements are in place, the platform will be able to tackle simulation and optimisation problems which are challenging for classical computers in search of a quantum advantage.

## Chapter 7

# Conclusions and Outlook

### 7.1 Conclusion

This thesis describes the development of the first neutral atom quantum computer based on tweezer arrays in the United Kingdom. The system has been assembled from the ground up and thoroughly characterised. By using the low-phase noise, high-power 1064 nm trapping laser provided by our industry partners, M Squared Lasers, we have been able to trap up to 225  $^{133}\text{Cs}$  atoms, which combined with our moving tweezer atom sorting set up, allows us to access over 100 deterministically loading qubits as demonstrated in the thesis of Elliot Diamond-Hitchcock [165]. The coherence times of our qubits have been measured and found to be competitive with state-of-the-art

performance in other alkali atom systems. Our  $T_2^*$  time is currently limited by uncompensated long-term drifts in our experiment due to the air conditioning system which could be addressed by inserting quick calibration sequences mid-measurement as discussed in Section 56. The reversible dephasing time of our qubits can be improved even further through the use of resolved Raman sideband cooling which has been included in the design of our experiment since its inception, but not yet demonstrated at the time of writing.

The global single qubit fidelity in our system has been characterised using microwave randomised benchmarking to obtain an average error per gate of  $7(2) \times 10^{-5}$  on an array of 225 trap sites, corresponding to  $>100$  deterministically loading qubits. To our knowledge, this is the highest single qubit gate fidelity achieved on a quantum computing platform of this scale across all platforms. This can be improved further by using adiabatic rapid passage BB1 pulses to suppress the system's sensitivity to resonance drifts that currently limits our  $T_2^*$  times and microwave gate fidelities. The demonstrated global single qubit operations can be converted to local operations using an AC-Stark-shifting crossed acousto-optic deflector (AOD) to bring single trap sites into resonance with a global microwave pulse as demonstrated in [68]. Alternatively, our platform has the capability to implement single-site laser-driven Raman transitions which are operational and can be characterised with the available randomised benchmarking infrastructure developed in the course of this work. Of course, implementing a digital quantum computation would also require multi-qubit gates which have not yet been thoroughly characterised in our experiment. Future work in this area will focus on the novel ARP-based multi-qubit gate developed in our group [159].

A unique feature of our experiment is the ability to perform non-destructive readout (NDRO) on arrays of up to 49 trap sites, the largest scale demonstration of this technique to date. The work described in this thesis also resulted in the first practical demonstration of a benefit resulting from NDRO. In

the context of randomised benchmarking, it was demonstrated that the state preparation and measurement errors due to atom loss can be suppressed by a factor of 1.7 compared to the conventional destructive imaging process. The performance of NDRO in our system is in line with the state of the art in terms of state detection fidelity, but the NDRO survival and leakage probabilities need to be improved in future iterations. This can be achieved using alternative dipole trapping methods that eliminate differential AC Stark shifts on the D2 line and improved imaging system collection efficiency to reduce the required number of photons scattered. In a future cryogenic set-up with long trap lifetimes, an additional benefit from NDRO could be extracted by operating for minutes at a time without the need to reload atoms from a magneto-optical trap since the atoms will not be pushed out from the traps upon detection. With a view of progressing towards fault-tolerant operation and error correction, the NDRO technique can be implemented in a mid-circuit type measurement scheme using dual species arrays to avoid cross-talk between data and ancilla qubits. Scaling up of the NDRO technique discussed in this work to even larger numbers of qubits will be challenging because of the requirement for significantly increased trap depth, but very recent work with  $^{87}\text{Rb}$  in reference [322] has been able to apply the technique to arrays of up to 280 physical qubits to realise mid-circuit read out on up to 48 logical qubits encoded using three-dimensional surface code blocks.

The ability of our system to perform simple analogue quantum simulations has been demonstrated by using the antiferromagnetic quantum 1D Ising model as a benchmarking tool. We have demonstrated the ability to identify the correct, lowest-energy target state of the problem Hamiltonian with high probability for chains of up to 9 atoms. While still well within the reach of classical simulation, this demonstration paves the way toward tackling more challenging problems with more qubits in two dimensions. Having developed the prerequisite knowhow with the simple 1D chain model, a number of exper-

imental improvements have been identified to reach the level of performance required for this next stage of problem complexity. Converting the Rydberg laser set-up to use a focussed beam in the acousto-optic modulator (AOM) crystal and procuring the appropriate AOM to operate in this configuration at high power have already shown improvements in the system performance. A range of additional improvements in the adiabatic sweep calibration and optimisation process will also need to be implemented to achieve state of the art performance. Combined with the planned upgrade to top-hat-shaped beam profiles for our Rydberg beams and the addition of a 20 W fibre amplifier for our 1039 nm laser so we can operate with faster Rabi frequencies at a larger intermediate state detuning for suppressed dissipation, the experiment will be in a position to attempt problems in two dimensions which are the current focus of other leading research groups across the world.

# Appendices

# Appendix A

## Single Qubit Clifford Gates

Table A.1: Single qubit Clifford gate set

Gate Index	$R_x(\theta)$	$R_y(\theta)$	$R_z(\theta)$	U	Basic Gate Sequence
0	$I$	$I$	$I$	$\begin{pmatrix} 1 & 0 \\ 0 & 1 \end{pmatrix}$	$R_0$
1	$I$	$I$	$\frac{\pi}{2}$	$e^{-i\pi/4} \begin{pmatrix} 1 & 0 \\ 0 & i \end{pmatrix}$	$R_1$
2	$I$	$I$	$\pi$	$-i \begin{pmatrix} 1 & 0 \\ 0 & -1 \end{pmatrix}$	$R_2$
3	$I$	$I$	$-\frac{\pi}{2}$	$e^{i\pi/4} \begin{pmatrix} 1 & 0 \\ 0 & -i \end{pmatrix}$	$R_3$
4	$I$	$\frac{\pi}{2}$	$I$	$\frac{1}{\sqrt{2}} \begin{pmatrix} 1 & -1 \\ 1 & 1 \end{pmatrix}$	$R_4$
5	$I$	$\pi$	$I$	$-1 \begin{pmatrix} 0 & 1 \\ -1 & 0 \end{pmatrix}$	$R_5$
6	$I$	$-\frac{\pi}{2}$	$I$	$\frac{1}{\sqrt{2}} \begin{pmatrix} 1 & 1 \\ -1 & 1 \end{pmatrix}$	$R_6$
7	$\frac{\pi}{2}$	$I$	$I$	$\frac{1}{\sqrt{2}} \begin{pmatrix} 1 & -i \\ -i & 1 \end{pmatrix}$	$R_7$
8	$\pi$	$I$	$I$	$-i \begin{pmatrix} 0 & 1 \\ 1 & 0 \end{pmatrix}$	$R_8$
9	$-\frac{\pi}{2}$	$I$	$I$	$\frac{1}{\sqrt{2}} \begin{pmatrix} 1 & i \\ i & 1 \end{pmatrix}$	$R_9$
10	$I$	$\pi$	$\frac{\pi}{2}$	$-e^{i\pi/4} \begin{pmatrix} 0 & 1 \\ i & 0 \end{pmatrix}$	$R_5R_1$
11	$\pi$	$I$	$\frac{\pi}{2}$	$e^{i\pi/4} \begin{pmatrix} 0 & 1 \\ -i & 0 \end{pmatrix}$	$R_8R_1$
12	$\pi$	$\frac{\pi}{2}$	$I$	$\frac{-i}{\sqrt{2}} \begin{pmatrix} 1 & 1 \\ 1 & -1 \end{pmatrix}$	$R_8R_4$
13	$\frac{\pi}{2}$	$I$	$\frac{\pi}{2}$	$\frac{e^{-i\pi/4}}{\sqrt{2}} \begin{pmatrix} 1 & 1 \\ -i & i \end{pmatrix}$	$R_7R_1$
14	$\frac{\pi}{2}$	$\pi$	$\frac{\pi}{2}$	$-\frac{e^{i\pi/4}}{\sqrt{2}} \begin{pmatrix} 1 & 1 \\ i & -i \end{pmatrix}$	$R_7R_5R_1$
15	$\pi$	$-\frac{\pi}{2}$	$I$	$\frac{i}{\sqrt{2}} \begin{pmatrix} 1 & -1 \\ -1 & -1 \end{pmatrix}$	$R_8R_6$
16	$-\frac{\pi}{2}$	$I$	$\frac{\pi}{2}$	$\frac{e^{-i\pi/4}}{\sqrt{2}} \begin{pmatrix} 1 & -1 \\ i & i \end{pmatrix}$	$R_9R_1$
17	$-\frac{\pi}{2}$	$\pi$	$\frac{\pi}{2}$	$\frac{e^{i\pi/4}}{\sqrt{2}} \begin{pmatrix} 1 & -1 \\ -i & -i \end{pmatrix}$	$R_9R_5R_1$
18	$-\frac{\pi}{2}$	$-\frac{\pi}{2}$	$I$	$\frac{e^{-i\pi/4}}{\sqrt{2}} \begin{pmatrix} 1 & i \\ -1 & i \end{pmatrix}$	$R_9R_6$
19	$-\frac{\pi}{2}$	$\frac{\pi}{2}$	$I$	$\frac{e^{i\pi/4}}{\sqrt{2}} \begin{pmatrix} 1 & i \\ 1 & -i \end{pmatrix}$	$R_9R_4$
20	$-\frac{\pi}{2}$	$\pi$	$I$	$\frac{i}{\sqrt{2}} \begin{pmatrix} 1 & i \\ -i & -1 \end{pmatrix}$	$R_9R_5$
21	$\frac{\pi}{2}$	$-\frac{\pi}{2}$	$I$	$\frac{e^{i\pi/4}}{\sqrt{2}} \begin{pmatrix} 1 & -i \\ -1 & -i \end{pmatrix}$	$R_7R_6$
22	$\frac{\pi}{2}$	$\pi$	$I$	$\frac{-i}{\sqrt{2}} \begin{pmatrix} 1 & -i \\ i & -1 \end{pmatrix}$	$R_7R_5$
23	$\frac{\pi}{2}$	$\frac{\pi}{2}$	$I$	$\frac{e^{-i\pi/4}}{\sqrt{2}} \begin{pmatrix} 1 & -i \\ 1 & i \end{pmatrix}$	$R_7R_4$

# Bibliography

- [1] “UK National Quantum Technologies Programme (NQTP) strategic intent, videos and publications.” [Accessed: 10-October-2023].
- [2] “National Quantum Initiative - NQI-Factsheet,” [Accessed: 10-October-2023].
- [3] R. P. Feynman, “Simulating physics with computers,” *International Journal of Theoretical Physics* **21**, 467 (1982).
- [4] M. A. Nielsen and I. L. Chuang, *Quantum Computation and Quantum Information: 10th Anniversary Edition* (Cambridge University Press, 2010).
- [5] V. M. Kendon *et al.*, “Quantum analogue computing,” *Philosophical Transactions: Mathematical, Physical and Engineering Sciences* **368**, 3609 (2010).
- [6] A. J. Daley *et al.*, “Practical quantum advantage in quantum simulation,” *Nature* **607**, 667 (2022).
- [7] D. Castelvecchi, “How would room-temperature superconductors change science?” *Nature* **621**, 18 (2023).
- [8] P. Bernstein and J. Noudem, “Superconducting magnetic levitation: principle, materials, physics and models,” *Superconductor Science and Technology* **33**, 033001 (2020).

- 
- [9] S. Speller, *A Materials Science Guide to Superconductors: and How to Make Them Super* (Oxford University Press, 2022).
- [10] M. Zak, “Quantum Analog Computing,” *Chaos Solitons & Fractals* **10**, 1583 (1999).
- [11] J. Preskill, “Quantum Computing in the NISQ era and beyond,” *Quantum* **2**, 79 (2018).
- [12] Y. Peng *et al.*, “Simuq: A framework for programming quantum hamiltonian simulation with analog compilation,” *Proceedings of the ACM on Programming Languages* **8**, 2425–2455 (2024).
- [13] S. Flannigan *et al.*, “Propagation of errors and quantitative quantum simulation with quantum advantage,” *Quantum Science and Technology* **7**, 045025 (2022).
- [14] D. Gottesman, “Stabilizer codes and quantum error correction,” (1997), arXiv:quant-ph/9705052 [quant-ph] .
- [15] E. T. Campbell *et al.*, “Roads towards fault-tolerant universal quantum computation,” *Nature* **549**, 172 (2017-09).
- [16] P.W. Shor, “Algorithms for quantum computation: discrete logarithms and factoring,” *Proceedings 35th Annual Symposium on Foundations of Computer Science* , 124 (1994).
- [17] L. K. Grover, “A Fast Quantum Mechanical Algorithm for Database Search,” *Proceedings of the twenty-eighth annual ACM symposium on Theory of Computing* , 212 (1996).
- [18] T. Monz *et al.*, “Realization of a scalable Shor algorithm,” *Science* **351**, 1068 (2016).

- 
- [19] U. Skosana and M. Tame, “Demonstration of Shor’s factoring algorithm for  $N = 21$  on IBM quantum processors,” *Scientific Reports* **11**, 16599 (2021).
- [20] V. Vedral *et al.*, “Quantum networks for elementary arithmetic operations,” *Physical Review A* **54**, 147 (1996).
- [21] J. Ha *et al.*, “Resource analysis of quantum computing with noisy qubits for Shor’s factoring algorithms,” *Quantum Information Processing* **21**, 60 (2022).
- [22] L. Chen *et al.*, *Report on Post-Quantum Cryptography*, Tech. Rep. (2016).
- [23] D. J. Bernstein and T. Lange, “Post-quantum cryptography,” *Nature* **549**, 188 (2017).
- [24] B. Bauer *et al.*, “Quantum algorithms for quantum chemistry and quantum materials science,” *Chemical Reviews* **120**, 12685 (2020).
- [25] Y. Lam *et al.*, “Applications of Quantum Chemistry in Pharmaceutical Process Development: Current State and Opportunities,” *Organic Processes Research & Development* **24**, 1496 (2020).
- [26] M. Reiher *et al.*, “Elucidating reaction mechanisms on quantum computers,” *Proceedings of the National Academy of Sciences* **114**, 7555 (2017).
- [27] I. Kassal *et al.*, “Simulating chemistry using quantum computers,” *Annual Review of Physical Chemistry* **62**, 185 (2011).
- [28] D. P. DiVincenzo, “The physical implementation of quantum computation,” *Fortschritte der Physik* **48**, 771 (2000).
- [29] F. Arute *et al.*, “Quantum supremacy using a programmable superconducting processor,” *Nature* **574**, 505 (2019).

- 
- [30] Y. Kim *et al.*, “Evidence for the utility of quantum computing before fault tolerance,” *Nature* **618**, 500 (2023).
- [31] M. Kjaergaard *et al.*, “Superconducting qubits: Current state of play,” *Annual Review of Condensed Matter Physics* **11**, 369 (2020).
- [32] “IBM Unveils 400 Qubit-Plus Quantum Processor and Next-Generation IBM Quantum System Two,” (2022), [Accessed: 10-October-2023].
- [33] C.-Y. Ding *et al.*, “Dynamical-Corrected Nonadiabatic Geometric Quantum Computation,” (2023), arXiv:2302.04167 [quant-ph].
- [34] J. P. Gaebler *et al.*, “High-fidelity universal gate set for  ${}^9\text{Be}^+$  ion qubits,” *Physical Review Letters* **117**, 060505 (2016).
- [35] C. J. Ballance *et al.*, “High-fidelity quantum logic gates using trapped-ion hyperfine qubits,” *Physical Review Letters* **117**, 060504 (2016).
- [36] C. D. Bruzewicz *et al.*, “Trapped-Ion Quantum Computing: Progress and Challenges,” *Applied Physics Reviews* **6**, 021314 (2019).
- [37] D. Kielpinski *et al.*, “Architecture for a large-scale ion-trap quantum computer,” *Nature* **417**, 709 (2002).
- [38] K. K. Mehta *et al.*, “Integrated optical addressing of an ion qubit,” *Nature* **11**, 1066 (2016).
- [39] R. J. Niffenegger *et al.*, “Integrated multi-wavelength control of an ion qubit,” *Nature* **586**, 538 (2020).
- [40] T. P. Harty *et al.*, “High-fidelity trapped-ion quantum logic using near-field microwaves,” *Physical Review Letters* **117**, 140501 (2016).
- [41] S. Weidt *et al.*, “Trapped-ion quantum logic with global radiation fields,” *Physical Review Letters* **117**, 220501 (2016).

- 
- [42] M. Malinowski *et al.*, “How to wire a 1000-qubit trapped ion quantum computer,” (2023), arXiv:2305.12773 [quant-ph].
- [43] D. DeMille, “Quantum Computation with Trapped Polar Molecules,” *Physical Review Letters* **88**, 067901 (2002).
- [44] A. M. Kaufman and K.-K. Ni, “Quantum science with optical tweezer arrays of ultracold atoms and molecules,” *Nature Physics* **17**, 1324 (2012).
- [45] K.-K. Ni *et al.*, “Dipolar exchange quantum logic gate with polar molecules,” *Chemical Science* **9**, 6830 (2018).
- [46] S. Slussarenko and G. J. Pryde, “Photonic quantum information processing: A concise review,” *Applied Physics Reviews* **6**, 041303 (2019).
- [47] T. Peyronel *et al.*, “Quantum nonlinear optics with single photons enabled by strongly interacting atoms,” *Nature* **488**, 57 (2012).
- [48] D. Maxwell *et al.*, “Storage and Control of Optical Photons Using Rydberg Polaritons,” *Physical Review Letters* **110**, 103001 (2013).
- [49] D. Paredes-Barato and C. S. Adams, “All-optical quantum information processing using rydberg gates,” *Physical Review Letters* **112**, 040501 (2014).
- [50] G. Burkard *et al.*, “Semiconductor spin qubits,” *Reviews of Modern Physics* **95**, 025003 (2023).
- [51] M. Gulka *et al.*, “Room-temperature control and electrical readout of individual nitrogen-vacancy nuclear spins,” *Nature Communications* **12**, 4421 (2021).
- [52] M. Saffman, “Quantum computing with atomic qubits and Rydberg interactions: progress and challenges,” *Journal of Physics B: Atomic, Molecular and Optical Physics* **49**, 202001 (2016).

- 
- [53] C. S. Adams *et al.*, “Rydberg atom quantum technologies,” *Journal of Physics B: Atomic, Molecular and Optical Physics* **53**, 012002 (2019).
- [54] I. S. Madjarov *et al.*, “High-fidelity entanglement and detection of alkaline-earth Rydberg atoms,” *Nature Physics* **16**, 857 (2020).
- [55] S. Ma *et al.*, “Universal Gate Operations on Nuclear Spin Qubits in an Optical Tweezer Array of  $^{171}\text{Yb}$  Atoms,” *Physical Review X* **12**, 021028 (2022).
- [56] R. Grimm *et al.*, “Optical dipole traps for neutral atoms,” (1999), arXiv:physics/9902072 [physics.atom-ph].
- [57] P. Huft *et al.*, “Simple, passive design for large optical trap arrays for single atoms,” *Physical Review A* **105**, 063111 (2022).
- [58] D. Ohl de Mello *et al.*, “Defect-Free Assembly of 2D Clusters of More Than 100 Single-Atom Quantum Systems,” *Physical Review Letters* **122**, 203601.
- [59] M. Endres *et al.*, “Atom-by-atom assembly of defect-free one-dimensional cold atom arrays,” *Science* **354**, 1024 (2016).
- [60] F. Nogrette *et al.*, “Single-Atom Trapping in Holographic 2D Arrays of Microtraps with Arbitrary Geometries,” *Physical Review X* **4**, 021034 (2014).
- [61] D. Barredo *et al.*, “Synthetic three-dimensional atomic structures assembled atom by atom,” *Nature* **561**, 79 (2018).
- [62] M. Schlosser *et al.*, “Scalable Multilayer Architecture of Assembled Single-Atom Qubit Arrays in a Three-Dimensional Talbot Tweezer Lattice,” *Physical Review Letters* **130**, 180601 (2023).
- [63] A. Fuhrmanek *et al.*, “Light-assisted collisions between a few cold atoms in a microscopic dipole trap,” *Physical Review A* **85**, 062708 (2012).

- 
- [64] B. J. Lester *et al.*, “Rapid Production of Uniformly Filled Arrays of Neutral Atoms,” *Physical Review Letters* **115**, 073003 (2015).
- [65] A. L. Shaw *et al.*, “Dark-state enhanced loading of an optical tweezer array,” (2023), arXiv:2302.10855 [physics, physics:quant-ph].
- [66] D. Barredo *et al.*, “An atom-by-atom assembler of defect-free arbitrary two-dimensional atomic arrays,” *Science* **354**, 1021 (2016).
- [67] W. Tian *et al.*, “Parallel Assembly of Arbitrary Defect-Free Atom Arrays with a Multitweezer Algorithm,” *Physical Reviews Applied* **19**, 034048 (2023).
- [68] T. Xia *et al.*, “Randomized benchmarking of single-qubit gates in a 2d array of neutral-atom qubits,” *Physical Review Letters* **114**, 100503 (2015).
- [69] H. Levine *et al.*, “Dispersive optical systems for scalable Raman driving of hyperfine qubits,” *Physical Review A* **105**, 032618 (2022).
- [70] C. Sheng *et al.*, “High-Fidelity Single-Qubit Gates on Neutral Atoms in a Two-Dimensional Magic-Intensity Optical Dipole Trap Array,” *Physical Review Letters* **121**, 240501 (2018).
- [71] D. Jaksch *et al.*, “Fast Quantum Gates for Neutral Atoms,” *Physical Review Letters* **85**, 2208 (2000).
- [72] M. D. Lukin *et al.*, “Dipole Blockade and Quantum Information Processing in Mesoscopic Atomic Ensembles,” *Physical Review Letters* **87**, 037901 (2001).
- [73] X.-F. Shi, “Quantum logic and entanglement by neutral Rydberg atoms: methods and fidelity,” *Quantum Science and Technology* **7**, 023002 (2022).

- 
- [74] L. Isenhower *et al.*, “Demonstration of a Neutral Atom Controlled-NOT Quantum Gate,” *Physical Review Letters* **104**, 010503 (2010).
- [75] H. Levine *et al.*, “Parallel Implementation of High-Fidelity Multi-qubit Gates with Neutral Atoms,” *Physical Review Letters* **123**, 170503 (2019).
- [76] S. Jandura and G. Pupillo, “Time-Optimal Two- and Three-Qubit Gates for Rydberg Atoms,” *Quantum* **6**, 712 (2022).
- [77] H. Levine *et al.*, “High-Fidelity Control and Entanglement of Rydberg-Atom Qubits,” *Physical Review Letters* **121**, 123603 (2018).
- [78] S. J. Evered *et al.*, “High-fidelity parallel entangling gates on a neutral atom quantum computer,” (2023), arXiv:2304.05420 [cond-mat, physics:physics, physics:quant-ph].
- [79] R. Acharya *et al.*, “Suppressing quantum errors by scaling a surface code logical qubit,” *Nature* **614**, 676 (2023).
- [80] “IonQ Forte: The First Software-Configurable Quantum Computer,” [Accessed: 10-October-2023].
- [81] D. Bluvstein *et al.*, “A quantum processor based on coherent transport of entangled atom arrays,” *Nature* **604**, 451 (2022).
- [82] A. Yu. Kitaev, “Fault-tolerant quantum computation by anyons,” *Annals of Physics* **303**, 2 (2003).
- [83] E. Dennis *et al.*, “Topological quantum memory,” *Journal of Mathematical Physics* **43**, 4452 (2002).
- [84] T. M. Graham *et al.*, “Multi-qubit entanglement and algorithms on a neutral-atom quantum computer,” *Nature* **604**, 457 (2022).
- [85] F. Schäfer *et al.*, “Tools for quantum simulation with ultracold atoms in optical lattices,” *Nature Reviews Physics* **2**, 411 (2020).

- 
- [86] P. Scholl *et al.*, “Quantum simulation of 2D antiferromagnets with hundreds of Rydberg atoms,” *Nature* **595**, 233 (2021).
- [87] S. Ebadi *et al.*, “Quantum phases of matter on a 256-atom programmable quantum simulator,” *Nature* **595**, 227 (2021).
- [88] G. Semeghini *et al.*, “Probing topological spin liquids on a programmable quantum simulator,” *Science* **374**, 1242 (2021).
- [89] S. Ebadi *et al.*, “Quantum Optimization of Maximum Independent Set using Rydberg Atom Arrays,” *Science* **376**, 1209 (2022).
- [90] R. S. Andrist *et al.*, “Hardness of the maximum-independent-set problem on unit-disk graphs and prospects for quantum speedups,” *Physical Review Research* **5**, 043277 (2023).
- [91] J. Wurtz *et al.*, “Industry applications of neutral-atom quantum computing solving independent set problems,” (2022), arXiv:2205.08500 [quant-ph].
- [92] C. Dalyac *et al.*, “Qualifying quantum approaches for hard industrial optimization problems. A case study in the field of smart-charging of electric vehicles,” *EPJ Quantum Technology* **8**, 1 (2021).
- [93] M. D’Arcangelo *et al.*, “Leveraging Analog Quantum Computing with Neutral Atoms for Solvent Configuration Prediction in Drug Discovery,” (2023), arXiv:2309.12129 [physics, physics:quant-ph].
- [94] C. J. Picken *et al.*, “Laser Systems for High Fidelity Control and Entanglement of Neutral Atomic Qubits,” (2023), arXiv:2304.08402 [physics:quant-ph].
- [95] D. Barredo *et al.*, “Three-Dimensional Trapping of Individual Rydberg Atoms in Ponderomotive Bottle Beam Traps,” *Physical Review Letters* **124**, 023201 (2020).

- 
- [96] A. G. Fowler *et al.*, “Surface codes: Towards practical large-scale quantum computation,” *Physical Review A* **86**, 032324 (2012).
- [97] K.-N. Schymik *et al.*, “Single Atoms with 6000-Second Trapping Lifetimes in Optical-Tweezer Arrays at Cryogenic Temperatures,” *Physical Review Applied* **16**, 034013 (2021).
- [98] P. Scholl *et al.*, “Erasure conversion in a high-fidelity Rydberg quantum simulator,” (2023), arXiv:2305.03406 [cond-mat, physics:physics, physics:quant-ph].
- [99] H. Wu *et al.*, “Millisecond-lived circular Rydberg atoms in a room-temperature experiment,” (2022), arXiv:2209.11654 [physics, physics:quant-ph].
- [100] K. Sahay *et al.*, “High threshold codes for neutral atom qubits with biased erasure errors,” (2023), arXiv:2302.03063 [quant-ph].
- [101] S. Huang and K. R. Brown, “Between Shor and Steane: A Unifying Construction for Measuring Error Syndromes,” *Physical Review Letters* **127**, 090505 (2021).
- [102] T. M. Graham *et al.*, “Mid-circuit measurements on a neutral atom quantum processor,” (2023), arXiv:2303.10051 [physics:quant-ph].
- [103] W. Xu *et al.*, “Fast Preparation and Detection of a Rydberg Qubit Using Atomic Ensembles,” *Physical Review Letters* **127**, 050501 (2021).
- [104] E. Deist *et al.*, “Mid-Circuit Cavity Measurement in a Neutral Atom Array,” *Physical Review Letters* **129**, 203602 (2022).
- [105] J. Ramette *et al.*, “Any-to-any connected cavity-mediated architecture for quantum computing with trapped ions or Rydberg arrays,” (2021), arXiv: 2109.11551 [quant-ph].

- 
- [106] K. Singh *et al.*, “Dual-Element, Two-Dimensional Atom Array with Continuous-Mode Operation,” *Physical Review X* **12**, 011040 (2022).
- [107] F. Cesa and H. Pichler, “Universal Quantum Computation in Globally Driven Rydberg Atom Arrays,” (2023), arXiv:2305.19220 [physics:quant-ph].
- [108] Q. Xu *et al.*, “Constant-Overhead Fault-Tolerant Quantum Computation with Reconfigurable Atom Arrays,” (2023), arXiv:2308.08648 [quant-ph].
- [109] D. González-Cuadra *et al.*, “Fermionic quantum processing with programmable neutral atom arrays,” (2023), arXiv:2303.06985 [cond-mat, physics:hep-lat, physics:quant-ph].
- [110] D. B. Tan *et al.*, “Compiling Quantum Circuits for Dynamically Field-Programmable Neutral Atoms Array Processors,” (2023), arXiv:2306.03487 [quant-ph].
- [111] T. M. Graham *et al.*, “Multiscale architecture for fast optical addressing and control of large-scale qubit arrays,” *Applied Optics* **62**, 3242 (2023).
- [112] B. Zhang *et al.*, “A scaled local gate controller for optically addressed qubits,” (2023), arXiv:2310.08539 [physics, physics:quant-ph].
- [113] A. Bauch, “Caesium atomic clocks: function, performance and applications,” *Measurement Science and Technology* **14**, 1159 (2003).
- [114] I. Georgescu, “Rubidium round-the-clock,” *Nature Chemistry* **7**, 1034 (2015).
- [115] N. Sibalic *et al.*, “ARC: An open-source library for calculating properties of alkali Rydberg atoms,” *Computer Physics Communications* **220**, 319 (2017).

- 
- [116] S. Weber *et al.*, “Calculation of Rydberg interaction potentials,” *Journal of Physics B: Atomic, Molecular and Optical Physics* **50**, 133001 (2017).
- [117] C. J. Foot, *Atomic Physics: 7 (Oxford Master Series in Physics)* (Oxford University Press, 2005).
- [118] A. Beyer *et al.*, “The rydberg constant and proton size from atomic hydrogen,” *Science* **358**, 79 (2017).
- [119] J. J. Sakurai, *Advanced Quantum Mechanics* (Pearson Education, Incorporated, 1967).
- [120] E.J. Robertson *et al.*, “Arc 3.0: An expanded python toolbox for atomic physics calculations,” *Computer Physics Communications* **261**, 107814 (2021).
- [121] J. Deiglmayr *et al.*, “Precision measurement of the ionization energy of Cs i,” *Physical Review A* **93**, 013424 (2016).
- [122] P. Goy *et al.*, “Millimeter-wave spectroscopy in cesium Rydberg states. Quantum defects, fine- and hyperfine-structure measurements,” *Physical Review A* **26**, 2733 (1982).
- [123] J. Emsley, *The Elements*, 2nd ed. (Clarendon Press, 1991).
- [124] A. Kastberg, *Structure of Multielectron Atoms: 112*, 1st ed. (Springer, Cham, 2020).
- [125] B. H. Bransden, *Quantum Mechanics*, 2nd ed. (Pearson, Harlow, England ; New York, 2000).
- [126] E. P. Wigner, “On the Matrices Which Reduce the Kronecker Products of Representations of S. R. Groups,” (Springer, Berlin, Heidelberg, 1993).

- 
- [127] I. I. Sobelman, *Atomic Spectra and Radiative Transitions*, 2nd ed., edited by J. P. Toennis (Springer, Berlin ; New York, 1992).
- [128] D. Steck, “Cesium D Line Data,” (1998), [Accessed: 10-October-2023].
- [129] V. Gerginov *et al.*, “Observation of the Nuclear Magnetic Octupole Moment of  $^{133}\text{Cs}$ ,” *Physical Review Letters* **91**, 072501 (2003).
- [130] J. Farley *et al.*, “Hyperfine-structure measurements in the Rydberg  $S$  and  $P$  states of rubidium and cesium,” *Physical Review A* **15**, 1530 (1977).
- [131] M. Allegrini *et al.*, “Survey of Hyperfine Structure Measurements in Alkali Atoms,” *Journal of Physical and Chemical Reference Data* **51**, 043102 (2022).
- [132] G. Breit and I. I. Rabi, “Measurement of Nuclear Spin,” *Physical Review* **38**, 2082 (1931).
- [133] J. Bai *et al.*, “Precise measurements of polarizabilities of cesium nS Rydberg states in an ultra-cold atomic ensemble,” *New Journal of Physics* **22**, 093032 (2020).
- [134] J. Stark, “Observation of the Separation of Spectral Lines by an Electric Field,” *Nature* **92**, 401 (1913).
- [135] J. Pritchard, *Cooperative Optical Non-linearity in a blockaded Rydberg Ensemble*, Ph.D. thesis, Durham University (2011).
- [136] M. T. Simons *et al.*, “Rydberg atom-based sensors for radio-frequency electric field metrology, sensing, and communications,” *Measurement: Sensors* **18**, 100273 (2021).
- [137] B. Liu *et al.*, “Electric field measurement and application based on Rydberg atoms,” (2023), arXiv:2305.16696 [physics:quant-ph].

- 
- [138] T. P. Harty, *High-fidelity microwave-driven quantum logic in intermediate-field  $^{43}\text{Ca}^+$* , Ph.D. thesis (2013).
- [139] D. Budker *et al.*, *Atomic Physics: An Exploration Through Problems and Solutions*, 2nd ed. (OUP Oxford, 2008).
- [140] C. Gerry and P. Knight, *Introductory Quantum Optics* (Cambridge University Press, Cambridge, 2004).
- [141] J. Garrison and R. Chiao, *Quantum Optics*, illustrated ed. (OUP Oxford, Oxford ; New York, 2008).
- [142] G. Lindblad, “On the generators of quantum dynamical semigroups,” *Communications in Mathematical Physics* **48**, 119 (1976).
- [143] D. Manzano, “A short introduction to the Lindblad master equation,” *AIP Advances* **10**, 025106 (2020).
- [144] L. Allen, *Optical Resonance and Two-Level Atoms*, revised ed. (Dover Publications Inc., 2003).
- [145] K. Jooya *et al.*, “Photon-scattering-rate measurement of atoms in a magneto-optical trap,” *Physical Review A* **88**, 063401 (2013).
- [146] C. J. Picken *et al.*, “Single atom imaging with an sCMOS camera,” *Applied Physics Letters* **111**, 164102 (2017).
- [147] S. Kuhr *et al.*, “Analysis of dephasing mechanisms in a standing-wave dipole trap,” *Physical Review A* **72**, 023406 (2005).
- [148] N. Zettili, *Quantum Mechanics: Concepts and Applications*, 2nd ed. (Wiley, 2009).
- [149] F. Bloch, “Nuclear Induction,” *Physical Review* **70**, 460 (1946).

- 
- [150] R. P. Feynman *et al.*, “Geometrical Representation of the Schrodinger Equation for Solving Maser Problems,” *Journal of Applied Physics* **28**, 49 (1957).
- [151] J. R. Johansson *et al.*, “QuTiP 2: A Python framework for the dynamics of open quantum systems,” *Computer Physics Communications* **184**, 1234 (2013).
- [152] M. Haas *et al.*, “Comparison of classical and second quantized description of the dynamic Stark shift,” (2006), arXiv:physics/0510160.
- [153] S. Kuhr, *A controlled quantum system of individual neutral atoms*, Ph.D. thesis, University of Bonn (2003).
- [154] M. S. Safronova *et al.*, “Frequency-dependent polarizabilities of alkali-metal atoms from ultraviolet through infrared spectral regions,” *Physical Review A* **73**, 022505 (2006).
- [155] F. Le Kien *et al.*, “Dynamical polarizability of atoms in arbitrary light fields: general theory and application to cesium,” *The European Physical Journal D* **67**, 92 (2013).
- [156] N. V. Vitanov *et al.*, “Stimulated Raman adiabatic passage in physics, chemistry, and beyond,” *Reviews of Modern Physics* **89**, 015006 (2017).
- [157] K. Mølmer and Y. Castin, “Monte Carlo wavefunctions in quantum optics,” *Quantum and Semiclassical Optics: Journal of the European Optical Society Part B* **8**, 49 (1996).
- [158] R. Han *et al.*, “Raman transitions without adiabatic elimination: a simple and accurate treatment,” *Journal of Modern Optics* **60**, 255 (2013).
- [159] G. Pelegrí *et al.*, “High-fidelity multiqubit Rydberg gates via two-photon adiabatic rapid passage,” *Quantum Science and Technology* **7**, 045020 (2022).

- 
- [160] K. M. Maller *et al.*, “Rydberg-blockade controlled-not gate and entanglement in a two-dimensional array of neutral-atom qubits,” *Physical Review A* **92**, 022336 (2015).
- [161] T. Amthor *et al.*, “Autoionization of an ultracold Rydberg gas through resonant dipole coupling,” *The European Physical Journal D* **53**, 329 (2009).
- [162] P. Huillery, *Few and Many-body Physics in Cold Rydberg Gases*, Ph.D. thesis, Universite Paris-Sud (2013).
- [163] A. Reinhard *et al.*, “Level shifts of rubidium Rydberg states due to binary interactions,” *Physical Review A* **75**, 032712 (2007).
- [164] W. Dür *et al.*, “Three qubits can be entangled in two inequivalent ways,” *Physical Review A* **62**, 062314 (2000).
- [165] Elliot Diamond-Hitchcock, *Unpublished*, Ph.D. thesis (2024).
- [166] J. A. Fedchak *et al.*, “Outgassing rate comparison of seven geometrically similar vacuum chambers of different materials and heat treatments,” *Journal of Vacuum Science & Technology B* **39**, 024201 (2021).
- [167] T. Arpornthip *et al.*, “Vacuum-pressure measurement using a magneto-optical trap,” *Physical Review A* **85**, 033420 (2012).
- [168] O. S. Burrow *et al.*, “Stand-alone vacuum cell for compact ultracold quantum technologies,” *Applied Physics Letters* **119**, 124002 (2021).
- [169] M. Audi *et al.*, *The Phenomenom of Leakage Current in Ion Pumps*, Tech. Rep. (Agilent, 2021).
- [170] D. Edwards, “Methane outgassing from a Ti sublimation pump,” *Journal of Vacuum Science and Technology* **17**, 279 (1980).

- 
- [171] R. W. G. Moore *et al.*, “Measurement of vacuum pressure with a magneto-optical trap: A pressure-rise method,” *Review of Scientific Instruments* **86**, 093108 (2015).
- [172] Y. R. P. Sortais *et al.*, “Diffraction-limited optics for single-atom manipulation,” *Physical Review A* **75**, 013406 (2007).
- [173] L. Béguin *et al.*, “Direct Measurement of the van der Waals Interaction between Two Rydberg Atoms,” *Physical Review Letters* **110**, 263201 (2013).
- [174] W. Alt, “An objective lens for efficient fluorescence detection of single atoms,” *Optik* **113**, 142 (2002).
- [175] J. D. Pritchard *et al.*, “Long working distance objective lenses for single atom trapping and imaging,” *Review of Scientific Instruments* **87**, 073107 (2016).
- [176] D. J. McCarron *et al.*, “Modulation transfer spectroscopy in atomic rubidium,” *Measurement Science and Technology* **19**, 105601 (2008).
- [177] R. K. Raj *et al.*, “High-Frequency Optically Heterodyned Saturation Spectroscopy Via Resonant Degenerate Four-Wave Mixing,” *Physical Review Letters* **44**, 1251 (1980).
- [178] M. Ducloy and D. Bloch, “Theory of degenerate four-wave mixing in resonant Doppler-broadened media. - II. Doppler-free heterodyne spectroscopy via collinear four-wave mixing in two- and three-level systems,” *Journal de Physique* **43**, 57 (1982).
- [179] M. L. Harris *et al.*, “Polarization spectroscopy in rubidium and cesium,” *Physical Review A* **73**, 062509 (2006).
- [180] H. Busche, *Contactless quantum non-linear optics with cold Rydberg atoms*, Ph.D. thesis, Durham University (2017).

- [181] K. Metzger, “Dreidimensionale Feldberechnung starr magnetisierter Permanentmagnete mit einer Anwendung in eisenlosen elektrischen Maschinen,” *Archiv für Elektrotechnik* **59**, 229 (1977).
- [182] C. Klempt *et al.*, “Ultraviolet light-induced atom desorption for large rubidium and potassium magneto-optical traps,” *Physical Review A* **73**, 013410 (2006).
- [183] A. Arnold, *Preparation and Manipulation of an  $^{87}\text{Rb}$  Bose-Einstein Condensate*, Ph.d. thesis, University of Sussex.
- [184] J. Dalibard and C. Cohen-Tannoudji, “Laser cooling below the Doppler limit by polarization gradients: simple theoretical models,” *Journal of the Optical Society of America B* **6**, 2023 (1989).
- [185] P. J. Ungar *et al.*, “Optical molasses and multilevel atoms: theory,” *Journal of the Optical Society of America B: Optical Physics* **6**, 2058 (1989).
- [186] S. Chu, “Laser Cooling and Trapping of Atoms,” *Proceedings of the 6th International Symposium on Advanced Nuclear Energy Research* (1995).
- [187] L. Russell *et al.*, “Measurements on release–recapture of cold  $^{85}\text{Rb}$  atoms using an optical nanofibre in a magneto-optical trap,” *Optics Communications* **309**, 313 (2013).
- [188] C. Salomon *et al.*, “Laser Cooling of Cesium Atoms Below  $3\ \mu\text{K}$ ,” *Europhysics Letters* **12**, 683 (1990).
- [189] M. Drewsen *et al.*, “Investigation of sub-Doppler cooling effects in a cesium magneto-optical trap,” *Applied Physics B* **59**, 283 (1994).
- [190] N. B. Delone and V. P. Krainov, “AC Stark shift of atomic energy levels,” *Physics-Uspekhi* **42**, 669 (1999).

- 
- [191] S. Chu *et al.*, “Experimental Observation of Optically Trapped Atoms,” *Physical Review Letters* **57**, 314 (1986).
- [192] K. Svoboda *et al.*, “Direct observation of kinesin stepping by optical trapping interferometry,” *Nature* **365**, 721 (1993).
- [193] A. Ashkin and J. M. Dziedzic, “Optical trapping and manipulation of viruses and bacteria,” *Science* **235**, 1517 (1987).
- [194] H. Bernien *et al.*, “Probing many-body dynamics on a 51-atom quantum simulator,” *Nature* **551**, 579 (2017).
- [195] H. Kim *et al.*, “In situ single-atom array synthesis using dynamic holographic optical tweezers,” *Nature Communications* **7**, 13317 (2016).
- [196] F. Reif, *Fundamentals of Statistical and Thermal Physics* (McGraw-Hill, 1965).
- [197] W. Alt *et al.*, “Single atoms in a standing-wave dipole trap,” *Physical Review A* **67**, 033403 (2003).
- [198] H. Labuhn, *Rydberg excitation dynamics and correlations in arbitrary 2D arrays of single atoms*, Ph.D. thesis, Université Paris Saclay (COMUE) (2016).
- [199] D. Kim *et al.*, “Large-scale uniform optical focus array generation with a phase spatial light modulator,” *Optics Letters* **44**, 3178 (2019).
- [200] T. Grünzweig *et al.*, “Using light-assisted collisions to consistently isolate individual atoms for quantum information processing,” *Quantum Information Processing* **10**, 925 (2011).
- [201] T. Grünzweig *et al.*, “Near-deterministic preparation of a single atom in an optical microtrap,” *Nature Physics* **6**, 951 (2010).

- 
- [202] B. Darquié, *Manipulation D'Atomes Dans Des Pieges Dipolaires Microscopiques Et Émission Contrôlée De Photons Par Un Atome Unique*, Ph.D. thesis, Université Paris Sud - Paris XI (2005).
- [203] C. Tuchendler *et al.*, “Energy distribution and cooling of a single atom in an optical tweezer,” *Physical Review A* **78**, 033425 (2008).
- [204] R. Grimm *et al.*, “Optical Dipole Traps for Neutral Atoms,” (Academic Press, 2000).
- [205] L. Beguin, *Measurement of the van der Waals interaction between two Rydberg atoms*, Ph.D. thesis, Institut d'Optique Graduate School (2013).
- [206] T. A. Savard *et al.*, “Laser-noise-induced heating in far-off resonance optical traps,” *Physical Review A* **56**, R1095 (1997).
- [207] M. D. Barrett *et al.*, “All-Optical Formation of an Atomic Bose-Einstein Condensate,” *Physical Review Letters* **87**, 010404 (2001).
- [208] G. Zürn *et al.*, “Fermionization of Two Distinguishable Fermions,” *Physical Review Letters* **108**, 075303 (2012).
- [209] S. De Leseleuc de Kerouara, *Quantum simulation of spin models with assembled arrays of Rydberg atoms*, Ph.D. thesis, Université Paris Saclay (COmUE) (2018).
- [210] K.-N. Schymik *et al.*, “In situ equalization of single-atom loading in large-scale optical tweezer arrays,” *Physical Review A* **106**, 022611 (2022).
- [211] M. Kwon *et al.*, “Parallel low-loss measurement of multiple atomic qubits,” *Physical Review Letters* **119**, 180504 (2017).
- [212] T. G. Walker and M. Saffman, “Chapter 2 - Entanglement of Two Atoms Using Rydberg Blockade,” (Academic Press, 2012).

- 
- [213] J. Heath *et al.*, “Mueller matrix maps of dichroic filters reveal polarization aberrations,” *Space Telescopes and Instrumentation 2020: Optical, Infrared, and Millimeter Wave, Space Telescopes and Instrumentation 2020: Optical, Infrared, and Millimeter Wave* **11443**, 1144341 (2020).
- [214] G. H. Zhang *et al.*, “Fast compact laser shutter using a direct current motor and three-dimensional printing,” *Review of Scientific Instruments* **86**, 126105 (2015).
- [215] H. Ball *et al.*, “The role of master clock stability in quantum information processing,” *npj Quantum Information* **2**, 1 (2016).
- [216] G. S. Uhrig, “Exact results on dynamical decoupling by pi pulses in quantum information processes,” *New Journal of Physics* **10**, 083024 (2008).
- [217] T. J. Green *et al.*, “Arbitrary quantum control of qubits in the presence of universal noise,” *New Journal of Physics* **15**, 095004 (2013).
- [218] M. J. Biercuk *et al.*, “Dynamical decoupling sequence construction as a filter-design problem,” *Journal of Physics B: Atomic, Molecular and Optical Physics* **44**, 154002 (2011).
- [219] J. Wang *et al.*, “Single-photon cesium Rydberg excitation spectroscopy using 318.6-nm UV laser and room-temperature vapor cell,” *Optics Express* **25**, 22510 (2017).
- [220] A. M. Hankin *et al.*, “Two-atom Rydberg blockade using direct  $6s$  to  $np$  excitation,” *Physical Review A* **89**, 033416 (2014).
- [221] X.-F. Shi, “Suppressing Motional Dephasing of Ground-Rydberg Transition for High-Fidelity Quantum Control with Neutral Atoms,” *Physical Review Applied* **13**, 024008 (2020).

- [222] S. de Léséleuc *et al.*, “Accurate Mapping of Multilevel Rydberg Atoms on Interacting Spin-1/2 Particles for the Quantum Simulation of Ising Models,” *Physical Review Letters* **120**, 113602 (2018).
- [223] H. J. Levine, *Quantum Information Processing and Quantum Simulation with Programmable Rydberg Atom Arrays*, Ph.D. thesis, Harvard University (2021).
- [224] I. R. Hill *et al.*, “Dual-axis cubic cavity for drift-compensated multi-wavelength laser stabilisation,” *Optics Express* **29**, 36758 (2021).
- [225] M. Sepiol, *Stabilization of a 729 nm laser to an ultra-high finesse reference cavity*, Master’s thesis, ETH Zurich (2012).
- [226] M. Zhao *et al.*, “Afterpulsing and its correction in fluorescence correlation spectroscopy experiments,” *Applied Optics* **42**, 4031 (2003).
- [227] A. Nevsky *et al.*, “Robust frequency stabilization of multiple spectroscopy lasers with large and tunable offset frequencies,” *Optics Letters* **38**, 4903 (2013).
- [228] J. Hald and V. Ruseva, “Efficient suppression of diode-laser phase noise by optical filtering,” *Journal of the Optical Society of America B* **22**, 2338 (2005).
- [229] S. de Léséleuc *et al.*, “Analysis of imperfections in the coherent optical excitation of single atoms to Rydberg states,” *Physical Review A* **97**, 053803 (2018).
- [230] L. Isenhower *et al.*, “Atom trapping in an interferometrically generated bottle beam trap,” *Optics Letters* **34**, 1159 (2009).
- [231] B. Ravon *et al.*, “Array of Individual Circular Rydberg Atoms Trapped in Optical Tweezers,” (2023), arXiv:2304.04831 [cond-mat, physics:physics, physics:quant-ph].

- 
- [232] W. D. Williams *et al.*, “Spectroscopic study of the  $7p_{1/2}$  and  $7p_{3/2}$  states in cesium-133,” *Laser Physics Letters* **15**, 095702 (2018).
- [233] R. Legaie, *Coherent control of Rydberg atoms using sub-kHz linewidth excitation lasers*, Ph.D. thesis, University of Strathclyde (2020).
- [234] N. Mielec *et al.*, “Atom interferometry with top-hat laser beams,” *Applied Physics Letters* **113**, 161108 (2018).
- [235] V. Pal *et al.*, “Generating flat-top beams with extended depth of focus,” *Applied Optics* **57**, 4583 (2018).
- [236] T. Preuschoff *et al.*, “Digital laser frequency and intensity stabilization based on the STEMLab platform (originally Red Pitaya),” *Review of Scientific Instruments* **91**, 083001 (2020).
- [237] G. Kasprowicz *et al.*, “Artiq and sinara: Open software and hardware stacks for quantum physics,” *OSA Quantum 2.0 Conference, OSA Quantum 2.0 Conference* , QTu8B.14 (2020).
- [238] P. B. Wigley *et al.*, “Fast machine-learning online optimization of ultracold-atom experiments,” *Scientific Reports* **6**, 25890 (2016).
- [239] M. Brune *et al.*, “Observing the Progressive Decoherence of the “Meter” in a Quantum Measurement,” *Physical Review Letters* **77**, 4887 (1996).
- [240] N. F. Ramsey, “A Molecular Beam Resonance Method with Separated Oscillating Fields,” *Physical Review* **78**, 695 (1950).
- [241] L. Essen and J. V. L. Parry, “An Atomic Standard of Frequency and Time Interval: A Cæsium Resonator,” *Nature* **176**, 280 (1955).
- [242] D. Schrader *et al.*, “An optical conveyor belt for single neutral atoms,” *Applied Physics B* **73**, 819 (2001).
- [243] M. F. Andersen *et al.*, “Echo Spectroscopy and Quantum Stability of Trapped Atoms,” *Physical Review Letters* **90**, 023001 (2003).

- [244] A. M. Kaufman *et al.*, “Cooling a Single Atom in an Optical Tweezer to Its Quantum Ground State,” *Physical Review X* **2**, 041014 (2012).
- [245] Engineering Toolbox, “Thermal expansion - linear expansion coefficients,” [Accessed: 10-October-2023].
- [246] L. Viola and S. Lloyd, “Dynamical suppression of decoherence in two-state quantum systems,” *Physical Review A* **58**, 2733 (1998).
- [247] E. L. Hahn, “Spin Echoes,” *Physical Review* **80**, 580 (1950).
- [248] A. M. Souza *et al.*, “Robust dynamical decoupling,” *Philosophical Transactions of the Royal Society A: Mathematical, Physical and Engineering Sciences* **370**, 4748 (2012).
- [249] D.W. Allan, “Statistics of atomic frequency standards,” *Proceedings of the IEEE* **54**, 221 (1966).
- [250] S. Wimperis, “Broadband, narrowband, and passband composite pulses for use in advanced NMR experiments,” *Journal of Magnetic Resonance, Series A* **109**, 221 (1994).
- [251] R. B. Blackman and J. W. Tukey, “The measurement of power spectra from the point of view of communications engineering — Part I,” *The Bell System Technical Journal* **37**, 185 (1958).
- [252] X. Li *et al.*, “3D Projection Sideband Cooling,” *Physical Review Letters* **108**, 103001 (2012).
- [253] J. Emerson *et al.*, “Scalable noise estimation with random unitary operators,” *Journal of Optics B: Quantum and Semiclassical Optics* **7**, S347 (2005).
- [254] C. Dankert *et al.*, “Exact and approximate unitary 2-designs and their application to fidelity estimation,” *Physical Review A* **80**, 012304 (2009).

- 
- [255] E. Knill *et al.*, “Randomized benchmarking of quantum gates,” *Physical Review A* **77**, 012307 (2008).
- [256] K. Boone *et al.*, “Randomized benchmarking under different gate sets,” *Physical Review A* **99**, 032329 (2019).
- [257] D. Grier and L. Schaeffer, “The Classification of Clifford Gates over Qubits,” *Quantum* **6**, 734 (2022).
- [258] E. Knill *et al.*, “An algorithmic benchmark for quantum information processing,” *Nature* **404**, 368 (2000).
- [259] D. C. McKay *et al.*, “Efficient  $Z$  gates for quantum computing,” *Physical Review A* **96**, 022330 (2017).
- [260] K. R. Brown *et al.*, “Single-qubit-gate error below  $10^{-4}$  in a trapped ion,” *Physical Review A* **84**, 030303 (2011).
- [261] T. P. Harty *et al.*, “High-fidelity preparation, gates, memory, and read-out of a trapped-ion quantum bit,” *Physical Review Letters* **113**, 220501 (2014).
- [262] S. Olmschenk *et al.*, “Randomized benchmarking of atomic qubits in an optical lattice,” *New Journal of Physics* **12**, 113007 (2010).
- [263] I. L. Chuang and M. A. Nielsen, “Prescription for experimental determination of the dynamics of a quantum black box,” *Journal of Modern Optics* **44**, 2455 (1997).
- [264] J. F. Poyatos *et al.*, “Complete Characterization of a Quantum Process: The Two-Bit Quantum Gate,” *Physical Review Letters* **78**, 390 (1997).
- [265] Y. S. Weinstein *et al.*, “Quantum process tomography of the quantum Fourier transform,” *The Journal of Chemical Physics* **121**, 6117 (2004).
- [266] K. Young *et al.*, *Diagnosing and Destroying Non-Markovian Noise*, Tech. Rep. (2020) [Accessed: 10-October-2023].

- 
- [267] H. Ball *et al.*, “Effect of noise correlations on randomized benchmarking,” *Physical Review A* **93**, 022303 (2016).
- [268] S. Kimmel *et al.*, “Robust calibration of a universal single-qubit gate set via robust phase estimation,” *Physical Review A* **92**, 062315 (2015).
- [269] K. M. Rudinger and E. Nielsen, *Quantum Characterization Verification & Validation (QCVV) Tutorial: Calibration-free Characterization (invited).*, Tech. Rep. (2016).
- [270] M. Kliesch and I. Roth, “Theory of Quantum System Certification,” *PRX Quantum* **2**, 010201 (2021).
- [271] Es. Magesan *et al.*, “Efficient Measurement of Quantum Gate Error by Interleaved Randomized Benchmarking,” *Physical Review Letters* **109**, 080505 (2012).
- [272] P. W. Shor, “Scheme for reducing decoherence in quantum computer memory,” *Physical Review A* **52**, R2493 (1995).
- [273] A. M. Steane, “Error Correcting Codes in Quantum Theory,” *Physical Review Letters* **77**, 793 (1996).
- [274] C. Ahn *et al.*, “Continuous quantum error correction via quantum feedback control,” *Physical Review A* **65**, 042301 (2002).
- [275] M. Sarovar and G. J. Milburn, “Continuous quantum error correction by cooling,” *Physical Review A* **72**, 012306 (2005).
- [276] M. A. Perlin *et al.*, “Fault-tolerant measurement-free quantum error correction with multi-qubit gates,” (2023), arXiv:2007.09804 [quant-ph].
- [277] R. Raussendorf and H. J. Briegel, “A One-Way Quantum Computer,” *Physical Review Letters* **86**, 5188 (2001).

- 
- [278] R. B. Griffiths and C.-S. Niu, “Semiclassical Fourier Transform for Quantum Computation,” *Physical Review Letters* **76**, 3228 (1996).
- [279] T.-C. Lu *et al.*, “Measurement as a Shortcut to Long-Range Entangled Quantum Matter,” *PRX Quantum* **3**, 040337 (2022).
- [280] B. Nikolov *et al.*, “Randomized benchmarking using nondestructive readout in a two-dimensional atom array,” *Physical Review Letters* **131**, 030602 (2023).
- [281] W. Huie *et al.*, “Repetitive Readout and Real-Time Control of Nuclear Spin Qubits in  $^{171}\text{Yb}$  Atoms,” *PRX Quantum* **4**, 030337 (2023).
- [282] J. W. Lis *et al.*, “Mid-circuit operations using the omg-architecture in neutral atom arrays,” (2023), arXiv:2305.19266 [cond-mat, physics:physics, physics:quant-ph].
- [283] M. A. Norcia *et al.*, “Mid-circuit qubit measurement and rearrangement in a  $^{171}\text{Yb}$  atomic array,” (2023), arXiv:2305.19119 [physics, physics:quant-ph].
- [284] J. Bochmann *et al.*, “Lossless State Detection of Single Neutral Atoms,” *Physical Review Letters* **104**, 203601 (2010).
- [285] J. Gallego *et al.*, “Strong Purcell Effect on a Neutral Atom Trapped in an Open Fiber Cavity,” *Physical Review Letters* **121**, 173603 (2018).
- [286] R. Gehr *et al.*, “Cavity-Based Single Atom Preparation and High-Fidelity Hyperfine State Readout,” *Physical Review Letters* **104**, 203602 (2010).
- [287] E. Deist *et al.*, “Superresolution microscopy of optical fields using tweezer-trapped single atoms,” *Physical Review Letters* **128**, 083201 (2022).

- [288] A. Fuhrmanek *et al.*, “Free-Space Lossless State Detection of a Single Trapped Atom,” *Physical Review Letters* **106**, 133003 (2011).
- [289] Y. Wang *et al.*, “Coherent addressing of individual neutral atoms in a 3d optical lattice,” *Physical Review Letters* **115**, 043003 (2015).
- [290] M. N. H. Chow *et al.*, “High-Fidelity State Detection of Alkali-Metal Atoms in Optical Tweezer Traps,” (2022), arXiv:2206.00144 [physics, physics:quant-ph].
- [291] M. Martinez-Dorantes *et al.*, “Fast Nondestructive Parallel Readout of Neutral Atom Registers in Optical Potentials,” *Physical Review Letters* **119**, 180503 (2017).
- [292] A. La Rooij *et al.*, “A comparative study of deconvolution techniques for quantum-gas microscope images,” (2023), arXiv:2207.08663 [cond-mat, physics:physics].
- [293] P. P. Man, “Wigner active and passive rotation matrices applied to NMR tensor,” *Concepts in Magnetic Resonance Part A* **45A**, e21385 (2016).
- [294] A. M. Steane and C. J. Foot, “Laser Cooling below the Doppler Limit in a Magneto-Optical Trap,” *Europhysics Letters* **14**, 231 (1991).
- [295] J. Werner *et al.*, “Atoms with anomalous Zeeman effect in a 1D-magneto-optical molasses,” *Optics Communications* **94**, 525 (1992).
- [296] M. Walhout *et al.*, “ $\sigma^+ - \sigma^-$  optical molasses in a longitudinal magnetic field,” *Journal of the Optical Society of America B* **9**, 1997 (1992).
- [297] M. J. Piotrowicz *et al.*, “Two-dimensional lattice of blue-detuned atom traps using a projected Gaussian beam array,” *Physical Review A* **88**, 013420 (2013).

- [298] T. M. Graham *et al.*, “Rydberg-mediated entanglement in a two-dimensional neutral atom qubit array,” *Physical Review Letters* **123**, 230501 (2019).
- [299] A. H. Myerson *et al.*, “High-Fidelity Readout of Trapped-Ion Qubits,” *Physical Review Letters* **100**, 200502 (2008).
- [300] H. K. Cummins *et al.*, “Tackling systematic errors in quantum logic gates with composite rotations,” *Physical Review A* **67**, 042308 (2003).
- [301] A. W. Carr, *Improving Quantum Computation with Neutral Cesium: Readout and Cooling on a Quadrupole Line, Conditions for Double Magic Traps and a Novel Dissipative Entanglement Scheme*, Ph.D. thesis, University of Wisconsin-Madison (2014).
- [302] E. Ising, “Beitrag zur Theorie des Ferromagnetismus,” *Zeitschrift für Physik* **31**, 253 (1925).
- [303] R.A. Serway and J. W. Jewett, *Physics for Scientists and Engineers* (Cengage Learning, 2014).
- [304] J. M. Yeomans, *Statistical Mechanics of Phase Transitions* (Oxford University Press, Oxford England : New York, 1993).
- [305] A. Dutta *et al.*, *Quantum Phase Transitions in Transverse Field Spin Models: From Statistical Physics to Quantum Information* (Cambridge University Press, Cambridge, 2015).
- [306] T. Pohl *et al.*, “Dynamical Crystallization in the Dipole Blockade of Ultracold Atoms,” *Physical Review Letters* **104**, 043002 (2010).
- [307] H. Labuhn *et al.*, “Tunable two-dimensional arrays of single Rydberg atoms for realizing quantum Ising models,” *Nature* **534**, 667 (2016).
- [308] J. Zeiher *et al.*, “Many-body interferometry of a Rydberg-dressed spin lattice,” *Nature Physics* **12**, 1095 (2016).

- 
- [309] J. B. Kogut, “An introduction to lattice gauge theory and spin systems,” *Reviews of Modern Physics* **51**, 659 (1979).
- [310] R. Islam *et al.*, “Emergence and Frustration of Magnetism with Variable-Range Interactions in a Quantum Simulator,” *Science* **340**, 583 (2013).
- [311] C. Song *et al.*, “10-Qubit Entanglement and Parallel Logic Operations with a Superconducting Circuit,” *Physical Review Letters* **119**, 180511 (2017).
- [312] P. Schauß *et al.*, “Crystallization in Ising quantum magnets,” *Science* **347**, 1455 (2015).
- [313] L. R. Liu *et al.*, “Molecular assembly of ground-state cooled single atoms,” *Physical Review X* **9**, 021039 (2019).
- [314] A. Impertro *et al.*, “An unsupervised deep learning algorithm for single-site reconstruction in quantum gas microscopes,” *Communications Physics* **6**, 1 (2023).
- [315] P. Virtanen *et al.*, “SciPy 1.0: fundamental algorithms for scientific computing in Python,” *Nature Methods* **17**, 261 (2020).
- [316] R. Storn and K. Price, “Differential Evolution – A Simple and Efficient Heuristic for global Optimization over Continuous Spaces,” *Journal of Global Optimization* **11**, 341 (1997).
- [317] E. Farhi *et al.*, “A quantum approximate optimization algorithm,” (2014), arXiv:1411.4028 [quant-ph] .
- [318] L. Zhou *et al.*, “Quantum Approximate Optimization Algorithm: Performance, Mechanism, and Implementation on Near-Term Devices,” *Physical Review X* **10**, 021067 (2020).

- 
- [319] E. A. Donley *et al.*, “Double-pass acousto-optic modulator system,” *Review of Scientific Instruments* **76**, 063112 (2005).
- [320] R. Song *et al.*, “Lifetime Measurement of Cesium Atoms Using a Cold Rydberg Gas,” *Applied Sciences* **12**, 2713 (2022).
- [321] J. Glaz and C. P. Sison, “Simultaneous confidence intervals for multinomial proportions,” *Journal of Statistical Planning and Inference* **82**, 251 (1999).
- [322] D. Bluvstein *et al.*, “Logical quantum processor based on reconfigurable atom arrays,” (2023), arXiv:2312.03982 [cond-mat, physics:physics, physics:quant-ph].